pain and suffering

University of Alberta

Non-Diffusive Numerical Simulations of Gravity Separation in Inclined Plate Settlers

by

Kevin C. Dorma ©

A thesis
submitted to the Faculty of Graduate Studies and Research
in partial fulfillment of the requirements for the degree of
Doctor of Philosophy

in

Chemical Engineering

Department of Chemical and Materials Engineering

Edmonton, Alberta
Spring 1998

National Library
of Canada

Acquisitions and
Bibliographic Services

395 Wellington Street
Ottawa ON K1A 0N4
Canada

Bibliothèque nationale
du Canada

Acquisitions et
services bibliographiques

395, rue Wellington
Ottawa ON K1A 0N4
Canada

Your file Votre référence

Our file Notre référence

The author has granted a non-exclusive licence allowing the National Library of Canada to reproduce, loan, distribute or sell copies of this thesis in microform, paper or electronic formats.

The author retains ownership of the copyright in this thesis. Neither the thesis nor substantial extracts from it may be printed or otherwise reproduced without the author's permission.

L'auteur a accordé une licence non exclusive permettant à la Bibliothèque nationale du Canada de reproduire, prêter, distribuer ou vendre des copies de cette thèse sous la forme de microfiche/film, de reproduction sur papier ou sur format électronique.

L'auteur conserve la propriété du droit d'auteur qui protège cette thèse. Ni la thèse ni des extraits substantiels de celle-ci ne doivent être imprimés ou autrement reproduits sans son autorisation.

0-612-29030-1

Canada

University of Alberta
Faculty of Graduate Studies and Research

The undersigned certify that they have read, and recommend to the Faculty of Graduate Studies and Research for acceptance, a thesis entitled **Non-Diffusive Numerical Simulations of Gravity Separation in Inclined Plate Settlers** submitted by **Kevin C. Dorma** in partial fulfillment of the requirements for the degree of **Doctor of Philosophy**.

Dr. K. Nandakumar (Supervisor)

Dr. J. H. Masliyah

Dr. W. H. Finlay

Dr. J. W. Yokota

Dr. M. N. Esmail (External examiner)

Date : Jan. 20, 1998.

Abstract

Inclined plate sedimentation is driven by strong buoyancy forces caused by the discontinuous dispersed phase volume fraction profile at suspension interfaces. Accurate shock capturing methods have been used successfully to model discontinuous flows in transonic aerodynamics for several years. A non-diffusive shock capturing method was applied to the numerical modelling of inclined plate sedimentation.

An efficient algorithm was developed to model sedimentation described by three differential equations: a material transport equation for the dispersed phase concentration plus a vorticity transport equation and a stream function equation for the homogenous mixture. The slip velocity of the dispersed phase was modelled with a Richardson & Zaki type of relation.

The simulation code was validated with a series of sedimentation examples. The numerical results compared well with those obtained by other researchers and with experimental results. The thickness of the clear fluid slit obtained with the simulation agreed well with experimental data.

The non-diffusive numerical results were compared with first order accurate results for several cases of batch sedimentation. The non-diffusive results captured several features observed in sedimentation experiments including the the correct wave length

of the disturbance between the suspension and the clear fluid slit. First order accurate simulations suffered from excessive numerical diffusion and did not model inclined plate sedimentation well with reasonable mesh sizes.

Results of the non-diffusive simulations were compared with experimental data for the location of the inception point of the wavy suspension interface for a range of parameters: liquid viscosities 18.8, 28.8 and 38.1 mPa s; inclinations of 5 – 50°; dispersed phase volume fractions of $\phi = 0.01 - 0.15$. This location is related to the growth rate of the wavy disturbance. The numerical results agreed well with the experimental data.

A parameter study was carried out to determine the effect of uniform internal resistance to motion on the flow in an inclined plate sedimentation vessel. The resistance was modelled in the manner of porous media with constant permeability and linear with the fluid velocity. The numerical results suggest that internal resistance stabilizes the wavy suspension interface and reduces the entrainment of suspension in the clear fluid.

Acknowledgments

Many people have played important roles in my life during my stay at the Department. Bob Barton did a lot more than keep the computer network alive and well or satisfy my insatiable need for CPU power. Bob trusted me with a few responsibilities in the computer lab. In return he received an eager Guinea pig to test new features on the network.

Several of my fellow students deserve mention for their moral support. Andy Jenkins provided a lot of support and the odd "reality check" throughout my research. His knowledge of practical engineering assisted me in numerous ways. Andy provided invaluable support in the later stages of the thesis preparation. Sean Sanders, Shulamit Kuttner, Norbert Alleborn, Randy Miller and Harvey Yarranton were often just as frustrated as I was. We shared enthusiasm when things worked and bashed our heads together when things did not. Although we had vastly different projects it was very useful to bounce ideas off each other. These people helped me get through the vicious cycle of elation/depression that accompanies a project that succeeds wildly and then fails.

My brother Brian deserves special credit for putting up with me when things were really difficult. Mom and Dad were behind me all of the way even though they did not understand what I was doing. Mom and Dad understood my frustrations when other people did not.

Jeff Yokota played a crucial role in the final ten months of my research. Jeff provided invaluable guidance on implementing accurate and fast algorithms in my code: this saved by thesis. He introduced me to new techniques used in computational aerodynamics. Jeff did not accept poor or mediocre work and he explained how to make the work better. He provided encouragement that my research was good even when there were problems. He also acknowledged that a successful research project often relies on "getting lucky."

One learns through making mistakes: I have learned a great deal.

Contents

Chapter 1

Introduction 1

1.1 Historical background 1

1.2 Research goals 5

1.3 Thesis overview 5

Chapter 2

Governing Equations 7

2.1 Two fluid model 7

2.2 Homogeneous model 10

2.2.1 Definition of the mixture velocity and dispersed phase slip velocity . 10

2.2.2 Material transport equation 11

2.2.3 Momentum equation for the homogeneous mixture 11

2.3 Simplifying assumptions 12

2.4 Comparison with the homogeneous model of Hill et al. 13

2.5 Governing equations in dimensionless form 14

2.6 Comparison with the governing equations of Acrivos et al. 15

2.7 Linear stability analysis of Herbolzheimer 16

2.8 Vorticity-stream function formulation 17

2.9 Summary 18

Chapter 3

Discretization and solution algorithm 19

3.1 Mesh description 20

3.2 Material transport equation 21

3.3 Vorticity transport equation 24

3.4 Stream function equation 26

3.5 Direct solution of the discretized vorticity and stream function equations . . 26

3.6 Summary 26

Chapter 4

Linear stability and truncation error analysis 28

4.1 Linear stability analysis 28

 4.1.1 First order upwind differencing 29

 4.1.2 UNO2 scheme 32

4.2 Truncation error analysis 38

 4.2.1 First order upwinding of the convection-diffusion equation 38

 4.2.2 UNO2 differencing of the convection-diffusion equation 41

4.3 Numerical results for vertical sedimentation 43

4.4 Truncation error of the buoyancy driving force 49

4.5 Effect of a smeared interface on the velocity profile 50

4.6 Summary 54

Chapter 5

Code validation 55

5.1 Driven cavity 55

5.2 One dimensional batch sedimentation 57

5.3 Batch inclined sedimentation: position of the horizontal interface 60

5.4 Batch inclined sedimentation: interface positions for large inclinations . . . 66

5.5 Batch inclined sedimentation: thickness of the clear fluid slit 70

 5.5.1 Development of the clear fluid zone 70

 5.5.2 Comparison with experimental and theoretical results 72

5.6 Summary 78

Chapter 6

Comparison of non-diffusive and first order results for inclined plate sedimentation **79**

6.1 Batch sedimentation of 67.7 mPa s suspension with 1 % concentration 80

6.2 Batch sedimentation of 67.7 mPa s suspension with 10 % concentration . . . 85

6.3 Batch sedimentation of 9.328 mPa s suspension 94

6.4 Batch sedimentation of 2.678 mPa s suspension 106

6.5 Discussion 112

6.6 Summary 112

Chapter 7

Inception of waves in inclined plate sedimentation **114**

7.1 Description of the runs 114

7.2 Effect of inclination angle on inception distance 118

7.3 Effect of concentration on inception distance 131

7.4 Comparison of the wave amplitude growth rates 139

7.5 Summary 141

Chapter 8

Sedimentation with a uniform internal resistance to motion **142**

8.1 Uniform resistance term 142

8.2 Dependance of batch sedimentation rate on equivalent wall separation . . . 143

8.3 Dependance of inverse inception distance on internal resistance and fluid viscosity 149

8.4 Dependance of inverse inception distance on internal resistance and inclination angle 159

8.5 Dependance of inverse inception distance on internal resistance and feed concentration 169

8.6 Summary 170

Chapter 9

Comparison of results with different buoyancy discretizations 171

9.1 Horizontal interface position 171

9.2 Velocity profiles 174

9.3 Inverse of the wave inception distance 181

9.4 Summary 183

Chapter 10

Summary 184

10.1 Conclusions 184

10.2 Recommendations for future work 185

Appendix A

Order of magnitude analysis of the two fluid momentum equations 192

A.1 Momentum interactions 192

A.2 Slip velocity 193

Appendix B

Derivation of the momentum equations for the homogeneous model 195

Appendix C

Flow of a stratified fluid between inclined parallel plates 198

List of Tables

6.1 Physical properties and characteristics of the suspensions for the accuracy comparison. 80

7.1 Inlet feed rate and split ratio for simulations with $\phi = 0.05$. 115

7.2 Inlet feed rate and split ratio for simulations with $\theta = 20°$. 115

List of Figures

1.1 Geometry for batch sedimentation between inclined parallel plates. 2

1.2 Dimensionless flux curve for $V_s/V_{s,\infty} = (1 - \phi_s)^{5.1}$. 4

3.1 Staggered mesh for $\hat{u}, \hat{v}, \hat{\phi}, \hat{\omega}, \hat{\psi}$. 20

4.1 Modulus of the growth rate for first order upwind differencing with $\beta_{\hat{\omega}} = 1/2$ and $N_D = 10$: $N_C = 0.5, 0.9, 1.1$. 31

4.2 Modulus of the growth rate for first order upwind differencing with $\beta_{\hat{\omega}} = 1/2$ and $\zeta = \pi$: $N_D = 0, 10$. 31

4.3 Modulus of the growth rate for UNO2 differencing (slope becomes more positive and inflection becomes more positive) with $\beta_{\hat{\omega}} = 1/2$ and $\zeta = \pi$: $N_D = 0, 10$. 35

4.4 Modulus of the growth rate for UNO2 differencing (slope becomes less positive and inflection becomes less negative) with $\beta_{\hat{\omega}} = 1/2$ and $\zeta = \pi$: $N_D = 0, 10$. 36

4.5 Modulus of the growth rate for UNO2 differencing (slope becomes more positive and inflection becomes less positive) with $\beta_{\hat{\omega}} = 1/2$ and $\zeta = \pi$: $N_D = 0, 10$. 37

4.6 Volume fraction profiles from UNO2 and first order upwind differencing for 1-D vertical sedimentation of 1 % suspension. 44

4.7 Volume fraction profiles from UNO2 and first order upwind differencing for 1-D vertical sedimentation of 10 % suspension. 45

4.8 Volume fraction profiles from UNO2 and first order upwind differencing for 1-D vertical sedimentation of 30 % suspension. 46

4.9 Grid resolution of the suspension interface for $\Delta\hat{x} = 1/20$, $1/100$ and $1/1000$. 48

4.10 Second through fifth order grid scale derivatives of the volume fraction profile calculated with finite differences ($\Delta\hat{x} = 1/100$). 48

4.11 Gravity driven flow of a density stratified fluid between inclined parallel plates. 51

4.12 Velocity profiles for gravity driven flow of a density stratified fluid between inclined parallel plates. 52

4.13 Velocity profiles for gravity driven flow of a fluid with a linear density variation between inclined parallel plates. 53

5.1 Sketch of the two dimensional geometry used in the simulations of batch sedimentation. 56

5.2 Streamlines for the driven cavity with Re = 400: $\hat{\psi}$ = -0.11, -0.10, -0.08, -0.06, -0.04, -0.02, -0.01, -0.00001, 0.000001, 0.00001, 0.0001, 0.001, 0.002. . 57

5.3 Interface positions for batch sedimentation of suspensions with $\hat{\phi} = 0.0200$, 0.04417 and 0.08838. Lines denote the simulation results, points denote the experimental data of Font [11]. 59

5.4 Position of horizontal suspension interface for simulations of batch sedimentation at inclinations $\theta = 0°$, 20°, 35° and 50°. Lines denote the numerical simulations, points denote the experimental data of Acrivos & Herbolzheimer [1]. 61

5.5 Velocity vectors and suspension interfaces at $\hat{t} = 0.02$ for 35° inclination and 10 % initial concentration. Vector length is proportional to $|\boldsymbol{u}|^{1/2}$. . . . 63

5.6 Velocity vectors and suspension interfaces at $\hat{t} = 0.1$ for 35° inclination and 10 % initial concentration. Vector length is proportional to $|\boldsymbol{u}|^{1/2}$. 64

5.7 Longitudinal velocity and concentration profile at $y = 0.625\,L$ at $\hat{t} = 0.1$ for 35° inclination and 10 % initial concentration. 65

5.8 Interface and velocity profiles obtained with a 40 × 200 mesh for $\hat{\phi} = 0.01$, $\theta = 80°$ and 1:100 aspect ratio for $\hat{t}$ = 0.002, 0.004, 0.006, 0.008 and 0.014. . 68

5.9 Interface and velocity profiles obtained with a 80 × 400 mesh for $\hat{\phi} = 0.01$, $\theta = 80°$ and 1:100 aspect ratio for $\hat{t}$ = 0.002, 0.004, 0.006, 0.008 and 0.014. . 69

5.10 Development of the clear fluid layer ($\hat{\phi}_s = 0.008, \mu_f = 9.328\,\mathrm{mPa\,s}, \theta = 45°$): $\hat{t}$ = 0.01, 0.02, 0.03, 0.04, 0.05. Points denote the experimental data of Shaqfeh & Acrivos [45]. 71

5.11 Thickness of the clear fluid layer for ($\hat{\phi} = 0.008, \bar{\mu}_f = 9.328\,\mathrm{mPa\,s}, \theta = 45°$): a is from the numerical simulation, b is from the analytic expression of Shaqfeh & Acrivos. Points denote the experimental data of Shaqfeh & Acrivos [45]. 73

5.12 Thickness of the clear fluid layer for ($\hat{\phi} = 0.005, \bar{\mu}_f = 9.328\,\mathrm{mPa\,s}, \theta = 35°$): a is from the numerical simulation, b is from the analytic expression of Shaqfeh & Acrivos. Points denote the experimental data of Shaqfeh & Acrivos [45]. 74

5.13 Thickness of the clear fluid layer for ($\hat{\phi} = 0.012, \bar{\mu}_f = 6.996\,\mathrm{mPa\,s}, \theta = 45^\circ$): a is from the numerical simulation, b is from the analytic expression of Shaqfeh & Acrivos. Points denote the experimental data of Shaqfeh & Acrivos [45]. 75

5.14 Thickness of the clear fluid layer for ($\hat{\phi} = 0.010, \bar{\mu}_f = 5.597\,\mathrm{mPa\,s}, \theta = 45^\circ$): a is from the numerical simulation, b is from the analytic expression of Shaqfeh & Acrivos. Points denote the experimental data of Shaqfeh & Acrivos [45]. 76

5.15 Thickness of the clear fluid layer for ($\hat{\phi} = 0.010, \bar{\mu}_f = 5.597\,\mathrm{mPa\,s}, \theta = 35^\circ$): a is from the numerical simulation, b is from the analytic expression of Shaqfeh & Acrivos. Points denote the experimental data of Shaqfeh & Acrivos [45]. 77

6.1 Velocity profile and concentration isolines for batch sedimentation (40×100 mesh, non-diffusive): $\hat{t} = 0.04$, $\phi = 0.01$, $\theta = 30^\circ$, $\bar{\mu}_f = 67.7\,\mathrm{mPa\,s}$. 81

6.2 Velocity profile and concentration isolines for batch sedimentation (80×400 mesh, non-diffusive): $\hat{t} = 0.04$, $\phi = 0.01$, $\theta = 30^\circ$, $\bar{\mu}_f = 67.7\,\mathrm{mPa\,s}$. 82

6.3 Velocity profile and concentration isolines for batch sedimentation (40×100 mesh, first order): $\hat{t} = 0.04$, $\phi = 0.01$, $\theta = 30^\circ$, $\bar{\mu}_f = 67.7\,\mathrm{mPa\,s}$. 83

6.4 Velocity profile and concentration isolines for batch sedimentation (80×400 mesh, first order): $\hat{t} = 0.04$, $\phi = 0.01$, $\theta = 30^\circ$, $\bar{\mu}_f = 67.7\,\mathrm{mPa\,s}$. 84

6.5 Velocity profile and concentration isolines for batch sedimentation (40×100 mesh, non-diffusive): $\hat{t} = 0.1$, $\phi = 0.1$, $\theta = 30^\circ$, $\bar{\mu}_f = 67.7\,\mathrm{mPa\,s}$. 87

6.6 Velocity profile and concentration isolines for batch sedimentation (80×400 mesh, non-diffusive): $\hat{t} = 0.1$, $\phi = 0.1$, $\theta = 30^\circ$, $\bar{\mu}_f = 67.7\,\mathrm{mPa\,s}$. 88

6.7 Velocity profile and concentration isolines for batch sedimentation (40×100 mesh, first order): $\hat{t} = 0.1$, $\phi = 0.1$, $\theta = 30^\circ$, $\bar{\mu}_f = 67.7\,\mathrm{mPa\,s}$. 89

6.8 Velocity profile and concentration isolines for batch sedimentation (80×400 mesh, first order): $\hat{t} = 0.1$, $\phi = 0.1$, $\theta = 30^\circ$, $\bar{\mu}_f = 67.7\,\mathrm{mPa\,s}$. 90

6.9 Velocity profile and concentration isolines for batch sedimentation (80×800 mesh, first order): $\hat{t} = 0.1$, $\phi = 0.1$, $\theta = 30^\circ$, $\bar{\mu}_f = 67.7\,\mathrm{mPa\,s}$. 91

6.10 Dispersed phase volume fraction profile across $y = L/2$ for the 40×100 and 80×400 meshes: $\hat{t} = 0.1$, $\phi = 0.1$, $\theta = 30^\circ$, $\bar{\mu}_f = 67.7\,\mathrm{mPa\,s}$. 92

6.11 Longitudinal mixture velocity profile across $y = L/2$ for the 40×100 and 80×400 meshes: $\hat{t} = 0.1$, $\phi = 0.1$, $\theta = 30^\circ$, $\bar{\mu}_f = 67.7\,\mathrm{mPa\,s}$. 92

6.12 Profile for the longitudinal clear fluid flux across $y = L/2$ for the 40×100 and 80×400 meshes: $\hat{t} = 0.1$, $\phi = 0.1$, $\theta = 30^\circ$, $\bar{\mu}_f = 67.7\,\mathrm{mPa\,s}$. 93

6.13 Velocity profile and concentration isolines for batch sedimentation (40×100 mesh, non-diffusive): $\hat{t} = 0.03$, $\theta = 30^\circ$, $\bar{\mu}_f = 9.328\,\mathrm{mPa\,s}$. 96

6.14 Velocity profile and concentration isolines for batch sedimentation (40×200 mesh, non-diffusive): $\hat{t} = 0.03$, $\theta = 30°$, $\bar{\mu}_f = 9.328\,\mathrm{mPa\,s}$. 97

6.15 Velocity profile and concentration isolines for batch sedimentation (40×400 mesh, non-diffusive): $\hat{t} = 0.03$, $\theta = 30°$, $\bar{\mu}_f = 9.328\,\mathrm{mPa\,s}$. 98

6.16 Velocity profile and concentration isolines for batch sedimentation (80×400 mesh, non-diffusive): $\hat{t} = 0.03$, $\theta = 30°$, $\bar{\mu}_f = 9.328\,\mathrm{mPa\,s}$. 99

6.17 Velocity profile and concentration isolines for batch sedimentation (40×400 mesh, non-diffusive): $\hat{t} = 0.032$, $\theta = 30°$, $\bar{\mu}_f = 9.328\,\mathrm{mPa\,s}$. 100

6.18 Velocity profile and concentration isolines for batch sedimentation (80×400 mesh, non-diffusive): $\hat{t} = 0.032$, $\theta = 30°$, $\bar{\mu}_f = 9.328\,\mathrm{mPa\,s}$. 101

6.19 Velocity profile and concentration isolines for batch sedimentation (40×100 mesh, first order): $\hat{t} = 0.03$, $\theta = 30°$, $\bar{\mu}_f = 9.328\,\mathrm{mPa\,s}$. 102

6.20 Velocity profile and concentration isolines for batch sedimentation (40×200 mesh, first order): $\hat{t} = 0.03$, $\theta = 30°$, $\bar{\mu}_f = 9.328\,\mathrm{mPa\,s}$. 103

6.21 Velocity profile and concentration isolines for batch sedimentation (40×400 mesh, first order): $\hat{t} = 0.03$, $\theta = 30°$, $\bar{\mu}_f = 9.328\,\mathrm{mPa\,s}$. 104

6.22 Velocity profile and concentration isolines for batch sedimentation (80×400 mesh, first order): $\hat{t} = 0.03$, $\theta = 30°$, $\bar{\mu}_f = 9.328\,\mathrm{mPa\,s}$. 105

6.23 Velocity profile and concentration isolines for batch sedimentation (40×100 mesh, non-diffusive): $\hat{t} = 0.05$, $\theta = 30°$, $\bar{\mu}_f = 2.678\,\mathrm{mPa\,s}$. 107

6.24 Velocity profile and concentration isolines for batch sedimentation (40×200 mesh, non-diffusive): $\hat{t} = 0.05$, $\theta = 30°$, $\bar{\mu}_f = 2.678\,\mathrm{mPa\,s}$. 108

6.25 Velocity profile and concentration isolines for batch sedimentation (40×400 mesh, non-diffusive): $\hat{t} = 0.05$, $\theta = 30°$, $\bar{\mu}_f = 2.678\,\mathrm{mPa\,s}$. 109

6.26 Velocity profile and concentration isolines for batch sedimentation (80×400 mesh, non-diffusive): $\hat{t} = 0.05$, $\theta = 30°$, $\bar{\mu}_f = 2.678\,\mathrm{mPa\,s}$. 110

6.27 Velocity profile and concentration isolines for batch sedimentation (80×400 mesh, first order): $\hat{t} = 0.05$, $\theta = 30°$, $\bar{\mu}_f = 2.678\,\mathrm{mPa\,s}$. 111

7.1 Sketch of the two dimensional geometry used in the simulations of continuous sedimentation. 116

7.2 Mean and 95 % confidence limits of the position of clear fluid interface ($\hat{\phi} = 0.05$, $\theta = 5°$, $\bar{\mu}_f = 18.8\,\mathrm{mPa\,s}$). 117

7.3 Statistical comparison of the wave amplitude with 25 % of the mean clear fluid thickness ($\hat{\phi} = 0.05$, $\theta = 5°$, $\bar{\mu}_f = 18.8\,\mathrm{mPa\,s}$). 117

7.4 Inverse of the inception distance for $\hat{\phi} = 0.05$, $\bar{\mu}_f = 38.1\,\mathrm{mPa\,s}$: ⋄ denotes the numerical simulation; + denotes the experimental data of Herbolzheimer [18]. 118

7.5 Inverse of the inception distance for $\hat{\phi} = 0.05$, $\bar{\mu}_f = 28.8\,\mathrm{mPa\,s}$: ⋄ denotes the numerical simulation; + denotes the experimental data of Herbolzheimer [18]. 119

7.6 Inverse of the inception distance for $\hat{\phi} = 0.05$, $\bar{\mu}_f = 18.8\,\mathrm{mPa\,s}$: ⋄ denotes the numerical simulation; + denotes the experimental data of Herbolzheimer [18]. 119

7.7 Flow pattern for $\hat{\phi} = 0.05$, $\bar{\mu}_f = 38.1\,\mathrm{mPa\,s}$, $\theta = 10°$. 121

7.8 Flow pattern for $\hat{\phi} = 0.05$, $\bar{\mu}_f = 38.1\,\mathrm{mPa\,s}$, $\theta = 15°$. 122

7.9 Flow pattern for $\hat{\phi} = 0.05$, $\bar{\mu}_f = 38.1\,\mathrm{mPa\,s}$, $\theta = 20°$. 123

7.10 Flow pattern for $\hat{\phi} = 0.05$, $\bar{\mu}_f = 28.8\,\mathrm{mPa\,s}$, $\theta = 10°$. 124

7.11 Flow pattern for $\hat{\phi} = 0.05$, $\bar{\mu}_f = 28.8\,\mathrm{mPa\,s}$, $\theta = 15°$. 125

7.12 Flow pattern for $\hat{\phi} = 0.05$, $\bar{\mu}_f = 28.8\,\mathrm{mPa\,s}$, $\theta = 20°$. 126

7.13 Flow pattern for $\hat{\phi} = 0.05$, $\bar{\mu}_f = 18.8\,\mathrm{mPa\,s}$, $\theta = 10°$. 127

7.14 Well mixed flow pattern for $\hat{\phi} = 0.05$, $\bar{\mu}_f = 18.8\,\mathrm{mPa\,s}$, $\theta = 15°$. 128

7.15 Uniform flow pattern for $\hat{\phi} = 0.05$, $\bar{\mu}_f = 18.8\,\mathrm{mPa\,s}$, $\theta = 15°$. 129

7.16 Flow pattern for $\hat{\phi} = 0.05$, $\bar{\mu}_f = 18.8\,\mathrm{mPa\,s}$, $\theta = 20°$. 130

7.17 Inverse of the inception distance for $\theta = 20°$, $\bar{\mu}_f = 38.1\,\mathrm{mPa\,s}$: ⋄ denotes the numerical simulation; + denotes the experimental data of Herbolzheimer [18]. 131

7.18 Inverse of the inception distance for $\theta = 20°$, $\bar{\mu}_f = 28.8\,\mathrm{mPa\,s}$: ⋄ denotes the numerical simulation; + denotes the experimental data of Herbolzheimer [18]. 132

7.19 Inverse of the inception distance for $\theta = 20°$, $\bar{\mu}_f = 18.8\,\mathrm{mPa\,s}$: ⋄ denotes the numerical simulation; + denotes the experimental data of Herbolzheimer [18]. 132

7.20 Flow pattern for $\hat{\phi} = 0.10$, $\bar{\mu}_f = 38.1\,\mathrm{mPa\,s}$, $\theta = 20°$. 134

7.21 Flow pattern for $\hat{\phi} = 0.15$, $\bar{\mu}_f = 38.1\,\mathrm{mPa\,s}$, $\theta = 20°$. 135

7.22 Flow pattern for $\hat{\phi} = 0.10$, $\bar{\mu}_f = 28.8\,\mathrm{mPa\,s}$, $\theta = 20°$. 136

7.23 Flow pattern for $\hat{\phi} = 0.15$, $\bar{\mu}_f = 28.8\,\mathrm{mPa\,s}$, $\theta = 20°$. 137

7.24 Flow pattern for $\hat{\phi} = 0.10$, $\bar{\mu}_f = 18.8\,\mathrm{mPa\,s}$, $\theta = 20°$. 138

7.25 Fractional deviation of the wave growth rate between the numerical simulation and the experimental data for $\hat{\phi} = 0.05$: ◇ is 18.8 mPa s; + is 28.8 mPa s; □ is 38.1 mPa s. 140

7.26 Fractional deviation of the wave growth rate between the numerical simulation and the experimental data for $\theta = 20°$: ◇ is 18.8 mPa s; + is 28.8 mPa s; □ is 38.1 mPa s. 140

8.1 Horizontal interface height for batch sedimentation with $\bar{\mu}_f = 18.8\,\mathrm{mPa\,s}$, $\phi = 0.05$, $\theta = 10°$ 144

8.2 Horizontal interface height for batch sedimentation with $\bar{\mu}_f = 18.8\,\mathrm{mPa\,s}$, $\phi = 0.05$, $\theta = 30°$ . . . 144

8.3 Flow pattern for batch sedimentation at $t = 0.1$ with $\phi = 0.05$, $\bar{\mu}_f = 18.8\,\mathrm{mPa\,s}$, $\theta = 10°$ and no internal resistance to motion. . . . 145

8.4 Flow pattern for batch sedimentation at $t = 0.1$ with $\phi = 0.05$, $\bar{\mu}_f = 18.8\,\mathrm{mPa\,s}$, $\theta = 10°$ and 20 mm equivalent wall separation. . . . 146

8.5 Flow pattern for batch sedimentation at $t = 0.05$ with $\phi = 0.05$, $\bar{\mu}_f = 18.8\,\mathrm{mPa\,s}$, $\theta = 30°$ and no internal resistance to motion. . . . 147

8.6 Flow pattern for batch sedimentation at $t = 0.05$ with $\phi = 0.05$, $\bar{\mu}_f = 18.8\,\mathrm{mPa\,s}$, $\theta = 30°$ and 20 mm equivalent wall separation. . . . 148

8.7 Dependance of the inverse of the inception distance on equivalent wall separation for $\phi = 0.05$, $\theta = 10°$: ◇ is 18.8 mPa s; + is 28.8 mPa s; □ is 38.1 mPa s. . . . 150

8.8 Flow pattern for $\phi = 0.05$, $\bar{\mu}_f = 18.8\,\mathrm{mPa\,s}$, $\theta = 10°$ and infinite equivalent wall separation. . . . 151

8.9 Flow pattern for $\phi = 0.05$, $\bar{\mu}_f = 18.8\,\mathrm{mPa\,s}$, $\theta = 10°$ and 20 mm equivalent wall separation. . . . 152

8.10 Flow pattern for $\phi = 0.05$, $\bar{\mu}_f = 18.8\,\mathrm{mPa\,s}$, $\theta = 10°$ and 15 mm equivalent wall separation. . . . 153

8.11 Flow pattern for $\phi = 0.05$, $\bar{\mu}_f = 18.8\,\mathrm{mPa\,s}$, $\theta = 10°$ and 10 mm equivalent wall separation. . . . 154

8.12 Flow pattern for $\phi = 0.05$, $\bar{\mu}_f = 18.8\,\mathrm{mPa\,s}$, $\theta = 10°$ and 7 mm equivalent wall separation. . . . 155

8.13 Flow pattern for $\phi = 0.05$, $\bar{\mu}_f = 18.8\,\mathrm{mPa\,s}$, $\theta = 10°$ and 5 mm equivalent wall separation. . . . 156

8.14 Dependance of the horizontal interface height on equivalent wall separation for $\phi = 0.05$, $\theta = 10°$: ◇ is 38.1 mPa s; + is 28.8 mPa s; □ is 18.8 mPa s; × is 10.0 mPa s. . . . 158

8.15 Dependance of the top outlet concentration on equivalent wall separation for $\phi = 0.05$, $\theta = 10°$: ◇ is 38.1 mPa s; + is 28.8 mPa s; □ is 18.8 mPa s; × is 10.0 mPa s. . . . 158

8.16 Dependance of the inverse of the inception distance on equivalent wall separation for various angles and $\bar{\mu}_f = 18.8$, mPa s, $\phi = 0.05$. . . . 160

8.17 Dependance of the inverse of the inception distance on equivalent wall separation for $\phi = 0.05$, $\bar{\mu}_f = 18.8\,\mathrm{mPa\,s}$: ◇ is 10°; + is 20°; □ is 30°. . . . 160

8.18 Flow pattern for $\phi = 0.05$, $\bar{\mu}_f = 18.8\,\mathrm{mPa\,s}$, $\theta = 20°$ and no internal resistance to motion. . . . 161

8.19 Flow pattern for $\phi = 0.05$, $\bar{\mu}_f = 18.8\,\mathrm{mPa\,s}$, $\theta = 20°$ and 20 mm equivalent wall separation. 162

8.20 Flow pattern for $\phi = 0.05$, $\bar{\mu}_f = 18.8\,\mathrm{mPa\,s}$, $\theta = 20°$ and 15 mm equivalent wall separation. 163

8.21 Flow pattern for $\phi = 0.05$, $\bar{\mu}_f = 18.8\,\mathrm{mPa\,s}$, $\theta = 20°$ and 10 mm equivalent wall separation. 164

8.22 Flow pattern for $\phi = 0.05$, $\bar{\mu}_f = 18.8\,\mathrm{mPa\,s}$, $\theta = 20°$ and 7 mm equivalent wall separation. 165

8.23 Flow pattern for $\phi = 0.05$, $\bar{\mu}_f = 18.8\,\mathrm{mPa\,s}$, $\theta = 20°$ and 5 mm equivalent wall separation. 166

8.24 Dependance of the inverse of the inception distance on equivalent wall separation for $\phi = 0.05$, $\bar{\mu}_f = 10.0\,\mathrm{mPa\,s}$: ◇ is 10°; + is 20°; □ is 30°. . . . 167

8.25 Dependance of the horizontal interface height on equivalent wall separation for $\phi = 0.05$, $\bar{\mu}_f = 10.0\,\mathrm{mPa\,s}$: ◇ is 10°; + is 20°; □ is 30°. 168

8.26 Dependance of the top outlet concentration on equivalent wall separation for $\phi = 0.05$, $\bar{\mu}_f = 10.0\,\mathrm{mPa\,s}$: ◇ is 10°; + is 20°; □ is 30°. 168

8.27 Dependance of the inverse of the inception distance on plate separation for various feed concentrations and $\bar{\mu}_f = 18.8$, mPa s, $\theta = 20°$. 169

9.1 Horizontal interface position for $\beta_{\hat{\phi}} = 0$, $\hat{\phi} = 0.05$, $\bar{\mu}_f = 18.8\,\mathrm{mPa\,s}$, $\theta = 10°$. 173

9.2 Horizontal interface position for $\beta_{\hat{\phi}} = 1$, $\hat{\phi} = 0.05$, $\bar{\mu}_f = 18.8\,\mathrm{mPa\,s}$, $\theta = 10°$. 173

9.3 $\beta_{\hat{\phi}} = 0$, $N_C \simeq 0.08$: flow pattern for $\hat{\phi} = 0.05$, $\bar{\mu}_f = 18.8\,\mathrm{mPa\,s}$, $\theta = 10°$. . . 175

9.4 $\beta_{\hat{\phi}} = 0$, $N_C \simeq 0.35$: flow pattern for $\hat{\phi} = 0.05$, $\bar{\mu}_f = 18.8\,\mathrm{mPa\,s}$, $\theta = 10°$. . . 176

9.5 $\beta_{\hat{\phi}} = 0$, $N_C \simeq 0.8$: flow pattern for $\hat{\phi} = 0.05$, $\bar{\mu}_f = 18.8\,\mathrm{mPa\,s}$, $\theta = 10°$. . . . 177

9.6 $\beta_{\hat{\phi}} = 1$, $N_C \simeq 0.08$: flow pattern for $\hat{\phi} = 0.05$, $\bar{\mu}_f = 18.8\,\mathrm{mPa\,s}$, $\theta = 10°$. . . 178

9.7 $\beta_{\hat{\phi}} = 1$, $N_C \simeq 0.35$: flow pattern for $\hat{\phi} = 0.05$, $\bar{\mu}_f = 18.8\,\mathrm{mPa\,s}$, $\theta = 10°$. . . 179

9.8 $\beta_{\hat{\phi}} = 1$, $N_C \simeq 0.8$: flow pattern for $\hat{\phi} = 0.05$, $\bar{\mu}_f = 18.8\,\mathrm{mPa\,s}$, $\theta = 10°$. . . . 180

9.9 Inverse of inception distance for $\beta_{\hat{\phi}} = 0$, $\hat{\phi} = 0.05$, $\bar{\mu}_f = 18.8\,\mathrm{mPa\,s}$, $\theta = 10°$. 181

9.10 Inverse of inception distance for $\beta_{\hat{\phi}} = 1$, $\hat{\phi} = 0.05$, $\bar{\mu}_f = 18.8\,\mathrm{mPa\,s}$, $\theta = 10°$. 182

C.1 Gravity driven flow of a density stratified fluid between inclined parallel plates. 199

Nomenclature

Scalar quantities are denoted by lightface miniscules and vectors by boldface miniscules. Second order tensors are denoted by boldface majescules. The only exception to this is the use of $\boldsymbol{\tau}$ for shear stress. Overbars on physical properties denote the property of the material: the viscosity of the pure continuous phase is $\bar{\mu}_f$. Dimensionless quantities are capped with a caret: for example the dimensional velocity is $\boldsymbol{u}$ and the dimensionless velocity is $\hat{\boldsymbol{u}}$.

a	wave speed or Rankine-Hugoniot velocity
b	width of the settling vessel
c	dispersed phase concentration from Acrivos & Herbolzheimer
d_s	particle diameter
D	inflection of the solution surface
$\boldsymbol{D}$	symmetric rate of strain tensor
$f(\phi_f)$	hindering expression of Wallis for the drag force
Fr	Froude number, $\mathrm{Fr} = V_{s,\infty}^2/(Lg)$
$\boldsymbol{g}$	gravity vector
G	growth rate of the Fourier mode
Gr	Grashof number from Acrivos & Herbolzheimer, $\mathrm{Gr} = 18\,R(L/d_s)^2\phi_0$
$h(\phi_f)$	hindering expression of Richardson & Zaki for the settling velocity
H	height of the horizontal suspension interface
i, j	discrete coordinate number for the ξ-η or x-y meshes
k	porous media permeability
L	length of the sedimentation vessel
$\boldsymbol{m}_{si}$	interphase momentum transfer for phase s.
n	hindering exponent for the Richardson & Zaki model
N_C	Courant number, $N_C = \lvert\hat{a}\rvert\Delta\hat{t}/\Delta\hat{x}$
N_D	diffusion number, $N_D = \Delta\hat{t}/(\mathrm{Re}\Delta\hat{x}^2)$
NI, NJ	number of grid points in ξ and η directions
p	pressure
$\hat{P}$	dimensionless pressure from Acrivos & Herbolzheimer
q	fitting parameter for the settling velocity data of Font

R	vessel Reynolds number from Acrivos & Herbolzheimer, $R = L\bar{\rho}_f V_{s,\infty}/\bar{\mu}_f$
Re	vessel Reynolds number, $\mathrm{Re} = \bar{\rho}_f L V_{s,\infty}/\mu_m$
$\mathrm{Re}_{s,\infty}$	particle Reynolds number at infinite dilution for dispersed phase s, $\mathrm{Re}_{s,\infty} = \bar{\rho}_f d_s V_{s,\infty}/\bar{\mu}_f$
s	Hele-Shaw equivalent wall separation for uniform internal resistance to motion, $s = \sqrt{12\,k}$
S	flux of clear liquid produced in the sedimentation vessel
S^x, S^y	slope of the solution surface in the x and y directions
St	Stokes number
t	time
$\boldsymbol{u}$	velocity vector
u, v	x and y components of velocity
V_s	settling velocity of dispersed phase s at the specified concentration
$V_{s,\infty}$	settling velocity of dispersed phase s at infinite dilution
w	width of the inlet port to the settling vessel
x, y	position in the real domain
y_i	wave inception distance
Greek	
α_N, α_R	numerical and real diffusivities
α, β_x	grid clustering parameters
$\beta_{\hat{\omega}}$, $\beta_{\hat{\phi}}$	implicitness factor for the stress term ($\hat{\omega}$) and the buoyancy driving force ($\hat{\omega}$)
ε	truncation error of the discretization method
ξ-η	positions in the computational domain
$\bar{\rho}_k$	material density of phase k
Γ	buoyancy ratio, $(\bar{\rho}_s - \bar{\rho}_f)/\bar{\rho}_f$.
Λ	ratio of a sedimentation Grashof number to R, $\Lambda = L^2 g(\bar{\rho}_s - \bar{\rho}_f)\phi_0/(V_{s,\infty}\bar{\mu}_f) = 18(L/d_s)^2\phi_0$
ϕ_k	volume fraction of phase k
ϕ_0	initial or inlet dispersed phase volume fraction
μ_k	viscosity of phase k
$\bar{\mu}_k$	viscosity of material k
θ	angle of inclination from vertical
$\boldsymbol{\theta}$	vector denoting the angle of inclination, $\boldsymbol{\theta} = [\sin\theta \;\; \cos\theta]$
$\boldsymbol{\tau}_k$	shear stress on phase k
ζ	phase angle for the Fourier mode
ψ	stream function of the homogeneous mixture
ω	vorticity of the homogeneous mixture
Ω	Fourier mode of ω

Subscripts

i, j	grid index on the regular mesh
i', j'	grid index on the staggered mesh
k	arbitrary phase k
f, s	fluid phase (continuous), dispersed phase (solid)
m	volume averaged mixture
x, y	x and y components of direction

Superscripts

c	interpolated value at the control volume face for UNO2 differencing
$n, n+1$	current and next time step
$'$	slip relative to the mixture

Operators

∇	gradient, $([\frac{\partial}{\partial x}, \frac{\partial}{\partial y}, \frac{\partial}{\partial z}])$

Chapter 1

Introduction

Sedimentation is an important unit operation in the chemical and mineral processing industries. For example, bitumen processing requires an efficient method to separate mixtures of bitumen, water and sand. Primary wastewater treatment involves clarification and thickening of raw effluent. Inclined plate or lamella settlers are used to increase the sedimentation rates in wastewater treatment and mineral processing.

1.1 Historical background

Boycott [5] noted that

> ...if oxalated or defibrinated blood is put to stand in narrow tubes, the corpuscles sediment a good deal faster if the tube is inclined than when it is vertical.

A simple kinematic theory was developed by Ponder [37] and simultaneously by Nakamura & Kuroda [32] (referred to as PNK theory) to correlate the rate of sedimentation with the aspect ratio and the angle of inclination of the plates shown in Figure 1.1 [1]:

$$\frac{dH}{dt} = -V_s\left(1 + \frac{H}{b}\sin\theta\right)$$

For sedimentation in the continuous mode the flux S of clear fluid produced in the vessel is

$$S = \frac{V_s b}{\cos\theta}\left(1 + \frac{H}{b}\sin\theta\right)$$

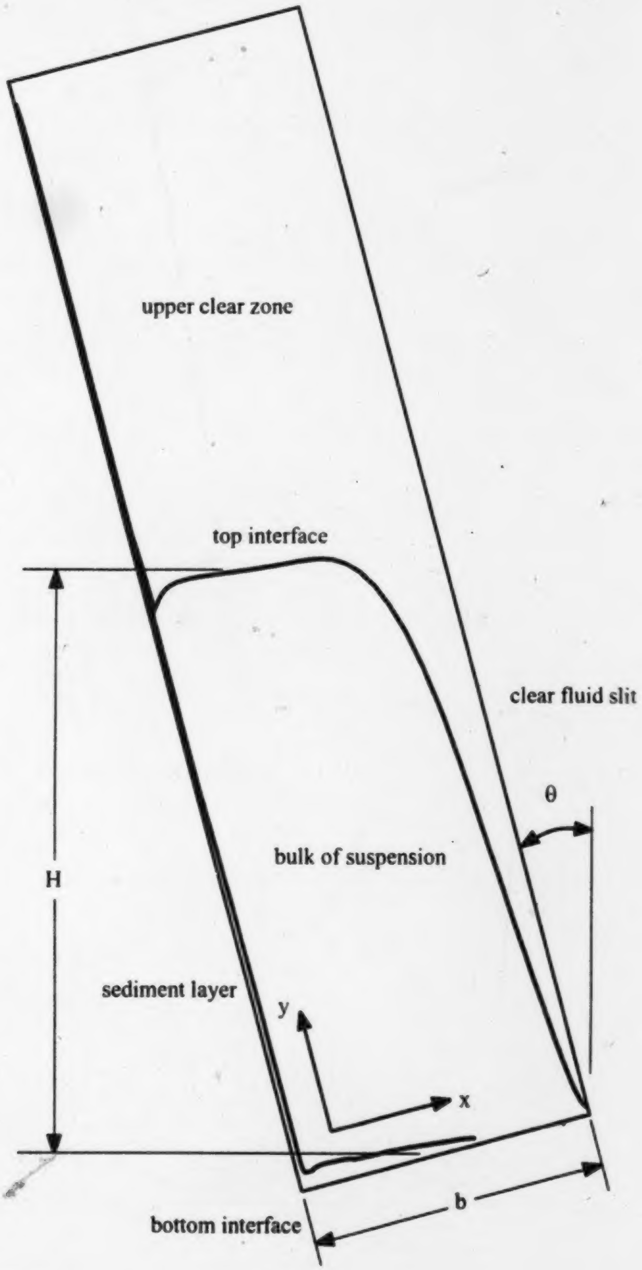
upper clear zone
top interface
clear fluid slit
θ
bulk of suspension
H
sediment layer
y
x
b
bottom interface

Figure 1.1: Geometry for batch sedimentation between inclined parallel plates.

PNK theory does not predict the velocity profiles inside the vessel and cannot account for the waves that resuspend the mixture and decrease the separation efficiency of the inclined plate device. A good numerical model is needed to predict the velocity profiles inside the vessel and to test new designs for settling devices.

Richardson & Zaki [38] performed a series of one dimensional sedimentation and fluidization experiments with various suspensions. They correlated the settling velocity of a suspension with

$$\frac{V_s}{V_{s,\infty}} = (1 - \phi_s)^n$$

where $V_{s,\infty}$ is the settling velocity at infinite dilution and the exponent n depends only on the particle Reynolds number. Wallis [51] used this correlation to obtain a general expression for the drag force between the continuous and dispersed phase. Masliyah [30] used the hindered drag force expression of Wallis to derive an expression for the settling velocities of a bidispersed suspension. Good agreement was found with experimental data.

Kynch [24] proposed a simple model for one dimensional sedimentation. He assumed the settling velocity is only a function of the local concentration and the concentration profile is dictated by the solution to the dispersed phase continuity equation:

$$\frac{\partial \phi_s}{\partial t} + \frac{\partial(\phi_s V_s)}{\partial y} = 0$$

The product $(\phi_s V_s)$ is the vertical flux of the dispersed phase: an example of the flux curve is shown in Figure 1.2. Kynch defined a wave speed to be the slope of the flux curve:

$$a(\phi_s) = \partial(\phi_s V_s)/\partial \phi_s$$

Vertical sedimentation is described by the solution to the quasilinear wave equation

$$\frac{\partial \phi_s}{\partial t} + a\frac{\partial \phi_s}{\partial y} = 0$$

Kynch noted this equation permitted weak solutions and shock waves: this is consistent with experimental observations of the compaction zone at the bottom of a settling vessel and sharp clear fluid/suspension interfaces. Results of batch settling tests (interface position *vs.* time) were represented well by this simple theory.

Experimental measurements are divided into two classes. The first class measured the position of the horizontal suspension interface over time [23, 34, 25]. These measurements give an overall picture of the process but do not provide details of the flow. The second class provided more detailed measurements of the flow. Acrivos and co-workers [1, 8, 18, 45] measured the thickness of the clear fluid zone beneath the upper inclined wall and the location of the inception point of the wavy interface. Herbolzheimer [18] notes the wave

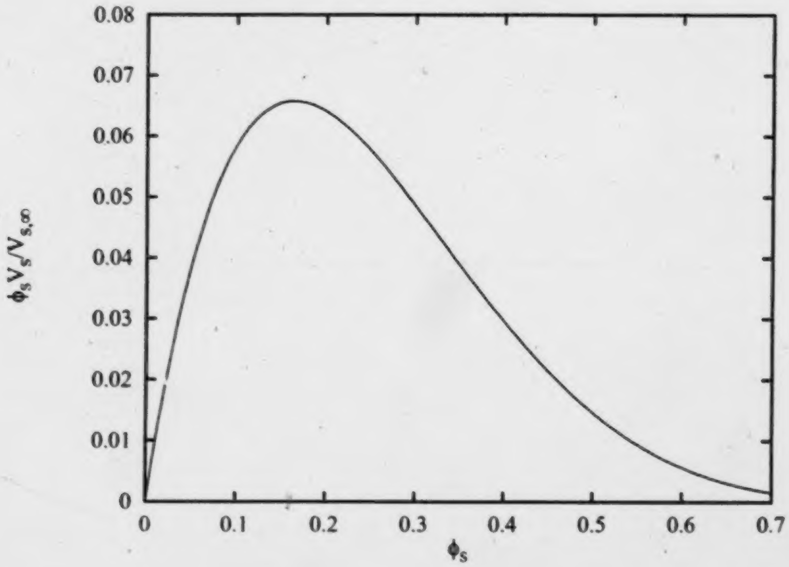

Figure 1.2: Dimensionless flux curve for $V_s/V_{s,\infty} = (1-\phi_s)^{5.1}$.

inception point is related to the growth rate of the unstable waves. Leung & Probstein [29] and Leung [28] also measured the inception point of unstable waves.

Prior to the mid-1960's most successful numerical simulations of incompressible single phase flow were performed with the vorticity-stream function equations. The Marker and Cell (MAC) method of Harlow & Welch [14] was the first widely accepted primitive variable (velocity/pressure) algorithm for single phase incompressible flow. Hill et al. [19] used a buoyancy driven single phase model and a variant of the MAC method to model Stokes sedimentation of a very dilute suspension under an inclined surface. Their finite difference scheme used a second order accurate central approximation for the convection terms in the momentum equations. Grid scale oscillations were apparent in the shape of the suspension interface.

Patankar & Spalding [35] developed the Semi-Implicit algorithm (SIMPLE) for the simulation of single phase incompressible flow in complicated three dimensional geometries. The driving force for multi-phase flow algorithms came in the mid 1970's with the need to model loss of coolant accidents (LOCA) in nuclear reactors. Spalding used the framework behind SIMPLE to develop the InterPhase Slip Algorithm (IPSA) for multi-phase flow.

The development of compressible flow algorithms followed a much different path from that of incompressible flow algorithms. Discontinuities are not valid solutions to the equations that describe incompressible flow while the hyperbolic transport equations

(Euler equations) for compressible flow do admit discontinuous solutions. Compressible flow algorithms focus on the accurate representation without overshoot of discontinuous solutions. The most desirable discretization methods admit solutions that satisfy the requirement of Total Variation Decreasing (TVD) developed by Harten [15, 16]. This concept ensures that local solution extrema do not grow over time and become errors. The review article by Rizzi & Engquist [39] describes the historical development of accurate methods in modelling discontinuous flows. Woodward & Colella [53] review the ability of several discretization methods to capture strong shocks.

Yokota & Huynh [56] noted

> The aerospace industry's wide acceptance of computational fluid dynamics is due mainly to the successful calculation of transonic flows. Shock capturing schemes, both upwind and central differenced, have revolutionized the way discontinuous flows are investigated.

Multiphase flows are discontinuous: the non-diffusive nature of the dispersed phase leads to discontinuous dispersed phase concentration and velocity profiles.

1.2 Research goals

The goal of this research was to apply accurate shock capturing techniques from computational aerodynamics to the numerical simulation of inclined plate sedimentation. Numerical results were compared with detailed experimental data obtained by Acrivos & Herbolzheimer [1], Herbolzheimer [18] and Shaqfeh & Acrivos [45] for batch and continuous sedimentation. Of primary concern was the ability of the numerical simulation to capture correctly the wavy suspension interface adjacent the upper inclined surface.

1.3 Thesis overview

Chapter 2. A homogeneous model is derived from a general two-fluid model. The governing equations are written in dimensionless vorticity-stream function form. Simplifications are made to enable rapid solution of the discrete equations.

Chapter 3. The dispersed phase material transport equation is discretized with the uniformly second order accurate non-oscillatory UNO2 method of Harten & Osher [17]. The UNO2 scheme is applied to the convection terms in the vorticity transport equation while the viscous terms are discretized with three point central finite difference expressions. An efficient solution algorithm is developed.

Chapter 4. A linear stability analysis and truncation error analysis are presented for the algorithm developed in Chapter 3. While discretized vorticity transport equation is first order accurate the dominant truncation error does not appear as numerical diffusion.

Chapter 5. The simulation code is validated with a series of examples. Numerical results are compared with the numerical results of other researchers and experimental data.

Chapter 6. Simulation results for batch inclined plate sedimentation are compared between the non-diffusive UNO2 method and first order accurate upwinding. These results demonstrate the superior accuracy of the non-diffusive shock capturing method.

Chapter 7. Simulation results for continuous inclined plate sedimentation are compared with detailed experimental data for the inception point of unstable waves for a range of viscosities, inclinations and dispersed phase concentrations.

Chapter 8. A parameter study of inclined plate sedimentation was performed where there is a porous media type of resistance to motion. The permeability of the media was the major parameter. The effect of internal resistance to motion flow patterns and the inception point of the wavy interface are predicted.

Chapter 9. Numerical results obtained with an alternative discretization of the buoyancy term are compared with the results obtained in Chapter 7. While this alternative discretization method is shown to be more accurate than that used in the previous chapters the new numerical results follow the same trends as the previous results.

Chapter 2

Governing Equations

The governing equations presented by Ishii & Kocamustafaogullari [22] for a two fluid model are simplified in the first section of this chapter. The two-phase suspensions of interest in this work are laminar isothermal suspensions of rigid solid particles in a continuous liquid phase. All materials are incompressible and there is no mass transfer between phases. Particle Reynolds numbers are $\mathrm{Re}_{s,\infty} < 0.1$ (Stokes settling) and the dispersed phase concentrations are small enough ($\phi_s < 0.15$) to prevent solid-like stresses from occurring in the dispersed phases.

A homogenous model is then developed from the two fluid model. The behaviour of the suspension is described by a momentum equation for the homogeneous mixture, the slip velocity of the dispersed phase relative to the mixture and a transport equation for the volume fraction of the dispersed phase. These equations are written in terms of vorticity and stream function to eliminate pressure.

2.1 Two fluid model

For an isothermal two-phase suspension the two fluid equations presented by Ishii & Kocamustafaogullari [22] are given below:

Continuity equation

$$\frac{\partial(\phi_k \bar{\rho}_k)}{\partial t} + \nabla \cdot (\phi_k \bar{\rho}_k \boldsymbol{u}_k) = \Lambda_k \tag{2.1}$$

Momentum equation

$$\begin{aligned} &\frac{\partial(\phi_k \bar{\rho}_k \boldsymbol{u}_k)}{\partial t} + \nabla \cdot (\phi_k \bar{\rho}_k \boldsymbol{u}_k \boldsymbol{u}_k) = \\ &\qquad -\phi_k \nabla p_k + \nabla \cdot \phi_k (\boldsymbol{\tau}_k + \boldsymbol{\tau}_k^t) + \phi_k \bar{\rho}_k \boldsymbol{g} + \boldsymbol{u}_{ki} \Lambda_k + \boldsymbol{m}_{ki} - \nabla \phi_k \cdot \boldsymbol{\tau}_i \end{aligned} \tag{2.2}$$

The subscript k denotes the phase and i denotes the value at the interface between the two phases. $\bar{\rho}_k$ is the density of the material comprising phase k. ϕ_k, $\boldsymbol{u}_k$ and p_k are the volume fraction, velocity and pressure of phase k. Λ_k and $\boldsymbol{m}_{ki}$ are the mass generation and interfacial drag force. $\boldsymbol{\tau}_k$, $\boldsymbol{\tau}_k^t$ and $\boldsymbol{\tau}_i$ are the laminar shear stress, turbulent shear stress and interfacial shear stress.

The densities $\bar{\rho}_k$ are constant since the phases are incompressible. $\Lambda_k = 0$ because there is no generation of mass in either phase or mass transfer between phases. The turbulent shear stress $\boldsymbol{\tau}_k^t$ is zero because the flow is laminar. The pressure field of each phase is assumed to be identical. Nunziato [33] notes interfacial drag force contribution $\nabla\phi_k \cdot \boldsymbol{\tau}_i$ can account for contact pressures in the dispersed phase at high concentrations and the diffusive motion of small particles at low concentrations. This research is not concerned with the behaviour of the concentrated sediment where contact pressures are important or the motion of small diffusive particles. This term is neglected.

Equations 2.1 and 2.2 are simplified:

Continuity equation

$$\frac{\partial\phi_k}{\partial t} + \nabla\cdot(\phi_k\boldsymbol{u}_k) = 0 \tag{2.3}$$

Momentum equation

$$\begin{aligned}\bar{\rho}_k\left(\frac{\partial(\phi_k\boldsymbol{u}_k)}{\partial t} + \nabla\cdot(\phi_k\boldsymbol{u}_k\boldsymbol{u}_k)\right) &= \\ -\phi_k\nabla p + \nabla\cdot\phi_k\boldsymbol{\tau}_k + \phi_k\bar{\rho}_k\boldsymbol{g} + \boldsymbol{m}_{ki}&\end{aligned} \tag{2.4}$$

The saturation constraint is added as an additional equation:

$$\phi_s + \phi_f = 1 \tag{2.5}$$

Several authors (for example Drew [9], Soo [47, page 256] and Nunziato [33]) have presented different constitutive equations for the shear stresses experienced by the continuous and dispersed phases. These researchers require the mixture stress to be recovered from the sum of the continuous and dispersed phase shear stresses:

$$\boldsymbol{\tau}_m = \boldsymbol{\tau}_f + \boldsymbol{\tau}_s \tag{2.6}$$

The interfacial drag force experienced by the continuous phase is the opposite of that force experienced by the dispersed phase:

$$\boldsymbol{m}_{fi} = -\boldsymbol{m}_{si} \tag{2.7}$$

The dominant interfacial force between the continuous and dispersed phase is the drag force. Other forces (such as Saffman lift, Faxén force, Ho & Leal lift, Basset force and virtual mass effect) are neglected.

A general form of the drag force interaction is given by Wallis [51]:

$$\boldsymbol{m}_{si} = \phi_s \frac{3\bar{\rho}_f}{4d_s} f(\phi_f) C_{D,s} \mid \boldsymbol{u}_f - \boldsymbol{u}_s \mid (\boldsymbol{u}_f - \boldsymbol{u}_s) \tag{2.8}$$

$f(\phi_f)$ is an empirical function that relates the drag force to the concentration of the suspension. The drag coefficient on a spherical particle, $C_{D,s}$, is a function of the sedimentation Reynolds number

$$\mathrm{Re}_s \equiv \frac{d_s \bar{\rho}_f \mid \boldsymbol{u}_f - \boldsymbol{u}_s \mid \phi_f}{\bar{\mu}_f}$$

For the low Reynolds number asymptote ($C_{D,s} = 24/\mathrm{Re}_s$) Equation 2.8 becomes.

$$\boldsymbol{m}_{si} = \phi_s \frac{18\bar{\mu}_f}{d_s^2} \frac{f(\phi_f)}{\phi_f} (\boldsymbol{u}_f - \boldsymbol{u}_s) \tag{2.9}$$

Richardson & Zaki [38] measured sedimentation and fluidization velocities with $\phi_s < 0.4$. They correlated the settling velocity of the suspension with

$$\frac{V_s}{V_\infty} = \phi_f^n \tag{2.10}$$

where the exponent n is a function of the sedimentation Reynolds number: $n = 4.65$ for $\mathrm{Re}_{p,s} < 0.2$ and $n = 2.39$ for $\mathrm{Re}_{p,s} > 500$.

Wallis correlated the data of Richardson & Zaki to determine the empirical hindering function $f(\phi_f)$. He suggested the hindering function

$$f(\phi_f) = \phi_f^{-1.7} \tag{2.11}$$

is a fair compromise to represent the settling velocity at the low Reynolds number asymptote ($C_{D,s} = 24/\mathrm{Re}_s$) and the high Reynolds number asymptote with constant drag coefficient. For $\mathrm{Re}_s \ll 1$ Garside & Al-Dibouni [12] recommends,

$$f(\phi_f) = \phi_f^{-2.1} \tag{2.12}$$

Barnea & Mizrahi [3] proposed a more complicated hindering function:

$$f(\phi_f) = \phi_f \left(1 + (1 - \phi_f)^{1/3} \exp\left[5(1 - \phi_f)/3\phi_f\right]\right) \tag{2.13}$$

For a two dimensional model with two phases Equations 2.3, 2.4, 2.5 form six coupled partial differential equations and one scalar constraint with the unknowns $\phi_f, \phi_s, u_f, v_f, u_s, v_s$ and p. Equations 2.9 and 2.12 describe the interfacial drag force.

2.2 Homogeneous model

In this section the two fluid model equations (2.3, 2.4 and 2.5) are used to develop equations for a homogeneous model.

The slip velocity of the dispersed phase relative to the continuous phase is assumed to be a function of concentration only [30]:

$$\boldsymbol{v}_s - \boldsymbol{v}_f = \boldsymbol{g}\frac{d_s^2(\bar{\rho}_s - \bar{\rho}_f)}{18\bar{\mu}_f}\frac{\phi_f^2}{f(\phi_f)} \tag{2.14}$$

This assumption is justified by the order of magnitude analysis in Appendix 11.

2.2.1 Definition of the mixture velocity and dispersed phase slip velocity

The homogeneous model is based on the definition of the volume averaged velocity of the two phase mixture:

$$\boldsymbol{u}_m \equiv \phi_f \boldsymbol{u}_f + \phi_s \boldsymbol{u}_s \tag{2.15}$$

This definition of the mixture velocity satisfies the incompressible continuity equation $\nabla \cdot \boldsymbol{u}_m = 0$. This is demonstrated by summing the continuity equations for the continuous and dispersed phases:

$$\frac{\partial \phi_f}{\partial t} + \nabla \cdot (\phi_f \boldsymbol{u}_f) = 0 \tag{2.16}$$

$$\frac{\partial \phi_s}{\partial t} + \nabla \cdot (\phi_s \boldsymbol{u}_s) = 0 \tag{2.17}$$

The sum is:

$$\left(\frac{\partial \phi_f}{\partial t} + \frac{\partial \phi_s}{\partial t}\right) + \nabla \cdot \boldsymbol{u}_m = 0 \tag{2.18}$$

The saturation constraint $\phi_f + \phi_s = 1$ is independent of time: the continuity equation for the homogeneous mixture is

$$\nabla \cdot \boldsymbol{u}_m = 0 \tag{2.19}$$

In the case of one dimensional batch sedimentation this definition of the mixture velocity yields $\boldsymbol{u}_m = 0$ over the length of the sedimentation vessel.

Equation 2.15 is written for the continuous phase velocity

$$\boldsymbol{u}_f = \frac{\boldsymbol{u}_m - \phi_s \boldsymbol{u}_s}{\phi_f} \tag{2.20}$$

This equation is substituted for v_f in Equation 2.14 and results in

$$v_s - v_m = \frac{g d_s^2(\bar{\rho}_s - \bar{\rho}_f)}{18\bar{\mu}_f}\frac{\phi_f^3}{f(\phi_f)} \tag{2.21}$$

The velocity of the dispersed phase relative to the mixture is

$$\boldsymbol{u}_s - \boldsymbol{u}_m = V_{s,\infty}\boldsymbol{\theta}\frac{\phi_f^3}{f(\phi_f)} = V_{s,\infty}h(\phi_f)\boldsymbol{\theta} \tag{2.22}$$

where $V_{s,\infty}$ is the settling velocity at infinite dilution and $\boldsymbol{\theta} = [\sin\theta \;\; \cos\theta]$ denotes the direction of the x and y axis relative to vertical. The function $h(\phi_f) = \phi_f^3/f(\phi_f)$ is identical to the hindered settling function for batch sedimentation.

The slip velocities for the continuous and dispersed phases are defined by

$$\begin{aligned} \boldsymbol{u}_f' &\equiv \boldsymbol{u}_f - \boldsymbol{u}_m \\ \boldsymbol{u}_s' &\equiv \boldsymbol{u}_s - \boldsymbol{u}_m \end{aligned} \tag{2.23}$$

The velocity of the dispersed phase relative to the continuous phase is then

$$\boldsymbol{u}_s - \boldsymbol{u}_f = \frac{\boldsymbol{u}_s'}{1-\phi_s} \tag{2.24}$$

2.2.2 Material transport equation

The transport equation for the dispersed phase volume fraction is

$$\frac{\partial\phi_s}{\partial t} + \nabla\cdot(\phi_s\boldsymbol{u}_s) = 0 \tag{2.25}$$

Equation 2.22 is substituted for $\boldsymbol{u}_s$ to produce

$$\frac{\partial\phi_s}{\partial t} + \nabla\cdot(\phi_s\boldsymbol{u}_m) + \nabla\cdot(\phi_s\boldsymbol{u}_s') = 0 \tag{2.26}$$

The continuous phase concentration is obtained from the saturation constraint: $\phi_f = 1 - \phi_s$.

2.2.3 Momentum equation for the homogeneous mixture

The momentum equation for the homogeneous mixture is derived from the sum of the continuous and dispersed phase momentum equations. The momentum equations for the continuous and dispersed phase are:

$$\bar{\rho}_f\left[\frac{\partial\phi_f\boldsymbol{u}_f}{\partial t} + \nabla\cdot(\phi_f\boldsymbol{u}_f\boldsymbol{u}_f)\right] = -\phi_f\nabla p + \nabla\cdot\boldsymbol{\tau}_f - \phi_f\bar{\rho}_f\boldsymbol{g} + \boldsymbol{m}_{si} \tag{2.27}$$

$$\bar{\rho}_s\left[\frac{\partial\phi_s\boldsymbol{u}_s}{\partial t} + \nabla\cdot(\phi_s\boldsymbol{u}_s\boldsymbol{u}_s)\right] = -\phi_s\nabla p + \nabla\cdot\boldsymbol{\tau}_s - \phi_s\bar{\rho}_s\boldsymbol{g} - \boldsymbol{m}_{si} \tag{2.28}$$

The momentum equation for the mixture is the sum of equations 2.27 and 2.28:

$$\bar{\rho}_f\left[\frac{\partial\phi_f\boldsymbol{u}_f}{\partial t} + \nabla\cdot(\phi_f\boldsymbol{u}_f\boldsymbol{u}_f)\right] + \bar{\rho}_s\left[\frac{\partial\phi_s\boldsymbol{u}_s}{\partial t} + \nabla\cdot(\phi_s\boldsymbol{u}_s\boldsymbol{u}_s)\right] = -\nabla p + \nabla\cdot\boldsymbol{\tau}_m - \rho_m\boldsymbol{g} \tag{2.29}$$

The mixture density is

$$\rho_m \equiv \phi_f \bar{\rho}_f + \phi_s \bar{\rho}_s \tag{2.30}$$

The shear stress $\boldsymbol{\tau}_m$ experienced by the mixture is related to the velocity gradient of the mixture:

$$\boldsymbol{\tau}_m = \mu_m(\nabla \boldsymbol{u}_m + (\nabla \boldsymbol{u}_m)^T) \tag{2.31}$$

$\boldsymbol{\tau}_m$, μ_m and $\boldsymbol{u}_m$ are the shear stress, viscosity and velocity of the mixture. The viscosity of a mixture of neutrally buoyant rigid spheres is correlated well by the equation of Batchelor & Green [4] for $\phi_s < 0.2$:

$$\frac{\mu_m}{\bar{\mu}_f} = 1 + 2.5\phi_s + 7.6\phi_s^2 \tag{2.32}$$

$\bar{\mu}_f$ is the viscosity of the pure continuous phase.

The momentum equation for the two phase homogeneous mixture is derived in Appendix A. The result is:

$$\rho_m \left[\frac{\partial \boldsymbol{u}_m}{\partial t} + \boldsymbol{u}_m \cdot \nabla \boldsymbol{u}_m\right] = -\nabla p + \nabla \cdot \boldsymbol{\tau}_m - \rho_m \boldsymbol{g} \tag{2.33}$$

Equation 2.33 is a natural convection model of the homogeneous mixture. The driving force is the variation in the mixture density ρ_m caused by the distribution of the dispersed phase concentration governed by Equation 2.26.

2.3 Simplifying assumptions

Three major assumptions are used to simplify the governing equations. First the hindering function chosen for this research was a compromise between Equation 2.11 of Wallis and Equation 2.12 of Garside & Al-Dibouni:

$$f(\phi_s) = (1 - \phi_s)^{-2} \tag{2.34}$$

For a 10 % suspension the settling velocities from this correlation are within 3 % and 1 % of the velocities obtained from the correlations of Wallis and Garside & Al-Dibouni, respectively. Simulations with the hindering function 2.34 required one third of the CPU time of those required by simulations with the hindering function of Garside & Al-Dibouni.

Second the Boussinesq approximation is used. The mixture density ρ_m appearing on the left hand side of the momentum Equation 2.33 is taken to be the density of the initial suspension (batch sedimentation) or the density of the feed suspension (continuous sedimentation).

Third the viscosity of the suspension is assumed to be constant. The viscosity is taken to be that of the initial suspension (batch sedimentation) or the feed suspension (continuous sedimentation). These last two assumptions permitted an efficient algorithm to be developed for solving the vorticity transport equation described in Chapter 3.

2.4 Comparison with the homogeneous model of Hill et al.

The homogeneous model of Hill, Rothfus & Li [19] assumes a dilute suspension of particles in fluid and rests on governing equations for the continuous and dispersed phases. Their model is:

Fluid momentum equation

$$\bar{\rho}_f\left[\frac{\partial \boldsymbol{u}_f}{\partial t}+\boldsymbol{u}_f\cdot\nabla\boldsymbol{u}_f\right]=-\nabla p+\nabla\cdot\boldsymbol{\tau}_f-\rho_m\boldsymbol{g} \tag{2.35}$$

Fluid continuity equation

$$\nabla\cdot\boldsymbol{u}_f=0 \tag{2.36}$$

Particle continuity equation

$$\frac{\partial\phi_s}{\partial t}+(\boldsymbol{u}_f+\boldsymbol{u}'_s)\cdot\nabla\phi_s=0 \tag{2.37}$$

Particle velocity equation

$$\boldsymbol{u}_s=\boldsymbol{u}_f+\boldsymbol{u}'_s \tag{2.38}$$

where the slip velocity $\boldsymbol{u}'_s$ is the settling velocity at infinite dilution.

The equations of Hill et al. reduce to the homogeneous model presented in this chapter in the limit of infinite dilution. Two differences arise for $\phi_s > 0$. First the dispersed phase slip velocity and the viscosity of the mixture are functions of concentration. Second the fluid continuity equation 2.36 is only valid for $\phi_s = 0$: for non-zero concentrations it is

$$\frac{\partial\phi_f}{\partial t}+\nabla\cdot(\phi_f\boldsymbol{u}_f)=0$$

In a batch sedimentation experiment this equation is responsible for the upwards displacement of fluid in the bulk of the suspension. This balances the downwards volumetric flux of particles.

The equations 2.35 – 2.38 of Hill et al. are analogous to the simplified model Equations 2.22, 2.26 and 2.33 if the fluid velocity $\boldsymbol{u}_f$ in their equations is replaced with the mixture velocity $\boldsymbol{u}_m$.

2.5 Governing equations in dimensionless form

The subscript m denoting the mixture is dropped where it is not ambiguous: the mixture velocity is $\boldsymbol{u}$, the mixture density is ρ and the mixture viscosity is μ. The subscript s is dropped from the dispersed phase volume fraction ϕ.

The density $\bar{\rho}_f$ of the continuous phase, the length L of the sedimentation vessel and the settling velocity at infinite dilution $V_{s,\infty}$ are used to define the dimensionless variables:

$$\begin{aligned}
\hat{x} &= \frac{x}{L} \\
\hat{y} &= \frac{y}{L} \\
\hat{t} &= \frac{tV_{s,\infty}}{L} \\
\hat{\phi} &= \phi \\
\hat{\rho} &= \frac{\rho}{\bar{\rho}_f} \\
\hat{\boldsymbol{u}} &= \frac{\boldsymbol{u}}{V_{s,\infty}} \\
\hat{\boldsymbol{u}}_s &= \frac{\boldsymbol{u}_s}{V_{s,\infty}} \\
\hat{\boldsymbol{u}}'_s &= \frac{\boldsymbol{u}'_s}{V_{s,\infty}}
\end{aligned}$$

The dimensionless material transport equation is

$$\frac{\partial \hat{\phi}_s}{\partial \hat{t}} + \hat{\nabla} \cdot (\hat{\phi} \hat{\boldsymbol{u}}_s) = 0 \tag{2.39}$$

The dimensionless momentum equation is

$$\hat{\rho}\left[\frac{\partial \hat{\boldsymbol{u}}}{\partial \hat{t}} + \hat{\boldsymbol{u}} \cdot \hat{\nabla} \hat{\boldsymbol{u}}\right] = -\hat{\nabla}\hat{p} + \frac{1}{\mathrm{Re}}\hat{\nabla}^2 \hat{\boldsymbol{u}} - (\hat{\phi}\Gamma + 1)\frac{1}{\mathrm{Fr}} \tag{2.40}$$

where the Froude number, Reynolds number and buoyancy ratio are defined by

$$\begin{aligned}
\mathrm{Fr} &= \frac{V_{s,\infty}^2}{Lg} \\
\mathrm{Re} &= \frac{\bar{\rho}_f L V_{s,\infty}}{\mu} \\
\Gamma &= \frac{\bar{\rho}_s - \bar{\rho}_f}{\bar{\rho}_f}
\end{aligned}$$

2.6 Comparison with the governing equations of Acrivos et al.

Acrivos & Herbolzheimer [1] determined the fully developed velocity profile near the clear fluid zone for sedimentation in an inclined vessel. Their analysis was the basis for subsequent work by other researchers [18, 43, 44, 45].

Acrivos & Herbolzheimer write the dimensionless ensemble-averaged momentum equation for a uniform particle concentration:

$$R\hat{\rho}(\hat{\phi})\left[\frac{\partial \hat{\boldsymbol{u}}}{\partial \hat{t}} + \hat{\boldsymbol{u}} \cdot \hat{\nabla}\hat{\boldsymbol{u}}\right] = -\nabla \hat{P} - (1-\hat{\phi})\Lambda\boldsymbol{\theta} + \hat{\mu}(\hat{\phi})\hat{\nabla}^2\hat{\boldsymbol{u}}^2 \tag{2.41}$$

The dimensionless density is $\hat{\rho}(\phi) = 1 + c_0\hat{\phi}(\bar{\rho}_s/\bar{\rho}_f - 1)$ and the dimensionless viscosity is $\hat{\mu}(\hat{\phi})$ where c_0 is the initial volume fraction of the dispersed phase. Their dimensionless volume fraction $\hat{\phi}$ is scaled with the initial concentration c_0: $\hat{\phi} = \phi/c_0$. In this section c is used to denote the concentration of the suspension: it is equivalent to ϕ or $\hat{\phi}$ used in this work.

The Reynolds number R and Λ, the ratio of a sedimentation Grashof number to R, are

$$R = \frac{L\bar{\rho}_f V_{s,\infty}}{\bar{\mu}_f} = \frac{L d_s^2 \bar{\rho}_f(\bar{\rho}_s - \bar{\rho}_f)g}{18\bar{\mu}_f^2} \tag{2.42}$$

$$\Lambda = \frac{L^2 g(\bar{\rho}_s - \bar{\rho}_f)c_0}{V_{s,\infty}\bar{\mu}_f} = 18\left(\frac{L}{d_s}\right)^2 c_0 \tag{2.43}$$

The sedimentation Grashof number is then a product of the Reynolds number and dispersed phase concentration:

$$\mathrm{Gr} = 18\,R\left(\frac{L}{d_s}\right)^2 c_0 \tag{2.44}$$

Acrivos & Herbolzheimer use the same definitions of the average mixture velocity $\hat{\boldsymbol{u}} = c\hat{\boldsymbol{u}}_s + (1-c)\hat{\boldsymbol{u}}_f$ and the dispersed phase slip velocity $\hat{\boldsymbol{u}}' = \hat{\boldsymbol{u}}_s - \hat{\boldsymbol{u}}$ as those used in this research.

The variable Λ used by Acrivos & Herbolzheimer is related to the dimensionless variables used in this work:

$$\begin{aligned}
\Lambda &= \frac{L^2 g(\bar{\rho}_s - \bar{\rho}_f)c_0}{V_{s,\infty}\bar{\mu}_f} \\
&= \frac{\bar{\rho}_f L V_{s,\infty}}{\bar{\mu}_f}\frac{Lg}{V_{s,\infty}^2}\frac{\bar{\rho}_s - \bar{\rho}_f}{\bar{\rho}_f}c_0 \\
&= \frac{\mathrm{Re}}{\mathrm{Fr}}\Gamma c_0
\end{aligned}$$

Acrivos & Herbolzheimer define P to be the dimensionless pressure minus the dimensionless hydrostatic head due to the suspension of concentration c_0.

$$\nabla \hat{P} = \nabla \hat{p} - \frac{gl^2}{\bar{\mu}_f V_{s,\infty}}(c_0 \bar{\rho}_s + (1 - c_0)\bar{\rho}_f)\boldsymbol{\theta} = \nabla \hat{p} - \Lambda \left(1 + \frac{1}{c_0}\frac{\bar{\rho}_f}{\bar{\rho}_s - \bar{\rho}_f}\right)\boldsymbol{\theta} \tag{2.45}$$

The sum of the pressure gradient and gravity terms in Equation 2.41 is then

$$-\nabla \hat{P} - \left(1 - \frac{c}{c_0}\right)\Lambda\boldsymbol{\theta} = -\nabla \hat{p} + \Lambda \left(1 + \frac{1}{c_0}\frac{\bar{\rho}_f}{\bar{\rho}_s - \bar{\rho}_f}\right)\boldsymbol{\theta} - \left(1 - \frac{c}{c_0}\right)\Lambda\boldsymbol{\theta} \tag{2.46}$$

The right-hand-side of Equation 2.46 simplifies to

$$-\nabla \hat{p} + \frac{\Lambda}{c_0}\left(\frac{\bar{\rho}_f}{\bar{\rho}_s - \bar{\rho}_f} + c\right)\theta \tag{2.47}$$

or

$$-\nabla \hat{p} + \frac{\Lambda}{c_0}\frac{\bar{\rho}_f}{\bar{\rho}_s - \bar{\rho}_f}\left(1 + c\frac{\bar{\rho}_s - \bar{\rho}_f}{\bar{\rho}_f}\right)\theta \tag{2.48}$$

In terms of the dimensionless groups used in this work the pressure gradient and buoyancy terms in Equation 2.48 are

$$-\nabla \hat{p} + \frac{\mathrm{Re}}{\mathrm{Fr}}(1 + c\Gamma)\theta \tag{2.49}$$

The buoyancy term used by Acrivos & Herbolzheimer reduces to the same expression as that used in this work.

Acrivos & Herbolzheimer [1] present a two-part boundary layer solution for Equation 2.41. The first part gives the thickness and the velocity profile in the clear fluid zone as a function of distance along the vessel. The suspension interface is treated as a discontinuity in the dispersed phase volume fraction. The second part gives the motion of the suspension and matches the no-slip and continuous stress conditions at the suspension/clear fluid interface. This two part solution allows the Boussinesq and constant viscosity assumptions to be relaxed: the suspension is treated as a single phase fluid with constant density and viscosity in each part.

The analysis of Acrivos & Herbolzheimer [1] was modified in the subsequent work of Shaqfeh & Acrivos [43, 44, 45]. It was also used in the stability analysis of Herbolzheimer [18] described in the next section.

2.7 Linear stability analysis of Herbolzheimer

Herbolzheimer [18] used the base velocity profile obtained by Acrivos & Herbolzheimer [1] to perform a linear stability analysis of the flow in the vicinity of the interface between the clear fluid slit and the suspension. This analysis is similar to that used by Yih [54] for the stability of viscous film flow down an inclined plate. The disturbances are assumed to grow spatially rather than temporally. The analysis of Herbolzheimer is restricted to disturbances whose wavelength is large compared to the thickness of the clear fluid layer but small compared to the width of the sedimentation vessel.

Herbolzheimer presents theoretical results for the imaginary part of the wavenumber (growth rate) and the real part of the wavenumber (inverse wavelength). The parameters chosen are the vessel Reynolds number, initial concentration and inclination. This stability analysis demonstrated that flows with higher vessel Reynolds number (lower viscosity) are unstable to disturbances of higher wavenumber (shorter wavelength).

2.8 Vorticity-stream function formulation

The dimensionless momentum equation 2.40 and the continuity equation $\hat{\nabla}\cdot\hat{\boldsymbol{u}} = 0$ are replaced by the two-dimensional vorticity transport and stream function equations.

The vorticity of the mixture is defined by

$$\hat{\omega} = \frac{\partial \hat{v}}{\partial \hat{x}} - \frac{\partial \hat{u}}{\partial \hat{y}} \tag{2.50}$$

for a two-dimensional field. The stream function $\hat{\psi}$ of the mixture is defined through

$$\hat{u} = \frac{\partial \hat{\psi}}{\partial \hat{y}}, \qquad \hat{v} = -\frac{\partial \hat{\psi}}{\partial \hat{x}} \tag{2.51}$$

The stream function equation is obtained from Equation 2.50 and the definition of the stream function:

$$\frac{\partial^2 \hat{\psi}}{\partial \hat{x}^2} + \frac{\partial^2 \hat{\psi}}{\partial \hat{y}^2} = -\hat{\omega} \tag{2.52}$$

The momentum equation 2.33 becomes the vorticity transport equation

$$\hat{\rho}\left(\frac{\partial \hat{\omega}}{\partial \hat{t}} + \frac{\partial(\hat{u}\hat{\omega})}{\partial \hat{x}} + \frac{\partial(\hat{v}\hat{\omega})}{\partial \hat{y}}\right) = -\frac{\Gamma}{\mathrm{Fr}}\left(\frac{\partial \hat{\phi}}{\partial \hat{x}}\theta_y - \frac{\partial \hat{\phi}}{\partial \hat{y}}\theta_x\right) + \frac{1}{\mathrm{Re}}\left(\frac{\partial^2 \hat{\omega}}{\partial \hat{x}^2} + \frac{\partial^2 \hat{\omega}}{\partial \hat{y}^2}\right) \tag{2.53}$$

The material transport equation is

$$\frac{\partial \hat{\phi}}{\partial \hat{t}} + \frac{\partial(\hat{\phi}\hat{u}_s)}{\partial \hat{x}} + \frac{\partial(\hat{\phi}\hat{v}_s)}{\partial \hat{y}} = 0 \tag{2.54}$$

2.9 Summary

Sedimentation is modelled with four simple equations. The motion of the homogeneous mixture is described by two PDEs: a vorticity transport equation and a stream function equation. The motion of the dispersed phase is described by an algebraic equation for the slip velocity of the dispersed phase and a material transport equation for the volume fraction of the dispersed phase. These governing equations are analogous to a vorticity-stream function formulation of the equations used by Hill et al. [19] except the slip velocity of the dispersed phase is a function of concentration and the viscosity of the bulk suspension is used rather than that of the continuous phase. The order of magnitude analysis of the two-fluid model in Appendix 11 and the derivation of the mixture momentum equation in Appendix A demonstrates this simple homogeneous mixture model is valid for low particle Reynolds numbers ($\mathrm{Re}_{s,\infty} < O(0.1)$) and for $\phi(\bar{\rho}_s - \bar{\rho}_f) \ll \rho$.

An accurate and efficient finite difference algorithm for solving these four equations is presented in the next chapter.

Chapter 3

Discretization and solution algorithm

The material transport Equation 2.26 is a nonlinear hyperbolic equation and admits shocks (discontinuities) as solutions. These properties are similar to those of the Euler equations used to model transonic flow [46]. Colella & Woodward [7] demonstrate the capabilities of several discretization methods to capture strong and weak shocks for transonic flow past several geometries.

The volume fraction discontinuity at the suspension/clear fluid interface provides the buoyancy driving force for the motion of the suspension. It is necessary for the numerical simulation to approximate this discontinuity sharply and without oscillatory behaviour to obtain an accurate model of sedimentation. Excessive smearing of the interface reduces the buoyancy driving force. Oscillatory behaviour introduces local pockets of low and high density suspension and causes abnormal buoyancy forces near the interface.

Harten & Osher [17] present the non-oscillatory second order accurate UNO2 scheme for the hyperbolic conservation equation

$$\frac{\partial u}{\partial t} + \frac{\partial(f(u))}{\partial x} = 0 \qquad (3.1)$$

They demonstrate the UNO2 scheme is total variation diminishing (TVD) and retains second order accuracy at local extrema.

The volume fraction equation is updated explicitly with the non-oscillatory second order accurate UNO2 scheme of Harten & Osher. The vorticity transport equation is coupled with the stream function equation and is solved implicitly. The convection term in the vorticity transport equation is calculated with the UNO2 scheme while the viscous terms are discretized with three point central finite difference expressions. The formulation

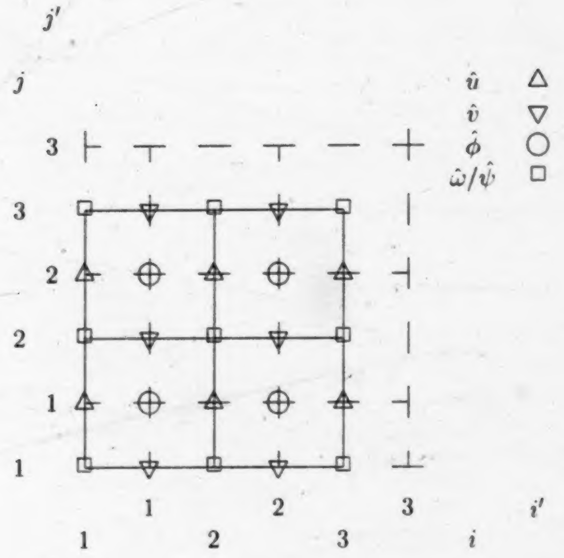

Figure 3.1: Staggered mesh for $\hat{u}, \hat{v}, \hat{\phi}, \hat{\omega}, \hat{\psi}$.

of the UNO2 scheme used in this work is based on the description presented by Yokota [55].

3.1 Mesh description

The variables $\hat{\omega}, \hat{\psi}, \hat{\phi}, \hat{u}$ and $\hat{v}$ were discretized on the staggered mesh shown in Figure 3.1. The vorticity transport and stream function equations were regarded as finite difference equations while the material transport equation was a cell centered finite volume equation.

The grid lines for the non-staggered and staggered meshes were indexed by i and i', respectively. The grid line i is at the same location as $i' - 1/2$ and denotes the left boundary of the control volume at i'.

The vorticity transport and stream function equations were discretized in generalized orthogonal coordinates (ξ, η) as described by Thompson [49]. The second derivative $\partial^2 \hat{\omega}/\partial \hat{x}^2$ was transformed to the generalized coordinates with

$$\frac{\partial^2 \hat{\omega}}{\partial \hat{x}^2} = \left(\frac{\partial^2 \hat{\omega}}{\partial \xi^2} - \frac{\partial^2 \hat{x}/\partial \xi^2}{\partial \hat{x}/\partial \xi} \frac{\partial \hat{\omega}}{\partial \xi} \right) \frac{1}{(\partial \hat{x}/\partial \xi)^2} \tag{3.2}$$

where $\partial \hat{x}/\partial \xi$ and $\partial^2 \hat{x}/\partial \xi^2$ are the first and second order metric transformation coefficients. A similar equation can be written for $\partial^2 \hat{\omega}/\partial \hat{y}^2$ in terms of the generalized coordinate η.

The grid clustering equations of Hoffmann [21] was used to cluster the $\hat{x}$ direction mesh uniformly near the lateral walls:

$$\hat{x} = \hat{w} \frac{\left(2\alpha - \beta_x + \left(\frac{\beta_x+1}{\beta_x-1} \right)^{\frac{\xi-\alpha}{1-\alpha}} (2\alpha + \beta_x) \right)}{(1+2\alpha) \left(1 + \left(\frac{\beta_x+1}{\beta_x-1} \right)^{\frac{\xi-\alpha}{1-\alpha}} \right)}$$

$$\frac{\partial \hat{x}}{\partial \xi} = \hat{w} \frac{2\beta_x \left(\frac{\beta_x+1}{\beta_x-1} \right)^{\frac{\alpha+\xi}{\alpha-1}} \ln(\frac{\beta_x+1}{\beta_x-1})}{(1-\alpha)\,(1+2\alpha) \left(\left(\frac{\beta_x+1}{\beta_x-1} \right)^{\frac{\alpha}{\alpha-1}} + \left(\frac{\beta_x+1}{\beta_x-1} \right)^{\frac{\xi}{\alpha-1}} \right)^2}$$

$$\frac{\partial^2 \hat{x}/\partial \xi^2}{\partial x/\partial \xi} = \frac{\left(\left(\frac{\beta_x+1}{\beta_x-1} \right)^{\frac{\alpha}{\alpha-1}} - \left(\frac{\beta_x+1}{\beta_x-1} \right)^{\frac{\xi}{\alpha-1}} \right) \ln(\frac{\beta_x+1}{\beta_x-1})}{(\alpha-1) \left(\left(\frac{\beta_x+1}{\beta_x-1} \right)^{\frac{\alpha}{\alpha-1}} + \left(\frac{\beta_x+1}{\beta_x-1} \right)^{\frac{\xi}{\alpha-1}} \right)}$$

where $\hat{w}$ is the width of the vessel, β_x is the grid clustering parameter ($\beta_x > 1$) and $\alpha = 0.5$. The grid spacing is given by

$$\Delta \hat{x} = \frac{\partial \hat{x}}{\partial \xi} \Delta \xi$$

3.2 Material transport equation

The discretized form of the volume fraction transport equation

$$\frac{\partial \hat{\phi}}{\partial \hat{t}} + \frac{\partial (\hat{u}_s \hat{\phi})}{\partial \hat{x}} + \frac{\partial (\hat{v}_s \hat{\phi})}{\partial \hat{y}} = 0 \tag{3.3}$$

is interpreted as a cell-centered finite volume expression. Data on the solution surface propagates with the characteristic velocities $\hat{a}^x$ and $\hat{a}^y$ where

$$\hat{a}^x = \frac{\partial (\hat{u}_s \hat{\phi})}{\partial \hat{\phi}} = \hat{u} + \frac{\partial (\hat{u}'_s(\hat{\phi}) \hat{\phi})}{\partial \hat{\phi}} \tag{3.4}$$

$$\hat{a}^y = \frac{\partial (\hat{v}_s \hat{\phi})}{\partial \hat{\phi}} = \hat{v} + \frac{\partial (\hat{v}'_s(\hat{\phi}) \hat{\phi})}{\partial \hat{\phi}} \tag{3.5}$$

The characteristic velocities are sum of the mixture velocity and the wave speed given by the slope of the flux curve.

A one-dimensional interpolation for $\hat{\phi}$ across the control volume is

$$\hat{\phi} = \hat{\phi}_{i',j'} + S^x_{i',j'}(\hat{x} - \hat{x}_{i',j'}) \tag{3.6}$$

where $S^x_{i',j'}$ is the slope across the control volume. The slope for the UNO2 scheme of Harten & Osher is

$$S^x_{i',j'} = \frac{\text{median}(0, \hat{\phi}^c_{i'+1/2,j'} - \hat{\phi}_{i',j'}, \hat{\phi}^c_{i',j'} - \hat{\phi}_{i'-1/2,j'})}{\Delta\hat{x}/2} \tag{3.7}$$

where $\hat{\phi}^c_{i'+1/2,j'}$ is obtained from the nonoscillatory quadratic interpolation

$$\hat{\phi}^c_{i'+1/2,j'} = 0.5(\hat{\phi}_{i',j'} + \hat{\phi}_{i'+1,j'}) - 0.25D_{i'+1/2,j'} \tag{3.8}$$

and the inflection $D_{i'+1/2,j'}$ is

$$D_{i'+1/2,j'} = \text{minmod}((\hat{\phi}_{i'+1,j'} - 2\hat{\phi}_{i',j'} + \hat{\phi}_{i'-1,j'}), (\hat{\phi}_{i'+2,j'} - 2\hat{\phi}_{i'+1,j'} + \hat{\phi}_{i',j'})) \tag{3.9}$$

and the minmod function is

$$\text{minmod}(a, b) = \text{sign}(a)\max(0, \text{sign}(ab)\min(|a|, |b|)) \tag{3.10}$$

Equation 3.9 was modified near the walls. At $i' = 1$, $\hat{\phi}_{i'-1,j'}$ was assumed to be equal to $\hat{\phi}_{i',j'}$. At $i' = NI'-1$, $\hat{\phi}_{i'+1,j'}$ was assumed to be equal to $\hat{\phi}_{i',j'}$. At $i' = NI'$, $\hat{\phi}_{i'+1,j'}$ was assumed to be equal to $\hat{\phi}_{i',j'}$ and the minmod calculation was not performed. Equation 3.8 was modified at $i = NI'$: $\hat{\phi}_{i'+1,j'}$ was assumed to be equal to $\hat{\phi}_{i',j'}$.

The volume fraction surface is evaluated at the intermediate time level $n + 1/2$ by following the solution characteristics to their positions at time level n. The characteristic velocity at the cell face $\hat{a}^x_{i'+1/2,j'}$ is

$$\hat{a}^x_{i'+1/2,j'} = \begin{cases} (\hat{u})^n_{i'+1/2,j'} + \\ \quad \dfrac{\hat{u}'_s(\hat{\phi}^n_{i'+1,j'})\hat{\phi}^n_{i'+1,j'} - \hat{u}'_s(\hat{\phi}^n_{i',j'})\hat{\phi}^n_{i',j'}}{\hat{\phi}^n_{i'+1,j'} - \hat{\phi}^n_{i',j'}} & \text{if } \hat{\phi}^n_{i',j'} \neq \hat{\phi}^n_{i'+1,j'} \\ (\hat{u})^n_{i'+1/2,j'} + \dfrac{\partial(\hat{u}'_s(\hat{\phi}^n_{i',j'})\hat{\phi}^n_{i',j'})}{\partial\hat{\phi}} & \text{if } \hat{\phi}^n_{i',j'} = \hat{\phi}^n_{i'+1,j'} \end{cases} \tag{3.11}$$

Equation 3.11 gives the Rankine-Hugoniot velocity for the propagation of a shock wave. The slip velocity at $i' + 1/2$ is evaluated with $\hat{\phi}^c_{i'+1/2,j'}$. The solution surface is constructed on the cell face at the $n + 1/2$ time level:

$$\hat{\phi}^{n+1/2}_{i'+1/2,j'} = \begin{cases} \hat{\phi}^{n}_{i',j'} + S^{x}_{i',j'} \dfrac{\Delta \hat{x}}{2} \left(1 - \dfrac{\hat{a}^{x}_{i'+1/2,j'} \Delta \hat{t}}{\Delta \hat{x}}\right) \\ \qquad - S^{y}_{i',j'} \dfrac{\hat{a}^{y}_{i'+1/2,j'} \Delta \hat{t}}{2} & \text{if } \hat{a}^{x}_{i'+1/2,j'} \geq 0 \\ \hat{\phi}^{n}_{i'+1,j'} - S^{x}_{i'+1,j'} \dfrac{\Delta \hat{x}}{2} \left(1 + \dfrac{\hat{a}^{x}_{i'+1/2,j'} \Delta \hat{t}}{\Delta \hat{x}}\right) \\ \qquad - S^{y}_{i'+1,j'} \dfrac{\hat{a}^{y}_{i'+1/2,j'} \Delta \hat{t}}{2} & \text{if } \hat{a}^{x}_{i'+1/2,j'} < 0 \end{cases} \tag{3.12}$$

$$\hat{\phi}^{n+1/2}_{i',j'+1/2} = \begin{cases} \hat{\phi}^{n}_{i',j'} + S^{y}_{i',j'} \dfrac{\Delta \hat{y}}{2} \left(1 - \dfrac{\hat{a}^{y}_{i',j'+1/2} \Delta \hat{t}}{\Delta \hat{y}}\right) \\ \qquad - S^{x}_{i',j'} \dfrac{\hat{a}^{x}_{i',j'+1/2} \Delta \hat{t}}{2} & \text{if } \hat{a}^{y}_{i',j'+1/2} \geq 0 \\ \hat{\phi}^{n}_{i',j'+1} - S^{y}_{i',j'+1} \dfrac{\Delta \hat{y}}{2} \left(1 + \dfrac{\hat{a}^{y}_{i',j'+1/2} \Delta \hat{t}}{\Delta \hat{y}}\right) \\ \qquad - S^{x}_{i',j'+1} \dfrac{\hat{a}^{x}_{i',j'+1/2} \Delta \hat{t}}{2} & \text{if } \hat{a}^{y}_{i',j'+1/2} < 0 \end{cases} \tag{3.13}$$

The volume fractions are updated with the midpoint rule

$$\hat{\phi}^{n+1}_{i',j'} = \hat{\phi}^{n}_{i',j'} - \Delta \hat{t} \left(\frac{(\hat{u}_s \hat{\phi})^{n+1/2}_{i'+1/2,j'} - (\hat{u}_s \hat{\phi})^{n+1/2}_{i'-1/2,j'}}{\Delta \hat{x}} + \frac{(\hat{v}_s \hat{\phi})^{n+1/2}_{i',j'+1/2} - (\hat{v}_s \hat{\phi})^{n+1/2}_{i',j'-1/2}}{\Delta \hat{y}} \right) \tag{3.14}$$

where

$$(\hat{u}_s)^{n+1/2}_{i'+1/2,j'} = (\hat{u})^{n}_{i'+1/2,j} + \hat{u}'_s(\hat{\phi}^{n+1/2}_{i'+1/2,j'}) \tag{3.15}$$

$$(\hat{v}_s)^{n+1/2}_{i'+1/2,j'} = (\hat{v})^{n}_{i'+1/2,j} + \hat{v}'_s(\hat{\phi}^{n+1/2}_{i'+1/2,j'}) \tag{3.16}$$

The mixture velocities $\hat{u}$ and $\hat{v}$ at the cell faces are obtained with central differencing of the stream function field at the n time level:

$$(\hat{u})^{n}_{i'+1/2,j'} = \frac{\hat{\psi}^{n}_{i+1,j+1} - \hat{\psi}^{n}_{i+1,j}}{\Delta \hat{x}} \tag{3.17}$$

$$(\hat{u})^{n}_{i'-1/2,j'} = \frac{\hat{\psi}^{n}_{i,j+1} - \hat{\psi}^{n}_{i,j}}{\Delta \hat{x}} \tag{3.18}$$

$$(\hat{v})^{n}_{i',j'+1/2} = \frac{\hat{\psi}^{n}_{i+1,j+1} - \hat{\psi}^{n}_{i,j+1}}{-\Delta \hat{y}} \tag{3.19}$$

$$(\hat{v})^{n}_{i',j'-1/2} = \frac{\hat{\psi}^{n}_{i+1,j} - \hat{\psi}^{n}_{i,j}}{-\Delta \hat{y}} \tag{3.20}$$

(3.21)

Zero flux was specified through faces that lay on walls. Inlets were modelled with constant flux of volume fraction. Outlets convected the concentration of the adjacent cell at the velocity of the outlet face.

The stability analysis presented in Chapter 4 demonstrates the UNO2 scheme requires the time step to satisfy the CFL condition

$$N_C = \frac{|\hat{a}|\Delta\hat{t}}{\Delta\hat{x}} \leq 1 \tag{3.22}$$

in both the $\hat{x}$ and $\hat{y}$ directions. The absolute value of the wave speed $|\hat{a}|$ was taken to be the largest values of $|\hat{u}| + |\hat{u}'_s|$ and $|\hat{v}| + |\hat{v}'_s|$ in the problem domain. The actual limit on the time step was more conservative than Equation 3.22: the Courant number was limited to 0.5.

3.3 Vorticity transport equation

The convection term was modelled with the UNO2 scheme and the buoyancy terms were discretized explicitly as a source term. The diffusion terms were discretized semi-implicitly with the Crank-Nicolson method. The stability analysis presented in Chapter 4 demonstrates the semi-implicit treatment of the viscous terms removes the stability limit on $\Delta\hat{t}$ required by an explicit discretization [21]:

$$N_D = \frac{\Delta\hat{t}}{\mathrm{Re}\Delta\hat{x}^2} \leq 0.5 \tag{3.23}$$

The time step is limited only by Equation 3.22.

The conservative first order convection terms $\partial(\hat{u}\hat{\omega})/\partial\hat{x} + \partial(\hat{v}\hat{\omega})/\partial\hat{y}$ were evaluated explicitly with the UNO2 scheme. Modifications were necessary for grid points adjacent the walls. The slope at $i = 2$ was assumed to be

$$S^x_{2,j} = \frac{\hat{\omega}^c_{2+1/2,j} - \hat{\omega}_{2,j}}{\Delta\hat{x}/2}$$

The $\hat{\omega}^c$ value at $i = 1 + 1/2$ was extrapolated from $\hat{\omega}_{2,j}$ and $\hat{\omega}^c_{2+1/2,j}$ with this slope:

$$\hat{\omega}^c_{1+1/2,j} = \hat{\omega}_{2,j} + 2\left(\hat{\omega}_{2,j} - \hat{\omega}^c_{2+1/2,j}\right)$$

The slope at $i = 1$ was

$$S^x_{1,j} = \frac{\hat{\omega}^c_{1+1/2,j} - \hat{\omega}_{1,j}}{\Delta\hat{x}/2}$$

Similar extrapolations were used for the slopes near the other walls.

The discretized vorticity transport equation is

$$
\begin{aligned}
\hat{\rho}\left(\frac{\hat{\omega}_{i,j}^{n+1}-\hat{\omega}_{i,j}^{n}}{\Delta\hat{t}}+\frac{(\hat{u}\hat{\omega})_{i+1/2,j}^{n+1/2}-(\hat{u}\hat{\omega})_{i-1/2,j}^{n+1/2}}{\Delta\hat{x}}+\frac{(\hat{v}\hat{\omega})_{i,j+1/2}^{n+1/2}-(\hat{v}\hat{\omega})_{i,j-1/2}^{n+1/2}}{\Delta\hat{y}}\right) = \\
\beta_{\hat{\omega}}\frac{1}{\mathrm{Re}}\left[\left(\frac{\hat{\omega}_{i-1,j}^{n+1}-2\hat{\omega}_{i,j}^{n+1}+\hat{\omega}_{i+1,j}^{n+1}}{\Delta\xi^2}-\left(\frac{\partial^2\hat{x}/\partial\xi^2}{\partial\hat{x}/\partial\xi}\right)\frac{\hat{\omega}_{i+1,j}^{n+1}-\hat{\omega}_{i-1,j}^{n+1}}{2\Delta\xi}\right)\frac{1}{(\partial\hat{x}/\partial\xi)^2}+\right. \\
\left.\left(\frac{\hat{\omega}_{i,j-1}^{n+1}-2\hat{\omega}_{i,j}^{n+1}+\hat{\omega}_{i,j+1}^{n+1}}{\Delta\eta^2}-\left(\frac{\partial^2\hat{y}/\partial\eta^2}{\partial\hat{y}/\partial\eta}\right)\frac{\hat{\omega}_{i,j+1}^{n+1}-\hat{\omega}_{i,j-1}^{n+1}}{2\Delta\eta}\right)\frac{1}{(\partial\hat{y}/\partial\eta)^2}\right] \\
+(1-\beta_{\hat{\omega}})\frac{1}{\mathrm{Re}}\left[\left(\frac{\hat{\omega}_{i-1,j}^{n}-2\hat{\omega}_{i,j}^{n}+\hat{\omega}_{i+1,j}^{n}}{\Delta\xi^2}-\left(\frac{\partial^2\hat{x}/\partial\xi^2}{\partial\hat{x}/\partial\xi}\right)\frac{\hat{\omega}_{i+1,j}^{n}-\hat{\omega}_{i-1,j}^{n}}{2\Delta\xi}\right)\frac{1}{(\partial\hat{x}/\partial\xi)^2}+\right. \\
\left.\left(\frac{\hat{\omega}_{i,j-1}^{n}-2\hat{\omega}_{i,j}^{n}+\hat{\omega}_{i,j+1}^{n}}{\Delta\eta^2}-\left(\frac{\partial^2\hat{y}/\partial\eta^2}{\partial\hat{y}/\partial\eta}\right)\frac{\hat{\omega}_{i,j+1}^{n}-\hat{\omega}_{i,j-1}^{n}}{2\Delta\eta}\right)\frac{1}{(\partial\hat{y}/\partial\eta)^2}\right] \\
+\beta_{\hat{\phi}}\frac{\Gamma}{\mathrm{Fr}}\frac{1}{2}\left[\hat{\phi}_{i',j'}^{n+1}\left(\frac{1}{\Delta\hat{x}}\theta_y-\frac{1}{\Delta\hat{y}}\theta_x\right)+\hat{\phi}_{i'-1,j'}^{n+1}\left(-\frac{1}{\Delta\hat{x}}\theta_y-\frac{1}{\Delta\hat{y}}\theta_x\right)\right. \\
\left.+\hat{\phi}_{i',j'-1}^{n+1}\left(\frac{1}{\Delta\hat{x}}\theta_y+\frac{1}{\Delta\hat{y}}\theta_x\right)+\hat{\phi}_{i'-1,j'-1}^{n+1}\left(-\frac{1}{\Delta\hat{x}}\theta_y+\frac{1}{\Delta\hat{y}}\theta_x\right)\right] \\
+(1-\beta_{\hat{\phi}})\frac{\Gamma}{\mathrm{Fr}}\frac{1}{2}\left[\hat{\phi}_{i',j'}^{n}\left(\frac{1}{\Delta\hat{x}}\theta_y-\frac{1}{\Delta\hat{y}}\theta_x\right)+\hat{\phi}_{i'-1,j'}^{n}\left(-\frac{1}{\Delta\hat{x}}\theta_y-\frac{1}{\Delta\hat{y}}\theta_x\right)\right. \\
\left.+\hat{\phi}_{i',j'-1}^{n}\left(\frac{1}{\Delta\hat{x}}\theta_y+\frac{1}{\Delta\hat{y}}\theta_x\right)+\hat{\phi}_{i'-1,j'-1}^{n}\left(-\frac{1}{\Delta\hat{x}}\theta_y+\frac{1}{\Delta\hat{y}}\theta_x\right)\right]
\end{aligned}
\tag{3.24}
$$

The implicitness factors are $\beta_{\hat{\omega}} = 1/2$ for the viscous term and $\beta_{\hat{\phi}} = 0$ for the buoyancy driving force term. A stability and truncation error analysis is presented in Chapter 4 for arbitrary choices of the implicitness factors. The truncation error analysis in Chapter 4 demonstrates the discretized vorticity transport equation 3.24 is first order accurate but does not suffer from numerical diffusion.

Only the time advancement and viscous terms of Equation 3.24 contain coefficients for $\hat{\omega}^{n+1}$. The Boussinesq approximation and the constant viscosity assumption ensure these coefficients depend only on the time step $\Delta\hat{t}$ for any grid point (i, j).

The boundary values for $\hat{\omega}^{n+1}$ were calculated with the second order accurate equation,

$$
\hat{\omega}_w^{n+1} = \frac{-3(\hat{\psi}_{w+1}^{n+1}-\hat{\psi}_w^{n+1})}{\Delta\hat{n}^2}-\frac{\hat{\omega}_{w+1}^{n+1}}{2}+O(\Delta\hat{n}^2)
\tag{3.25}
$$

The subscripts w and $w+1$ refer to the values at the wall and one node away from the wall. $\Delta\hat{n}$ is the grid spacing in the direction normal to the wall. This vorticity boundary condition coupled the solution of the vorticity transport equation with the stream function equation.

For continuous sedimentation the inlet was assumed to be irrotational ($\hat{\omega}^{n+1} = 0$) and the vorticity at the outlets were taken to be $\hat{\omega}_{i,1}^{n+1} = \hat{\omega}_{i,2}^{n+1}$ and $\hat{\omega}_{i,NJ}^{n+1} = \hat{\omega}_{i,NJ-1}^{n+1}$.

3.4 Stream function equation

Equation 2.52 was discretized with second order accurate three point central difference to produce the finite difference equation for stream function at the $n+1$ time level:

$$\begin{aligned}\left(\frac{\hat{\psi}^{n+1}_{i-1,j}-2\hat{\psi}^{n+1}_{i,j}+\hat{\psi}^{n+1}_{i+1,j}}{\Delta\xi^2}-\left(\frac{\partial^2\hat{x}/\partial\xi^2}{\partial\hat{x}/\partial\xi}\right)\frac{\hat{\psi}^{n+1}_{i+1,j}-\hat{\psi}^{n+1}_{i-1,j}}{2\Delta\xi}\right)\frac{1}{(\partial\hat{x}/\partial\xi)^2} &\quad + \\ \left(\frac{\hat{\psi}^{n+1}_{i,j-1}-2\hat{\psi}^{n+1}_{i,j}+\hat{\psi}^{n+1}_{i,j+1}}{\Delta\eta^2}-\left(\frac{\partial^2\hat{y}/\partial\eta^2}{\partial\hat{y}/\partial\eta}\right)\frac{\hat{\psi}^{n+1}_{i,j+1}-\hat{\psi}^{n+1}_{i,j-1}}{2\Delta\eta}\right)\frac{1}{(\partial\hat{y}/\partial\eta)^2} &\quad = \quad -\hat{\omega}^{n+1}_{i,j}\end{aligned} \tag{3.26}$$

The term $\hat{\omega}^{n+1}_{i,j}$ couples the stream function equation with the vorticity transport equation.

Stream function is constant along walls. Plug flow was assumed at the inlet and outlets: a linear profile was prescribed for $\hat{\psi}$.

3.5 Direct solution of the discretized vorticity and stream function equations

The discretized vorticity transport equation 3.24, stream function equation 3.26 and the boundary conditions for vorticity and stream function yield a set of linear equations for $\hat{\omega}^{n+1}$ and $\hat{\psi}^{n+1}$. This matrix equation was solved by sparse *LU* decomposition with subroutines in the SPARSPAK library [13].

Sparse *LU* decomposition is much more time consuming than matrix multiplication. The Boussinesq approximation and constant viscosity assumption ensured the coefficients in the matrix equation remained constant provided the time step remained constant. Experience showed the maximum velocity fluctuated typically by ±30 % over short time intervals. Allowing the maximum courant number to float in the range 0.2 – 0.5 avoided excessive LU factorizations over the short term fluctuations in the maximum velocity. A new time step corresponding to $\max(N_C) = 0.35$ was selected if the largest Courant number fell outside this range. The matrix coefficients were recalculated and the matrix was factored again. Subsequent solutions to the matrix equation were obtained quickly by matrix multiplications with different right hand side vectors. Simulations with this direct method required one tenth of the time needed by simulations where the sparse matrix equation was factored at each time step.

3.6 Summary

The uniformly second order accurate UNO2 method of Harten & Osher was applied to the convection terms in the material transport and vorticity transport equations.

The three simplifying assumptions made in the previous chapter (integer power for the hindering function, Boussinesq approximation and constant viscosity) permitted an efficient solution algorithm. The application of shock-capturing TVD methods (usually found in computational aerodynamics) to the numerical simulation of sedimentation is new.

Chapter 4

Linear stability and truncation error analysis

A von Neumann stability analysis and a truncation error (consistency) analysis are presented for the model one-dimensional convection-diffusion equation. The convection term of this equation is discretized with the UNO2 scheme presented in the previous chapter and the diffusion term is discretized with three point central differencing. Numerical results from first order upwinding and the UNO2 scheme are compared for one-dimensional vertical sedimentation. Results from the UNO2 method are used to determine the order of magnitude of the truncation error associated with the buoyancy driving force in the vorticity transport equation. The effect of a smeared suspension interface on the velocity profile is determined with two limiting cases for a model problem.

Algebraic simplifications and substitutions were performed with the symbolic mathematics package Mathematica [52]. Details of the analysis are presented for the simple case of first order upwinding. Only the results are presented for the more lengthy analysis of the UNO2 discretization method.

4.1 Linear stability analysis

A linear stability analysis is performed on the one dimensional convection-diffusion equation where the convection and diffusion terms are discretized in the manner presented for the vorticity transport equation:

$$\frac{\partial \hat{\omega}}{\partial \hat{t}} + \hat{u}\frac{\partial \hat{\omega}}{\partial \hat{x}} = \frac{1}{\mathrm{Re}}\frac{\partial^2 \hat{\omega}}{\partial \hat{x}^2}$$

The convection velocity $\hat{u}$ is assumed to be positive and constant. The buoyancy source term is neglected. This equation is analogous to the material transport equation for $\text{Re} \to \infty$ and the velocity $\hat{u}$ is the velocity of the dispersed phase. The stability analysis is demonstrated with first order upwind differencing of the convection term are presented first. This is followed by the stability results for UNO2 discretization of the convection term.

4.1.1 First order upwind differencing

The finite difference expression for first order upwind differencing is

$$\frac{\hat{\omega}_i^{n+1} - \hat{\omega}_i^n}{\Delta\hat{t}} + \hat{u}\frac{\hat{\omega}_i^n - \hat{\omega}_{i-1}^n}{\Delta\hat{x}} =$$
$$\beta_{\hat{\omega}}\frac{1}{\text{Re}}\frac{\hat{\omega}_{i+1}^{n+1} - 2\hat{\omega}_i^{n+1} + \hat{\omega}_{i-1}^{n+1}}{\Delta\hat{x}^2} + (1 - \beta_{\hat{\omega}})\frac{1}{\text{Re}}\frac{\hat{\omega}_{i+1}^n - 2\hat{\omega}_i^n + \hat{\omega}_{i-1}^n}{\Delta\hat{x}^2}$$

The Courant number is defined by $N_C = \hat{u}\Delta\hat{t}/\Delta\hat{x}$ and the diffusion number is defined by $N_D = \Delta\hat{t}/(\text{Re}\Delta\hat{x}^2)$. The finite difference expression becomes

$$\begin{aligned}\hat{\omega}_i^{n+1} &= \hat{\omega}_i^n - N_C(\hat{\omega}_i^n - \hat{\omega}_{i-1}^n) \\ &+\beta_{\hat{\omega}}N_D(\hat{\omega}_{i+1}^{n+1} - 2\hat{\omega}_i^{n+1} + \hat{\omega}_{i-1}^{n+1}) + (1 - \beta_{\hat{\omega}})N_D(\hat{\omega}_{i+1}^n - 2\hat{\omega}_i^n + \hat{\omega}_{i-1}^n)\end{aligned} \tag{4.1}$$

The solution $\hat{\omega}_i^n$ at the time level n and grid point i is represented by the Fourier component

$$\hat{\omega}_i^n = \Omega^n e^{I\zeta i} \tag{4.2}$$

where ζ is the phase angle $(0 \leq \zeta \leq \pi)$ and $I = \sqrt{-1}$. The Fourier components for grid points to the left and right of i are

$$\hat{\omega}_{i\pm1}^n = \Omega^n e^{I\zeta(i\pm1)}$$

The Fourier component for the solution at the time level $n + 1$ is

$$\hat{\omega}_i^{n+1} = \Omega^n e^{I\zeta i}$$

These expressions for the Fourier components are substituted for $\hat{\omega}_i^n$ in the finite difference Equation 4.1 and $e^{I\zeta i}$ is factored out.

$$\begin{aligned}&\Omega^{n+1}\left(1 - \beta_\Omega N_D(e^{I\zeta} - 2 + e^{-I\zeta}\right) = \\ &\Omega^n\left(1 - N_C(1 - e^{-I\zeta}) + (1 - \beta_\Omega)N_D(e^{I\zeta} - 2 + e^{-I\zeta}\right)\end{aligned} \tag{4.3}$$

The growth rate G is defined by $\Omega^{n+1} = G\Omega^n$. The stability requirement is $|G|^2 \leq 1$ where $|G|^2 = G\bar{G}$ and $\bar{G}$ is the conjugate of G.

A few relations between trigonometric and complex functions are required in the analysis:

$$\begin{aligned}\cos\theta &= \frac{e^{I\theta}+e^{-I\theta}}{2}\\ \sin\theta &= \frac{e^{I\theta}-e^{-I\theta}}{2}\\ \cos\theta - I\sin\theta &= e^{-I\theta}\end{aligned}$$

These trigonometric identities were applied and simplified with the symbolic mathematics package Mathematica.

The growth rate for the Equation 4.3 is

$$G = \frac{1 - 2N_C\sin^2\zeta/2 - 4(1-\beta_{\dot{\omega}})N_D\sin^2\zeta/2 - IN_C\sin\zeta}{1 + 4\beta_{\dot{\omega}}N_D\sin^2\zeta/2} \tag{4.4}$$

In the limit of infinite diffusion $N_D \to \infty$ the growth rate is $G = 1 - 1/\beta_{\dot{\omega}}$: the scheme is unconditionally stable for all diffusion numbers.

Figure 4.1 shows the phase angle $\zeta = \pi$ gives the most restrictive condition for the Courant number. Figure 4.2 shows the numerical scheme is stable with large diffusion numbers ($N_D = 10$) for $N_C \leq 1$.

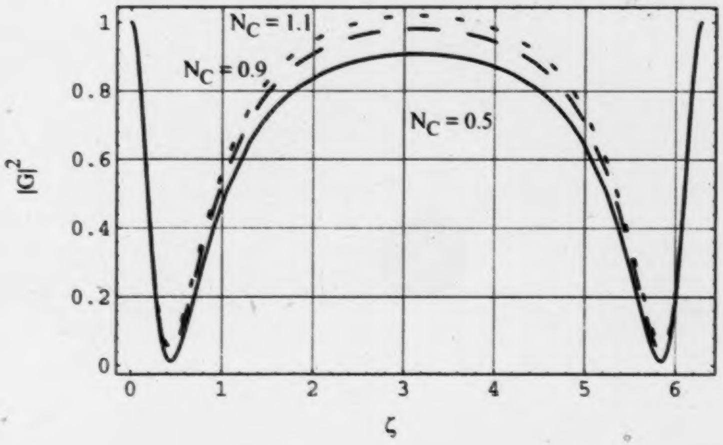

Figure 4.1: Modulus of the growth rate for first order upwind differencing with $\beta_{\dot{\omega}} = 1/2$ and $N_D = 10$: $N_C = 0.5, 0.9, 1.1$.

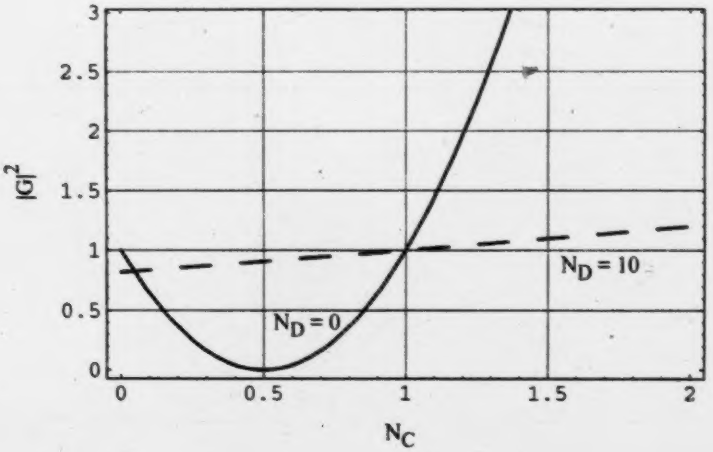

Figure 4.2: Modulus of the growth rate for first order upwind differencing with $\beta_{\dot{\omega}} = 1/2$ and $\zeta = \pi$: $N_D = 0, 10$.

4.1.2 UNO2 scheme

The stability analysis of the UNO2 scheme is more involved than the analysis for first order upwind differencing. For the positive constant convection speed $\hat{u}$ the convection term is

$$\frac{(\hat{u}\hat{\omega})^{n+1/2}_{i+1/2} - (\hat{u}\hat{\omega})^{n+1/2}_{i+1/2}}{\Delta\hat{x}}$$

The one-dimensional convection-diffusion equation is discretized with the UNO2 scheme for the convection term and implicit central difference for the diffusion term:

$$\begin{aligned} &\frac{\hat{\omega}^{n+1}_i - \hat{\omega}^n_i}{\Delta\hat{t}} + \frac{(\hat{u}\hat{\omega})^{n+1/2}_{i+1/2} - (\hat{u}\hat{\omega})^{n+1/2}_{i+1/2}}{\Delta\hat{x}} = \\ &\quad \beta_{\hat{\omega}}\frac{1}{\mathrm{Re}}\frac{\hat{\omega}^{n+1}_{i+1} - 2\hat{\omega}^{n+1}_i + \hat{\omega}^{n+1}_{i-1}}{\Delta\hat{x}^2} + (1-\beta_{\hat{\omega}})\frac{1}{\mathrm{Re}}\frac{\hat{\omega}^n_{i+1} - 2\hat{\omega}^n_i + \hat{\omega}^n_{i-1}}{\Delta\hat{x}^2} \end{aligned}$$

or

$$\begin{aligned} &\hat{\omega}^{n+1}_i - \beta_{\hat{\omega}} N_D(\hat{\omega}^{n+1}_{i+1} - 2\hat{\omega}^{n+1}_i + \hat{\omega}^{n+1}_{i-1}) = \\ &\quad \hat{\omega}^n_i - N_C((\hat{\omega})^{n+1/2}_{i+1/2} - (\hat{\omega})^{n+1/2}_{i+1/2}) + (1-\beta_{\hat{\omega}})N_D(\hat{\omega}^n_{i+1} - 2\hat{\omega}^n_i + \hat{\omega}^n_{i-1}) \end{aligned} \tag{4.5}$$

The cell face values for the convection term are calculated at the $n + 1/2$ time level with

$$\hat{\omega}^{n+1/2}_{i+1/2} = \hat{\omega}^n_i + S_i\frac{\Delta\hat{x}}{2}(1 - N_C)$$

The slope S_i may have three values:

$$S_i = \mathrm{median}(0, \hat{\omega}^c_{i+1/2} - \hat{\omega}_i, \hat{\omega}_i - \hat{\omega}^c_{i-1/2})/(\Delta\hat{x}/2)$$

Each value of $\hat{\omega}^c$ can have three possible values through the minmod function:

$$\hat{\omega}^c_{i+1/2} = (\hat{\omega}^n_{i+1} + \hat{\omega}^n_i)/2 - (1/4)\mathrm{minmod}(\hat{\omega}^n_{i+2} - 2\hat{\omega}^n_{i+1} + \hat{\omega}^n_i, \hat{\omega}^n_{i+1} - 2\hat{\omega}^n_i + \hat{\omega}^n_{i-1},)$$

The minmod function selects the inflection closest to zero or zero if the two inflections have opposite signs.

The growth rates were calculated for five of the ten possible calculation methods of the slope S_i. In each example it is assumed that the calculation method of the slope is applied to all grid points and time steps. The first case considers two types of grid scale oscillations. The next four cases consider different choices for the slope and inflection calculations of the solution surface.

Grid scale oscillation Two types of grid scale oscillations are considered, both of which are characterized by the inflection changing sign at each grid point. The inflection returned by the minmod function is zero and

$$\hat{\omega}^c_{i+1/2} = (\hat{\omega}^n_{i+1} + \hat{\omega}^n_i)/2$$

The first type of oscillation considered has the slope changing sign at each grid point and the value oscillates evenly about an average value: the function looks like a triangle wave pattern. The slope returned by the median function is $S_i = 0$ for all points i. The finite difference expression is

$$\begin{aligned}&\frac{\hat{\omega}^{n+1}_i - \hat{\omega}^n_i}{\Delta \hat{t}} + \hat{u}\frac{\hat{\omega}^n_i - \hat{\omega}^n_{i-1}}{\Delta \hat{x}} = \\ &\qquad \beta_{\hat{\omega}}\frac{1}{\mathrm{Re}}\frac{\hat{\omega}^{n+1}_{i+1} - 2\hat{\omega}^{n+1}_i + \hat{\omega}^{n+1}_{i-1}}{\Delta \hat{x}^2} + (1-\beta_{\hat{\omega}})\frac{1}{\mathrm{Re}}\frac{\hat{\omega}^n_{i+1} - 2\hat{\omega}^n_i + \hat{\omega}^n_{i-1}}{\Delta \hat{x}^2}\end{aligned}$$

The UNO2 scheme reduces to first order upwind differencing in this case. This scheme was shown to be stable for all diffusion numbers and $N_C \leq 1$.

The second type of oscillation considered has alternating high and low slopes in a staircase manner. This function is taken to increase with increasing x. The point i considered is at the base of a step upwards. The values of $\hat{\omega}^c_{i+1/2}$ are the average of $\hat{\omega}^n_i$ and $\hat{\omega}^n_{i+1}$. The slope returned by the median function for the point i is $S_i = (\hat{\omega}^n_i - \hat{\omega}^c_{i-1/2})/(\Delta\hat{x}/2)$ or $S_i = (\hat{\omega}^n_i/2 - \hat{\omega}^n_{i-1}/2)/(\Delta\hat{x}/2)$. The slope returned by the median function for $i-1$ is $S_{i-1} = (\hat{\omega}^c_{i-1/2} - \hat{\omega}^n_{i-1})/(\Delta\hat{x}/2)$ or $S_{i-1} = (\hat{\omega}^n_i/2 - \hat{\omega}^n_{i-1}/2)/(\Delta\hat{x}/2)$: this is the same slope as S_i. The finite difference expression is

$$\begin{aligned}&\frac{\hat{\omega}^{n+1}_i - \hat{\omega}^n_i}{\Delta \hat{t}} + \hat{u}\frac{\hat{\omega}^n_i - \hat{\omega}^n_{i-1}}{\Delta \hat{x}} = \\ &\qquad \beta_{\hat{\omega}}\frac{1}{\mathrm{Re}}\frac{\hat{\omega}^{n+1}_{i+1} - 2\hat{\omega}^{n+1}_i + \hat{\omega}^{n+1}_{i-1}}{\Delta \hat{x}^2} + (1-\beta_{\hat{\omega}})\frac{1}{\mathrm{Re}}\frac{\hat{\omega}^n_{i+1} - 2\hat{\omega}^n_i + \hat{\omega}^n_{i-1}}{\Delta \hat{x}^2}\end{aligned}$$

This case also reduces to first order upwind differencing: it is stable for all diffusion numbers and $N_C \leq 1$.

Slope becomes more positive and inflection becomes more positive In this case the function value increases, the slope becomes more positive and inflection becomes more positive in the positive x direction. The slopes returned by the minmod function for i and $i-1$ are

$$\begin{aligned}S_i &= (\hat{\omega}^n_i - \hat{\omega}^c_{i-1/2})/(\Delta\hat{x}/2) \\ S_{i-1} &= (\hat{\omega}^n_{i-1} - \hat{\omega}^c_{i-3/2})/(\Delta\hat{x}/2)\end{aligned}$$

The values of $\hat{\omega}^c$ are

$$\begin{aligned}\hat{\omega}^c_{i-1/2} &= (\hat{\omega}^n_i + \hat{\omega}^n_{i-1})/2 - (1/4)d_{i-1/2}\\ \hat{\omega}^c_{i-3/2} &= (\hat{\omega}^n_{i-1} + \hat{\omega}^n_{i-2})/2 - (1/4)d_{i-3/2}\end{aligned}$$

The inflections d are

$$\begin{aligned}d_{i-1/2} &= (\hat{\omega}^n_i - 2\hat{\omega}^n_{i-1} + \hat{\omega}^n_{i-2})\\ d_{i-3/2} &= (\hat{\omega}^n_{i-1} - 2\hat{\omega}^n_{i-2} + \hat{\omega}_{i-3})\end{aligned}$$

The Fourier components of the inflections d simplify to

$$\begin{aligned}d_{i-1/2} &= (\sin^2\zeta/2)(-4\cos\zeta + 4I\sin\zeta)\\ d_{i-3/2} &= (\sin^2\zeta/2)(-4\cos 2\zeta + 4I\sin 2\zeta)\end{aligned}$$

The Fourier components of $\hat{\omega}^c$ simplify to

$$\begin{aligned}\hat{\omega}^c_{i-1/2} &= (\cos\zeta/2 - (I/2)\sin\zeta)(2 + I\sin\zeta)\\ d_{i-3/2} &= (2 + I\sin\zeta)((1/2)\cos 2\zeta - (I/2)\sin 2\zeta)\end{aligned}$$

The slopes are

$$\begin{aligned}S_i &= (4\sin^4\zeta/2)/\Delta\hat{x} + (2I(\sin\zeta - \sin 2\zeta/4))/\Delta\hat{x}\\ S_{i-1} &= (-2 + 2\cos\zeta + I\sin\zeta)(\cos 2\zeta/\Delta\hat{x} - (I\sin 2\zeta)/\Delta\hat{x})\end{aligned}$$

The Fourier terms for the cell face values simplify to

$$\begin{aligned}\hat{\omega}^{n+1/2}_{i+1/2} &= 1 + 2(1 - N_C)\sin^4\zeta/2 + I(1 - N_C)(\sin\zeta - \sin 2\zeta/4)\\ \hat{\omega}^{n+1/2}_{i-1/2} &= (-2 + 2N_C + 4\cos\zeta - 2N_C\cos\zeta + 3I\sin\zeta - IN_C\sin\zeta)\\ &\quad((1/2)\cos 2\zeta - (I/2)\sin 2\zeta)\end{aligned}$$

The amplification factor G for the finite difference expression becomes

$$\begin{aligned}G = {}&\\ &\frac{1 - 4(1-\beta_{\hat{\omega}})N_D\sin^2\zeta/2 + N_C(-2 + 3\cos\zeta - 3N_C\cos\zeta - \cos 2\zeta + N_C\cos 2\zeta)\sin^2\zeta/2}{1 + 4\beta_{\hat{\omega}}N_D\sin^2\zeta/2}\\ &-\frac{(I/2)N_C(6 - 4N_C - 5\cos\zeta + 5N_C\cos\zeta + \cos 2\zeta - N_C\cos 2\zeta)\sin\zeta}{1 + 4\beta_{\hat{\omega}}N_D\sin^2\zeta/2}\end{aligned}$$

Figure 4.3 suggests this scheme is unstable for $1/2 < N_C < 1$ and for $N_C > 1.5$ with zero diffusion. However the analysis assumes this particular choice of discretization scheme

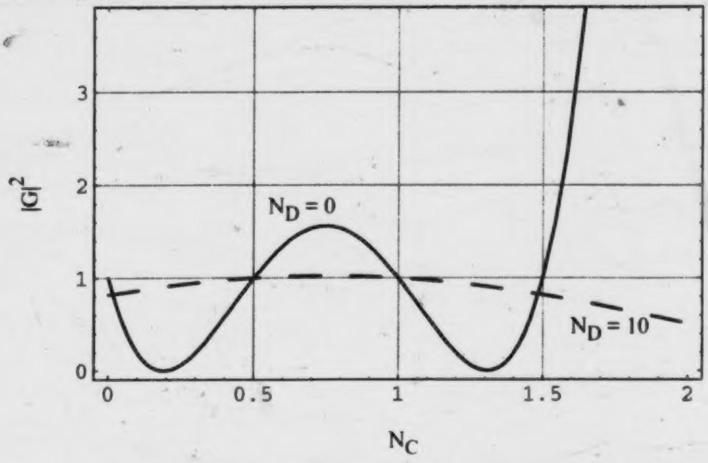

Figure 4.3: Modulus of the growth rate for UNO2 differencing (slope becomes more positive and inflection becomes more positive) with $\beta_{\hat{\omega}} = 1/2$ and $\zeta = \pi$: $N_D = 0, 10$.

is applied over the entire domain for all time. The UNO2 method uses the shape of the solution to choose which discretization scheme is applied. An instability associated with $1/2 < N_C < 1$ will alter the smoothness of the solution by a small amount: both the slope and inflection of the solution will be effected. The UNO2 method will choose a different discretization method at the next time step to eliminate the grid scale oscillation and to capture the solution accurately. This different discretization method may smear the grid scale oscillation with numerical diffusion.

Slope becomes less positive and inflection becomes less negative In this case the function value increases, the slope becomes less positive and inflection becomes less negative in the positive x direction.

The slopes returned by the minmod function for i and $i-1$ are

$$\begin{aligned} S_i &= (\hat{\omega}^c_{i+1/2} - \hat{\omega}_i)/(\Delta\hat{x}/2) \\ S_{i-1} &= (\hat{\omega}^c_{i-1/2} - \hat{\omega}_{i-1})/(\Delta\hat{x}/2) \end{aligned}$$

The values of $\hat{\omega}^c$ are

$$\hat{\omega}^c_{i+1/2} = (\hat{\omega}_{i+1} + \hat{\omega}_i)/2 - (1/4)d_{i+1/2}$$
$$\hat{\omega}^c_{i-1/2} = (\hat{\omega}_i + \hat{\omega}_{i-1})/2 - (1/4)d_{i-1/2}$$

The inflections d are

$$d_{i+1/2} = (\hat{\omega}_{i+2} - 2\hat{\omega}_{i+1} + \hat{\omega}_i)$$

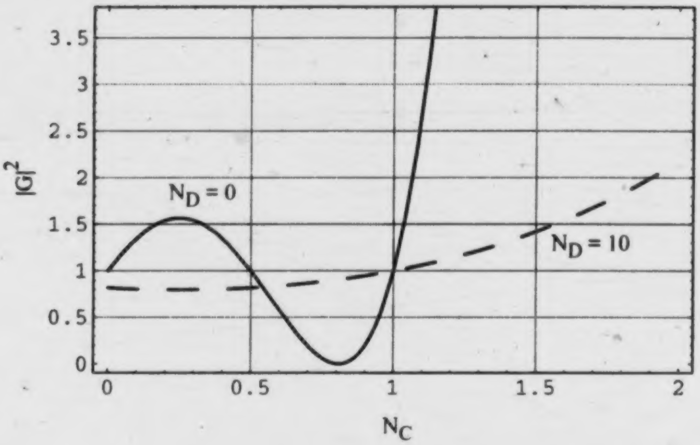

Figure 4.4: Modulus of the growth rate for UNO2 differencing (slope becomes less positive and inflection becomes less negative) with $\beta_{\hat{\omega}} = 1/2$ and $\zeta = \pi$: $N_D = 0,\ 10$.

$$d_{i-1/2} = (\hat{\omega}_{i+1} - 2\hat{\omega}_i + \hat{\omega}_{i-1})$$

Figure 4.4 shows that $|G|^2 > 1$ for pure convection with $0 < N_C < 1/2$ and $N_C > 1$. For $0 < N_C < 1/2$ any small grid scale oscillations present at the next time step will be suppressed with numerical diffusion. With diffusion ($N_D = 10$) this choice of the discretization method is unstable for $N_C > 1$.

Slope becomes more positive and inflection becomes less positive In this case the function value increases, the slope becomes more positive and inflection becomes less positive in the positive x direction.

The slopes returned by the minmod function for points i and $i-1$ are

$$\begin{aligned} S_i &= (\hat{\omega}_i - \hat{\omega}^c_{i-1/2})/(\Delta\hat{x}/2) \\ S_{i-1} &= (\hat{\omega}_{i-1} - \hat{\omega}^c_{i-3/2})/(\Delta\hat{x}/2) \end{aligned}$$

The values of $\hat{\omega}^c$ are

$$\begin{aligned} \hat{\omega}^c_{i-1/2} &= (\hat{\omega}^n_i + \hat{\omega}^n_{i-1})/2 - (1/4)d_{i-1/2} \\ \hat{\omega}^c_{i-3/2} &= (\hat{\omega}^n_{i-1} + \hat{\omega}^n_{i-2})/2 - (1/4)d_{i-3/2} \end{aligned}$$

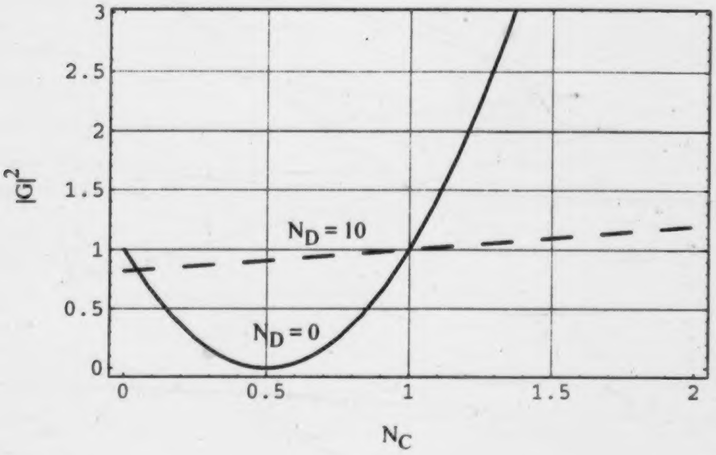

Figure 4.5: Modulus of the growth rate for UNO2 differencing (slope becomes more positive and inflection becomes less positive) with $\beta_{\hat{\omega}} = 1/2$ and $\zeta = \pi$: $N_D = 0,\ 10$.

The inflections d are

$$\begin{aligned} d_{i-1/2} &= (\hat{\omega}^n_{i+1} - 2\hat{\omega}^n_i + \hat{\omega}^n_{i-1}) \\ d_{i-3/2} &= (\hat{\omega}^n_i - 2\hat{\omega}^n_{i-1} + \hat{\omega}_{i-2}) \end{aligned}$$

In this example Figure 4.5 shows that $|G|^2 > 1$ for $N_C > 1$ with no diffusion and with $N_D = 10$.

Slope becomes less positive and inflection becomes more negative In this case the function value increases, the slope becomes less positive and inflection becomes more negative in the positive x direction.

The slopes returned by the minmod function for points i and $i - 1$ are

$$\begin{aligned} S_i &= (\hat{\omega}^c_{i+1/2} - \hat{\omega}_i)/(\Delta\hat{x}/2) \\ S_{i-1} &= (\hat{\omega}^c_{i-1/2} - \hat{\omega}_{i-1})/(\Delta\hat{x}/2) \end{aligned}$$

The values of $\hat{\omega}^c$ are

$$\begin{aligned} \hat{\omega}^c_{i+1/2} &= (\hat{\omega}_{i+1} + \hat{\omega}_i)/2 - (1/4)d_{i+1/2} \\ \hat{\omega}^c_{i-1/2} &= (\hat{\omega}_i + \hat{\omega}_{i-1})/2 - (1/4)d_{i-1/2} \end{aligned}$$

The inflections d are

$$\begin{aligned} d_{i+1/2} &= (\hat{\omega}_{i+1} - 2\hat{\omega}_i + \hat{\omega}_{i-1}) \\ d_{i-1/2} &= (\hat{\omega}_i - 2\hat{\omega}_{i-1} + \hat{\omega}_{i-2}) \end{aligned}$$

The growth rate for this example was identical to that calculated for the previous example: $|G|^2 > 1$ for $N_C > 1$ with no diffusion and with $N_D = 10$.

Any grid scale oscillation (or instability) consistent with $0 < N_C < 1$ will be suppressed with UNO2 because the scheme will select first order upwinding at the next time step. This damps grid scale oscillations locally before they become large errors. A sharp but consistent change in the solution is not damped.

4.2 Truncation error analysis

The one-dimensional convection-diffusion equation is

$$\frac{\partial \hat{\omega}}{\partial \hat{t}} + \hat{u}\frac{\partial \hat{\omega}}{\partial \hat{x}} - \frac{1}{\text{Re}}\frac{\partial^2 \hat{\omega}}{\partial \hat{x}^2} = 0 \qquad (4.6)$$

A truncation error analysis was performed to determine the dominant error term in the discrete forms of Equation 4.6. The process is illustrated for first order upwinding. Results for the UNO2 discretization are presented afterwards. The truncation error associated with the buoyancy driving force is considered separately. Series expansions, algebraic substitutions and simplifications were performed with the software Mathematica.

4.2.1 First order upwinding of the convection-diffusion equation

The first order upwind difference equation for the one-dimensional convection-diffusion equation is

$$\begin{aligned} &\frac{\hat{\omega}_i^{n+1} - \hat{\omega}_i^n}{\Delta \hat{t}} + \hat{u}\frac{\hat{\omega}_i^n - \hat{\omega}_{i-1}^n}{\Delta \hat{x}} \\ &-\beta_{\hat{\omega}}\frac{1}{\text{Re}}\frac{\hat{\omega}_{i+1}^n - 2\hat{\omega}_i^n + \hat{\omega}_{i-1}^n}{\Delta \hat{x}^2} - (1-\beta_{\hat{\omega}})\frac{1}{\text{Re}}\frac{\hat{\omega}_{i+1}^{n+1} - 2\hat{\omega}_i^{n+1} + \hat{\omega}_{i-1}^{n+1}}{\Delta \hat{x}^2} = 0 \end{aligned} \qquad (4.7)$$

where $\hat{x}_i = \hat{x}_0$, $\hat{x}_{i+1} = \hat{x}_0 + \Delta \hat{x}$, $\hat{t}^n = \hat{t}_0$ and $\hat{t}^{n+1} = \hat{t}_0 + \Delta \hat{t}$. The variable $\hat{\omega}$ is expanded as a third order Taylor series about $(\hat{x}_0, \hat{t}_0)$:

$$\begin{aligned} &\hat{\omega}(\hat{x}, \hat{t}) = \qquad (4.8) \\ &\quad \hat{\omega}(\hat{x}_0, \hat{t}_0) + (\hat{t} - \hat{t}_0)\left.\frac{\partial \hat{\omega}}{\partial t}\right|_{(\hat{x}_0, \hat{t}_0)} \end{aligned}$$

$$
\begin{aligned}
&\qquad + \frac{(\hat{t}-\hat{t}_0)^2}{2} \left.\frac{\partial^2 \hat{\omega}}{\partial \hat{t}^2}\right|_{(\hat{x}_0,\hat{t}_0)} + \frac{(\hat{t}-\hat{t}_0)^3}{6} \left.\frac{\partial^3 \hat{\omega}}{\partial \hat{t}^3}\right|_{(\hat{x}_0,\hat{t}_0)} + O((\hat{t}-\hat{t}_0)^4) \\
+ &\ (\hat{x}-\hat{x}_0) \left(\left.\frac{\partial \hat{\omega}}{\partial \hat{x}}\right|_{(\hat{x}_0,\hat{t}_0)} + (\hat{t}-\hat{t}_0) \left.\frac{\partial^2 \hat{\omega}}{\partial \hat{x}\partial \hat{t}}\right|_{(\hat{x}_0,\hat{t}_0)} \right. \\
&\qquad \left. + \frac{(\hat{t}-\hat{t}_0)^2}{2} \left.\frac{\partial^3 \hat{\omega}}{\partial \hat{x}\partial \hat{t}^2}\right|_{(\hat{x}_0,\hat{t}_0)} + \frac{(\hat{t}-\hat{t}_0)^3}{6} \left.\frac{\partial^4 \hat{\omega}}{\partial \hat{x}\partial \hat{t}^3}\right|_{(\hat{x}_0,\hat{t}_0)} + O((\hat{t}-\hat{t}_0)^4) \right) \\
+ &\ (\hat{x}-\hat{x}_0)^2 \left(\frac{1}{2} \left.\frac{\partial^2 \hat{\omega}}{\partial \hat{x}^2}\right|_{(\hat{x}_0,\hat{t}_0)} + \frac{(\hat{t}-\hat{t}_0)}{2} \left.\frac{\partial^3 \hat{\omega}}{\partial \hat{x}^2\partial \hat{t}}\right|_{(\hat{x}_0,\hat{t}_0)} \right. \\
&\qquad \left. + \frac{(\hat{t}-\hat{t}_0)^2}{4} \left.\frac{\partial^4 \hat{\omega}}{\partial \hat{x}^2\partial \hat{t}^2}\right|_{(\hat{x}_0,\hat{t}_0)} + \frac{(\hat{t}-\hat{t}_0)^3}{12} \left.\frac{\partial^5 \hat{\omega}}{\partial \hat{x}^2\partial \hat{t}^3}\right|_{(\hat{x}_0,\hat{t}_0)} + O((\hat{t}-\hat{t}_0)^4) \right) \\
+ &\ (\hat{x}-\hat{x}_0)^3 \left(\frac{1}{6} \left.\frac{\partial^3 \hat{\omega}}{\partial \hat{x}^3}\right|_{(\hat{x}_0,\hat{t}_0)} + \frac{(\hat{t}-\hat{t}_0)}{6} \left.\frac{\partial^4 \hat{\omega}}{\partial \hat{x}^3\partial \hat{t}}\right|_{(\hat{x}_0,\hat{t}_0)} \right. \\
&\qquad \left. + \frac{(\hat{t}-\hat{t}_0)^2}{12} \left.\frac{\partial^5 \hat{\omega}}{\partial \hat{x}^3\partial \hat{t}^2}\right|_{(\hat{x}_0,\hat{t}_0)} + \frac{(\hat{t}-\hat{t}_0)^3}{36} \left.\frac{\partial^6 \hat{\omega}}{\partial \hat{x}^3\partial \hat{t}^3}\right|_{(\hat{x}_0,\hat{t}_0)} + O((\hat{t}-\hat{t}_0)^4) \right) \\
+ &\ O((\hat{x}-\hat{x}_0)^4)
\end{aligned}
$$

The Taylor series expansion 4.8 for ω was substituted for $\hat{\omega}^n_{i+1} = \hat{\omega}(\hat{x}+\Delta\hat{x},\hat{t})$, $\hat{\omega}^{n+1}_i = \hat{\omega}(\hat{x},\hat{t}+\Delta\hat{t})$ ... in Equation 4.7. This results in

$$
\begin{aligned}
&\left.\frac{\partial \hat{\omega}}{\partial t}\right|_{(\hat{x}_0,\hat{t}_0)} + \hat{u} \left.\frac{\partial \hat{\omega}}{\partial x}\right|_{(\hat{x}_0,\hat{t}_0)} - \frac{1}{\mathrm{Re}} \left.\frac{\partial^2 \omega}{\partial x^2}\right|_{(\hat{x}_0,\hat{t}_0)} \\
&\quad + \frac{\Delta\hat{t}}{2} \left.\frac{\partial^2 \hat{\omega}}{\partial \hat{t}^2}\right|_{(\hat{x}_0,\hat{t}_0)} + \frac{\Delta\hat{t}^2}{6} \left.\frac{\partial^3 \hat{\omega}}{\partial \hat{t}^3}\right|_{(\hat{x}_0,\hat{t}_0)} \\
&\quad + \hat{u} \left(\left.\frac{\partial \hat{\omega}}{\partial x}\right|_{(\hat{x}_0,\hat{t}_0)} - \frac{\Delta\hat{x}}{2} \left.\frac{\partial^2 \omega}{\partial x^2}\right|_{(\hat{x}_0,\hat{t}_0)} - \frac{\Delta\hat{x}^2}{6} \left.\frac{\partial^3 \hat{\omega}}{\partial \hat{x}^3}\right|_{(\hat{x}_0,\hat{t}_0)} \right) \\
&\quad - \frac{1}{\mathrm{Re}} \left(\beta_{\hat{\omega}} \Delta\hat{t} \left.\frac{\partial^3 \hat{\omega}}{\partial \hat{x}^2\partial \hat{t}}\right|_{(\hat{x}_0,\hat{t}_0)} + \beta_{\hat{\omega}} \frac{\Delta\hat{t}^2}{2} \left.\frac{\partial^4 \hat{\omega}}{\partial \hat{x}^2\partial \hat{t}^2}\right|_{(\hat{x}_0,\hat{t}_0)} + \beta_{\hat{\omega}} \frac{\Delta\hat{t}^3}{6} \left.\frac{\partial^5 \hat{\omega}}{\partial \hat{x}^2\partial \hat{t}^3}\right|_{(\hat{x}_0,\hat{t}_0)} \right) = 0
\end{aligned}
\tag{4.9}
$$

Equation 4.9 is subtracted from the PDE 4.6 to give the truncation error:

$$
\begin{aligned}
&\varepsilon(\hat{x}_0,\hat{t}_0) = \\
&\quad + \frac{\Delta\hat{t}}{2} \left.\frac{\partial^2 \hat{\omega}}{\partial \hat{t}^2}\right|_{(\hat{x}_0,\hat{t}_0)} + \frac{\Delta\hat{t}^2}{6} \left.\frac{\partial^3 \hat{\omega}}{\partial \hat{t}^3}\right|_{(\hat{x}_0,\hat{t}_0)} \\
&\quad + \hat{u} \left(\left.\frac{\partial \hat{\omega}}{\partial x}\right|_{(\hat{x}_0,\hat{t}_0)} - \frac{\Delta\hat{x}}{2} \left.\frac{\partial^2 \omega}{\partial x^2}\right|_{(\hat{x}_0,\hat{t}_0)} - \frac{\Delta\hat{x}^2}{6} \left.\frac{\partial^3 \hat{\omega}}{\partial \hat{x}^3}\right|_{(\hat{x}_0,\hat{t}_0)} \right)
\end{aligned}
\tag{4.10}
$$

$$
\begin{aligned}
&-\frac{1}{\mathrm{Re}}\left(\beta_{\hat\omega}\Delta\hat t\,\frac{\partial^3\hat\omega}{\partial\hat x^2\partial\hat t}\bigg|_{(\hat x_0,\hat t_0)}+\beta_{\hat\omega}\frac{\Delta\hat t^2}{2}\,\frac{\partial^4\hat\omega}{\partial\hat x^2\partial\hat t^2}\bigg|_{(\hat x_0,\hat t_0)}+\beta_{\hat\omega}\frac{\Delta\hat t^3}{6}\,\frac{\partial^5\hat\omega}{\partial\hat x^2\partial\hat t^3}\bigg|_{(\hat x_0,\hat t_0)}\right)\\
&+\mathrm{HOT}
\end{aligned}
$$

where HOT are the higher order terms in the Taylor expansion.

The time derivatives in Equation 4.10 are written in terms of the spatial derivatives to make Equation 4.10 more compact. The partial derivatives of Equation 4.6 are taken with respect to $\hat t$ and $\hat x$:

$$\frac{\partial^2\hat\omega}{\partial\hat t^2}+\hat u\frac{\partial^2\hat\omega}{\partial\hat x\partial\hat t}-\frac{1}{\mathrm{Re}}\frac{\partial^3\hat\omega}{\partial^2 x\partial\hat t} = 0 \tag{4.11}$$

$$\frac{\partial^2\hat\omega}{\partial\hat x\partial\hat t}+\hat u\frac{\partial^2\hat\omega}{\partial\hat x^2}-\frac{1}{\mathrm{Re}}\frac{\partial^3\hat\omega}{\partial^3 x} = 0 \tag{4.12}$$

Equations 4.11 and 4.12 are combined to remove the term $\partial^2\hat\omega/\partial\hat x\partial\hat t$:

$$\frac{\partial^2\omega}{\partial t^2}=\frac{1}{\mathrm{Re}}\frac{\partial^3\hat\omega}{\partial^2 x\partial\hat t}+\hat u\left(\hat u\frac{\partial^2\omega}{\partial x^2}-\frac{1}{\mathrm{Re}}\frac{\partial^3\hat\omega}{\partial\hat x^3}\right) \tag{4.13}$$

The term $\partial^3\hat\omega/\partial^2 x\partial\hat t$ is written in terms of spatial derivatives by taking the partial derivative of Equation 4.12 with respect to x:

$$\frac{\partial^3\hat\omega}{\partial\hat x^2\partial\hat t}=-\hat u\frac{\partial^3\hat\omega}{\partial\hat x^3}+\frac{1}{\mathrm{Re}}\frac{\partial^4\hat\omega}{\partial\hat x^4} \tag{4.14}$$

Second partial derivatives of Equation 4.6 are taken with respect to t^2 and xt:

$$\frac{\partial^3\hat\omega}{\partial\hat t^3}+\hat u\frac{\partial^3\hat\omega}{\partial\hat x\partial\hat t^2}-\frac{1}{\mathrm{Re}}\frac{\partial^4\hat\omega}{\partial^2 x\partial\hat t^2} = 0 \tag{4.15}$$

$$\frac{\partial^3\hat\omega}{\partial\hat x\partial\hat t^2}+\hat u\frac{\partial^3\hat\omega}{\partial\hat x^2\partial\hat t}-\frac{1}{\mathrm{Re}}\frac{\partial^4\hat\omega}{\partial^3 x\partial\hat t} = 0 \tag{4.16}$$

Equation 4.14 is used to eliminate $\partial^3\hat\omega/\partial^2 x\partial\hat t$ from Equation 4.16. This result is combined with Equation 4.15 to eliminate $\partial^3\hat\omega/\partial\hat x\partial^2 t$:

$$\frac{\partial^3\hat\omega}{\partial\hat t^3}=\frac{1}{\mathrm{Re}}\frac{\partial^4\hat\omega}{\partial\hat x^2\partial\hat t^2}-\hat u\left(\hat u^2\frac{\partial^3\hat\omega}{\partial\hat x^3}+\frac{1}{\mathrm{Re}}\frac{\partial^4\hat\omega}{\partial\hat x^3\partial\hat t}-\hat u\frac{1}{\mathrm{Re}}\frac{\partial^4\hat\omega}{\partial\hat x^4}\right) \tag{4.17}$$

The discretization error becomes:

$$
\begin{aligned}
&\varepsilon(\hat x_0,\hat t_0)= \\
&\quad-\frac{\hat u\Delta\hat x}{2}(1-N_C)\,\frac{\partial^2\hat\omega}{\partial\hat x^2}\bigg|_{(\hat x_0,\hat t_0)}\\
&\quad+\left((1-\beta_{\hat\omega})\frac{\hat u\Delta\hat t}{\mathrm{Re}}-\frac{\hat u\Delta\hat x^2}{6}+\frac{\hat u^3\Delta\hat t^2}{6}\right)\frac{\partial^3\hat\omega}{\partial\hat x^3}\bigg|_{(\hat x_0,\hat t_0)}
\end{aligned}
\tag{4.18}
$$

$$
\begin{aligned}
&-\left((1-2\beta_{\hat{\omega}})\frac{\Delta\hat{t}}{2\mathrm{Re}^2}+\frac{\hat{u}^2\Delta\hat{t}^2}{6\mathrm{Re}}\right)\left.\frac{\partial^4\hat{\omega}}{\partial\hat{x}^4}\right|_{(\hat{x}_0,\hat{t}_0)} \\
&+\left(\beta_{\hat{\omega}}\frac{\Delta\hat{t}^2}{2\mathrm{Re}}-\frac{\Delta\hat{t}^2}{6\mathrm{Re}}\right)\left.\frac{\partial^4\hat{\omega}}{\partial\hat{x}^2\partial\hat{t}^2}\right|_{(\hat{x}_0,\hat{t}_0)}+\beta_{\hat{\omega}}\frac{\Delta\hat{t}^3}{6\mathrm{Re}}\left.\frac{\partial^5\hat{\omega}}{\partial\hat{x}^2\partial\hat{t}^3}\right|_{(\hat{x}_0,\hat{t}_0)} \\
&+\mathrm{HOT}
\end{aligned}
$$

The first three terms of discretization error in Equation 4.18 demonstrate this finite difference scheme has a first order truncation error in $\Delta\hat{x}$ and $\Delta\hat{t}$. The first term $\hat{u}\Delta\hat{x}(1-N_C)\partial^2\hat{\omega}/\partial\hat{x}^2$ is the numerical diffusion term associated with first order upwind differencing. The terms $(1-\beta_{\hat{\omega}})\hat{u}\Delta\hat{t}/\mathrm{Re}\,\partial^3\hat{\omega}/\partial\hat{x}^3$ and $(1-2\beta_{\hat{\omega}})\Delta\hat{t}/(2\mathrm{Re}^2)\partial^4\hat{\omega}/\partial\hat{x}^4$ confirm that truncation errors in the diffusion term will be present for any choice of the implicitness factor $\beta_{\hat{\omega}}$. Choosing $\beta_{\hat{\omega}}=1$ removes the error proportional to the third derivative of vorticity at the expense of a truncation error with a fourth derivative of vorticity. This fourth derivative error is large for low Reynolds numbers. With $\beta_{\hat{\omega}}=1/2$ the fourth derivative term (proportional to $1/\mathrm{Re}^2$) is eliminated.

4.2.2 UNO2 differencing of the convection-diffusion equation

The consistency analysis for the UNO2 discretization method was performed with a fourth order Taylor series expansion for $\hat{\omega}$. This Taylor series was substituted for the discrete values of $\hat{\omega}$ in the finite difference equations described in the stability analysis section.

For the four calculation methods of the slope and inflection of the solution surface the dominant error terms are:

Slope becomes more positive and inflection becomes more positive

$$
\begin{aligned}
&\epsilon(\hat{x}_0,\hat{t}_0)= \qquad\qquad (4.19)\\
&\left((1-\beta_{\hat{\omega}})\frac{\hat{u}\Delta\hat{t}}{\mathrm{Re}}+\frac{\hat{u}\Delta\hat{x}^2}{12}-\frac{\hat{u}^2\Delta\hat{x}\Delta\hat{t}}{4}+\frac{\hat{u}^3\Delta\hat{t}^2}{6}\right)\left.\frac{\partial^3\hat{\omega}}{\partial\hat{x}^3}\right|_{(\hat{x}_0,\hat{t}_0)} \\
&+\left(-(1-2\beta_{\hat{\omega}})\frac{\Delta\hat{t}}{2\mathrm{Re}^2}+\frac{\Delta\hat{x}^2}{12\mathrm{Re}}+\frac{\hat{u}\Delta\hat{x}^3}{8}-\frac{\hat{u}^2\Delta\hat{x}^2\Delta\hat{t}}{12}-\frac{\hat{u}^2\Delta\hat{t}^2}{6\mathrm{Re}}\right)\left.\frac{\partial^4\hat{\omega}}{\partial\hat{x}^4}\right|_{(\hat{x}_0,\hat{t}_0)} \\
&+\mathrm{HOT}
\end{aligned}
$$

Slope becomes less positive and inflection becomes less negative

$$
\epsilon(\hat{x}_0,\hat{t}_0)= \qquad\qquad (4.20)
$$

$$\left((1-\beta_{\hat{\omega}})\frac{\hat{u}\Delta\hat{t}}{\mathrm{Re}} - \frac{\hat{u}\Delta\hat{x}^2}{12} - \frac{\hat{u}^2\Delta\hat{x}\Delta\hat{t}}{4} + \frac{\hat{u}^3\Delta\hat{t}^2}{6}\right)\left.\frac{\partial^3\hat{\omega}}{\partial\hat{x}^3}\right|_{(\hat{x}_0,\hat{t}_0)}$$
$$+\left(-(1-2\beta_{\hat{\omega}})\frac{\Delta\hat{t}}{2\mathrm{Re}^2} + \frac{\Delta\hat{x}^2}{12\mathrm{Re}} + \frac{\hat{u}\Delta\hat{x}^3}{8} - \frac{\hat{u}^2\Delta\hat{x}^2\Delta\hat{t}}{12} - \frac{\hat{u}^2\Delta\hat{t}^2}{6\mathrm{Re}}\right)\left.\frac{\partial^4\hat{\omega}}{\partial\hat{x}^4}\right|_{(\hat{x}_0,\hat{t}_0)}$$
$$+\mathrm{HOT}$$

Slope becomes more positive and inflection becomes less positive

$$\varepsilon(\hat{x}_0,\hat{t}_0) = \tag{4.21}$$
$$\left((1-\beta_{\hat{\omega}})\frac{\hat{u}\Delta\hat{t}}{\mathrm{Re}} + \frac{\hat{u}\Delta\hat{x}^2}{12} - \frac{\hat{u}^2\Delta\hat{x}\Delta\hat{t}}{4} + \frac{\hat{u}^3\Delta\hat{t}^2}{6}\right)\left.\frac{\partial^3\hat{\omega}}{\partial\hat{x}^3}\right|_{(\hat{x}_0,\hat{t}_0)}$$
$$+\left(-(1-2\beta_{\hat{\omega}})\frac{\Delta\hat{t}}{2\mathrm{Re}^2} + \frac{\Delta\hat{x}^2}{12\mathrm{Re}} - \frac{\hat{u}\Delta\hat{x}^3}{8} + \frac{\hat{u}^2\Delta\hat{x}^2\Delta\hat{t}}{6} + \frac{\hat{u}^2\Delta\hat{t}^2}{6\mathrm{Re}}\right)\left.\frac{\partial^4\hat{\omega}}{\partial\hat{x}^4}\right|_{(\hat{x}_0,\hat{t}_0)}$$
$$+\mathrm{HOT}$$

Slope becomes less positive and inflection becomes more negative

$$\varepsilon(\hat{x}_0,\hat{t}_0) = \tag{4.22}$$
$$\left((1-\beta_{\hat{\omega}})\frac{\hat{u}\Delta\hat{t}}{\mathrm{Re}} + \frac{\hat{u}\Delta\hat{x}^2}{12} - \frac{\hat{u}^2\Delta\hat{x}\Delta\hat{t}}{4} + \frac{\hat{u}^3\Delta\hat{t}^2}{6}\right)\left.\frac{\partial^3\hat{\omega}}{\partial\hat{x}^3}\right|_{(\hat{x}_0,\hat{t}_0)}$$
$$+\left(-(1-2\beta_{\hat{\omega}})\frac{\Delta\hat{t}}{2\mathrm{Re}^2} + \frac{\Delta\hat{x}^2}{12\mathrm{Re}} - \frac{\hat{u}\Delta\hat{x}^3}{8} + \frac{\hat{u}^2\Delta\hat{x}^2\Delta\hat{t}}{6} - \frac{\hat{u}^2\Delta\hat{t}^2}{6\mathrm{Re}}\right)\left.\frac{\partial^4\hat{\omega}}{\partial\hat{x}^4}\right|_{(\hat{x}_0,\hat{t}_0)}$$
$$+\mathrm{HOT}$$

The UNO2 scheme is more accurate than first order upwind differencing of the model convection-diffusion equation. The truncation error for the UNO2 discretization method does not have the first order numerical diffusion term dominant in the first order upwind discretization. The UNO2 discretization has the same first order truncation errors as the first order upwind method in the third and fourth derivatives. Additional second order truncation errors associated with the convection term have been introduced in the third and fourth derivatives: these second order truncation errors have the same magnitude as the truncation errors common between first order upwinding and UNO2.

Setting $\beta_{\hat{\omega}} = 1/2$ eliminated the first order truncation error in the fourth derivative. This error is large for diffusion dominated phenomena (Re → 0).

4.3 Numerical results for vertical sedimentation

Numerical results from UNO2 and first order upwind differencing were compared for vertical 1-D sedimentation discretized with 100 points. The initial concentrations were $\hat{\phi} = 0.01$, 0.10 and 0.30. The material transport equation is approximately linear with constant velocity for sedimentation with $\hat{\phi} = 0.01$. A small cosine bump (height 0.001) was added to the initial concentration to observe the characteristic wave speed (Rankine-Hugoniot velocity) and to observe the effect of numerical diffusion on small perturbations. The time step $\Delta\hat{t} = 0.005$ was used for all cases: this corresponded to a Courant number of 0.5 for sedimentation at infinite dilution.

The concentration profiles after 100 time steps are shown in Figure 4.6 $\hat{\phi} = 0.01$. The UNO2 scheme captured the suspension interface with seven grid points while first order upwinding required 18 points. The volume fraction bump had 95 % of the initial amplitude with the UNO2 scheme and 44.5 % of the amplitude with the first order method.

Volume fraction profiles shown in Figure 4.7 for the 10 % suspension show the UNO2 scheme captured the suspension interface with three nodes while the first order method required six nodes. The volume fraction bump had 98.6 % of the original amplitude with UNO2 and only 44.2 % with first order differencing.

Both the UNO2 and first order discretization schemes capture the suspension interface very well for the 30 % suspension. This is due to the large self-sharpening effect caused by the solution characteristics running into the interface from both sides of the interface. The weak solution at the bottom of the vessel was captured by both methods. The magnitude of the cosine bump was 95.3 % of the original size with the UNO2 scheme and 56.7 % for the first order discretization method.

The UNO2 discretization method is much more accurate than first order upwind discretization for modelling 1-D vertical sedimentation. The suspension interface is captured with fewer points and small perturbations in volume fraction are convected with more accuracy compared to first order upwind differencing.

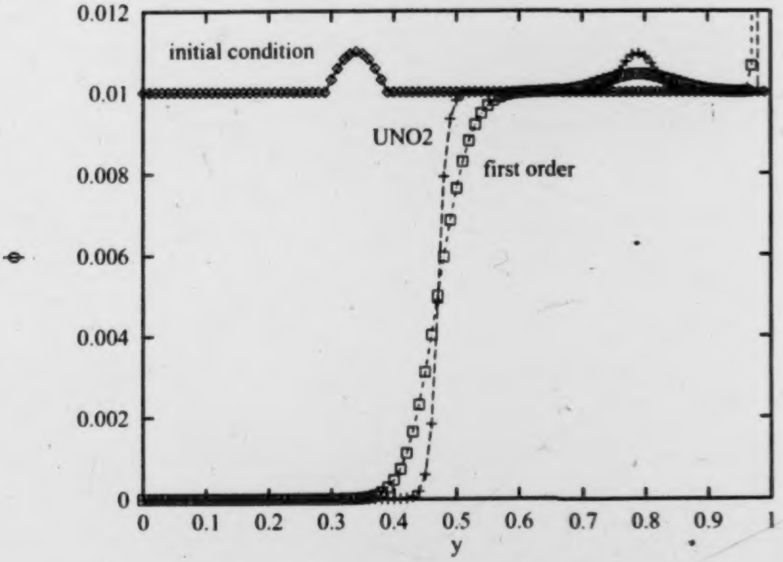

Figure 4.6: Volume fraction profiles from UNO2 and first order upwind differencing for 1-D vertical sedimentation of 1 % suspension.

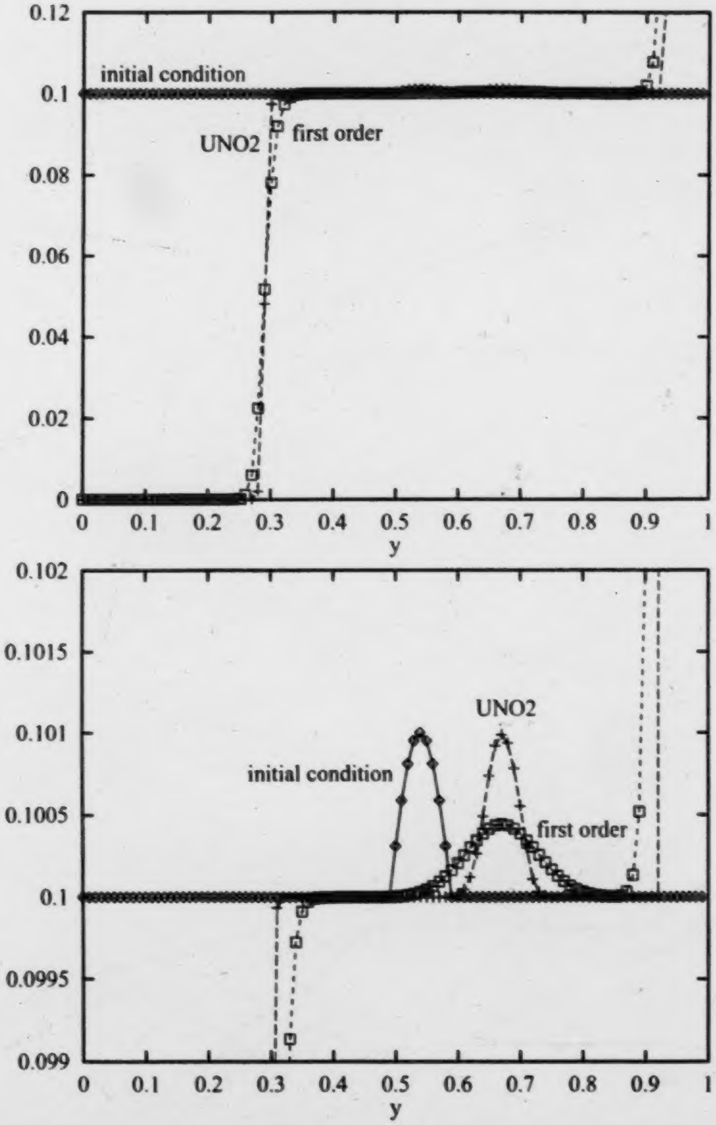

Figure 4.7: Volume fraction profiles from UNO2 and first order upwind differencing for 1-D vertical sedimentation of 10 % suspension.

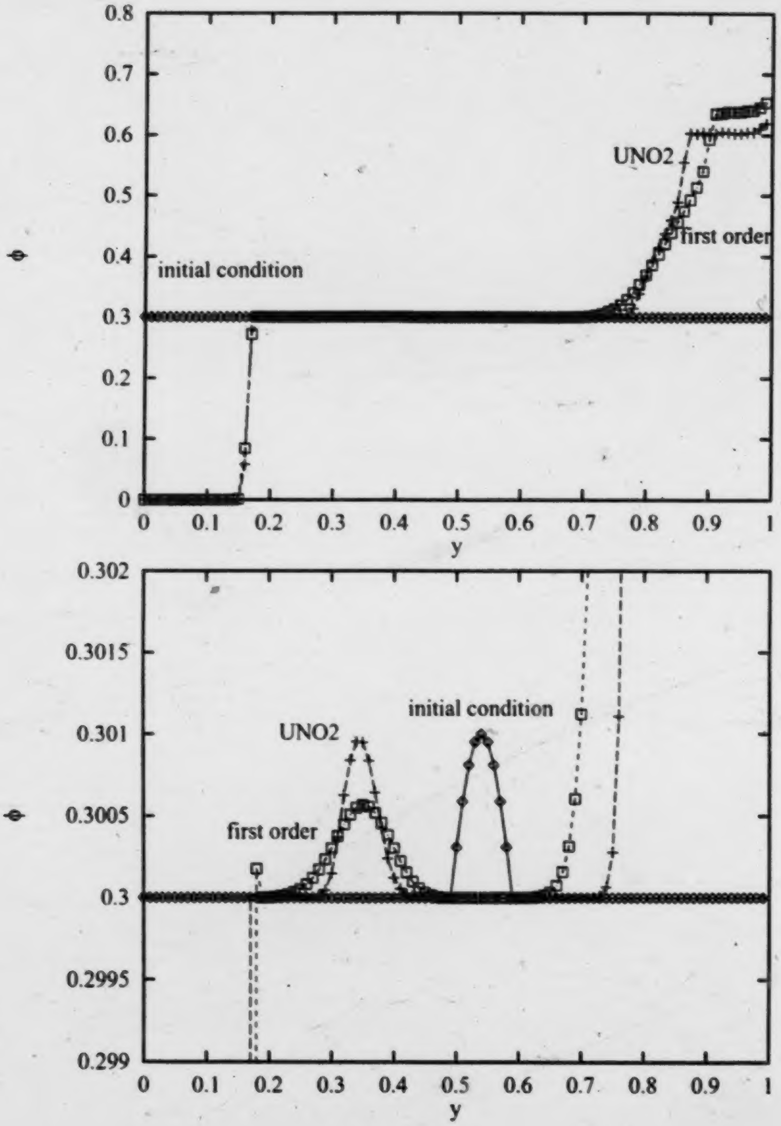

Figure 4.8: Volume fraction profiles from UNO2 and first order upwind differencing for 1-D vertical sedimentation of 30 % suspension.

Figure 4.9 shows the UNO2 method captures a shock with the same number of grid points regardless of the grid spacing. For the region near a discontinuity there is very little difference between the shapes of the suspension interfaces for grid resolutions of $\Delta\hat{x} = 1/20$, $1/100$ and $1/1000$. The derivatives of the function are also independent of the grid size because the shape of the function is independent of the grid size:

$$\frac{\partial^n \hat{\phi}}{\partial \hat{x}^n} = \frac{1}{\Delta\hat{x}^n} \frac{\partial^n \hat{\phi}}{\partial i^n} \tag{4.23}$$

where i is the grid number. The term $\partial^n \hat{\phi}/\partial i^n$ is referred to as the grid scale derivative.

Values of $\partial^n \hat{\phi}/\partial i^n$ for $\Delta\hat{x} = 1/100$ were calculated with finite difference expressions for the second through fifth derivatives for the region near a discontinuity. Figure 4.10 shows that fourth and fifth grid scale derivatives are somewhat larger than the second and third derivatives but they have the same magnitude. For the region near a discontinuity this magnitude is denoted as K. The magnitude of the volume fraction derivatives near the suspension interface is then

$$O\left(\frac{\partial^n \hat{\phi}}{\partial \hat{x}^n}\right) = \frac{K}{\Delta\hat{x}^n} \tag{4.24}$$

Figure 4.10 shows that fourth and fifth derivatives are more oscillatory than second and third derivatives over the region where the suspension interface is captured.

Equations 4.23 and 4.24 are not applicable to regions away from a discontinuity. In these regions the solution is smooth and the higher (fourth and fifth) derivatives have a smaller magnitude than the lower (second and third) derivatives. In this case the smooth solution is independent of the grid spacing as $\Delta\hat{x} \to 0$ and the higher derivatives have smaller magnitudes than the lower derivatives: fewer derivatives are required to represent the function with a Taylor series.

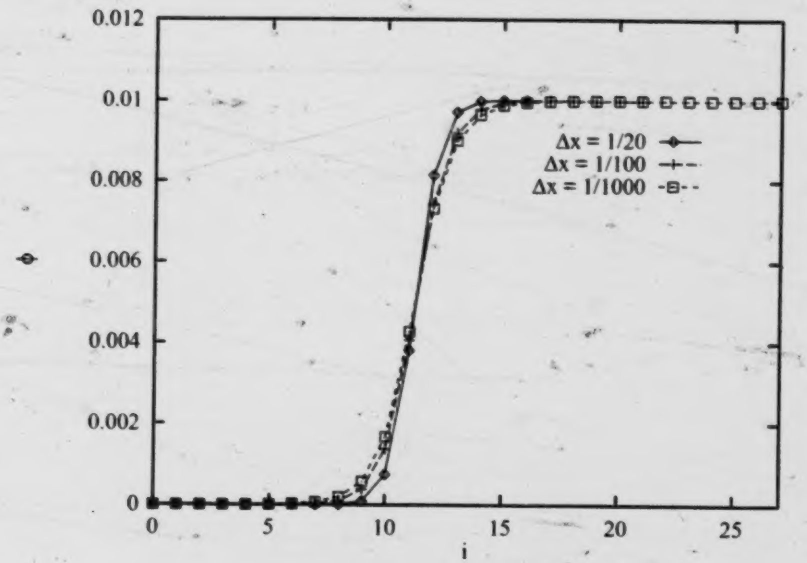

Figure 4.9: Grid resolution of the suspension interface for $\Delta\hat{x} = 1/20$, $1/100$ and $1/1000$.

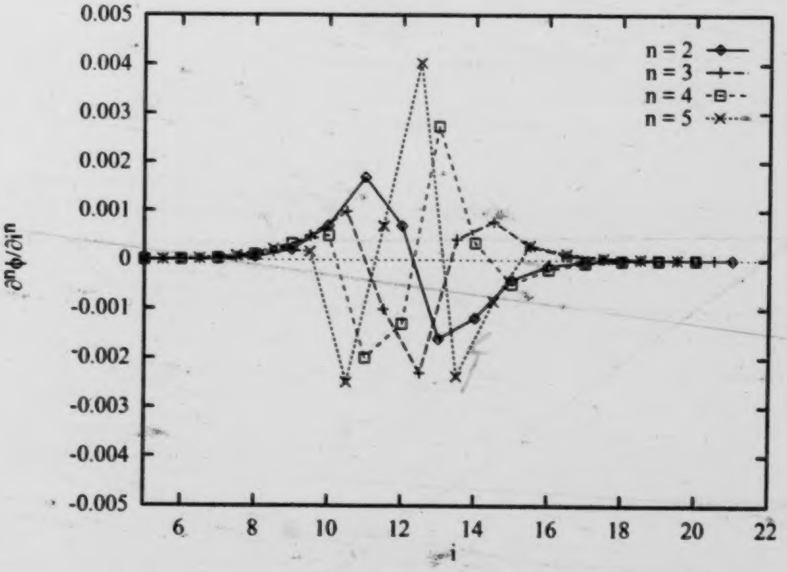

Figure 4.10: Second through fifth order grid scale derivatives of the volume fraction profile calculated with finite differences ($\Delta\hat{x} = 1/100$).

4.4 Truncation error of the buoyancy driving force

The truncation error for the buoyancy driving force $(\Gamma/\mathrm{Fr})\partial\hat{\phi}/\partial\hat{x}$ is now considered. The model equation is

$$\frac{\partial\hat{\omega}}{\partial t}+\hat{u}\frac{\partial\hat{\omega}}{\partial x}-\frac{1}{\mathrm{Re}}\frac{\partial^2\omega}{\partial x^2}-\frac{\Gamma}{\mathrm{Fr}}\frac{\partial\hat{\phi}}{\partial x}=0 \tag{4.25}$$

The UNO2 scheme is used to evaluate the convection terms: the discrete equation is

$$\begin{aligned}&\frac{\hat{\omega}_i^{n+1}-\hat{\omega}_i^{n}}{\Delta\hat{t}}+\frac{(\hat{u}\hat{\omega})_{i+1/2}^{n+1/2}-(\hat{u}\hat{\omega})_{i-1/2}^{n+1/2}}{\Delta\hat{x}}\\ &-\beta_{\hat{\omega}}\frac{1}{\mathrm{Re}}\frac{\hat{\omega}_{i+1}^{n+1}-2\hat{\omega}_i^{n+1}+\hat{\omega}_{i-1}^{n+1}}{\Delta\hat{x}^2}-(1-\beta_{\hat{\omega}})\frac{1}{\mathrm{Re}}\frac{\hat{\omega}_{i+1}^{n}-2\hat{\omega}_i^{n}+\hat{\omega}_{i-1}^{n}}{\Delta\hat{x}^2}\\ &-\beta_{\hat{\phi}}\frac{\Gamma}{\mathrm{Fr}}\frac{\hat{\phi}_{i+1/2}^{n+1}-\hat{\phi}_{i-1/2}^{n+1}}{\Delta\hat{x}}-(1-\beta_{\hat{\phi}})\frac{\Gamma}{\mathrm{Fr}}\frac{\hat{\phi}_{i+1/2}^{n}-\hat{\phi}_{i-1/2}^{n}}{\Delta\hat{x}}=0\end{aligned} \tag{4.26}$$

where $\beta_{\hat{\phi}}$ is the implicitness factor for the buoyancy term. The implicitness factor for the diffusion term is $\beta_{\hat{\omega}}=1/2$. The variable $\hat{\phi}$ was expanded as an eighth order Taylor series about (x_0,t_0) and substituted into the discrete Equation 4.26. Temporal derivatives of $\hat{\phi}$ were written as spatial derivatives through the material transport equation and derivatives of the material transport equation $\partial\hat{\phi}/\partial\hat{t}=-\hat{u}\partial\hat{\phi}/\partial\hat{x}$.

The leading terms in the truncation error from the buoyancy term are

$$\begin{align}&\varepsilon_{\hat{\phi}}(\hat{x}_0,\hat{t}_0)= \tag{4.27}\\ &\quad\Delta\hat{x}\left((1-\beta_{\hat{\phi}})N_C\frac{\Gamma}{\mathrm{Fr}}\right)\left.\frac{\partial^2\hat{\phi}}{\partial\hat{x}^2}\right|_{(\hat{x}_0,\hat{t}_0)} \notag\\ &\quad+\Delta\hat{x}^2\left((1-\beta_{\hat{\phi}})\frac{N_C^2}{2}\frac{\Gamma}{\mathrm{Fr}}-\frac{1}{24}\frac{\Gamma}{\mathrm{Fr}}\right)\left.\frac{\partial^3\hat{\phi}}{\partial\hat{x}^3}\right|_{(\hat{x}_0,\hat{t}_0)} \notag\\ &\quad-\Delta\hat{x}^3\left(\beta_{\hat{\phi}}\frac{N_C^3}{6}\frac{\Gamma}{\mathrm{Fr}}+\beta_{\hat{\phi}}\frac{N_C}{24}\frac{\Gamma}{\mathrm{Fr}}\right)\left.\frac{\partial^4\hat{\phi}}{\partial\hat{x}^4}\right|_{(\hat{x}_0,\hat{t}_0)} \notag\\ &\quad+\Delta\hat{x}^4\left(+\beta_{\hat{\phi}}\frac{N_C^4}{24}\frac{\Gamma}{\mathrm{Fr}}+\beta_{\hat{\phi}}\frac{1}{1920}\frac{\Gamma}{\mathrm{Fr}}\right)\left.\frac{\partial^5\hat{\phi}}{\partial\hat{x}^5}\right|_{(\hat{x}_0,\hat{t}_0)} \notag\\ &\quad+\mathrm{HOT} \tag{4.28}\end{align}$$

where $N_C=\hat{u}\Delta\hat{t}/\Delta\hat{x}$. It is clear that $\beta_{\hat{\phi}}=1$ results in a second order accurate discretization of the buoyancy term. The other UNO2 examples gave the same leading terms in the truncation error.

For regions adjacent the suspension interface the magnitude of the spatial derivatives is given by Equation 4.24. Near this discontinuity the magnitude of the truncation error is

$$O(\varepsilon_{\hat{\phi}}(\hat{x}_0, \hat{t}_0)) = \tag{4.29}$$
$$\frac{K}{\Delta \hat{x}} \frac{\Gamma}{\mathrm{Fr}} \left((1 - \beta_{\hat{\phi}}) N_C + (1 - \beta_{\hat{\phi}}) \frac{N_C^2}{2} + \frac{1}{24} + \beta_{\hat{\phi}} \frac{N_C^3}{6} + \beta_{\hat{\phi}} \frac{N_C}{24} + \beta_{\hat{\phi}} \frac{N_C^4}{24} + \beta_{\hat{\phi}} \frac{1}{1920} \right)$$

For the Courant number $N_C = 1$ Equation 4.29 evaluates to

$$O(\varepsilon_{\hat{\phi}}(\hat{x}_0, \hat{t}_0)) = K \frac{\Gamma}{\mathrm{Fr}} \frac{1}{\Delta \hat{x}} (1.54), \qquad \beta_{\hat{\phi}} = 0$$
$$O(\varepsilon_{\hat{\phi}}(\hat{x}_0, \hat{t}_0)) = K \frac{\Gamma}{\mathrm{Fr}} \frac{1}{\Delta \hat{x}} (0.29), \qquad \beta_{\hat{\phi}} = 1$$

The total truncation error with $\beta_{\hat{\phi}} = 0$ has the same magnitude as the error for $\beta_{\hat{\phi}} = 1$. However the dominant error terms for $\beta_{\hat{\phi}} = 0$ appear as second and third derivatives of $\hat{\phi}$ where the error terms for $\beta_{\hat{\phi}} = 1$ appear as fourth and fifth derivatives. Figure 4.10 shows that fourth and fifth derivatives of the volume fraction are more oscillatory and have similar magnitudes compared to the second and third derivatives for the region near the suspension interface. In this region the oscillatory truncation errors in the buoyancy driving force appear as oscillatory source terms in the vorticity transport equation. The vorticity field near the suspension interface at the next time step will have oscillations that reflect the truncation error of the buoyancy term. The fourth and fifth derivatives associated with $\beta_{\hat{\phi}} = 1$ will produce a more oscillatory vorticity field than the second and third derivatives for $\beta_{\hat{\phi}} = 0$ near the suspension interface.

Equation 4.29 suggests the magnitude of these grid scale oscillations becomes very small for $N_C \ll 1$.

4.5 Effect of a smeared interface on the velocity profile

The suspension/clear fluid interface is, analytically, a discontinuity. However the numerical solution represents this discontinuity as a continuous profile with a steep gradient. The flow profiles for a model problem are compared for two limiting cases: a) the density is discontinuous, b) the density varies smoothly across the flow.

The model problem chosen is the fully developed gravity driven flow of a density stratified fluid shown in Figure 4.11. The lighter fluid has density $\rho - \delta\rho/2$ and travels with the velocity v_l, the heavier fluid has density $\rho + \delta\rho/2$ and travels with the velocity v_h. The viscosity of the two fluids are equal. Leung & Probstein [29], Amberg & Dahlkid [2] and Tripathi & Acrivos [50] used similar models to describe the mixture velocity field for sedimentation between inclined parallel plates.

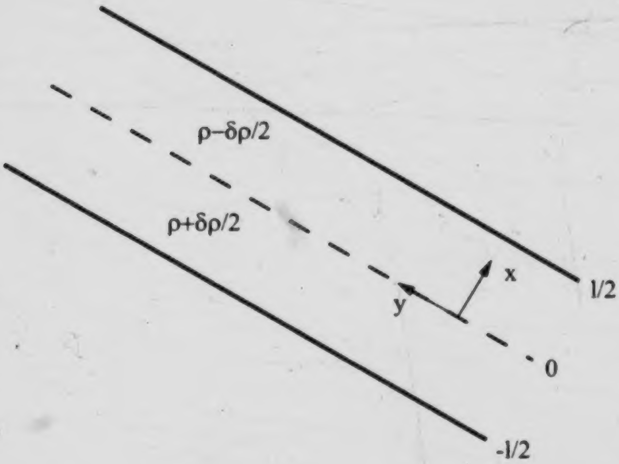

Figure 4.11: Gravity driven flow of a density stratified fluid between inclined parallel plates.

For fully developed flow the y-direction momentum equations for the two fluids are

$$0 = -\frac{\partial p}{\partial y} + \mu \frac{\partial^2 v_l}{\partial x^{2^2}} - (\rho - \delta\rho/2) g_y \tag{4.30}$$

$$0 = -\frac{\partial p}{\partial y} + \mu \frac{\partial^2 v_h}{\partial x^{2^2}} - (\rho + \delta\rho/2) g_y \tag{4.31}$$

The boundary conditions are no slip at the walls,

$$v_h(-l/2) = 0, \qquad v_l(l/2) = 0$$

the velocity field is continuous at the interface $x = 0$,

$$v_h(0) = v_l(0)$$

and the shear stress is continuous at the interface $x = 0$,

$$\frac{\partial v_h(0)}{\partial x} = \frac{\partial v_l(0)}{\partial x}$$

The global material balance requires the net flow across the channel to be zero

$$0 = \int_{-l/2}^{0} v_h \, dx + \int_{0}^{l/2} v_l \, dx$$

These momentum equations and boundary conditions were solved with Mathematica: the details are in Appendix B.

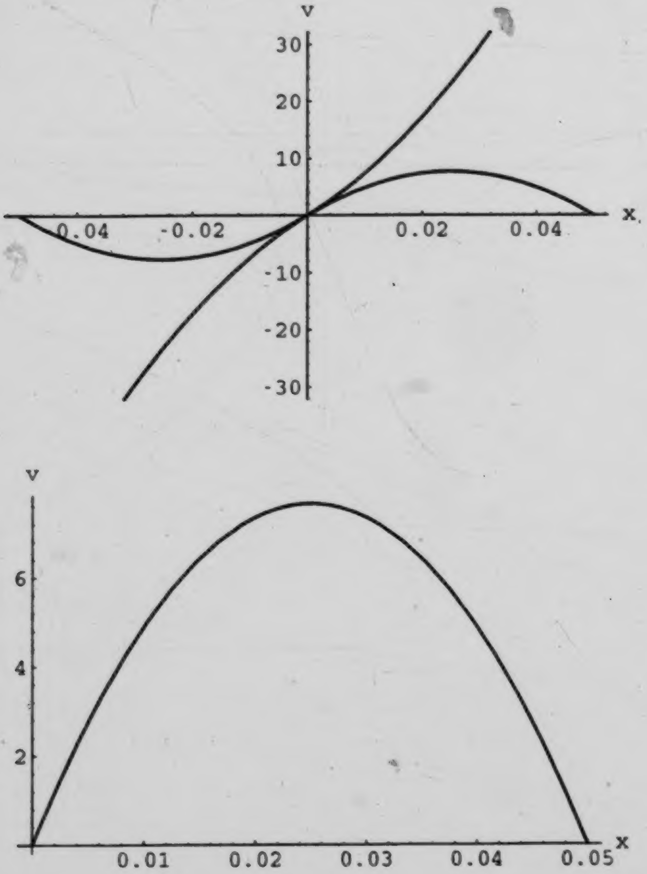

Figure 4.12: Velocity profiles for gravity driven flow of a density stratified fluid between inclined parallel plates.

Typical flow profiles of the heavy and light fluids are shown in Figure 4.12. The velocity profile of each flow is parabolic. For the example considered the velocity profile varies between the values -8 and 8.

A similar problem is considered where the fluid density varies linearly across the width of the channel. This is the limiting case suggested by a suspension interface that is smeared over a finite distance and is represented by a continuous function. The y-direction momentum equation is

$$0 = -\frac{\partial p}{\partial y} + \mu \frac{\partial^2 v}{\partial x^{2^2}} - \left(\rho + \frac{x\,\delta\rho}{l}\right) g_y \tag{4.32}$$

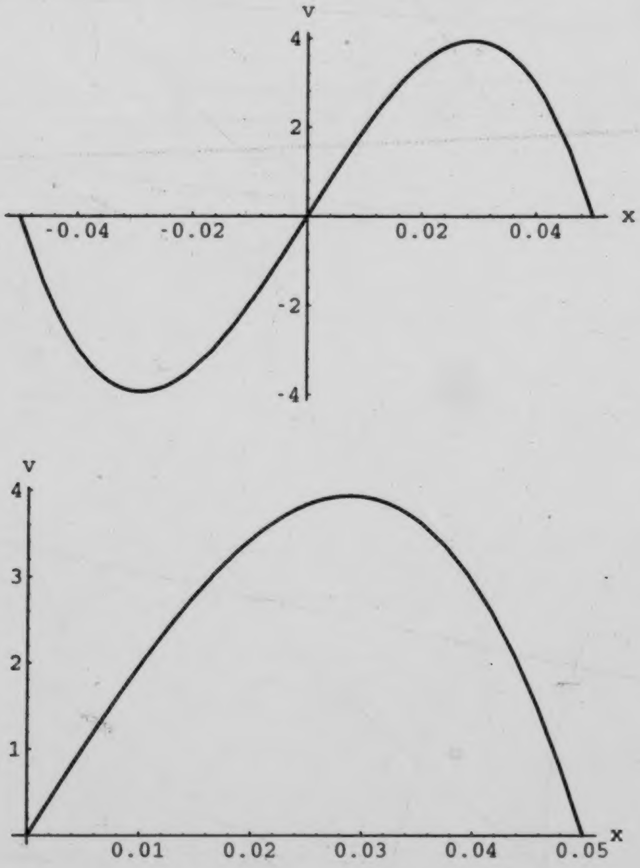

Figure 4.13: Velocity profiles for gravity driven flow of a fluid with a linear density variation between inclined parallel plates.

The boundary conditions are no slip at the walls,

$$v(-l/2) = 0, \qquad v(l/2) = 0$$

The net flow across the channel is zero

$$0 = \int_{-l/2}^{l/2} v\, dx$$

The details of the solution to this momentum equation and the boundary conditions are in Appendix B.

The flow profile in Figure 4.13 is not parabolic for $0 < x < l/2$. With the same viscosity and density difference used previously the fluid velocity ranges between -4 and 4: this is half of the range for the stratified flow.

The discontinuity in the mixture density is the driving force for the longitudinal velocity profile for inclined plate sedimentation. A numerical scheme that represents this discontinuity as a smooth curve will yield a different velocity profile. Increased grid resolution represents a discontinuity as a steeper gradient over a smaller distance. This changes the driving force for the flow circulation in an inclined vessel. The examples given suggest that increased grid resolution of a discontinuity will lead to higher velocities near the suspension interface.

4.6 Summary

The linear stability of the UNO2 discretization method depends on which solution values are used to evaluate the inflection and the slope of the solution at the n time level. The von Neumann stability analysis has shown the UNO2 method is unstable with $N_C < 1$ for two cases. For these two cases a small error develops and is suppressed at the next time step because the UNO2 method resorts to first order upwinding to prevent the solution from becoming oscillatory.

The consistency analysis demonstrated the explicit treatment of the convection term with UNO2 and the semi-implicit treatment of the diffusion term yields a consistent numerical scheme: the truncation error goes to zero as $\Delta\hat{x} \to 0$. However the discretization method is first order accurate for mixed convection-diffusion problems. The implicitness factor $\beta_{\hat{\omega}} = 1/2$ for the diffusion term leads to a first order truncation error proportional to $(\Delta\hat{x} N_C/\mathrm{Re})\partial^3\hat{\omega}/\partial\hat{x}^3$. The UNO2-based discretization method presented for the vorticity transport equation does not suffer from numerical diffusion $\Delta\hat{x}(1-N_C)\partial^2\hat{\omega}/\partial\hat{x}^2$ in regions where the solution is smooth. First order upwinding suffers from numerical diffusion in all regions including areas where the solution is smooth. The UNO2-based discretization scheme developed in the previous chapter for the vorticity transport equation is referred to as the non-diffusive method. The UNO2 scheme is second order accurate for pure convection.

The consistency analysis of the buoyancy driving force suggests this term can be discretized in a second order accurate manner by choosing the implicitness factor $\beta_{\hat{\phi}} = 1$. This eliminates the first order truncation error proportional to $\Delta\hat{x}\partial^2\hat{\phi}/\partial\hat{x}^2$ but replaces it with more oscillatory errors proportional to $\Delta\hat{x}^3\partial^4\hat{\phi}/\partial\hat{x}^4$ and $\Delta\hat{x}^4\partial^5\hat{\phi}/\partial\hat{x}^5$. For regions near the suspension interface these high order truncation errors have the same order of magnitude as the first order truncation error even with $\Delta\hat{x} \to 0$. The implicitness factor for the buoyancy term $\beta_{\hat{\phi}} = 0$ eliminated truncation errors exhibiting grid scale oscillations for regions near the suspension interface. This prevents the vorticity field from becoming oscillatory at the next time step.

Chapter 5

Code validation

The two dimensional vorticity-stream function code was validated with a series of examples in this chapter. Numerical results obtained with the simulation code are compared with numerical results obtained by other researchers and experimental data.

The first example is the single phase lid driven square cavity problem. The rest of the examples are for batch sedimentation with the geometry shown in Figure 5.1.

5.1 Driven cavity

Results for a lid driven cavity with Re = 0 and 400 were compared with the numerical results (central difference) of Schreiber & Keller [42, 41]. For this example the Reynolds number is defined as

$$\mathrm{Re} = \frac{\rho L U_l}{\mu} \tag{5.1}$$

where U_l is the lid velocity and the characteristic length L is the cavity width. The vorticity boundary condition at the driven lid was

$$\hat{\omega}_w^{n+1} = \frac{-3(\hat{\psi}_{w+1}^{n+1} - \hat{\psi}_w^{n+1})}{\Delta \hat{n}^2} - \frac{\hat{\omega}_{w+1}^{n+1}}{2} + 3\frac{\hat{U}_l}{\Delta \hat{y}} + O(\Delta \hat{n}^2) \tag{5.2}$$

where the lid velocity is $U_l = 1$.

Transient simulations were performed and the final results were taken at $\hat{t} = 50$.

Results for Re = 0 were obtained by turning off the convection terms in the vorticity transport equation while retaining the viscous terms. The maximum and minimum values of the stream function obtained with a uniform 140 × 140 mesh were 2.182×10^{-6} and -0.1009. Schreiber & Keller report values for Re = 1 with a 120×120 mesh: the maximum

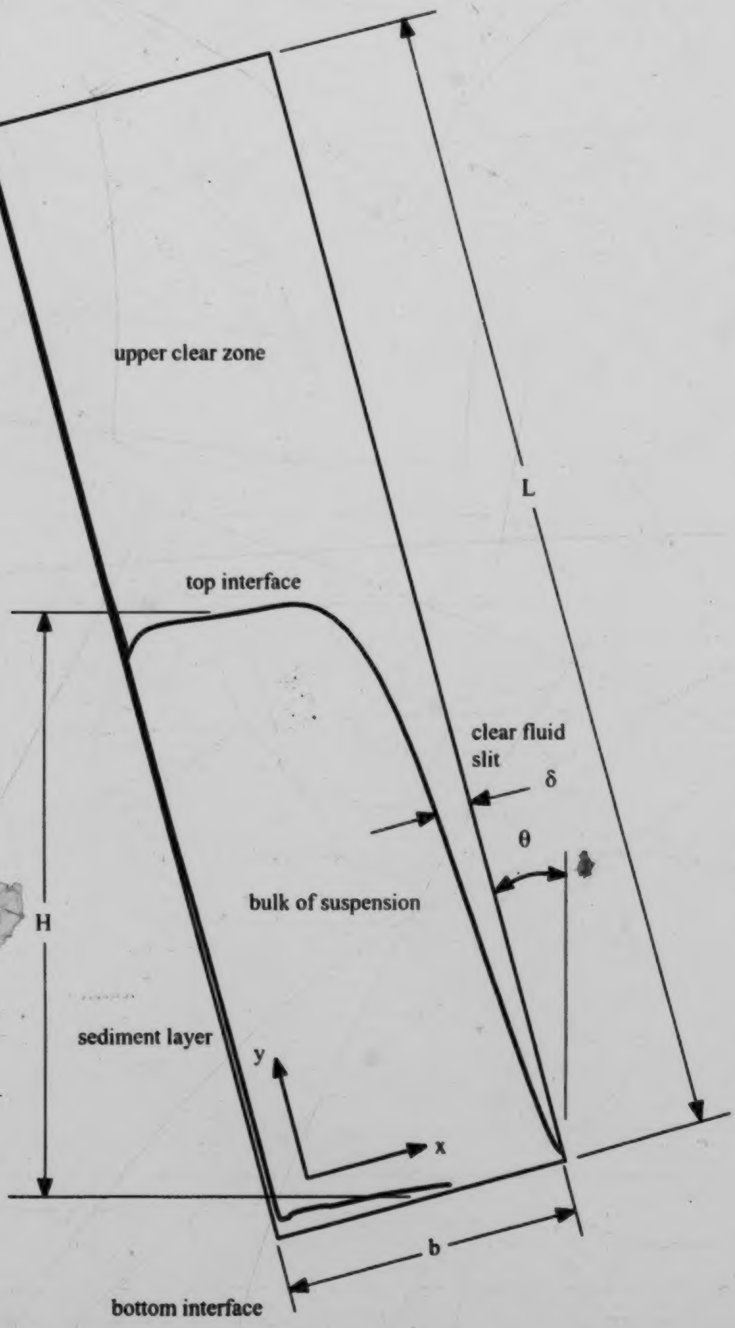
upper clear zone
L
top interface
clear fluid slit
δ
θ
bulk of suspension
H
sediment layer
y
x
b
bottom interface

Figure 5.1: Sketch of the two dimensional geometry used in the simulations of batch sedimentation.

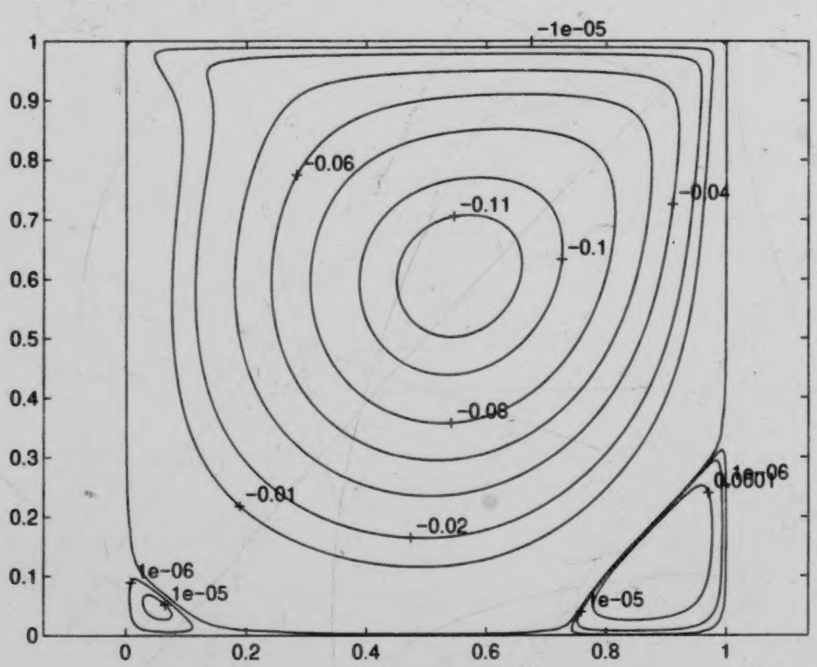

Figure 5.2: Streamlines for the driven cavity with Re = 400: $\hat{\psi}$ = -0.11, -0.10, -0.08, -0.06, -0.04, -0.02, -0.01, -0.00001, 0.000001, 0.00001, 0.0001, 0.001, 0.002.

and minimum values of the stream function were 2.47×10^{-6} and -0.1006. The discrepancy between the two results was attributed to Schreiber & Keller's use of first order accurate vorticity boundary conditions while second order approximations were used in this work.

Results were obtained for Re = 400 on a uniform 140×140 mesh with the non-diffusive discretization method. The maximum and minimum values of the stream function were 6.6712×10^{-4} and -0.1162. These values agree well with the results of Schreiber & Keller (maximum 6.44×10^{-4}, minimum -0.11297). The streamlines shown in Figure 5.2 are identical to those reported by Schreiber & Keller.

The results obtained with this example demonstrated the validity of the vorticity-stream function algorithm with the non-diffusive discretization method.

5.2 One dimensional batch sedimentation

The two dimensional sedimentation code was used to simulate batch one dimensional sedimentation. This test verified the two dimensional simulation code reduced to the correct limits for one dimensional sedimentation. The vorticity and stream function fields were both zero over the vessel: these fields represent the correct values for one dimensional sedimentation.

The hindering function of Font [11] was used:

$$h(\hat{\phi}) = (q/5.924)^{-1/3}(1 - q\hat{\phi})^{4.65} \tag{5.3}$$

where

$$q = 5.924 \quad \text{for} \quad \hat{\phi} < 0.0631$$
$$q = 7.742 = 33\hat{\phi} + 52.196\hat{\phi}^2 \quad \text{for} \quad \hat{\phi} > 0.0631$$

The immobility of the sediment was modelled by setting the hindering function to zero for $\hat{\phi} > 0.4$.

Figure 5.3 compares the position of the upper suspension interface obtained with the simulation with the experimental data of Font. The simulation results for $\hat{\phi} = 0.0200$ and 0.08838 match the experimental data very well. The simulation captured correctly the initial linear settling regime and the gradual decrease in the settling rate that follows. This decrease in the settling rate is attributed to the weak solution that joins the solution characteristics of the suspension with the characteristics of the concentrated sediment. These numerical results match the experimental results obtained by Font.

The simulation results do not agree well with the experimental data for the $\hat{\phi} = 0.04417$ suspension. The initial slope of the interface curve in Figure 5.3 gives a hindered settling velocity of $V_s = 129 \times 10^{-6}$ m/s. This is very similar to the settling velocity $V_s = 128.4 \times 10^{-6}$ m/s obtained with Equation 5.3. The initial slope of batch settling curve for the experimental data gives a hindered settling velocity of $V_s = 152 \times 10^{-6}$ m/s. It is concluded that the experimental data reported by Font for the $\hat{\phi} = 0.04417$ was for a concentration lower than $\hat{\phi} = 0.04417$.

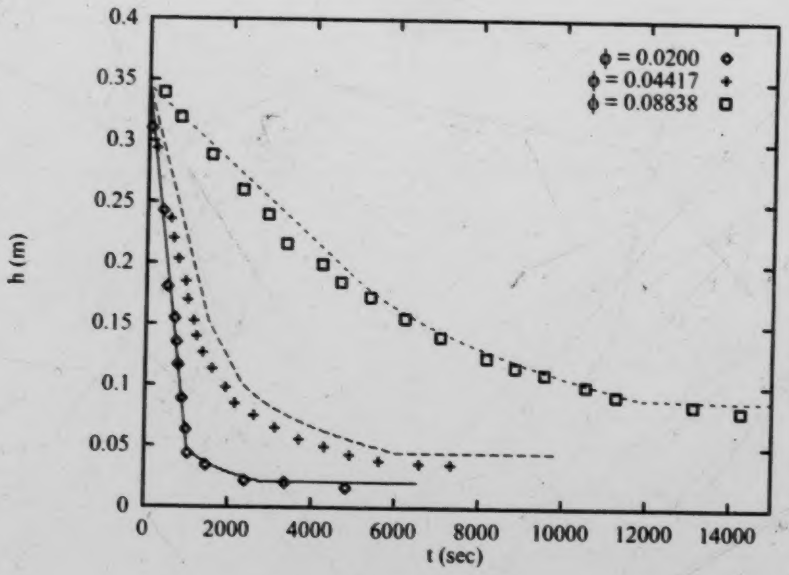

Figure 5.3: Interface positions for batch sedimentation of suspensions with $\hat{\phi}$ = 0.0200, 0.04417 and 0.08838. Lines denote the simulation results, points denote the experimental data of Font [11].

5.3 Batch inclined sedimentation: position of the horizontal interface

Simulations were performed on a uniform 40 × 200 mesh where the physical properties and geometry matched the experimental work of Acrivos & Herbolzheimer [1]. They measured the position of the horizontal interface over time for batch sedimentation and made qualitative observations about the flow inside the sedimentation vessel.

The physical properties of the suspension were $\gamma_f = 992\,\mathrm{kg/m^3}$, $\gamma_s = 2420\,\mathrm{kg/m^3}$, $\bar{\mu}_f = 67.7\,\mathrm{mPa\,s}$, $d_s = 137 \times 10^{-6}\,\mathrm{m}$. The initial concentration was $\phi_0 = 0.10$. The apparatus in their experiments was 5 cm wide and filled with suspension to a level of 40 cm above the base when the vessel was inclined. The numerical simulations used a slightly different geometry: a rectangular vessel with length $(0.4/\cos\theta)$ m was filled with the suspension. This geometry was required because the finite difference equations were written for an orthogonal coordinate system. The interface height was estimated by finding the location of $\phi = 0.5\phi_0$ along the center of the sedimentation vessel.

The physical properties of the suspension yield $V_{s,\infty} = 213 \times 10^{-6}\,\mathrm{m/s}$ and a hindered settling velocity of $126 \times 10^{-6}\,\mathrm{m/s}$. The experimental data of Acrivos & Herbolzheimer yield a hindered settling velocity of $100 \times 10^{-6}\,\mathrm{m/s}$ for the $\phi = 0.10$ suspension: $V_{s,\infty} = 169 \times 10^{-6}\,\mathrm{m/s}$ as calculated with the hindering expression $h(\hat{\phi}) = (1-\phi)^5$. The 26 % discrepancy in the hindered settling velocity may be attributed to the accuracy of the Richardson & Zaki correlation or the physical properties used to calculate the settling velocity at infinite dilution.

Figure 5.4 shows the numerical simulation predicts the initial falling velocity of the suspension interface is greater than the experimental data for all angles. This disagreement is attributed to the discrepancy in the calculated and measured settling velocity of the $\hat{\phi} = 0.10$ suspension. The interface heights obtained with the simulation level out near $h = 0.07$ m while the experimental data for 35° and 50° appear to level out near $h = 0.05$ m. This discrepancy is attributed to the point where the suspension height is measured from. In this research the suspension height was measured from base of the vessel at the centerline shown in Figure 5.1. Acrivos & Herbolzheimer measured the suspension height from the bottom right corner of the vessel in Figure 5.1: this height is $0.5b\sin\theta$ smaller than the height measured from the centerline. For the 50° inclination this discrepancy is 0.019 m and the corrected final suspension height agrees with the numerical simulation. In general the simulation results capture the falling rate of the horizontal suspension interface well.

Figure 5.5 shows a fairly rapid motion throughout the settling vessel at $\hat{t} = 0.02$. By $\hat{t} = 0.1$ this rapid motion has died in the top half of the core shown in Figure 5.6. A strong circulation persists in the center of the suspension. Acrivos & Herbolzheimer [1] reported a

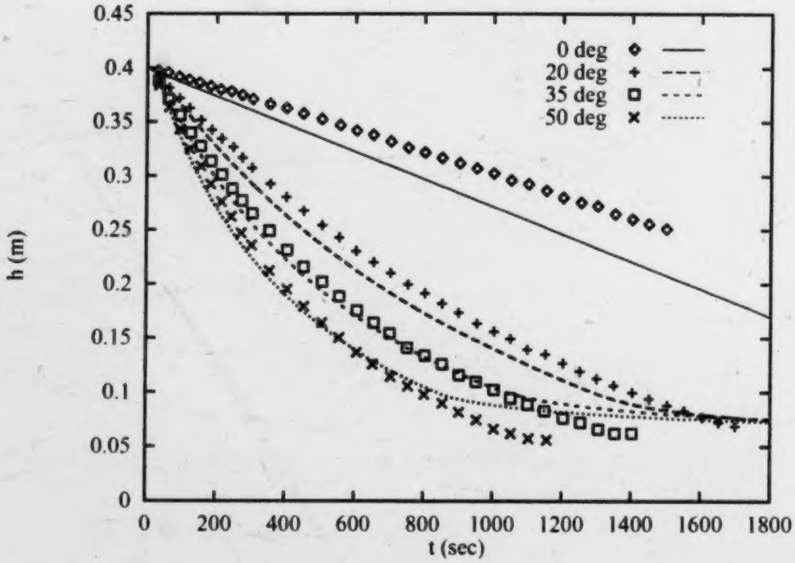

Figure 5.4: Position of horizontal suspension interface for simulations of batch sedimentation at inclinations $\theta = 0°$, $20°$, $35°$ and $50°$. Lines denote the numerical simulations, points denote the experimental data of Acrivos & Herbolzheimer [1].

rapid circulation at the start of most experiments. At later times Acrivos & Herbolzheimer found the circulating motion was relatively slow in the bulk of the suspension.

Several comparisons were made with the qualitative observations of Acrivos & Herbolzheimer regarding the flow patterns in the sedimentation vessel. First they estimated the thickness of the fast moving zone adjacent the clear fluid slit to be approximately five times that of the clear fluid layer. They estimated the maximum velocity near the top of the clear fluid slit was one to two orders of magnitude faster than the settling velocity. The velocity and concentration profiles at $y = 0.625\,L$ in Figure 5.7 show the suspension interface ($\hat{\phi} = 0.05$) is at $x = 0.0482\,\mathrm{m}$ while the fast moving region ($\hat{v} > 10$) adjacent the clear fluid slit begins at $x = 0.0457\,\mathrm{m}$. The thickness of the fast moving region is 4.3 mm and the thickness of the clear fluid slit is 1.8 mm at this position: the thickness of the fast moving zone is 2.4 times that of the clear fluid slit. The maximum velocity at this position is $\hat{v} = 96$. The results of the numerical simulations reflected these qualitative observations of the velocity profile in the experimental apparatus.

Secondly Acrivos & Herbolzheimer noted that "thin streams of rapidly moving suspension were observed to break away from the main flow [near the top of the suspension] and to descend rapidly into the bulk of the suspension." Volume fraction profiles from the numerical simulation at $\hat{t} = 0.1$ showed a "bump" on the horizontal suspension interface adjacent the clear fluid slit. The high velocities in the clear fluid zone near the top of the suspension carried the mixture above the level of the horizontal interface. This bump indicated the thin stream of suspension reported by Acrivos & Herbolzheimer.

Finally they reported the suspension moved downwards rapidly in a thin layer adjacent that where the clear fluid and suspension were rising rapidly. The numerical results shown in Figure 5.6 display this phenomena. This phenomena is the consequence of a global material balance of the dispersed phase. The region of high longitudinal velocity near the clear fluid zone straddles the suspension interface and carries both clear fluid and suspension upwards. This creates a large positive flux of particles into the region above plane AA' in Figure 5.6. However the net flux of particles into this region is negative because particles settle out due to gravity. The large positive flux of particles is balanced by a large negative flux elsewhere on plane AA'. It is likely that only a small fraction of the upwards moving particles have sufficient momentum to overcome viscous stresses and form a stream that is carried to the far wall. The majority of the particles at the right-hand-side of the bump are carried to the top of the bump and then down the left-hand-side of the bump by gravity. This closes the material balance on the dispersed phase and places a large negative flux of particles adjacent the upwards moving stream.

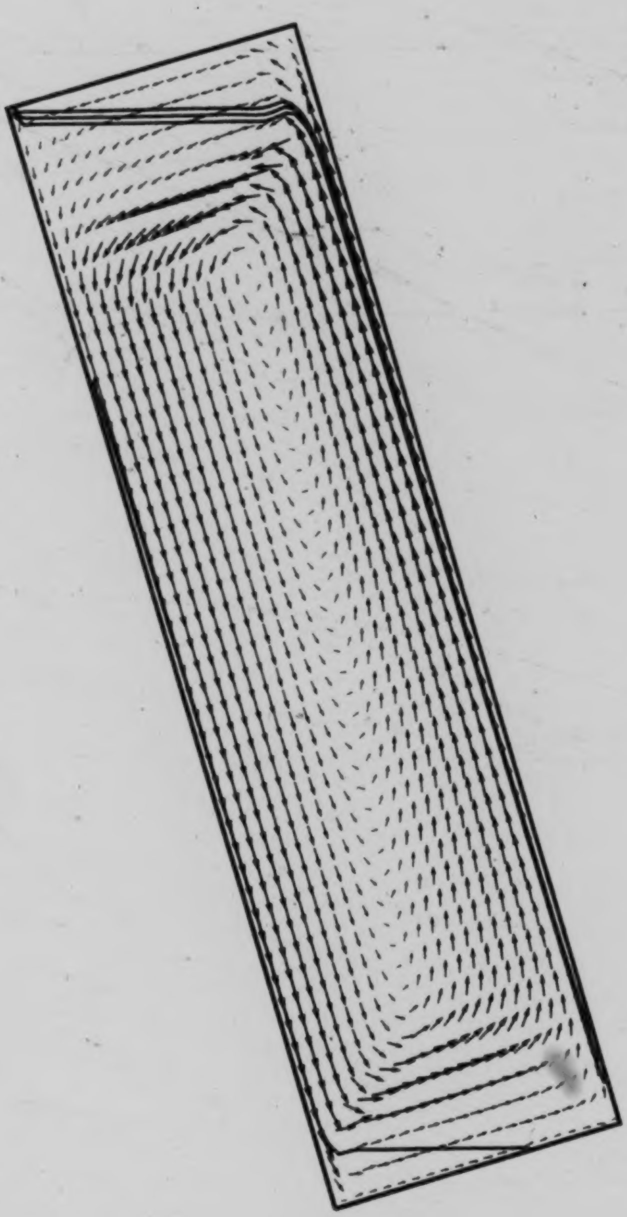

Figure 5.5: Velocity vectors and suspension interfaces at $\hat{t} = 0.02$ for 35° inclination and 10 % initial concentration. Vector length is proportional to $|\boldsymbol{u}|^{1/2}$.

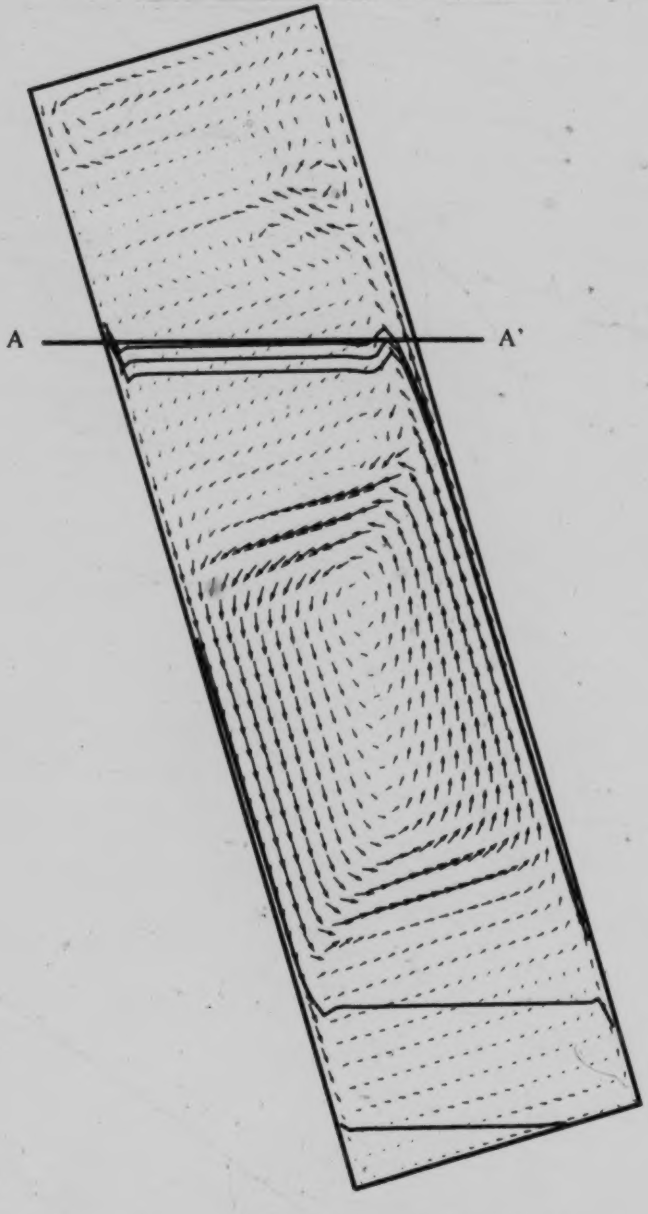

Figure 5.6: Velocity vectors and suspension interfaces at $\hat{t} = 0.1$ for 35° inclination and 10 % initial concentration. Vector length is proportional to $|\boldsymbol{u}|^{1/2}$.

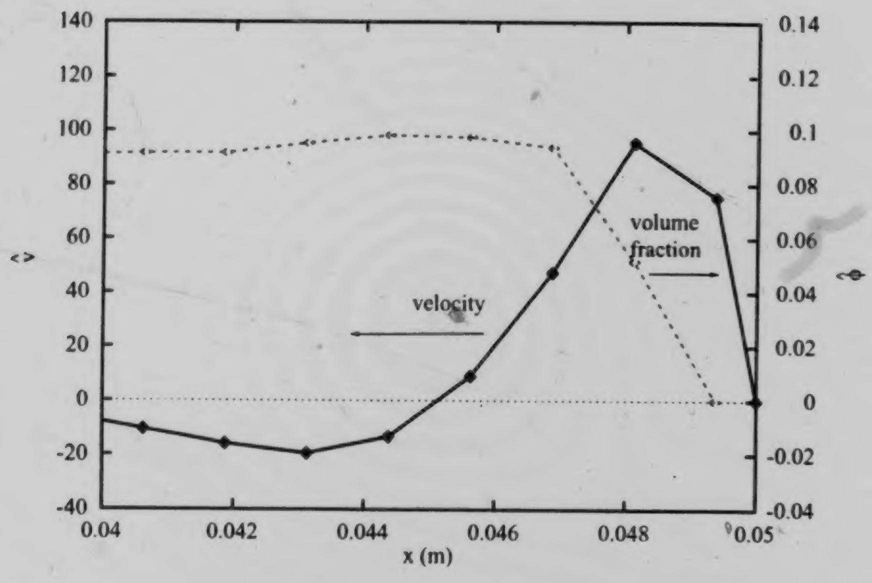

Figure 5.7: Longitudinal velocity and concentration profile at $y = 0.625\,L$ at $\hat{t} = 0.1$ for 35° inclination and 10 % initial concentration.

5.4 Batch inclined sedimentation: interface positions for large inclinations

Amberg & Dahlkid [2] used a method of characteristics to track the suspension and sediment interfaces for batch sedimentation at large inclinations ($\theta \simeq 80^\circ$). They assumed the lateral velocity was zero and the longitudinal velocity profile across the width of the vessel was modelled well by

$$0 = -\frac{\partial \hat{p}}{\partial \hat{y}} + \frac{1}{Re}\frac{\partial^2 \hat{v}}{\partial \hat{x}^2} - \frac{\Gamma}{\mathrm{Fr}}\hat{\phi} \tag{5.4}$$

subject to no-slip conditions at the vessel walls. Both $\hat{v}$ and $\partial\hat{v}/\partial\hat{x}$ were continuous at the clear fluid/suspension and suspension/sediment interfaces. The derivation of this velocity profile is similar to that given by Leung & Probstein [29] and Tripathi & Acrivos [50].

Amberg & Dahlkid present the evolution of the suspension interface for batch sedimentation with $\hat{\phi} = 0.01$. They do not specify the inclination and state the aspect ratio of the vessel was 1:100 typically.

The simulation code developed for this research was used to model sedimentation of a $\hat{\phi} = 0.01$ suspension in a 5 cm × 500 cm vessel tilted at 80°. The vessel was discretized with a 40 × 200 mesh. The fluid and dispersed phase properties were taken to be those of the 67.7 mPa s suspension of Acrivos & Herbolzheimer described earlier. Figure 5.8 shows the suspension interface and velocity profiles at $\hat{t} = 0.002$, 0.004, 0.006, 0.008 and 0.014. These dimensionless times are similar to the non-dimensional times $\hat{t} = 0.4$, 0.8, 1.2, 1.6 and 2.8 of Amberg & Dahlkid in their Figure 3.

The velocity profile at $\hat{t} = 0.002$ is uniform along the length of the vessel except near the ends of the vessel. The suspension has fallen away from the upper wall in a uniform manner and created a flow of clear fluid towards the top-left corner of the vessel. A sharp interface is beginning to form at the left side of the vessel. By $\hat{t} = 0.004$ the suspension interface at the left side has extended to the bottom of the vessel. The suspension near the right side of the vessel has not fallen away from the top wall as much as the suspension in the middle of the vessel. This interface profile is similar to that given by Amberg & Dahlkid except their profile is sharper. At $\hat{t} = 0.006$ an inflection in the interface position is apparent approximately 1/4 of the distance from the right wall. This corresponds to the shock apparent in the solution of Amberg & Dahlkid at their dimensionless time $\hat{t} = 1.2$. By $\hat{t} = 0.008$ this inflection in the interface position has strengthened at the right side of the vessel. The interface located 1/3 of the length from the left side has spread over a large distance. At $\hat{t} = 0.014$ there is very little suspension at the bottom and a wall of suspension has formed near the right side of the vessel.

Results in Figure 5.9 obtained with a finer (80 × 400) mesh were similar to the results in Figure 5.8 obtained on a 40 × 200 mesh. The suspension interface profiles in Figure 5.8 are similar to those obtained with the method of characteristics by Amberg & Dahlkid. The suspension interface at $\hat{t} = 0.008$ obtained by Amberg & Dahlkid has a pronounced step at the location where the inflection occurs in Figure 5.8.

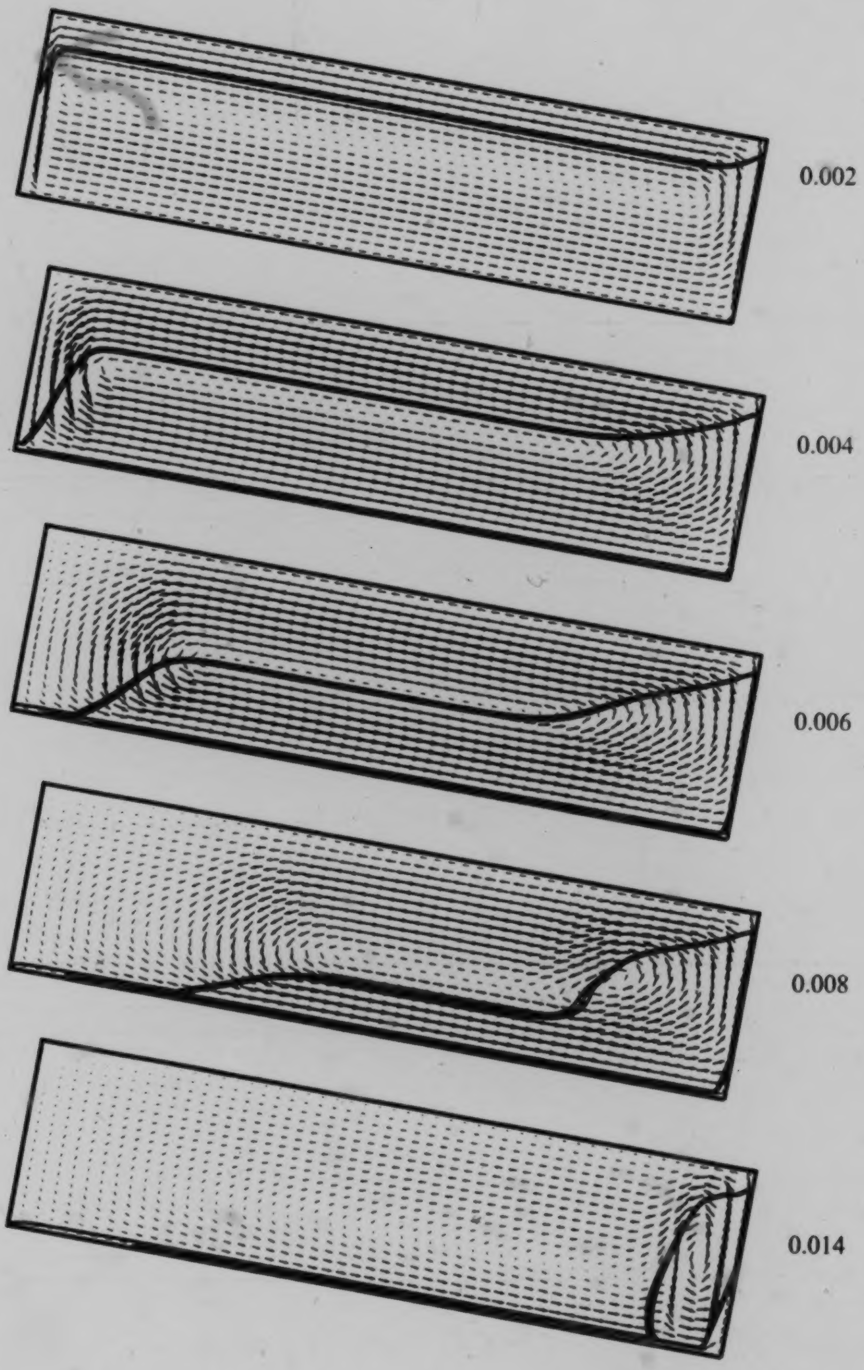

Figure 5.8: Interface and velocity profiles obtained with a 40×200 mesh for $\hat{\phi} = 0.01$, $\theta = 80°$ and 1:100 aspect ratio for $\hat{t} = 0.002$, 0.004, 0.006, 0.008 and 0.014.

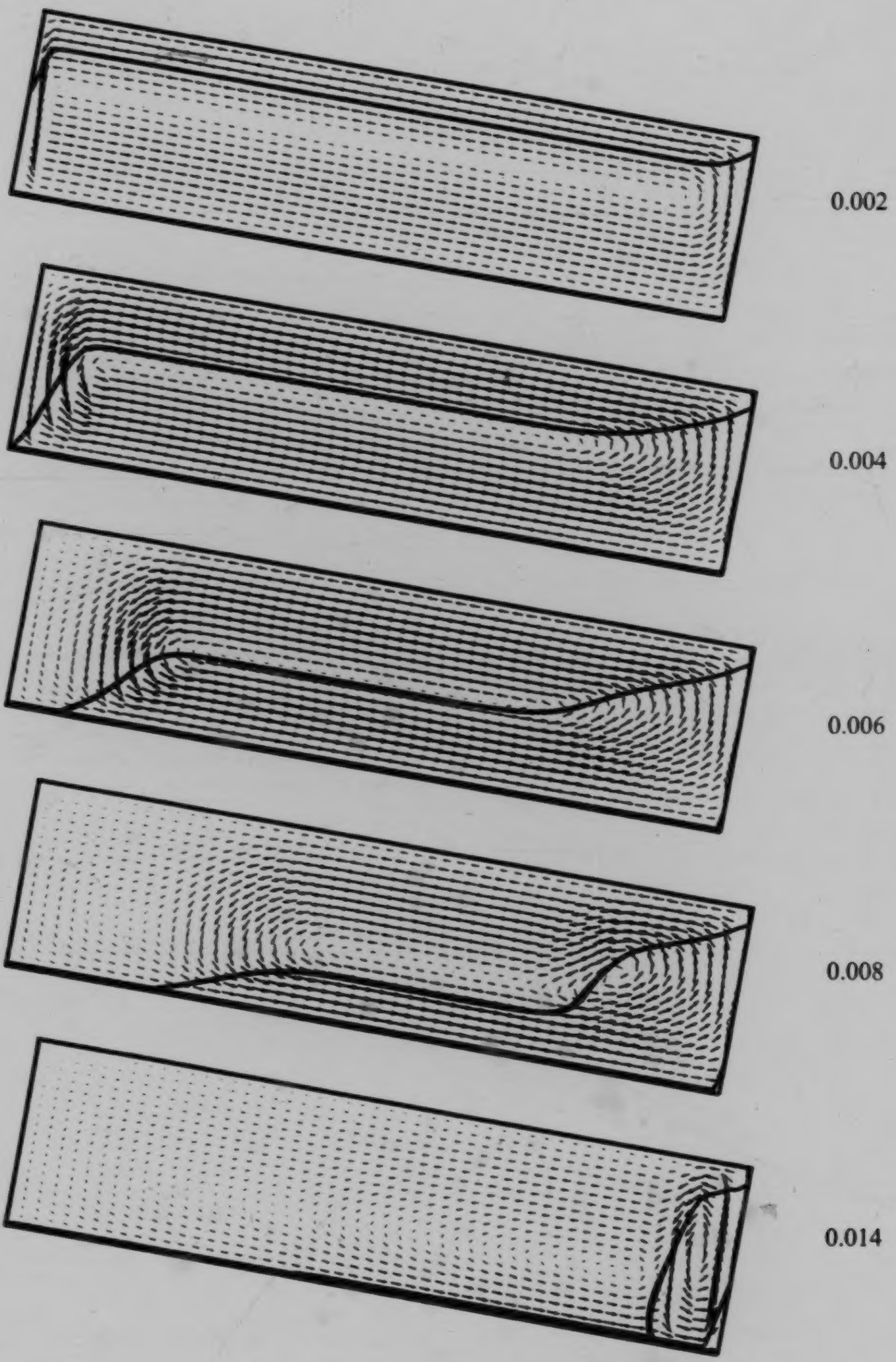

Figure 5.9: Interface and velocity profiles obtained with a 80×400 mesh for $\hat{\phi} = 0.01$, $\theta = 80^\circ$ and 1:100 aspect ratio for $\hat{t} = 0.002, 0.004, 0.006, 0.008$ and 0.014.

5.5 Batch inclined sedimentation: thickness of the clear fluid slit

Shaqfeh & Acrivos [45] measured the clear fluid thicknesses δ shown in Figure 5.1. Experiments were performed for inclined plate sedimentation in the batch and continuous bottom feed modes for five suspensions: $\bar{\rho}_f = 1000\,\mathrm{kg/m^3}, \bar{\rho}_s = 2530\,\mathrm{kg/m^3}, \bar{\mu}_f =$ 5.6–9.3 mPa s, $d_s = 140\,\mu\mathrm{m}, \phi \simeq 0.01$. Their experimental apparatus was 5 cm × 4.5 cm × 80 cm in size and fitted with 3/8 inch ports for bringing in feed and withdrawing clear fluid. The bottom feed and withdrawal ports were separated by a 5 cm high baffle.

Numerical results were obtained for the thickness of the clear fluid slit during batch sedimentation: there was considerable short circuiting from the feed to withdrawal port in the continuous simulations. The location of the interface was defined by the isoline at one half of the initial concentration. All simulations were performed on a 40 × 200 mesh with even grid spacing along the length and grid clustering across the width towards the vessel walls.

5.5.1 Development of the clear fluid zone

Figure 5.10 shows the suspension is still falling away from the upper wall at $\hat{t} = 0.01$. By $\hat{t} = 0.02$ a large wave is present at $y = 0.3\,\mathrm{m}$ and propagates upwards. By $\hat{t} = 0.04$ this initial disturbance has moved outside the range where Shaqfeh & Acrivos collected experimental data. The simulation predicts that waves remained near the top of the suspension ($y > 0.4\,\mathrm{m}$) at $\hat{t} = 0.05$.

The small waves apparent for $\hat{t} = 0.04$ below $y = 0.35\,\mathrm{m}$ are artifacts of the interpolation algorithm used for constructing the contour lines. The interpolation algorithm assumes the volume fraction surface is continuous while the numerical simulation admits discontinuous solutions.

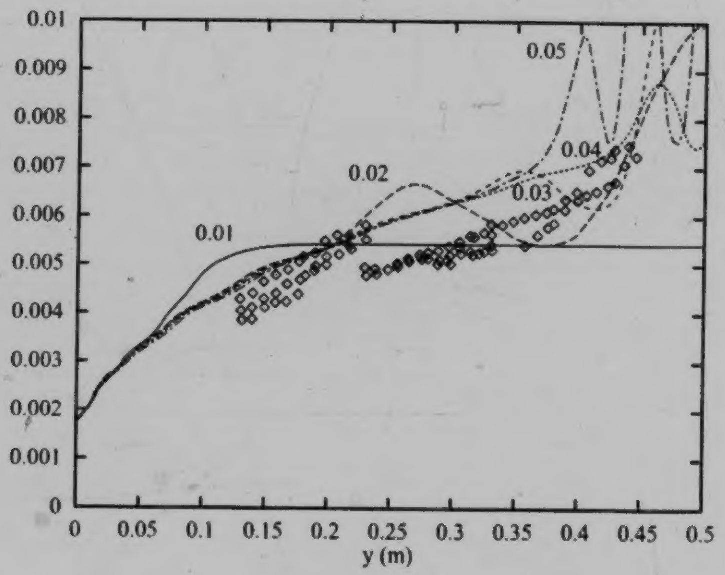

Figure 5.10: Development of the clear fluid layer ($\hat{\phi}_s = 0.008, \mu_f = 9.328\,\mathrm{mPa\,s}, \theta = 45°$): $\hat{t} = 0.01, 0.02, 0.03, 0.04, 0.05$. Points denote the experimental data of Shaqfeh & Acrivos [45].

5.5.2 Comparison with experimental and theoretical results

Interface positions were obtained at $t = 0.05$ from the numerical simulation: the initial wavy disturbance moved past the region where Shaqfeh & Acrivos collected experimental data. Shaqfeh & Acrivos did not measure the clear fluid thickness if the flow was too unstable. They present several photographs of waves at the suspension/clear fluid interface in Reference [45].

Figures 5.11 – 5.15 show the clear fluid layer thicknesses obtained from the simulations were within 10–15 % of the experimental data and the analytical expression of Shaqfeh & Acrivos [45, Equations 4, 5, 6]. Large waves were present for $y > 0.3$ m in the numerical simulations with the 5.597 mPa s suspension. Shaqfeh & Acrivos report that large waves were present near the top of the suspension for these runs.

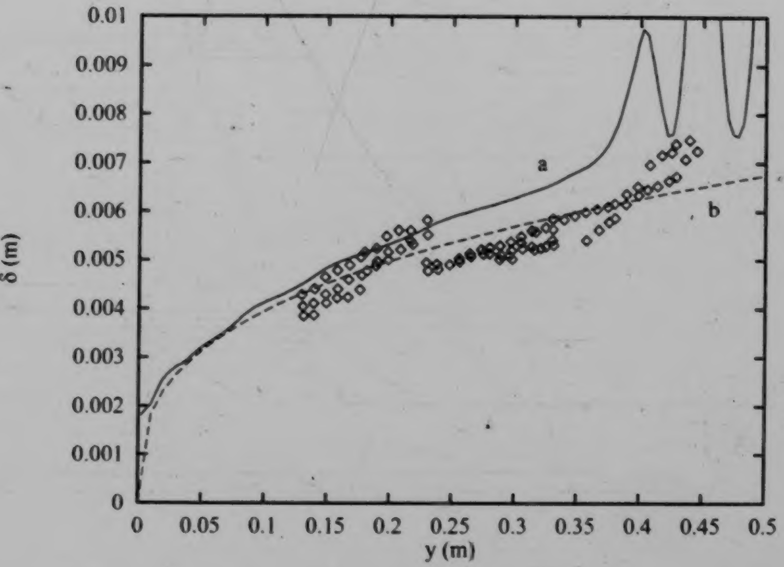

Figure 5.11: Thickness of the clear fluid layer for ($\hat{\phi} = 0.008, \bar{\mu}_f = 9.328\,\mathrm{mPa\,s}, \mathring{\theta} = 45°$): a is from the numerical simulation, b is from the analytic expression of Shaqfeh & Acrivos. Points denote the experimental data of Shaqfeh & Acrivos [45].

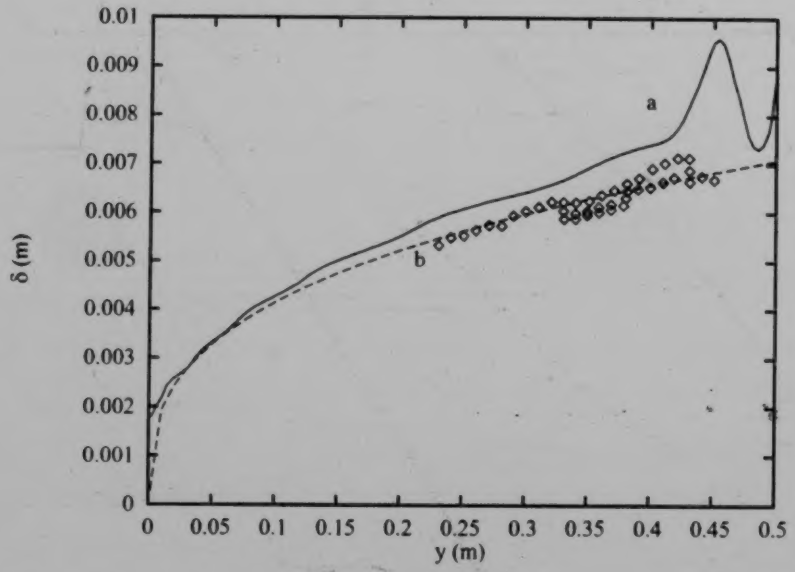

Figure 5.12: Thickness of the clear fluid layer for ($\hat{\phi} = 0.005, \bar{\mu}_f = 9.328\,\mathrm{mPa\,s}, \theta = 35^\circ$): a is from the numerical simulation, b is from the analytic expression of Shaqfeh & Acrivos. Points denote the experimental data of Shaqfeh & Acrivos [45].

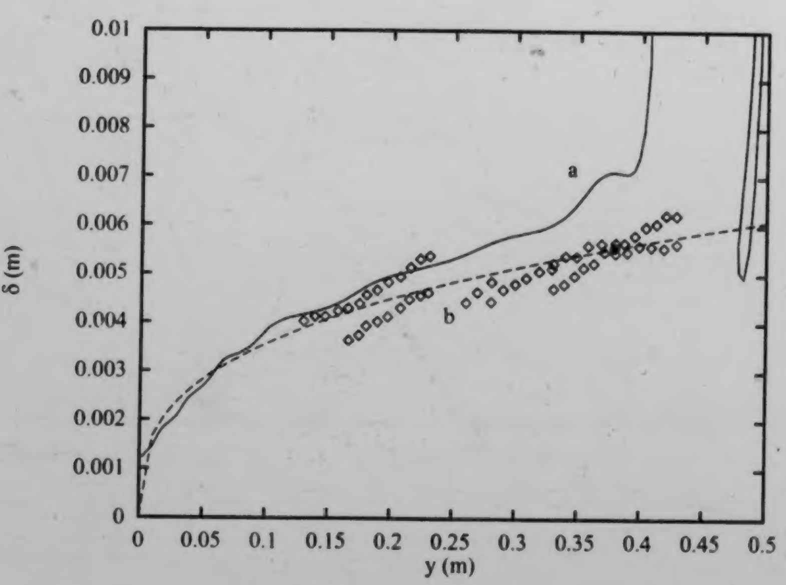

Figure 5.13: Thickness of the clear fluid layer for ($\hat{\phi} = 0.012, \bar{\mu}_f = 6.996\,\mathrm{mPa\,s}, \theta = 45°$): a is from the numerical simulation, b is from the analytic expression of Shaqfeh & Acrivos. Points denote the experimental data of Shaqfeh & Acrivos [45].

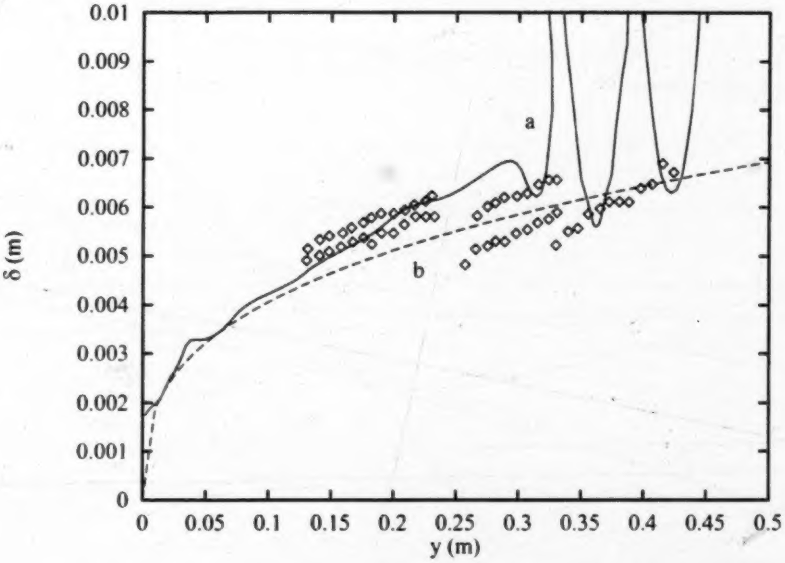

Figure 5.14: Thickness of the clear fluid layer for ($\hat{\phi} = 0.010, \bar{\mu}_f = 5.597\,\mathrm{mPa\,s}, \theta = 45°$): a is from the numerical simulation, b is from the analytic expression of Shaqfeh & Acrivos. Points denote the experimental data of Shaqfeh & Acrivos [45].

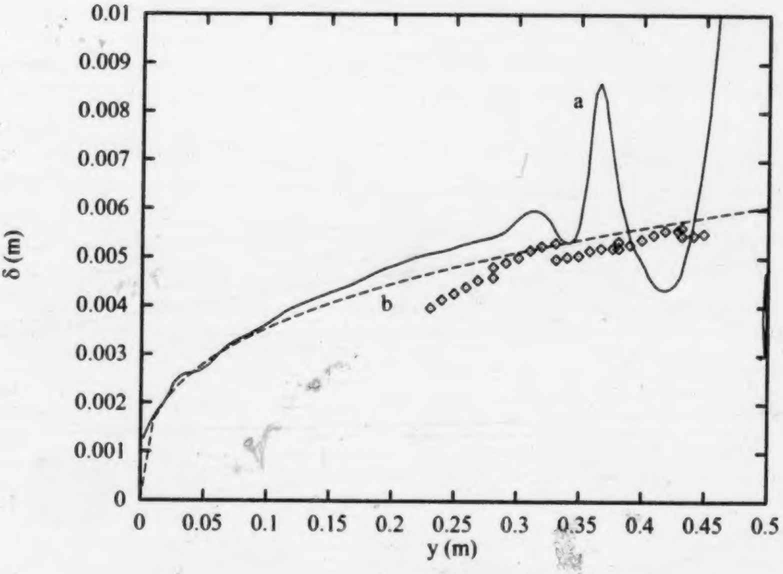

Figure 5.15: Thickness of the clear fluid layer for ($\hat{\phi} = 0.010, \bar{\mu}_f = 5.597\,\mathrm{mPa\,s}, \theta = 35°$): a is from the numerical simulation, b is from the analytic expression of Shaqfeh & Acrivos. Points denote the experimental data of Shaqfeh & Acrivos [45].

5.6 Summary

The simulation results agreed well with numerical results and experimental data obtained by other researchers for a wide variety of problems. The results obtained with these examples demonstrate the validity of the simulation code for modelling sedimentation between inclined plates. The numerical simulation captured the wavy suspension interfaces observed by Shaqfeh & Acrivos for sedimentation with low viscosity fluids. This phenomena is explored in greater detail in subsequent chapters.

Chapter 6

Comparison of non-diffusive and first order results for inclined plate sedimentation

The ability of the non-diffusive numerical scheme to capture fine flow details in inclined plate sedimentation is demonstrated in this chapter. Qualitative comparisons are made between results obtained with the non-diffusive and first order upwinding methods with different grid resolutions. First order upwinding is often used in numerical simulations to guarantee convergence. The results are compared with the phenomena observed in sedimentation experiments of Acrivos & Herbolzheimer [1] and Shaqfeh & Acrivos [45].

The behaviour of four suspensions were studied for batch sedimentation. The dispersed phase density and diameter were $\bar{\rho}_s = 2530\,\mathrm{kg/m^3}$ and $d_s = 140\,\mu\mathrm{m}$. The most viscous suspension was similar to that used in the experiments of Acrivos & Herbolzheimer: $\bar{\mu}_f = 67.7\,\mathrm{mPa\,s}$ with $\phi = 0.01$ and $\phi = 0.10$. The suspensions of intermediate and low viscosity were similar to materials used by Shaqfeh & Acrivos: $\bar{\mu}_f = 9.328$ and $2.678\,\mathrm{mPa\,s}$ and the concentration was $\phi = 0.01$. The geometry for all cases was a rectangular vessel $5 \times 80\,\mathrm{cm}$ inclined at 30° illustrated in Figure 5.1.

Table 6.1: Physical properties and characteristics of the suspensions for the accuracy comparison.

$\bar{\mu}_f$, mPa s	67.7	67.7	9.328	2.678
ϕ	0.01	0.10	0.01	0.01
$V_{s,\infty}$, mm/s	0.241	0.241	1.752	6.10
$\mathrm{Re}_{s,\infty}$	0.0005	0.0005	0.026	0.32
Re	2.78	2.15	146	1 777

The velocity vectors and concentration isolines are plotted in a rectangular domain with 1:4 aspect ratio while the aspect ratio of the real geometry is 1:16. This distorts the shape of the suspension interface but allows one to see the details of the flow field. Most of the suspensions had initial or feed concentrations of $\phi = 0.01$. Three concentration isolines are drawn to resolve the suspension interface ($\phi = 0.003, 0.005, 0.007$) and two are drawn to capture the behaviour near the concentrated sediment layer ($\phi = 0.02, 0.04$). The isolines for the 67.7 mPa s simulations with 10 % were at $\phi = 0.03$, 0.05, 0.07, 0.2 and 0.4.

6.1 Batch sedimentation of 67.7 mPa s suspension with 1 % concentration

The upper suspension interface for the non-diffusive simulation shown in Figure 6.1 is much sharper than the interface from the first order simulation in Figure 6.3 for the 40 × 100 mesh. The non-diffusive results shown in Figure 6.2 for a fine (80 × 400) mesh has a sharper suspension interface and more pronounced lateral velocity at the top of the suspension than the results obtain on the 40 × 100 mesh. This is consistent with the increased spatial resolution. The single vortex in the bulk of the suspension is analogous to the unicellular convection patterns seen in experimental and numerical results for low Grashof number natural convection in vertical enclosures [27, 6].

The upper suspension interface obtained with first order upwinding is twice as broad as the interface obtained with the non-diffusive simulation for the same meshes. The lateral velocity near the top of the suspension is not as strong as with the non-diffusive results. The first order accurate simulation does capture the gross features of the flow. This is because the flow does not contain fine details that need to be resolved with accurate discretization methods.

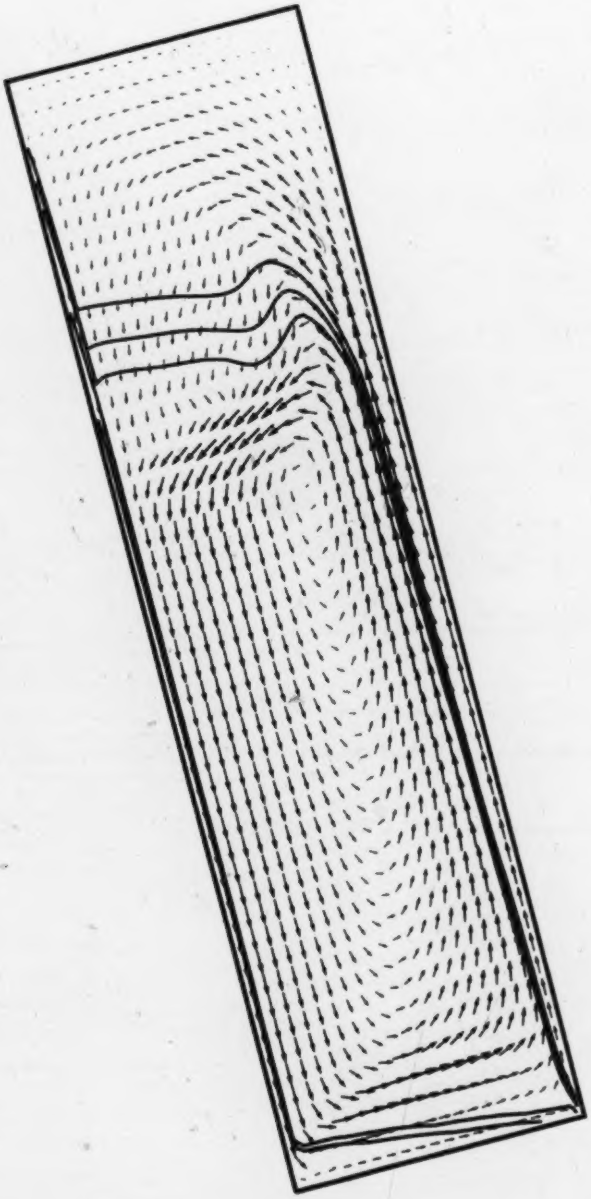

Figure 6.1: Velocity profile and concentration isolines for batch sedimentation (40 × 100 mesh, non-diffusive): $\hat{t} = 0.04$, $\phi = 0.01$, $\theta = 30°$, $\bar{\mu}_f = 67.7\,\mathrm{mPa\,s}$.

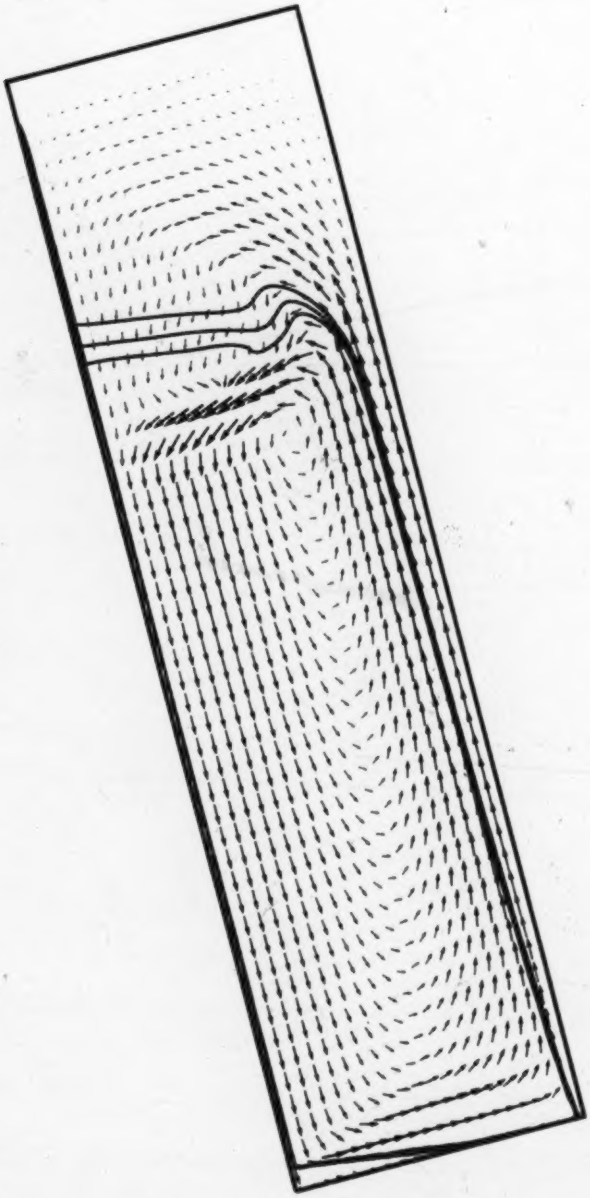

Figure 6.2: Velocity profile and concentration isolines for batch sedimentation (80 × 400 mesh, non-diffusive): $\hat{t} = 0.04$, $\phi = 0.01$, $\theta = 30°$, $\bar{\mu}_f = 67.7\,\mathrm{mPa\,s}$.

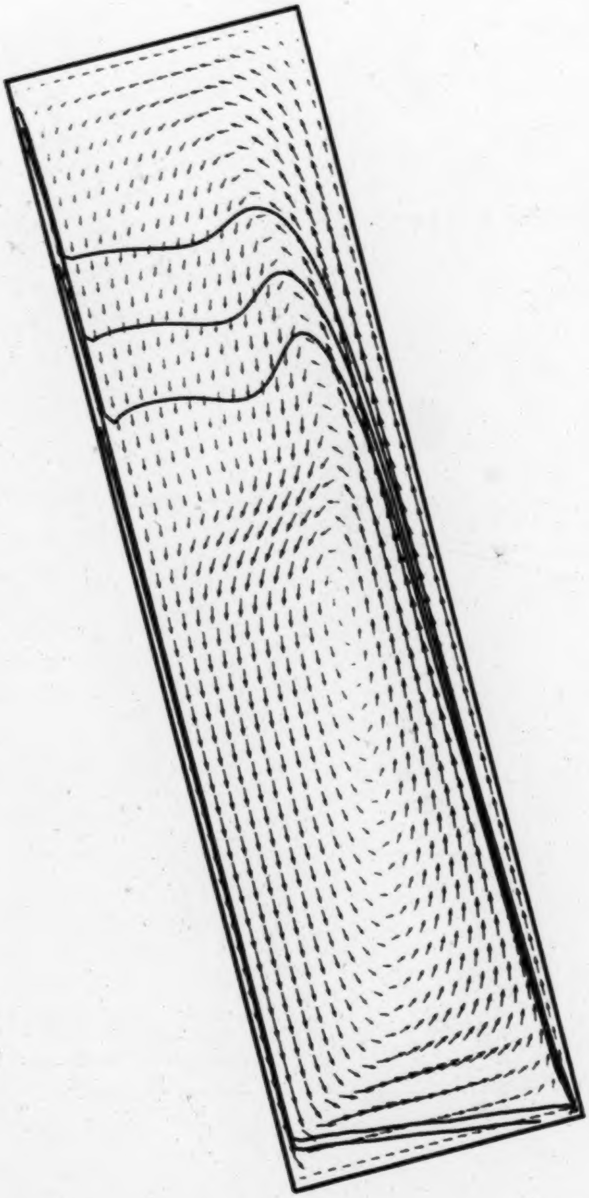

Figure 6.3: Velocity profile and concentration isolines for batch sedimentation (40 × 100 mesh, first order): $\hat{t} = 0.04$, $\phi = 0.01$, $\theta = 30°$, $\bar{\mu}_f = 67.7\,\mathrm{mPa\,s}$.

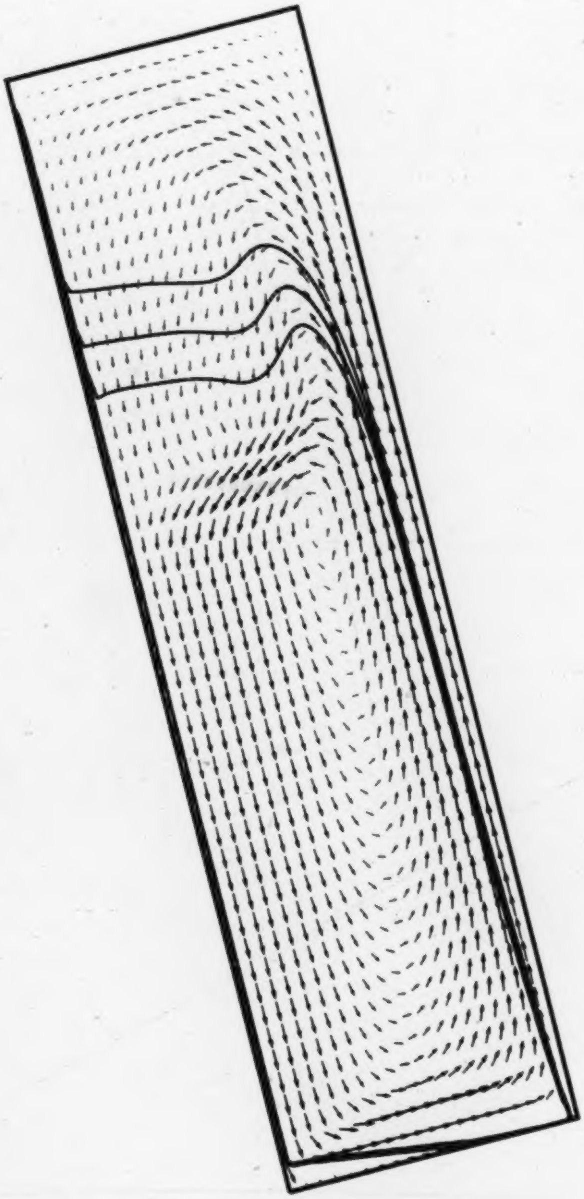

Figure 6.4: Velocity profile and concentration isolines for batch sedimentation (80 × 400 mesh, first order): $\hat{t} = 0.04$, $\phi = 0.01$, $\theta = 30°$, $\bar{\mu}_f = 67.7\,\mathrm{mPa\,s}$.

6.2 Batch sedimentation of 67.7 mPa s suspension with 10 % concentration

Figure 6.5 shows a large single vortex is evident in the bulk of the suspension for the coarse mesh (40×100) simulation. This large vortex did not appear in the fine 80×40 mesh simulation shown Figure 6.6: there is series of smaller stacked vortices at this resolution. These stacks of vortices were not present for simulations with shorter vessels. Similar multicellular solutions have been obtained by Lee & Korpela [27] and Chikhaoui et al. [6] for high Grashof number natural convection in vessels with the aspect ratio greater than 12.

The horizontal suspension interface for the first order accurate solution on the 40×100 mesh in Figure 6.7 is much broader than the non-diffusive solution on the same mesh. Figure 6.8 shows the horizontal interface is sharper and the central vortex is larger with the spatial resolution increased to 80×400. Further increase in the resolution (80×800) shows the formation of a small stream of suspension at the top of the clear fluid slit and a recirculation zone above the main vortex. These two features are similar to those patterns in the non-diffusive simulation with the coarser 80×400 mesh. The non-diffusive simulation required less mesh resolution to obtain results similar to those obtained with first order upwinding.

The heights of the horizontal suspension interfaces are different between the results obtained with the non-diffusive method on the 40×100 and 80×400 meshes. The explanation of this discrepancy is provided by examining the volume fraction and velocity profiles across the vessel at $y = L/2$. Figure 6.10 shows suspension interface at $y = L/2$ is captured with three grid points on both the 40×100 and 80×400 meshes. It follows that the thickness of this interface on the fine mesh is one half of the thickness on the coarse mesh. At the suspension interface the lateral volume fraction gradient on the fine mesh is twice that on the coarse mesh. Figure 6.11 shows the maximum velocity obtained with the fine mesh is 30 % greater than that obtained with the coarse mesh. The peak velocities for both meshes lie near the suspension interface. This increase in the peak velocity associated with increased resolution of the suspension interface is consistent with the flow profiles obtained in Section 4.5 for a model gravity driven flow of a density stratified fluid between inclined parallel plates.

Define the normalized clear fluid concentration to be

$$c_f = 1 - \hat{\phi}/\hat{\phi}_0 \tag{6.1}$$

The longitudinal flux of clear fluid at any point along the cross section is given by vc_f. Figure 6.12 shows the flux of clear fluid is much larger for the 80×400 simulation than for the 40 × 100 simulation. The integrated or total upwards flux of clear fluid along the section $y = L/2$ is $\int v c_f \, d\xi$: the total upwards fluxes obtained with the 40 × 100 and 80 × 400 meshes are 1.47 and 1.93, respectively. PNK relates the flux of clear fluid in the clear fluid slit to the falling rate of the horizontal suspension interface. The discrepancy in the horizontal interface position between the 40 × 100 and 80 × 400 meshes is due to the difference in the mixture velocity near the clear fluid slit.

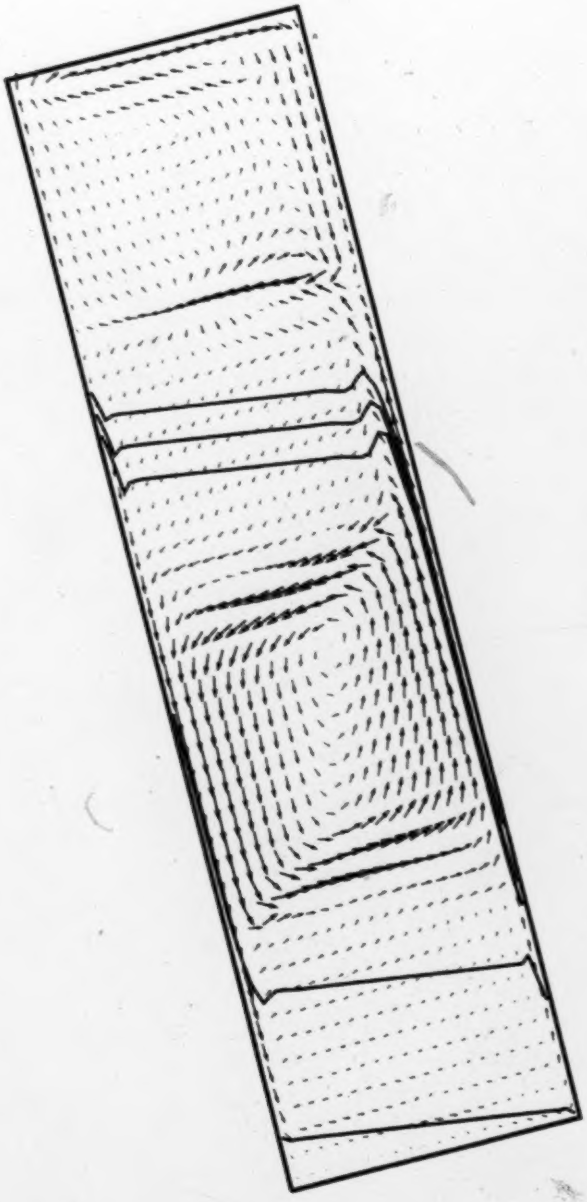

Figure 6.5: Velocity profile and concentration isolines for batch sedimentation (40 × 100 mesh, non-diffusive): $\hat{t} = 0.1$, $\phi = 0.1$, $\theta = 30°$, $\bar{\mu}_f = 67.7\,\mathrm{mPa\,s}$.

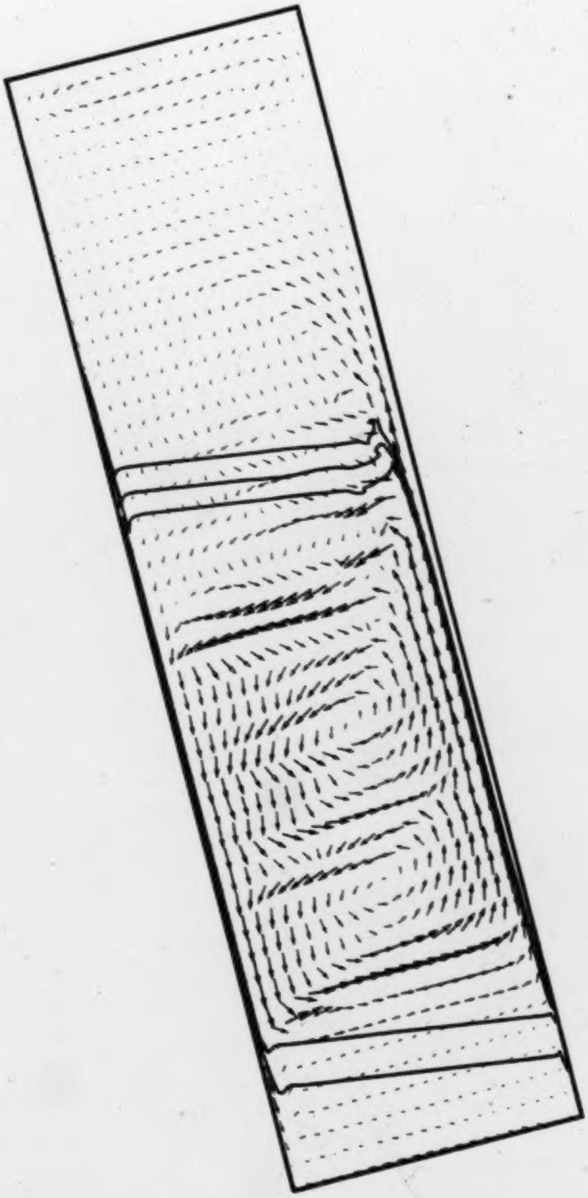

Figure 6.6: Velocity profile and concentration isolines for batch sedimentation (80 × 400 mesh, non-diffusive): $\hat{t} = 0.1$, $\phi = 0.1$, $\theta = 30°$, $\bar{\mu}_f = 67.7\,\mathrm{mPa\,s}$.

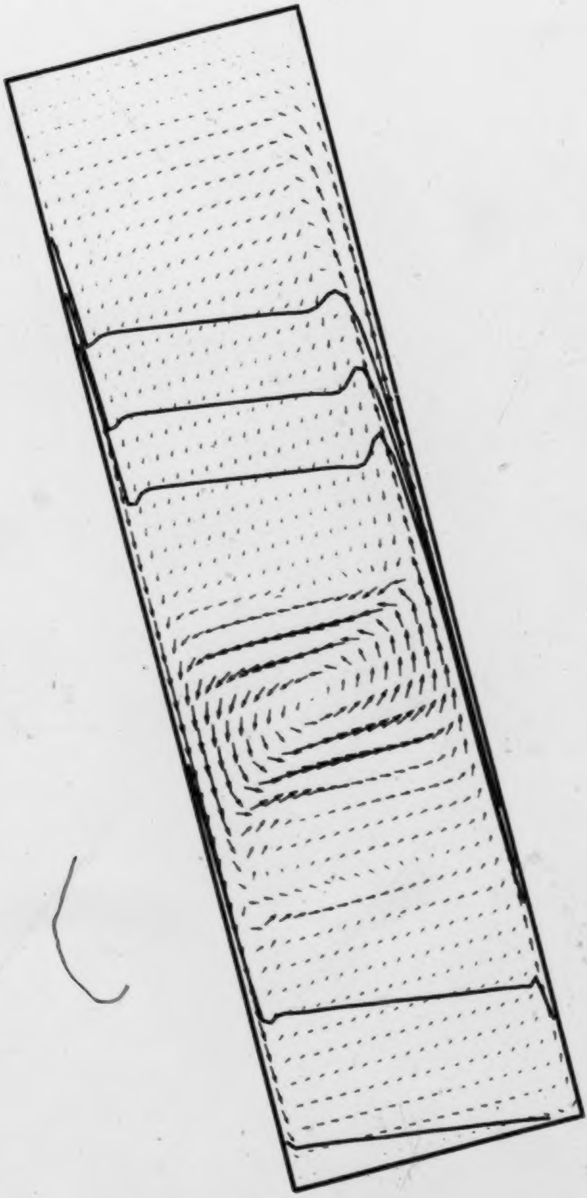

Figure 6.7: Velocity profile and concentration isolines for batch sedimentation (40 × 100 mesh, first order): $\hat{t} = 0.1$, $\phi = 0.1$, $\theta = 30°$, $\bar{\mu}_f = 67.7\,\mathrm{mPa\,s}$.

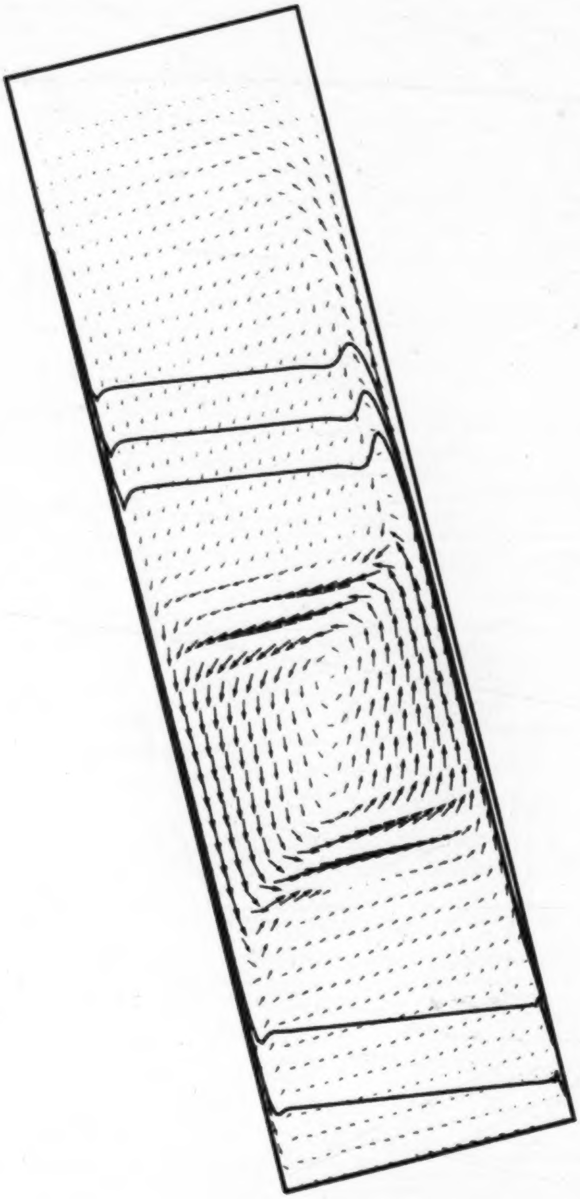

Figure 6.8: Velocity profile and concentration isolines for batch sedimentation (80×400 mesh, first order): $\hat{t} = 0.1$, $\phi = 0.1$, $\theta = 30^\circ$, $\bar{\mu}_f = 67.7\,\mathrm{mPa\,s}$.

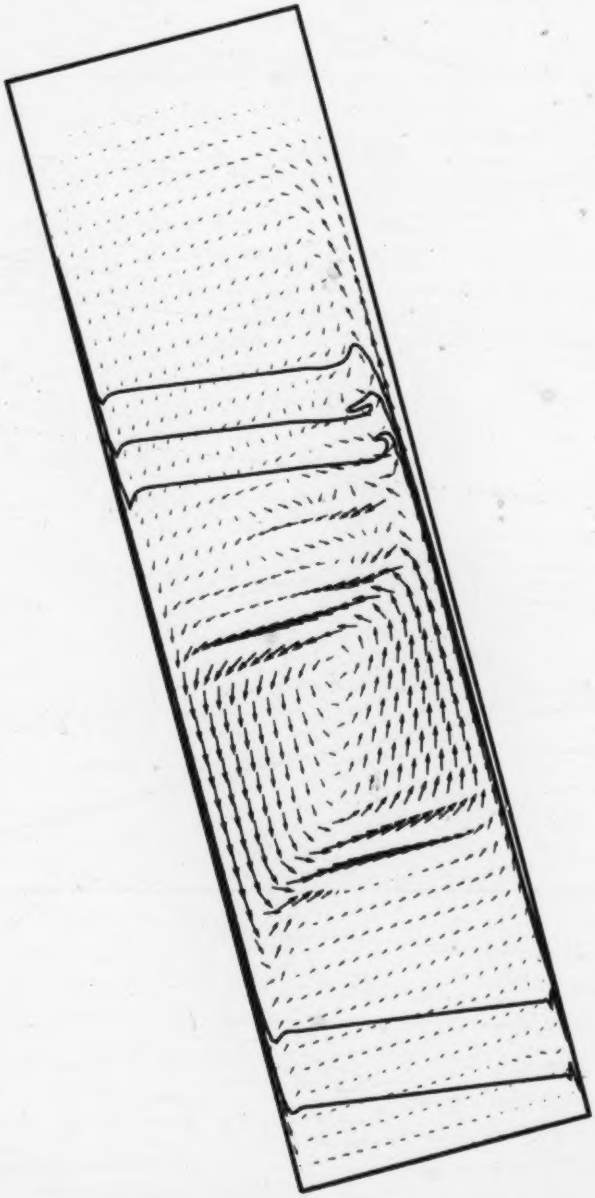

Figure 6.9: Velocity profile and concentration isolines for batch sedimentation (80 × 800 mesh, first order): $\hat{t} = 0.1$, $\phi = 0.1$, $\theta = 30°$, $\bar{\mu}_f = 67.7\,\mathrm{mPa\,s}$.

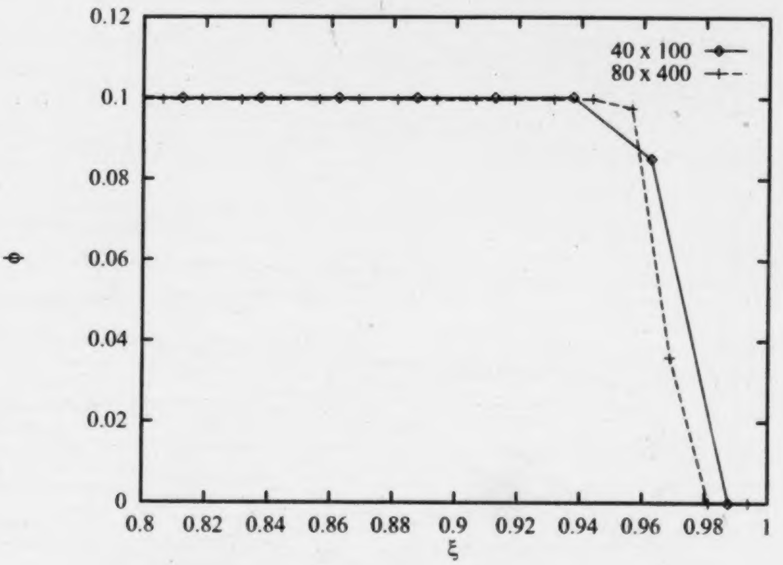

Figure 6.10: Dispersed phase volume fraction profile across $y = L/2$ for the 40 × 100 and 80 × 400 meshes: $\hat{t} = 0.1$, $\phi = 0.1$, $\theta = 30°$, $\bar{\mu}_f = 67.7\,\mathrm{mPa\,s}$.

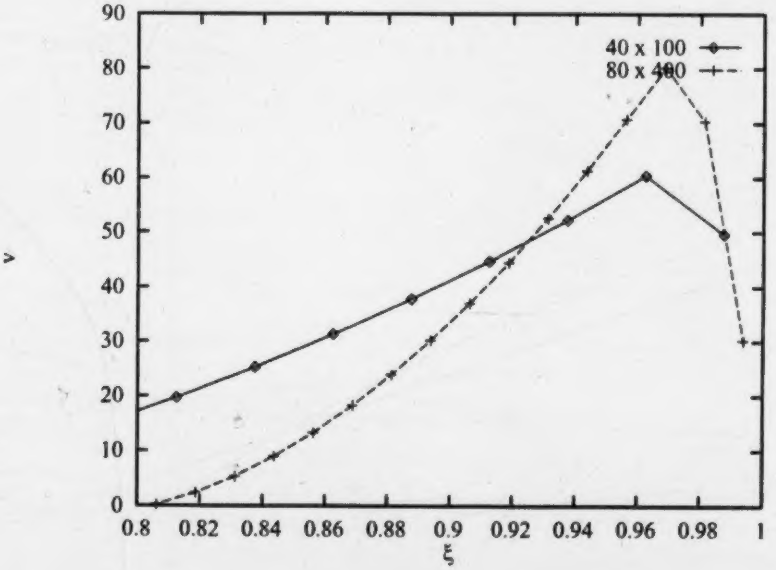

Figure 6.11: Longitudinal mixture velocity profile across $y = L/2$ for the 40 × 100 and 80 × 400 meshes: $\hat{t} = 0.1$, $\phi = 0.1$, $\theta = 30°$, $\bar{\mu}_f = 67.7\,\mathrm{mPa\,s}$.

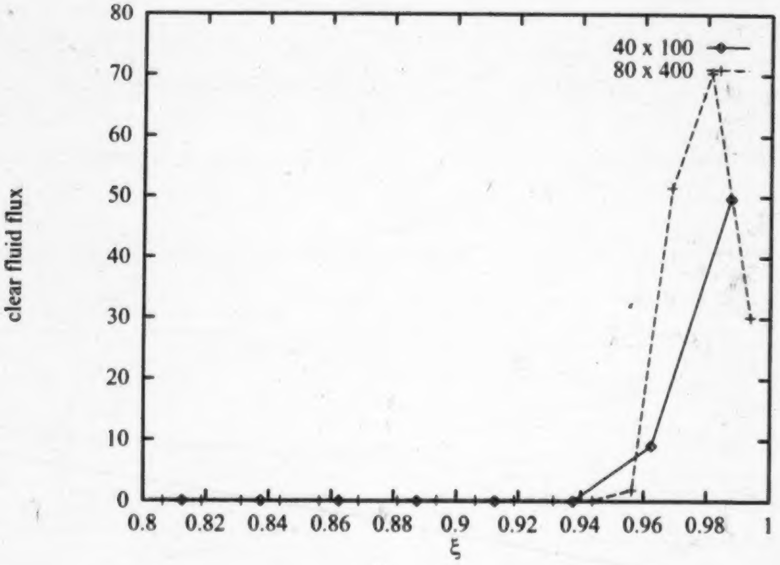

Figure 6.12: Profile for the longitudinal clear fluid flux across $y = L/2$ for the 40×100 and 80×400 meshes: $\hat{t} = 0.1$, $\phi = 0.1$, $\theta = 30°$, $\bar{\mu}_f = 67.7\,\text{mPa s}$.

6.3 Batch sedimentation of 9.328 mPa s suspension

Three noticeable features are visible with the non-diffusive solution at $\hat{t} = 0.03$ for the 40×100 mesh shown in Figure 6.13. First is the stream of suspension originating from the top of the clear fluid slit and travelling towards the opposite wall. The vessel Reynolds number for this flow is 53 times larger than that for the 1 % suspension in 67.7 mPa s fluid considered earlier.

Second is the isolated pocket of suspension above the stream of suspension. This feature is a remnant of the first stream of suspension formed at the onset of sedimentation. The low density clear fluid under this stream moves to the right and cuts off the stream by means of a gravity instability. This leaves a pocket of rotating suspension near the top of the vessel. The increase in grid resolution from Figure 6.13 to Figure 6.16 captures these two features with more precision and demonstrate the discontinuous nature of the volume fraction profile.

Third is the wavy suspension interface near the top of the clear fluid slit. Figures 6.14 – 6.16 resolve this wavy motion with finer meshes and show the wavelength is approximately 7 cm. Shaqfeh & Acrivos [45] photographed waves under similar conditions (25° inclination and initial concentration 0.008): the wavelength in the photograph was approximately 9 cm. The wavelength observed in the numerical simulation agrees well with that in the experiment of Shaqfeh & Acrivos.

The concept of mesh independence is valid only for solutions with continuous second derivatives: the volume fraction is discontinuous at the suspension interface. These simulations are transient and the solutions on different meshes will evolve in different manners. This evolution may cause the volume fraction and velocity profiles obtained with different meshes to be different for any particular instance. The wavelength of the suspension interface is an average property of the flow and did not change between the 40×200 and 80×400 meshes.

The interface profile obtained with the 40×400 mesh shown in Figure 6.15 has three well developed waves while the profile obtained with the 80×400 mesh in Figure 6.16 has only one well developed wave. The waves on the 40×400 and 80×400 mesh have the same wavelength. Increased grid resolution changes the buoyancy driving force near the suspension interface. The unstable waves evolve in a different manner because the flow is highly nonlinear. Figures 6.15 and 6.16 are a snap-shot of the sedimentation process at $\hat{t} = 0.03$. Figures 6.17 and 6.18 show the interface profile at $\hat{t} = 0.032$ on 40×400 and 80×400 meshes. Both of these results have a single well defined wave near the clear fluid slit. They also have large wave that distorts the flow at the top of the clear fluid slit and two isolated pockets of suspension. A thin stream of suspension is visible at the right-hand-side of the horizontal interface. The simulation on the 40 × 400 mesh captured a wavy instability of the concentrated sediment flowing down the left surface. Similar instabilities at the sediment/suspension interface were observed in the experimental work of Leung [28]. Two small perturbations in the isolines for the concentrated sediment are visible 1/4 and 1/3 down the length of the vessel in the 80 × 400 simulation.

First order upwinding was used to obtain the results in Figures 6.19 - 6.22. The suspension interfaces in these results are much broader than the interfaces obtained with the non-diffusive simulations on the same meshes. The thin stream of suspension at the top of the clear fluid slit is not captured with the 40 × 100 mesh. A small amplitude wave is visible on the 40 × 200 mesh. The solution on the finest mesh (80 × 400) does not capture the thin stream of suspension seen in the non-diffusive results with the coarsest mesh (40 × 100). The results obtained with first order upwinding are not as good as those obtained with the non-diffusive simulation.

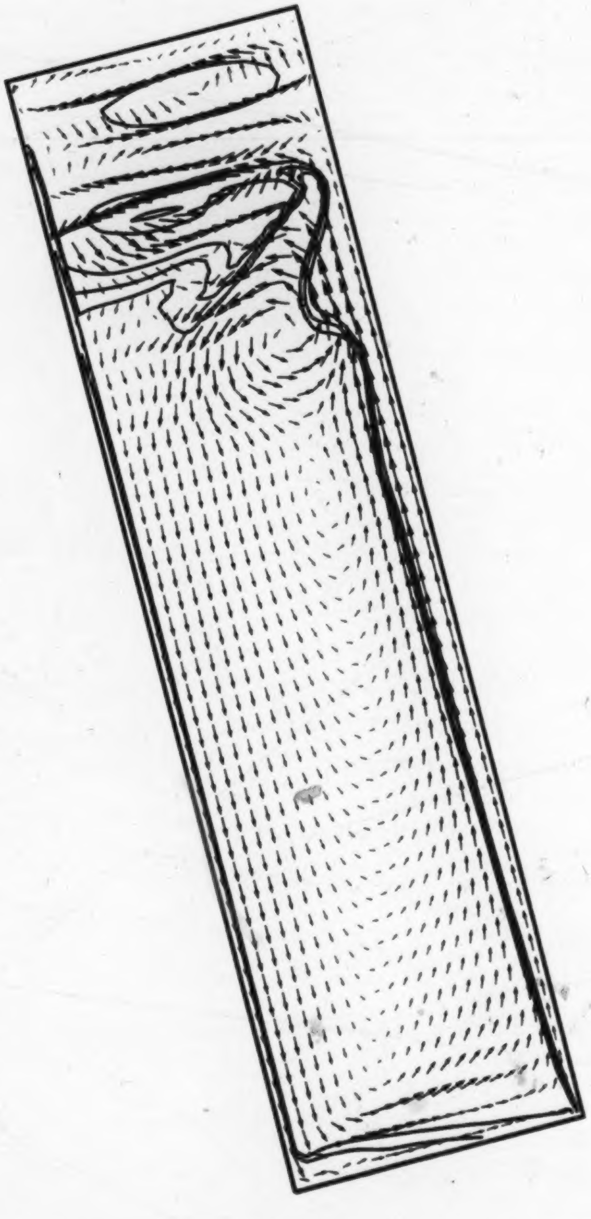

Figure 6.13: Velocity profile and concentration isolines for batch sedimentation (40 × 100 mesh, non-diffusive): $\hat{t} = 0.03$, $\theta = 30°$, $\bar{\mu}_f = 9.328\,\mathrm{mPa\,s}$.

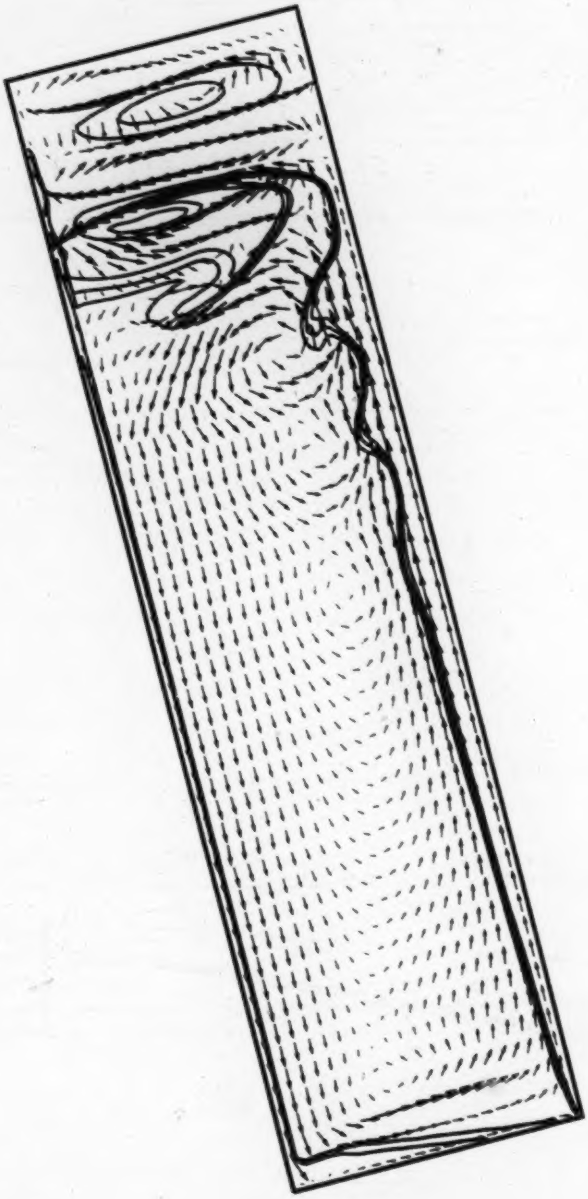

Figure 6.14: Velocity profile and concentration isolines for batch sedimentation (40×200 mesh, non-diffusive): $\hat{t} = 0.03$, $\theta = 30^\circ$, $\bar{\mu}_f = 9.328\,\mathrm{mPa\,s}$.

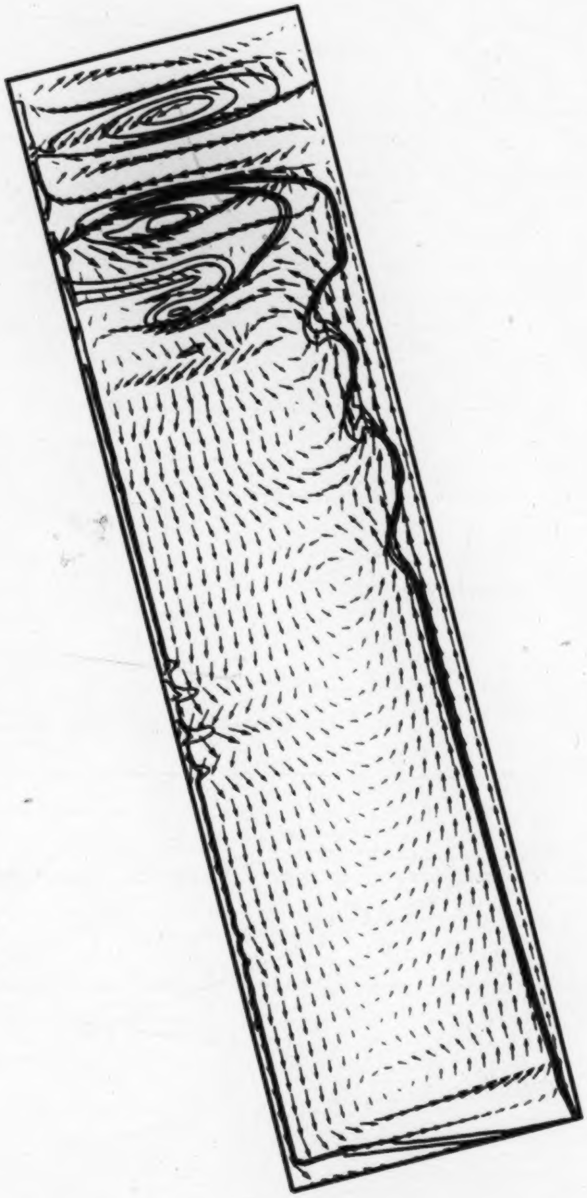

Figure 6.15: Velocity profile and concentration isolines for batch sedimentation (40 × 400 mesh, non-diffusive): $\hat{t} = 0.03$, $\theta = 30°$, $\bar{\mu}_f = 9.328\,\mathrm{mPa\,s}$.

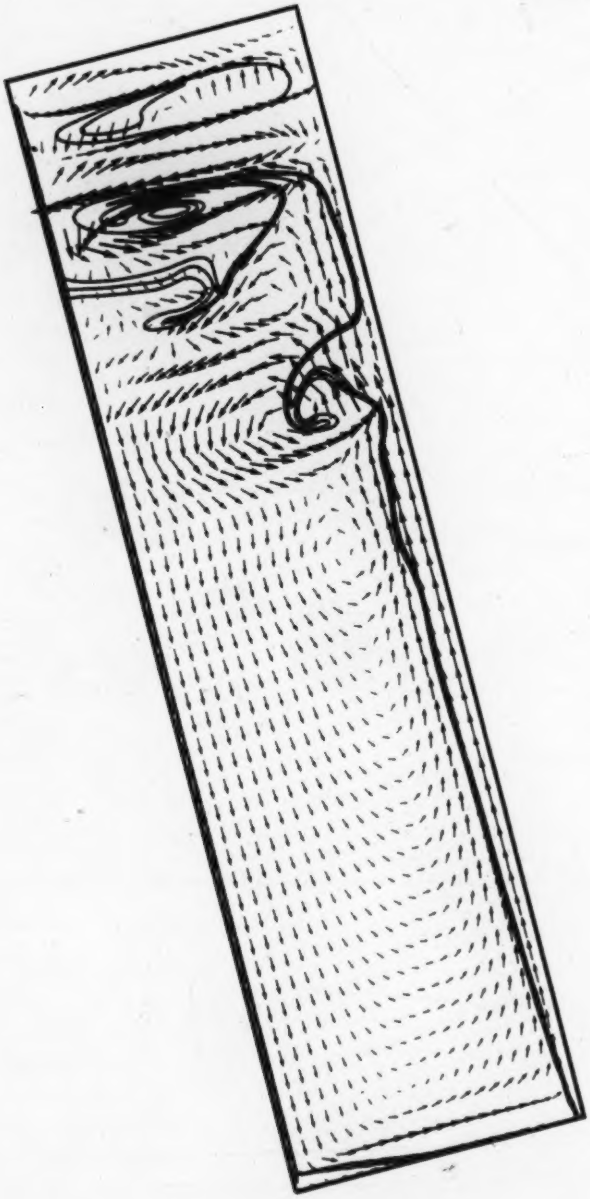

Figure 6.16: Velocity profile and concentration isolines for batch sedimentation (80 × 400 mesh, non-diffusive): $\hat{t} = 0.03$, $\theta = 30°$, $\bar{\mu}_f = 9.328\,\mathrm{mPa\,s}$.

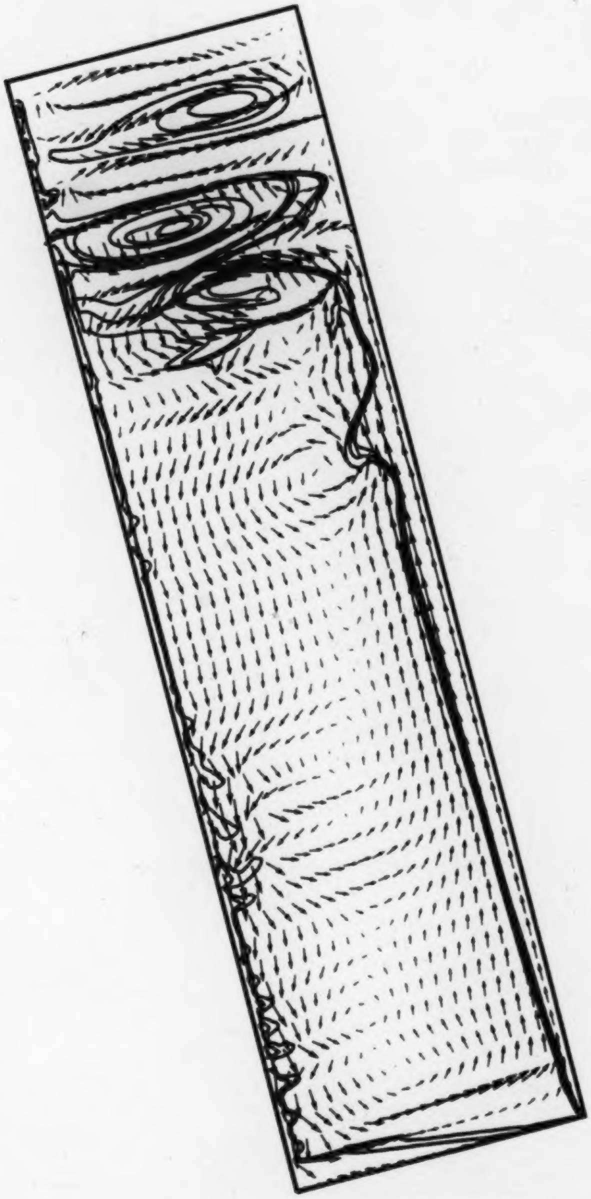

Figure 6.17: Velocity profile and concentration isolines for batch sedimentation (40 × 400 mesh, non-diffusive): $\hat{t} = 0.032$, $\theta = 30°$, $\bar{\mu}_f = 9.328\,\mathrm{mPa\,s}$.

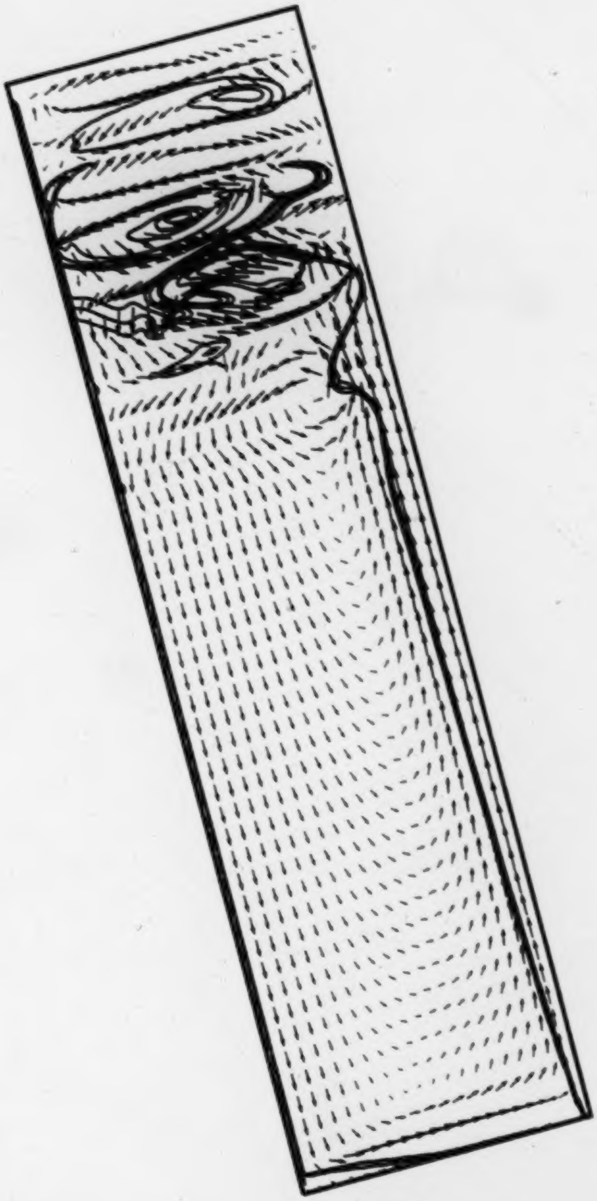

Figure 6.18: Velocity profile and concentration isolines for batch sedimentation (80 × 400 mesh, non-diffusive): $\hat{t} = 0.032$, $\theta = 30°$, $\bar{\mu}_f = 9.328\,\mathrm{mPa\,s}$.

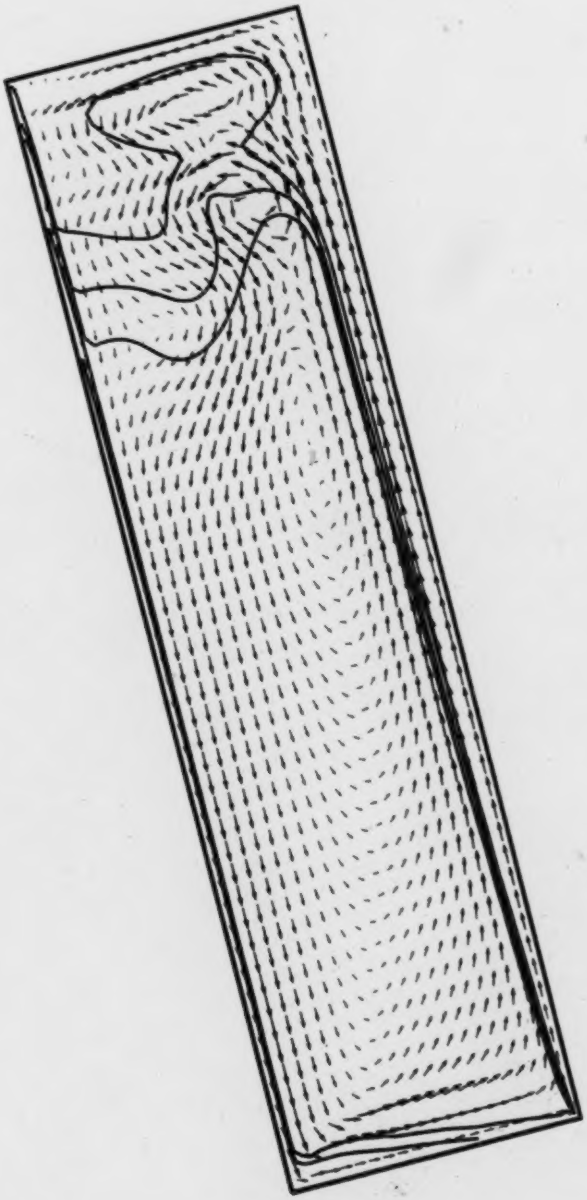

Figure 6.19: Velocity profile and concentration isolines for batch sedimentation (40 × 100 mesh, first order): $\hat{t} = 0.03$, $\theta = 30°$, $\bar{\mu}_f = 9.328\,\mathrm{mPa\,s}$.

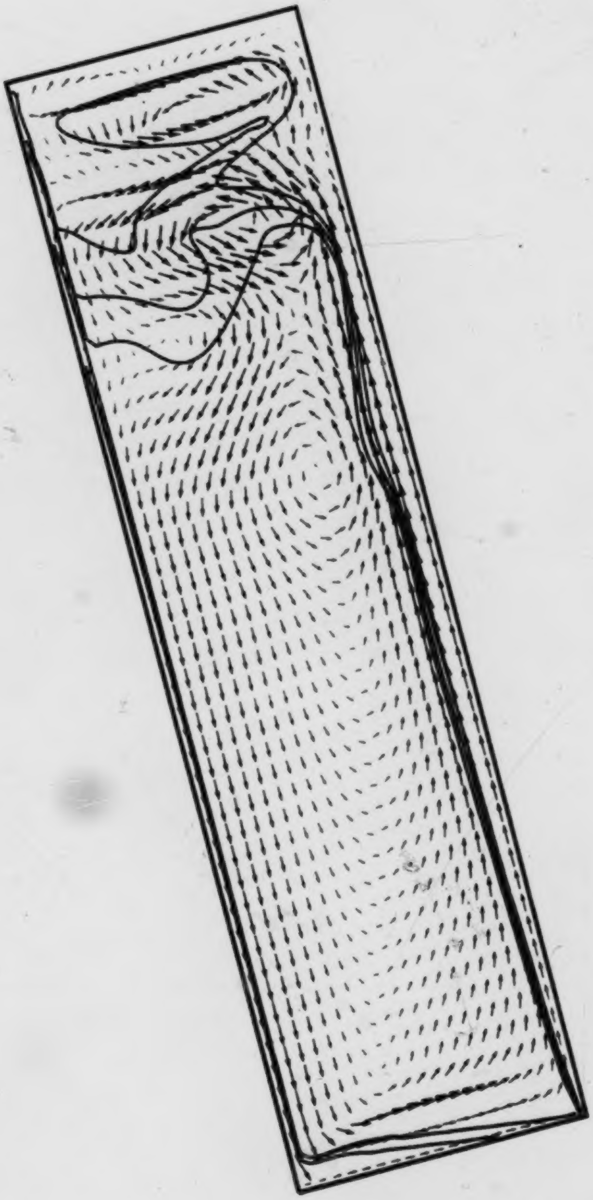

Figure 6.20: Velocity profile and concentration isolines for batch sedimentation (40 × 200 mesh, first order): $\hat{t} = 0.03$, $\theta = 30^\circ$, $\bar{\mu}_f = 9.328\,\mathrm{mPa\,s}$.

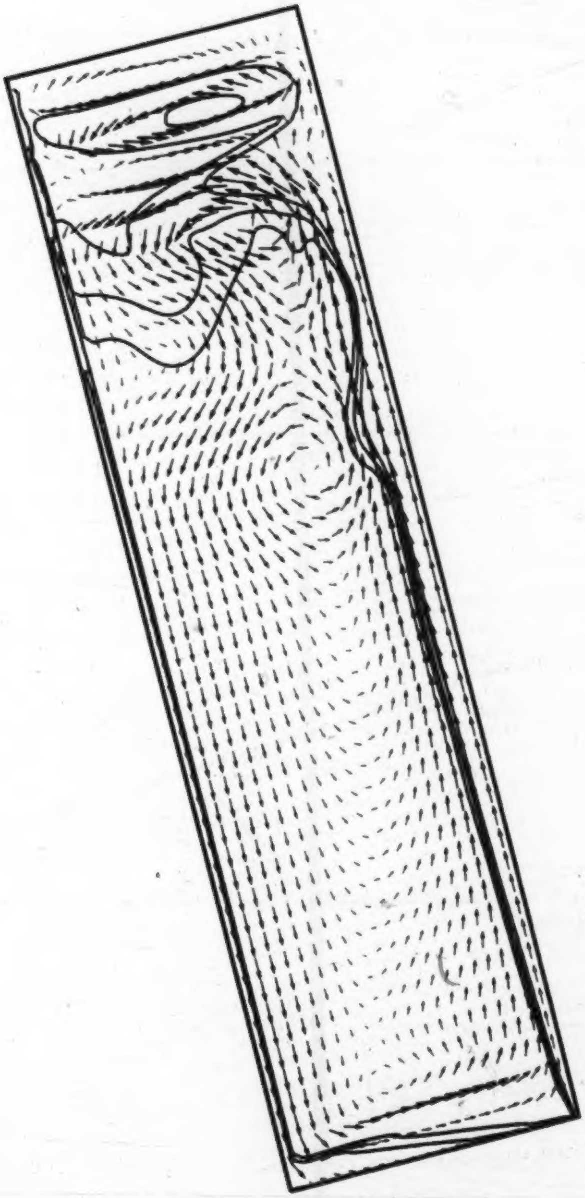

Figure 6.21: Velocity profile and concentration isolines for batch sedimentation (40 × 400 mesh, first order): $\hat{t} = 0.03$, $\theta = 30°$, $\bar{\mu}_f = 9.328\,\mathrm{mPa\,s}$.

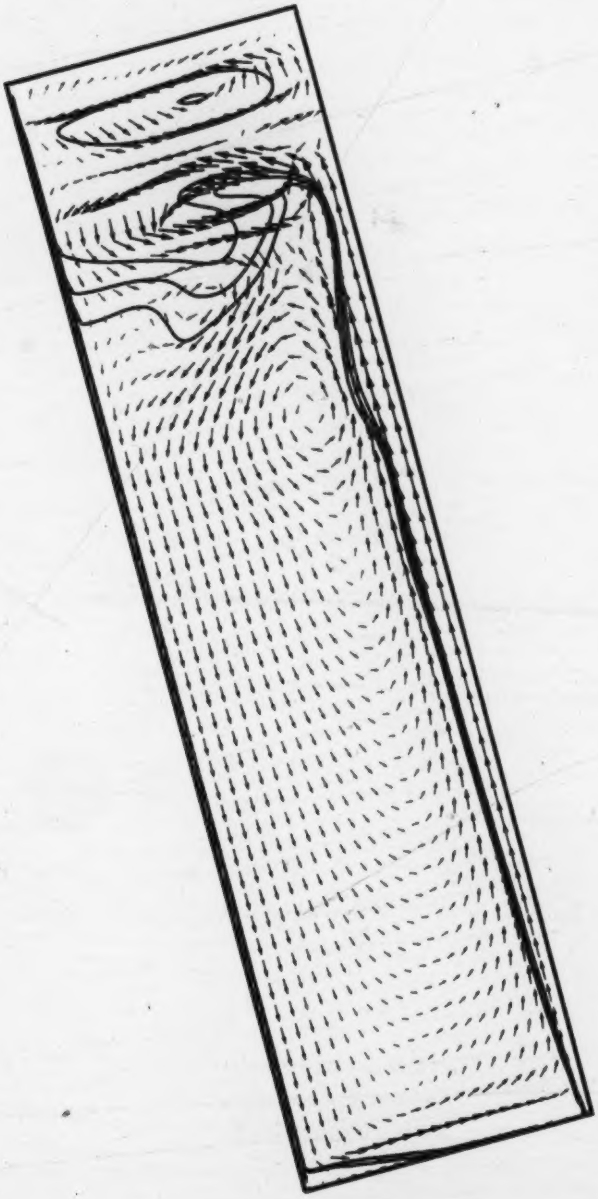

Figure 6.22: Velocity profile and concentration isolines for batch sedimentation (80×400 mesh, first order): $\hat{t} = 0.03$, $\theta = 30°$, $\bar{\mu}_f = 9.328\,\mathrm{mPa\,s}$.

6.4 Batch sedimentation of 2.678 mPa s suspension

The most noticeable feature in the 40×100 mesh non-diffusive solution shown in Figure 6.23 is the wavy suspension interface at the clear fluid slit. This wavy instability causes a gravity instability when the wave rolls over sufficiently for the more dense suspension to reside above the less dense clear fluid. Three vortices are visible above the suspension interface. These features are more visible with further mesh refinement show in Figures 6.24 - 6.26. On the 40×100 mesh the interface has a wavelength of 6 cm. With the 40×200 mesh this wavelength has dropped to 4.3 cm. On the 40×400 mesh the waves in the lower half of the vessel have wavelength 4.3 cm while there are smaller disturbances in the upper half. The fine 80×400 mesh picks up 2.1 cm wavelengths in the lower half and 2.9 cm wavelengths in the upper half. Shaqfeh & Acrivos reported small (1 - 2 cm) as well as longer wavelengths under similar conditions.

The linear stability analysis of Herbolzheimer [18] demonstrates that sedimentation flows of high Reynolds numbers are unstable to small wavelengths. The numerical simulation can only capture disturbances with a wavelength larger than the grid size. This is why only large waves were observed on the coarse 40×100 mesh. The fine mesh solution has enough spatial resolution to capture small perturbations in the suspension interface.

The first order accurate profile on the finest mesh (80×400) shown in Figure 6.27 does not capture the sharp wavy patterns observed in the non-diffusive results with the same mesh. The velocity field in the first order result does not reflect the chaotic nature of the flow observed by Shaqfeh & Acrivos.

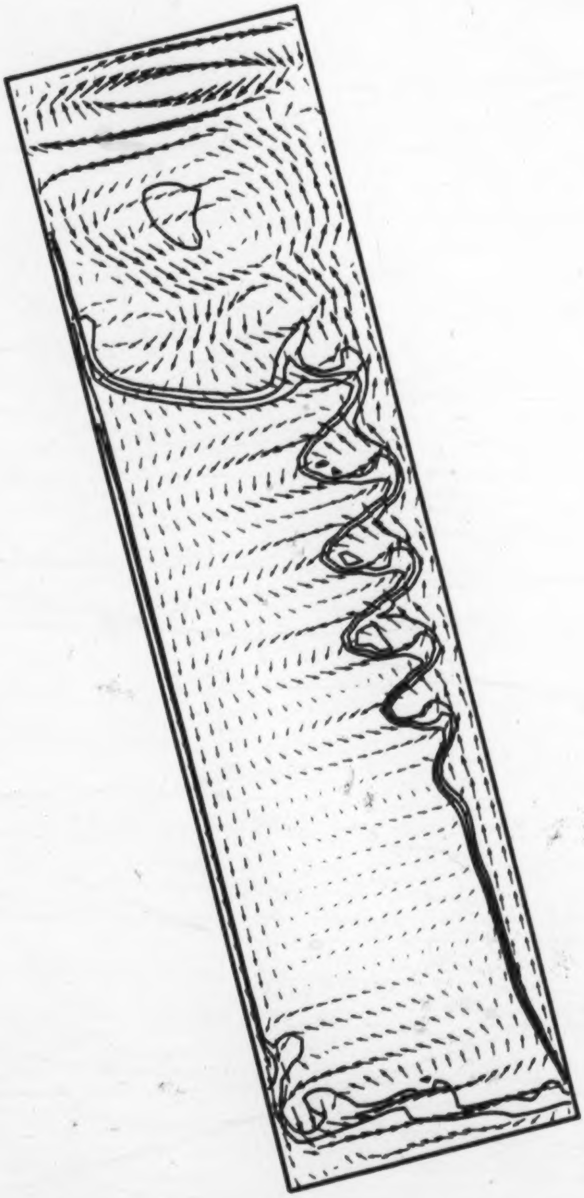

Figure 6.23: Velocity profile and concentration isolines for batch sedimentation (40 × 100 mesh, non-diffusive): $\hat{t} = 0.05$, $\theta = 30°$, $\bar{\mu}_f = 2.678\,\mathrm{mPa\,s}$.

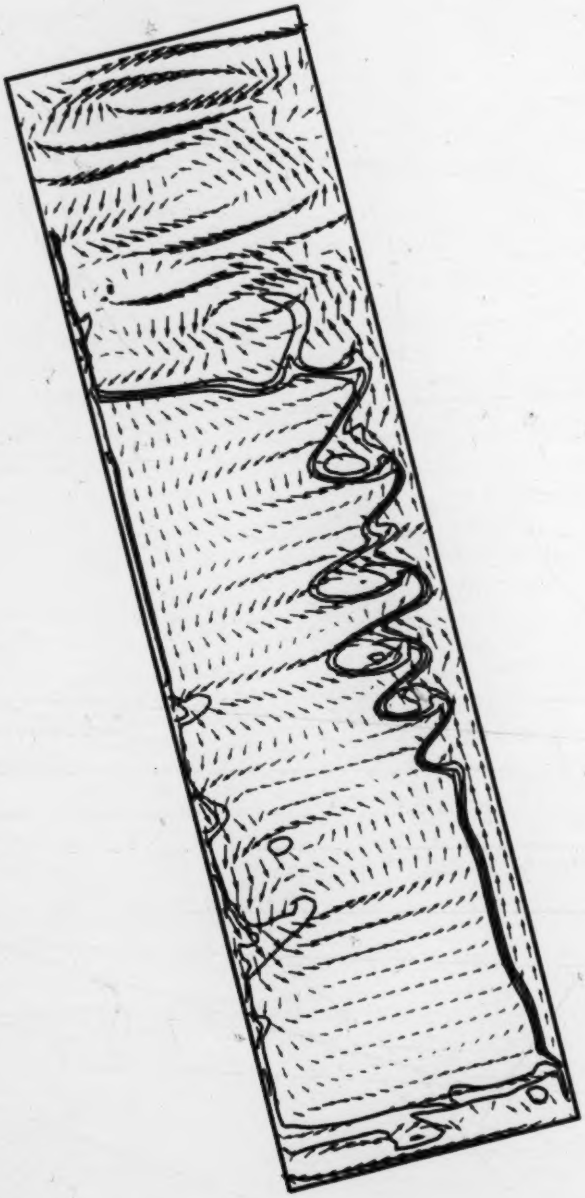

Figure 6.24: Velocity profile and concentration isolines for batch sedimentation (40 × 200 mesh, non-diffusive): $\hat{t} = 0.05$, $\theta = 30°$, $\bar{\mu}_f = 2.678\,\mathrm{mPa\,s}$.

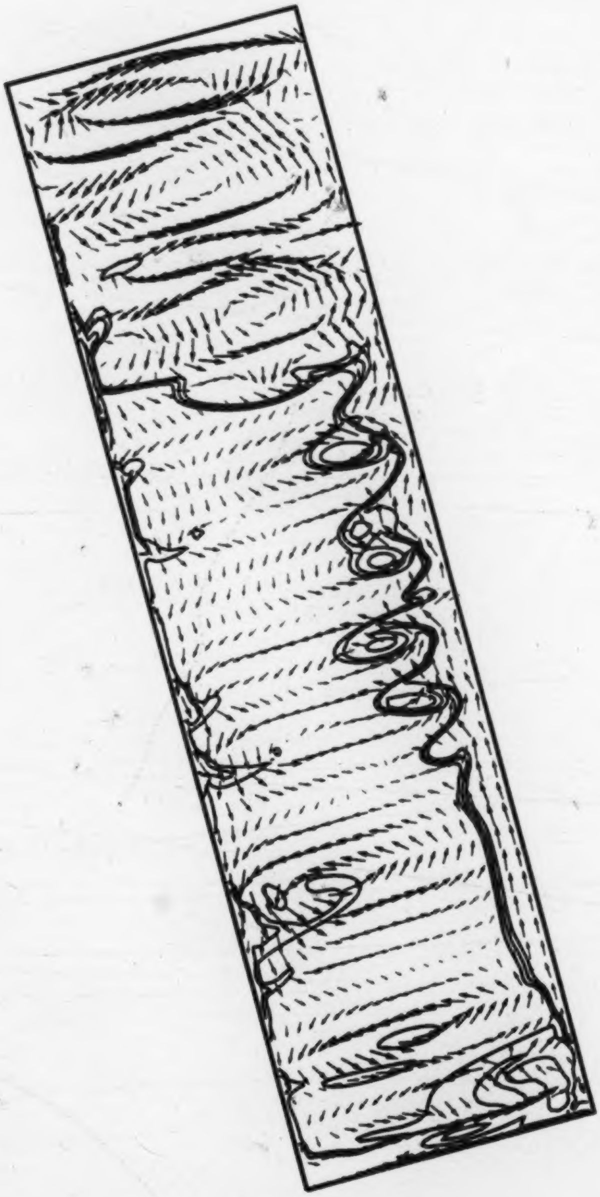

Figure 6.25: Velocity profile and concentration isolines for batch sedimentation (40 × 400 mesh, non-diffusive): $\hat{t} = 0.05$, $\theta = 30°$, $\bar{\mu}_f = 2.678\,\mathrm{mPa\,s}$.

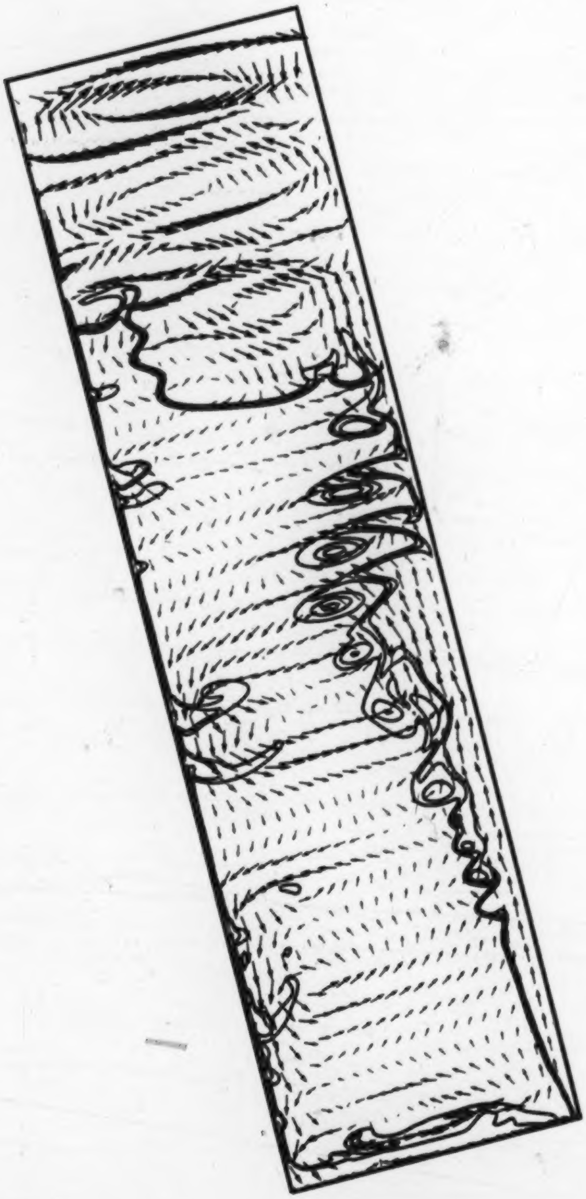

Figure 6.26: Velocity profile and concentration isolines for batch sedimentation (80 × 400 mesh, non-diffusive): $\hat{t} = 0.05$, $\theta = 30°$, $\bar{\mu}_f = 2.678\,\mathrm{mPa\,s}$.

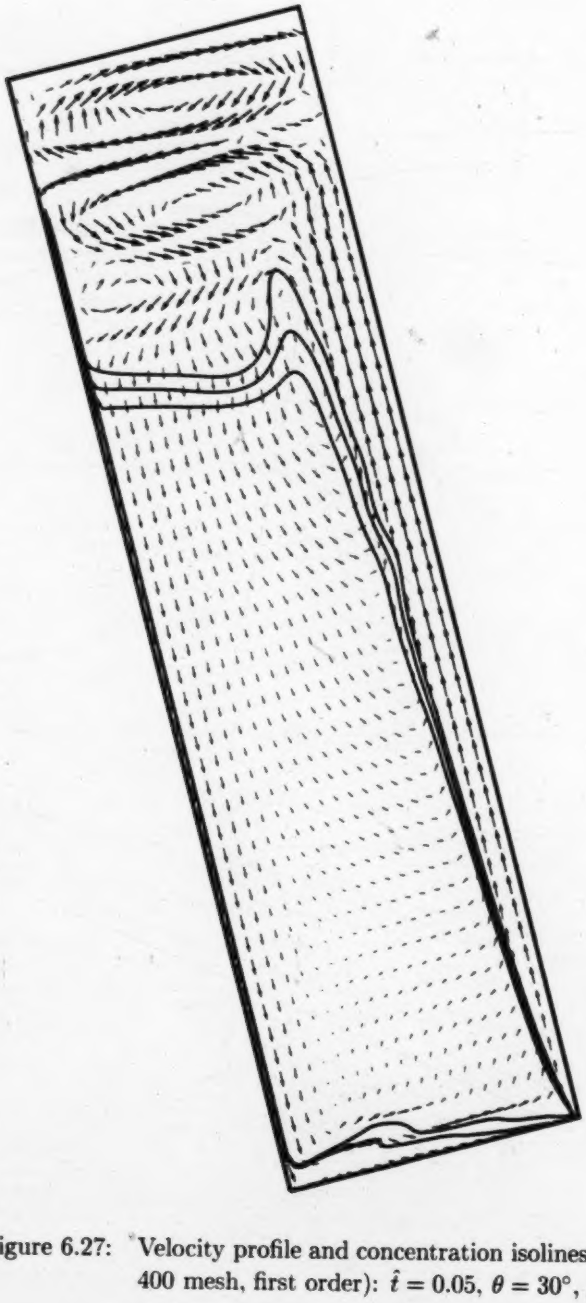

Figure 6.27: Velocity profile and concentration isolines for batch sedimentation (80 × 400 mesh, first order): $\hat{t} = 0.05$, $\theta = 30^\circ$, $\bar{\mu}_f = 2.678\,\mathrm{mPa\,s}$.

6.5 Discussion

The non-diffusive solutions on coarse meshes (40 × 100) captured the formation of interfacial waves, streams of suspension and the mixing inside an inclined sedimentation vessel. Increased grid resolution clarified these features but did not change the overall flow.

The first order solutions on the coarse 40 × 100 mesh compared well with the non-diffusive results only for the 67.7 mPa s sedimentation example. Excessive numerical diffusion dominated the solution to the vorticity transport equation for the two other examples. This is consistent with the amount of numerical diffusion associated with the first order discretization of the convective terms in the vorticity transport equation:

$$\alpha_N = \frac{\hat{v}\Delta\hat{y}}{2}(1 - N_C) \tag{6.2}$$

The real diffusivity in the vorticity transport equation is

$$\alpha_R = \frac{1}{\mathrm{Re}} \tag{6.3}$$

The longitudinal velocity $\hat{v}$ is $O(10)$ or greater in much of the sedimentation vessel. The numerical diffusion coefficients for problems with 100, 200 and 400 grid points in the longitudinal direction are 0.05, 0.025 and 0.0125, respectively. From Table 6.1 it is clear that numerical diffusion is smaller than real diffusion only for the 67.7 mPa s sedimentation examples: numerical diffusion is much larger than real diffusion for the other sedimentation examples.

Equation 6.2 also gives the amount of numerical diffusion for the first order accurate discretization of the material transport equation. The dimensional numerical diffusion coefficients for the 2.678 mPa s suspension are 2.4×10^{-4}, 1.2×10^{-4} and $6.1 \times 10^{-5}\,\mathrm{m}^2/\mathrm{s}$ for the simulations with 100, 200 and 400 vertical grid points, respectively. These numerical diffusion coefficients are four to five orders of magnitude larger than typical physical diffusion coefficients for chemicals dissolved in water ($D = O(10^{-9}\,\mathrm{m}^2/\mathrm{s})$) [36, pages 3-258 – 3-259]. First order upwind differencing models non-diffusive dispersed particles as being far more diffusive than most chemical species. The diffusive nature of the first order discretization eliminates steep volume fraction gradients at the suspension interface and reduces the driving force for the physical instability.

6.6 Summary

The non-diffusive discretization method provides accurate results for inclined plate sedimentation on coarse meshes (40 × 200) for suspensions of moderate to high viscosity

($\bar{\mu}_f > 9\,\mathrm{mPa\,s}$). Suspensions with lower viscosity are unstable to very small interface wavelengths and require a much finer mesh (80 × 400) to capture the wave growth of the unstable interface.

The non-diffusive results captured the correct wavelength of the suspension-clear fluid interface for the 9.328 and 2.678 mPa s suspensions. Numerical diffusion dominated the real diffusion in the first order accurate simulations of sedimentation of 9.328 and 2.678 mPa s suspension: these first order accurate results did not reflect the sedimentation process.

Chapter 7

Inception of waves in inclined plate sedimentation

Herbolzheimer [18, 8] measured the wave inception distance for inclined plate sedimentation in the continuous mode with a point source feed in the middle of the vessel. Three fluids were used for the continuous phase: the viscosities were 38.1, 28.8 and 18.8 mPa s and the density was $1080\,\mathrm{kg/m^3}$. The particles were glass beads with diameter $132\,\mu\mathrm{m}$ and density $2440\,\mathrm{kg/m^3}$. The apparatus was 5cm × 5cm × 100cm. Herbolzheimer notes that "... within a few centimeters from the inception point their [wave] amplitudes were comparable to the thickness of the clear-fluid layer." Herbolzheimer points out the inverse of the inception distance, $1/y_i$, is related to the growth rate of the unstable wavy interface.

Numerical results were obtained to compare the predicted wave inception point with the experimental data of Herbolzheimer [18]. This comparison tests the ability of the numerical model to capture phenomena related to the growth rate of unstable waves.

7.1 Description of the runs

Numerical results were obtained for continuous sedimentation in the bottom feed mode with 1 cm ports in the 5 cm × 100 cm vessel shown in Figure 7.1. The clear outlet rates were calculated to give suspension heights of 0.8 m according to PNK theory[1]:

$$\hat{v}_{clear} = \frac{h(\hat{\phi})}{\cos\theta}\frac{b}{w}\left(1+\frac{H}{b}\sin\theta\right) \qquad (7.1)$$

---

[1] The feed rates for the runs at 50° inclination were calculated with 0.7 m suspension height

Table 7.1: Inlet feed rate and split ratio for simulations with $\hat{\phi} = 0.05$.

θ	split ratio	$\hat{v}_{\text{clear}}$	$\hat{v}_{\text{feed}}$
5°	0.30	9.3	13.3
10°	0.30	14.8	21.2
15°	0.30	20.6	29.4
20°	0.30	26.6	38.1
30°	0.30	40.2	57.4
40°	0.30	57.0	81.4
50°	0.30	70.6	100.8

Table 7.2: Inlet feed rate and split ratio for simulations with $\theta = 20°$.

$\hat{\phi}$	split ratio	$\hat{v}_{\text{clear}}$	$\hat{v}_{\text{feed}}$
0.01	0.10	32.8	36.4
0.02	0.20	31.1	38.9
0.05	0.30	26.6	38.0
0.10	0.40	20.3	33.9
0.15	0.40	15.3	25.5

The fraction of feed diverted to the sludge outlet was set according to the feed concentration to prevent the accumulation of sediment in the bottom of the vessel. The split ratios, clear outlet velocities and feed velocities are given in Table 7.1 for the runs with $\hat{\phi} = 0.05$ and various angles and in Table 7.2 for the runs with $\theta = 20°$ and various inlet concentrations.

All simulations were performed on a 40 × 200 mesh with even grid spacing along the length and grid clustering across the width towards the vessel walls. A 40 × 200 mesh was considered to accurate enough to capture the wavy suspension interface for these suspensions of moderate viscosity.

The initial flow development was complete by $\hat{t} = 1$ and results were obtained at $\hat{t} = 2$. The wave inception point was determined by a statistical test. The location of the interface was found at every time step over the sample interval $\Delta\hat{t} = 0.1$ (roughly 5 000 points). The mean and standard deviation of the interface location was calculated for each point along the length of the vessel. For each point along the length of the vessel the wave amplitude was calculated as four standard deviations and a "comparable" thickness of the clear fluid layer was set as 0.25 of the mean thickness. Figures 7.2 and 7.3 show the onset of waves is quite sharp and the statistical test gives an accurate measure of the wave inception point.

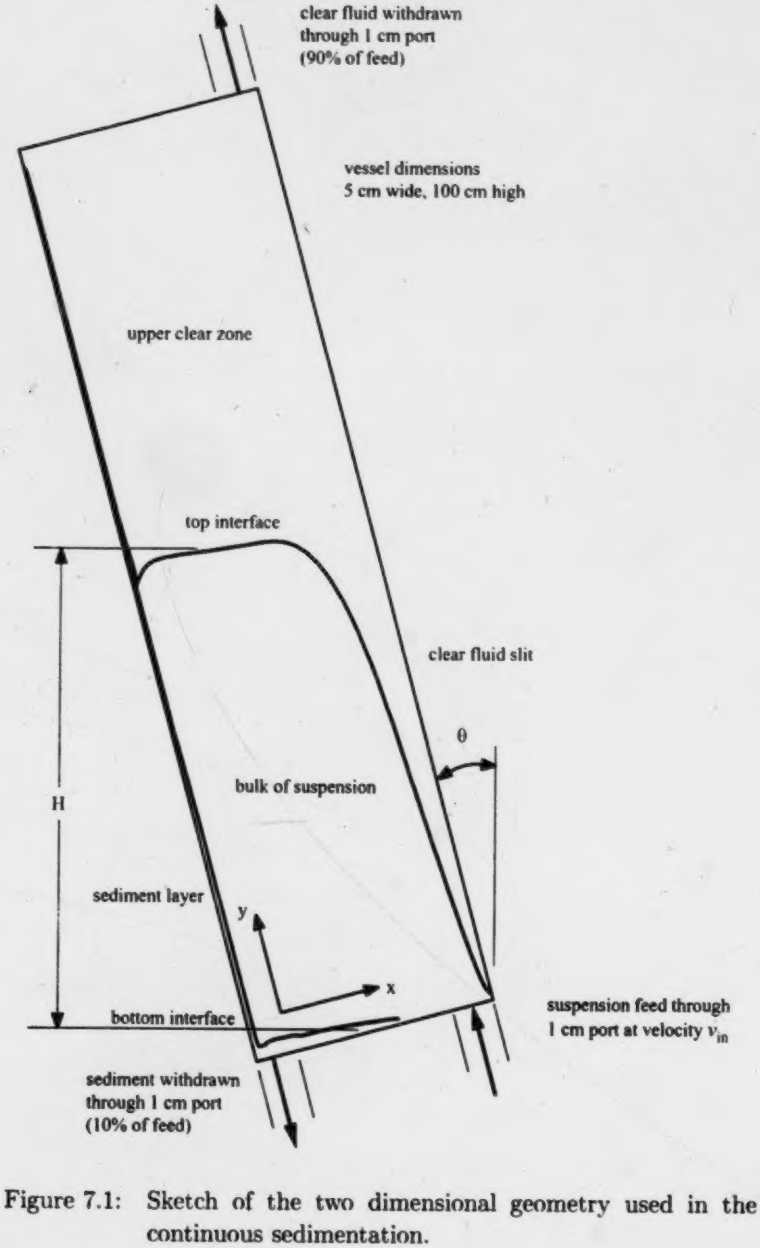
clear fluid withdrawn
through 1 cm port
(90% of feed)
vessel dimensions
5 cm wide, 100 cm high
upper clear zone
top interface
clear fluid slit
θ
bulk of suspension
H
sediment layer
y
x
bottom interface
suspension feed through
1 cm port at velocity v_{in}
sediment withdrawn
through 1 cm port
(10% of feed)

Figure 7.1: Sketch of the two dimensional geometry used in the simulations of continuous sedimentation.

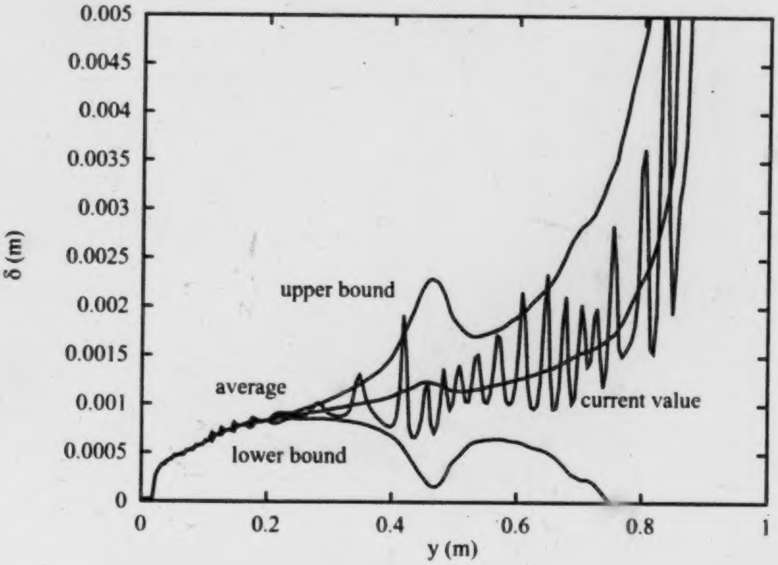

Figure 7.2: Mean and 95 % confidence limits of the position of clear fluid interface ($\hat{\phi} = 0.05$, $\theta = 5°$, $\bar{\mu}_f = 18.8\,\mathrm{mPa\,s}$).

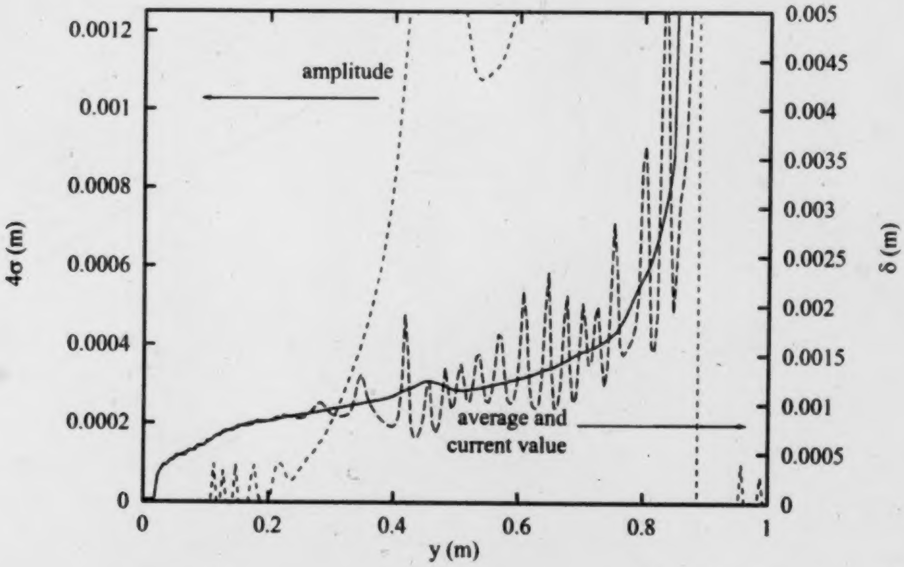

Figure 7.3: Statistical comparison of the wave amplitude with 25 % of the mean clear fluid thickness ($\hat{\phi} = 0.05$, $\theta = 5°$, $\bar{\mu}_f = 18.8\,\mathrm{mPa\,s}$).

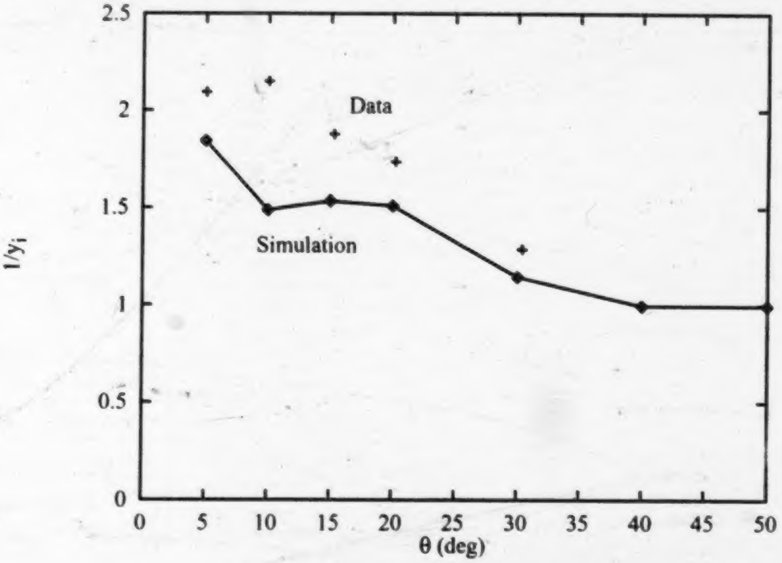

Figure 7.4: Inverse of the inception distance for $\hat{\phi} = 0.05$, $\bar{\mu}_f = 38.1\,\mathrm{mPa\,s}$: ◇ denotes the numerical simulation; + denotes the experimental data of Herbolzheimer [18].

7.2 Effect of inclination angle on inception distance

Numerical simulations were carried out for suspensions with $\hat{\phi} = 0.05$ and viscosities of 38.1, 28.8 and 18.8 mPa s. Figures 7.4 - 7.6 show the inverse of the inception distances obtained by the numerical simulations were in general, smaller than those measured by Herbolzheimer [18] but showed the same trends. The maximum value of L/y_i occurred near $\theta = 10°$ and decreased with increasing angle. The inverse of the inception distance (and hence the wave growth rate) increased with decreasing fluid viscosity.

Figures 7.7 - 7.16 show the flow patterns and the suspension interface with concentration isolines at $\hat{\phi} = 0.02, 0.025$ and 0.03. Two large well defined vortices are visible in Figure 7.7 for the 38.1 mPa s suspension tilted at 10°. This feature is similar to the the multicellular patterns discussed in Chapter 6 with the $\hat{\phi} = 0.10$ and $\bar{\mu}_f = 67.7\,\mathrm{mPa\,s}$. There is thorough mixing in the upper clear zone and the suspension interface is quite fuzzy indicated by the distances between the concentration isolines. The flow pattern in Figure 7.8 shows the upper interface is sharper for 15° inclination than for 10° inclination. At 20° inclination the upper interface is sharper than for 15° and the two vortices in the bulk of the suspension are weaker.

The suspension interface for the 28.8 mPa s suspension is broader than that of the

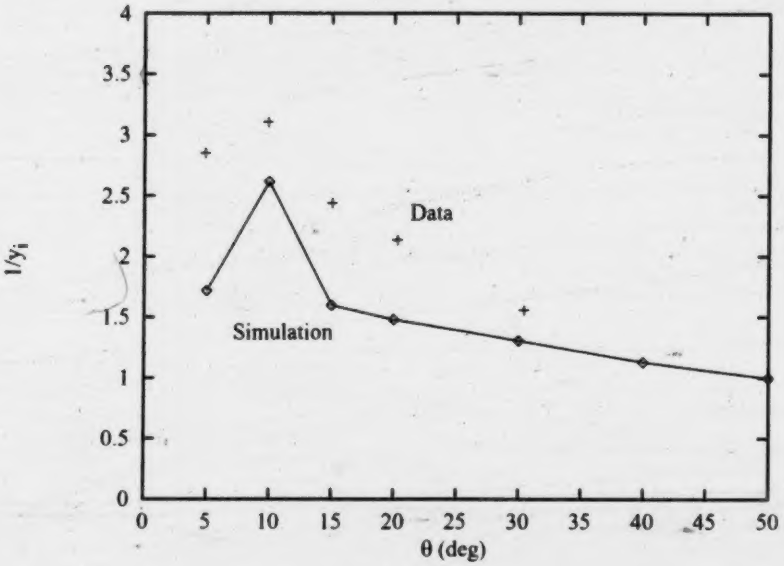

Figure 7.5: Inverse of the inception distance for $\hat{\phi} = 0.05$, $\bar{\mu}_f = 28.8\,\mathrm{mPa\,s}$: ⋄ denotes the numerical simulation; + denotes the experimental data of Herbolzheimer [18].

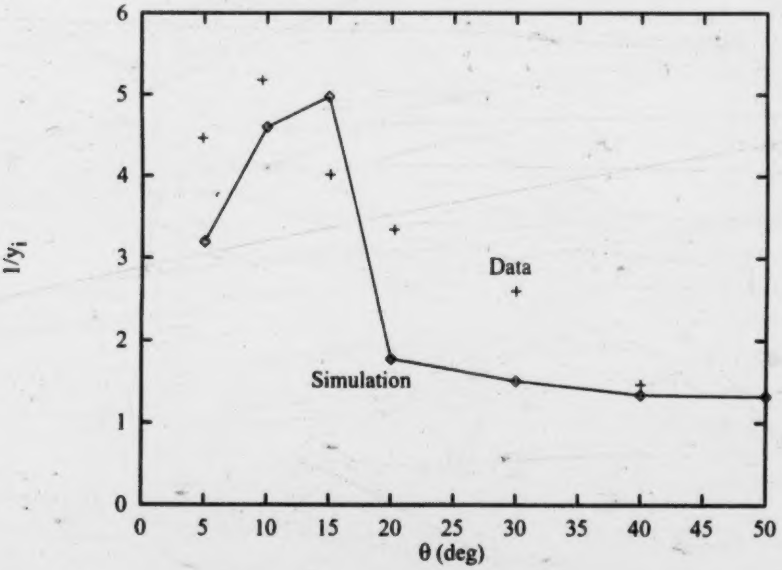

Figure 7.6: Inverse of the inception distance for $\hat{\phi} = 0.05$, $\bar{\mu}_f = 18.8\,\mathrm{mPa\,s}$: ⋄ denotes the numerical simulation; + denotes the experimental data of Herbolzheimer [18].

38.1 mPa s suspension at 10° inclination seen in Figure 7.10. The well mixed zone at the top of the vessel has extended into the bulk of the suspension. The two vortices in the bottom half of the vessel are lower than their positions on the 38.1 mPa s suspension. The well mixed zone occupies smaller portions of the vessel as the inclination is increased to 10° and 15° shown in Figures 7.11 and 7.12.

Figure 7.13 shows the flow pattern for the 18.8 mPa s suspension at 10° inclination is much different than the previous patterns. The well mixed zone occupies the entire length of the sedimentation vessel and there are no well defined vortices. The suspension interface becomes wavy near the bottom of the vessel. Two different flow patterns were observed for 15° inclination. Figure 7.14 is well mixed and has a broad upper suspension interface similar to Figure 7.13 for 10° inclination. The other flow pattern is more stable. The well mixed zone in Figure 7.15 is confined to the upper portion of the sedimentation vessel and there are two smooth vortices in the bulk of the suspension. The wave inception point is near the top of the clear fluid slit. This flow profile is similar to that of 20° inclination shown in Figure 7.16. The well mixed zone occupies the upper portion of the vessel and two smooth vortices occupy the lower portion. The wave inception point is near the top of the clear fluid slit.

The results for the 18.8 mPa s suspension suggest there are two distinct flow patterns for inclined plate sedimentation. One is uniform and is associated with the wave inception point near the top of the clear fluid slit. The other is well-mixed and the wave inception point is near the bottom of the vessel. The transition from the uniform to the well-mixed flow pattern is associated with the increased wave growth rate near 10° inclination.

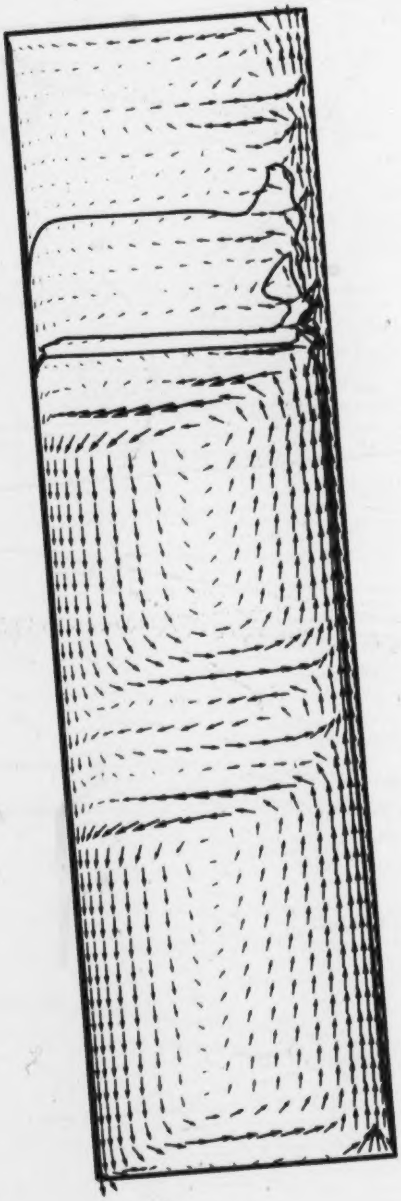

Figure 7.7: Flow pattern for $\hat{\phi} = 0.05$, $\bar{\mu}_f = 38.1\,\mathrm{mPa\,s}$, $\theta = 10°$.

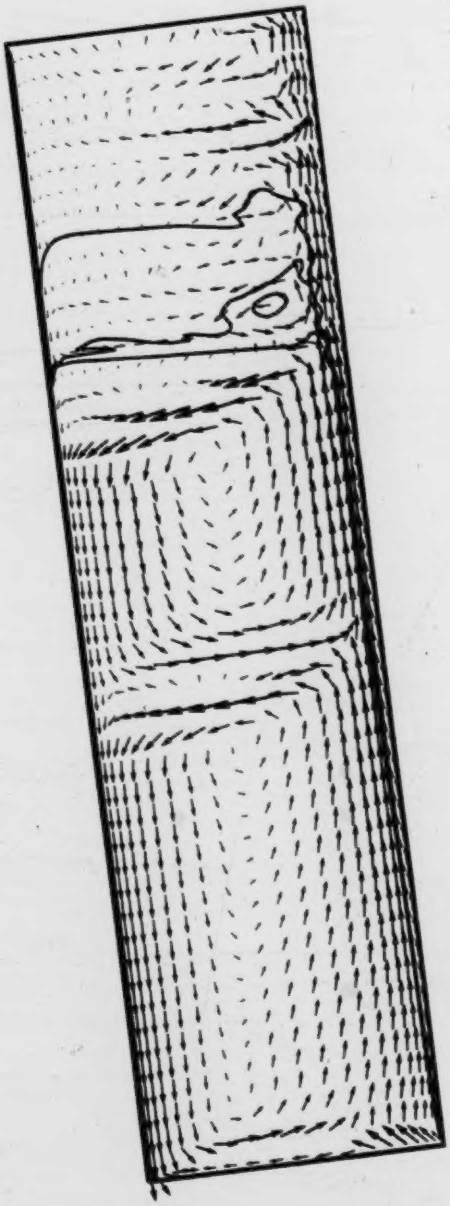

Figure 7.8: Flow pattern for $\hat{\phi} = 0.05$, $\bar{\mu}_f = 38.1\,\mathrm{mPa\,s}$, $\theta = 15°$.

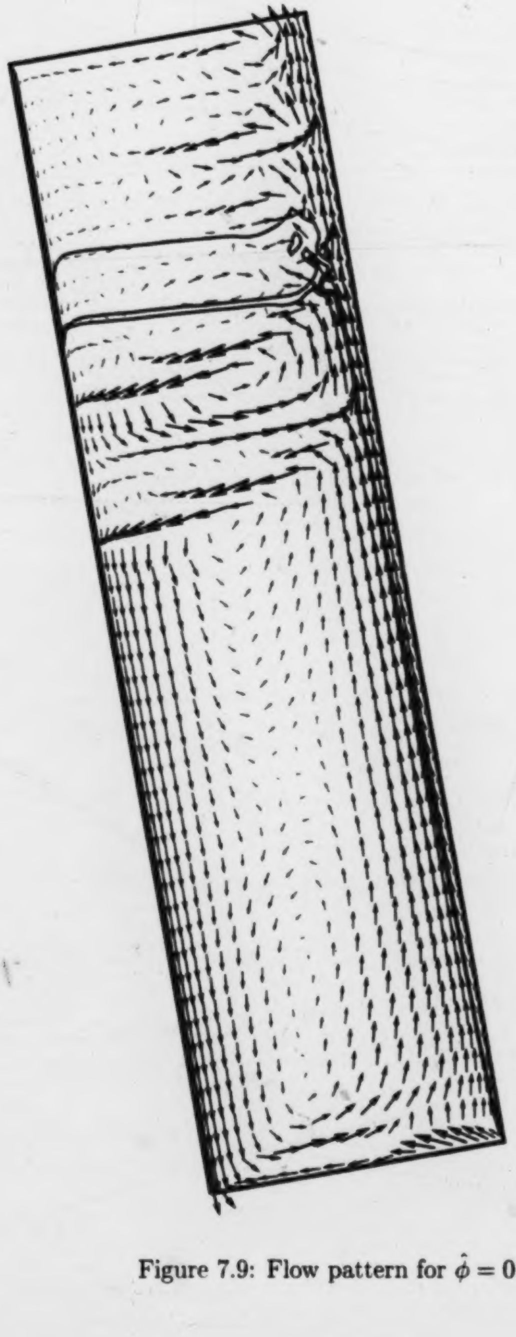

Figure 7.9: Flow pattern for $\hat{\phi} = 0.05$, $\bar{\mu}_f = 38.1\,\mathrm{mPa\,s}$, $\theta = 20°$.

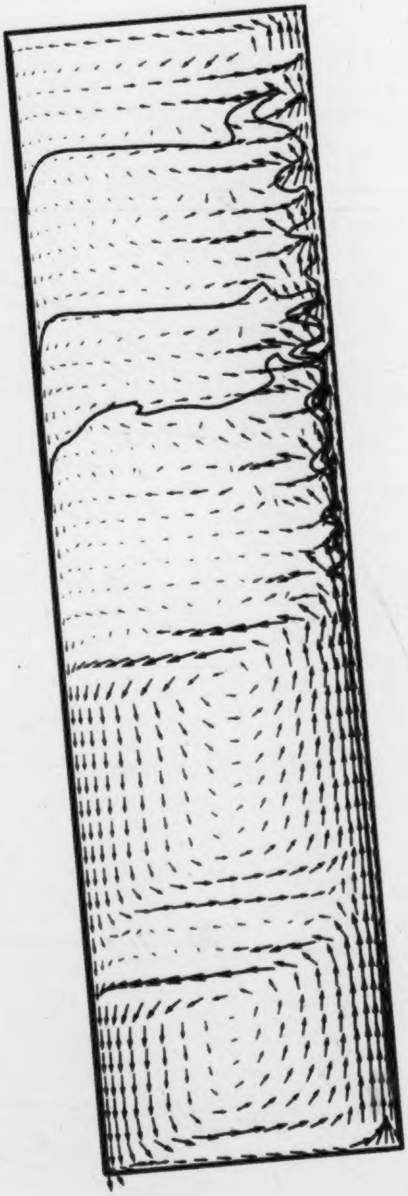

Figure 7.10: Flow pattern for $\hat{\phi} = 0.05$, $\bar{\mu}_f = 28.8\,\mathrm{mPa\,s}$, $\theta = 10°$.

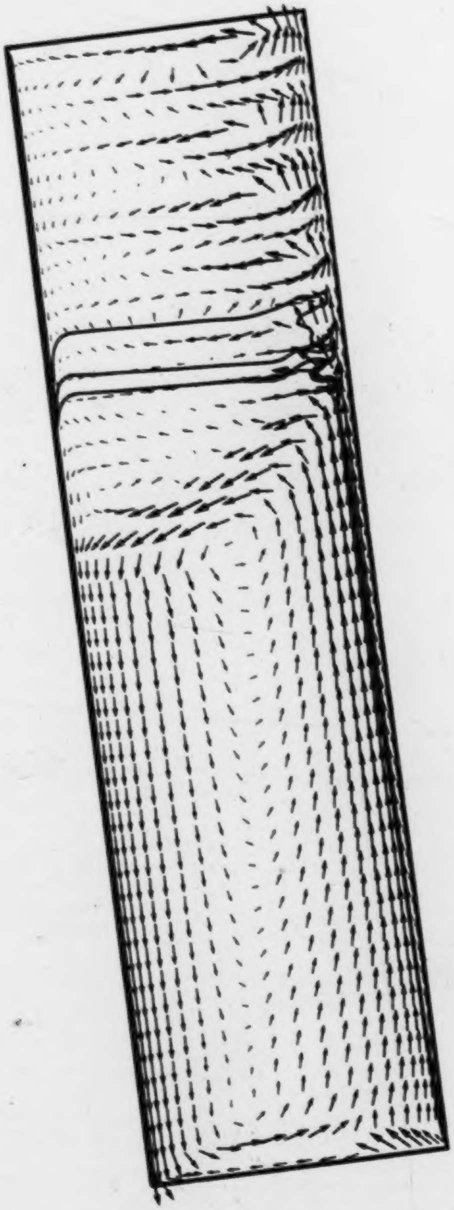

Figure 7.11: Flow pattern for $\hat{\phi} = 0.05$, $\bar{\mu}_f = 28.8\,\mathrm{mPa\,s}$, $\theta = 15°$.

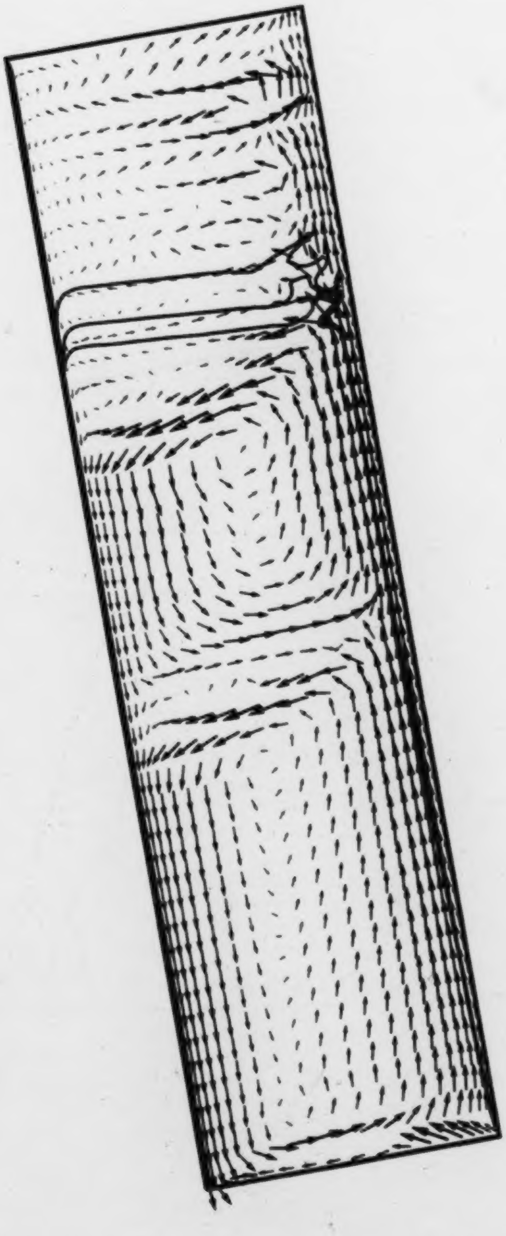

Figure 7.12: Flow pattern for $\hat{\phi} = 0.05$, $\bar{\mu}_f = 28.8\,\mathrm{mPa\,s}$, $\theta = 20°$.

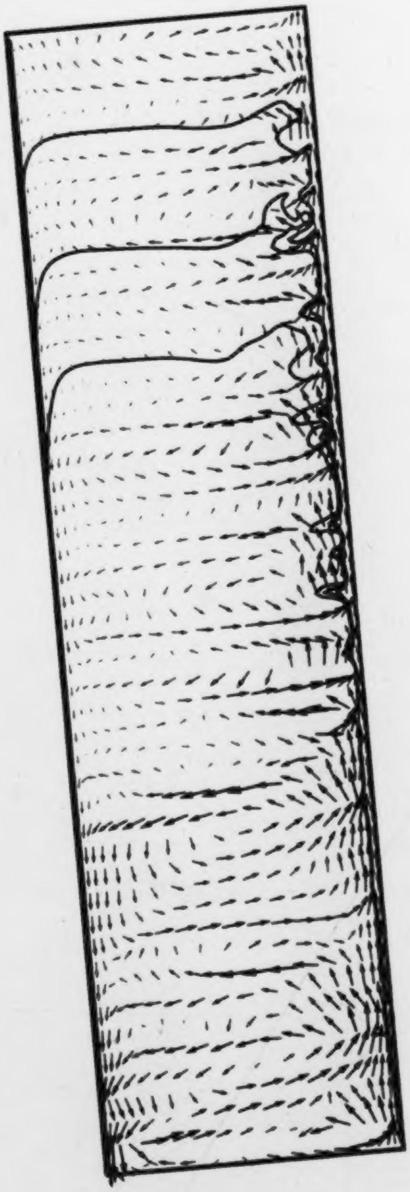

Figure 7.13: Flow pattern for $\hat{\phi} = 0.05$, $\bar{\mu}_f = 18.8\,\mathrm{mPa\,s}$, $\theta = 10°$.

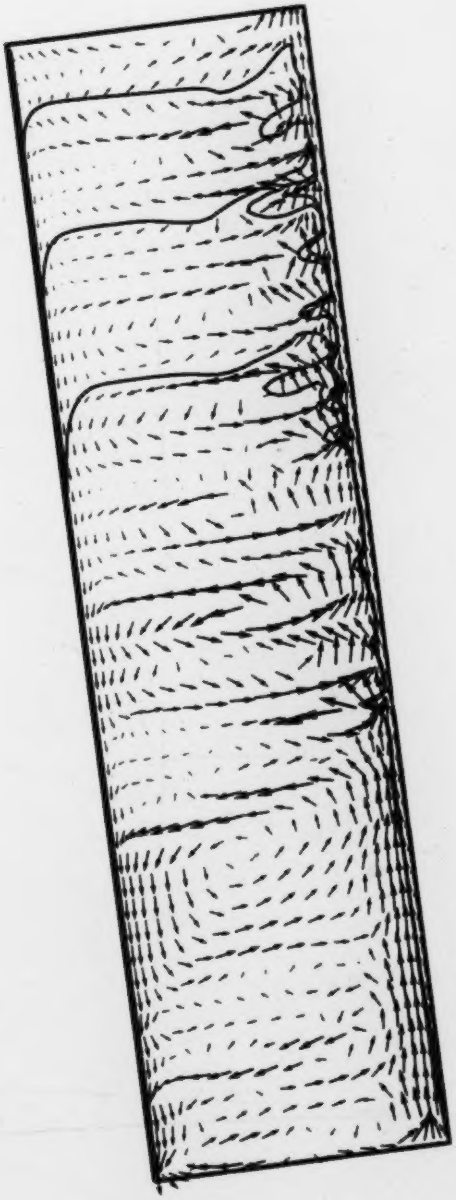

Figure 7.14: Well mixed flow pattern for $\hat{\phi} = 0.05$, $\bar{\mu}_f = 18.8\,\mathrm{mPa\,s}$, $\theta = 15°$.

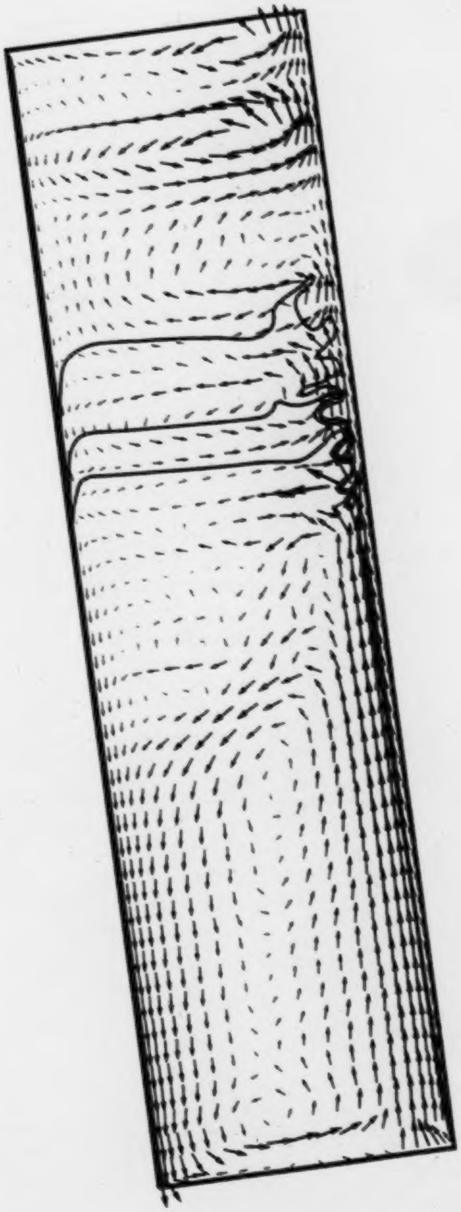

Figure 7.15: Uniform flow pattern for $\hat{\phi} = 0.05$, $\bar{\mu}_f = 18.8\,\mathrm{mPa\,s}$, $\theta = 15°$.

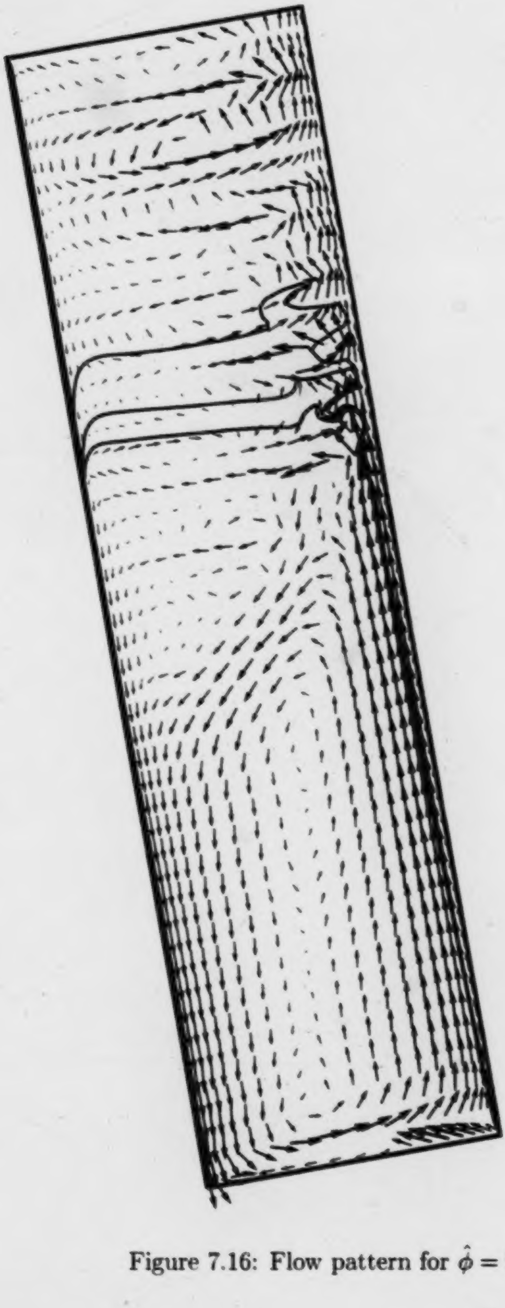

Figure 7.16: Flow pattern for $\hat{\phi} = 0.05$, $\bar{\mu}_f = 18.8\,\mathrm{mPa\,s}$, $\theta = 20°$.

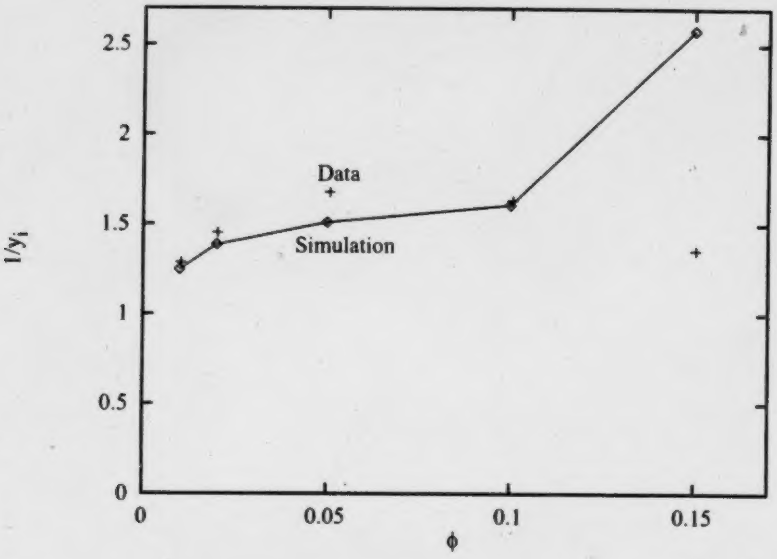

Figure 7.17: Inverse of the inception distance for $\theta = 20°$, $\bar{\mu}_f = 38.1\,\mathrm{mPa\,s}$: ⋄ denotes the numerical simulation; + denotes the experimental data of Herbolzheimer [18].

7.3 Effect of concentration on inception distance

Simulations were performed at various concentrations and 20° inclination. Figures 7.17 - 7.19 show the inverse of the inception point obtained from the numerical simulation increases with concentration. The numerical results show the same general trend as the experimental data of Herbolzheimer: the inverse inception distance increases with the dispersed phase concentration and decreasing viscosity. The 38.1 mPa s suspensions showed the best agreement with experimental data except for the result at $\hat{\phi} = 0.15$. The simulation results shown in Figure 7.19 for the 18.8 mPa s suspensions did not agree with the experimental data as well as those for the 38.1 mPa s suspensions. The simulations with the 18.8 mPa s suspensions under-predicted the inverse inception distances for $\hat{\phi} \leq 0.05$ and over-predicted the inverse inception distances for $\hat{\phi} = 0.10$ and 0.15. The poor agreement between the simulation results and experimental results for large concentrations suggests the constant viscosity or Boussinesq approximations are not valid for these concentrations.

Figure 7.20 shows the well mixed region occupies the upper portion of the settling device and two large vortices fill the bulk of the suspension for the 38.8 mPa s suspension with $\hat{\phi} = 0.10$. At $\hat{\phi} = 0.15$ the well mixed region in Figure 7.21 occupies a larger portion of the vessel and the two vortices at the bottom are noticeably smaller.

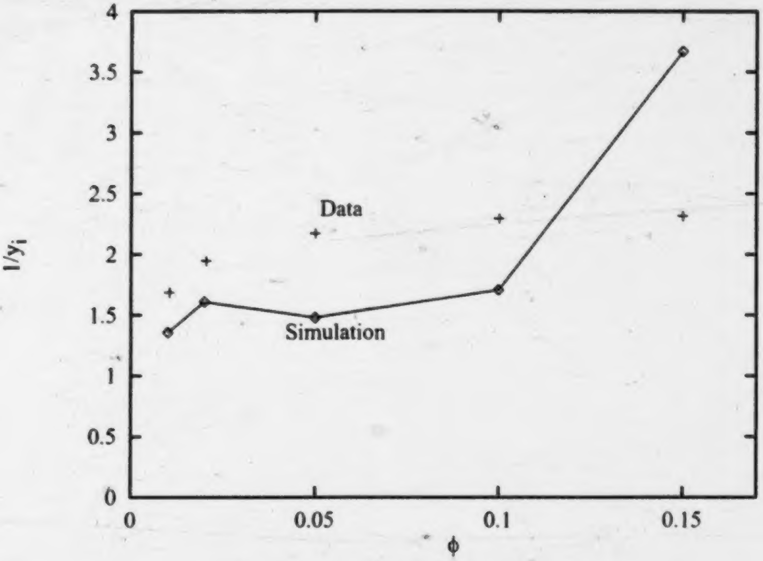

Figure 7.18: Inverse of the inception distance for $\theta = 20°$, $\bar{\mu}_f = 28.8\,\mathrm{mPa\,s}$: $\diamond$ denotes the numerical simulation; + denotes the experimental data of Herbolzheimer [18].

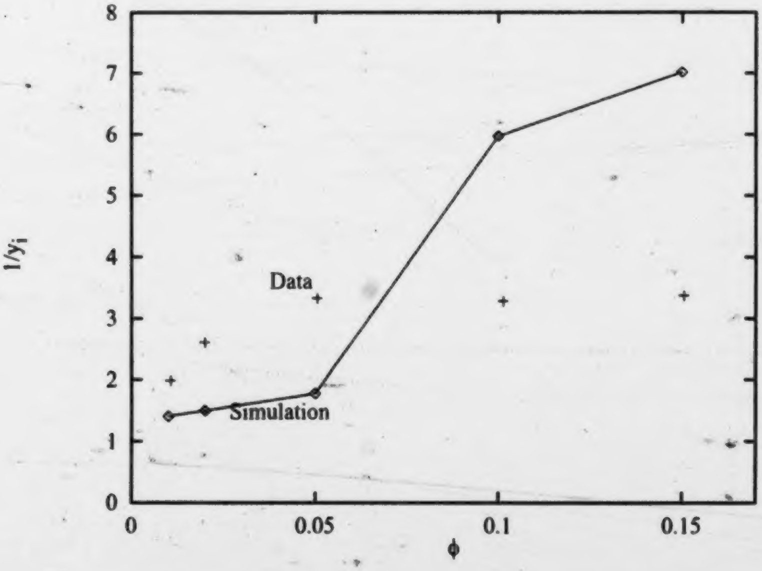

Figure 7.19: Inverse of the inception distance for $\theta = 20°$, $\bar{\mu}_f = 18.8\,\mathrm{mPa\,s}$: $\diamond$ denotes the numerical simulation; + denotes the experimental data of Herbolzheimer [18].

The transition from the uniform to well mixed flow pattern with increased dispersed phase concentration is depicted well in Figures 7.22 and 7.23 for the 28.8 mPa s suspension.

This transition moved to lower concentrations for the 18.8 mPa s runs. The flow pattern in Figure 7.16 is fairly uniform in the bulk of the 5 % suspension while Figure 7.24 shows the vessel is thoroughly mixed for $\hat{\phi} = 0.10$.

The experimental data of Herbolzheimer do not indicate the transition from the uniform to the well mixed flow patterns with increased concentration as predicted by the numerical simulation. One reason for the discrepancy may be the difference in the geometry: the simulations used a bottom feed while the experiments of Herbolzheimer used a point source feed in the center of the vessel. The flow surrounding the point source feed is irrotational. This may suppress the formation of small vortices apparent in the simulations where the bulk of the suspension is well mixed.

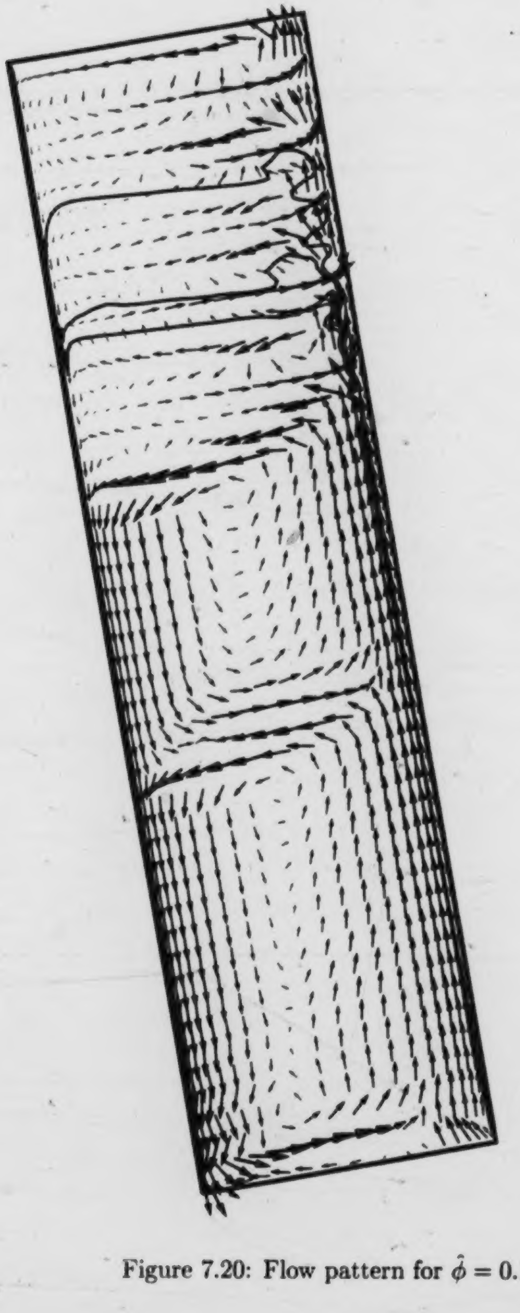

Figure 7.20: Flow pattern for $\hat{\phi} = 0.10$, $\bar{\mu}_f = 38.1\,\mathrm{mPa\,s}$, $\theta = 20°$.

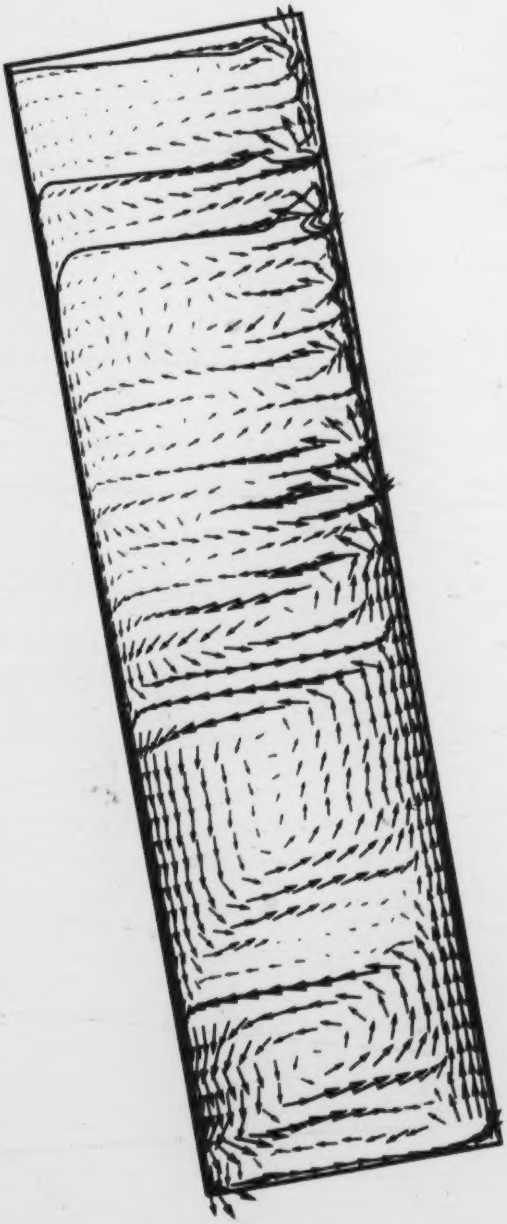

Figure 7.21: Flow pattern for $\hat{\phi} = 0.15$, $\bar{\mu}_f = 38.1\,\mathrm{mPa\,s}$, $\theta = 20°$.

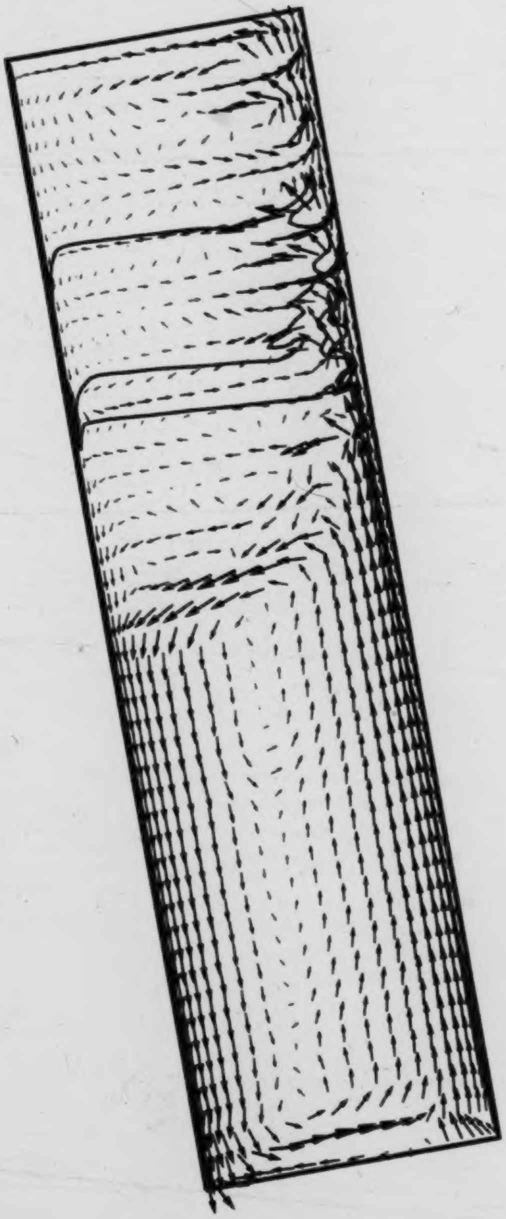

Figure 7.22: Flow pattern for $\hat{\phi} = 0.10$, $\bar{\mu}_f = 28.8\,\mathrm{mPa\,s}$, $\theta = 20°$.

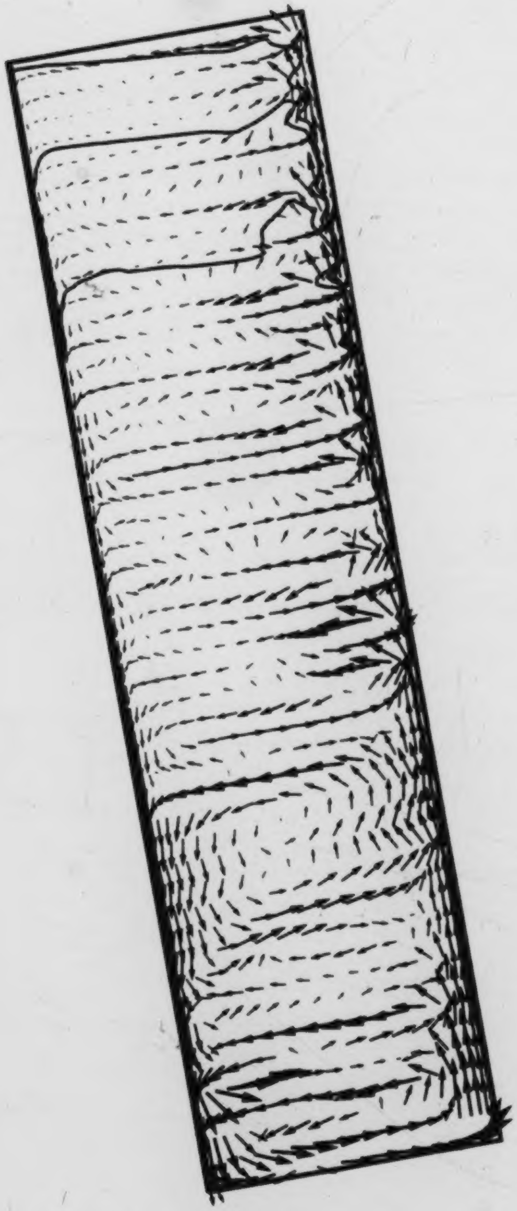

Figure 7.23: Flow pattern for $\hat{\phi} = 0.15$, $\bar{\mu}_f = 28.8\,\mathrm{mPa\,s}$, $\theta = 20°$.

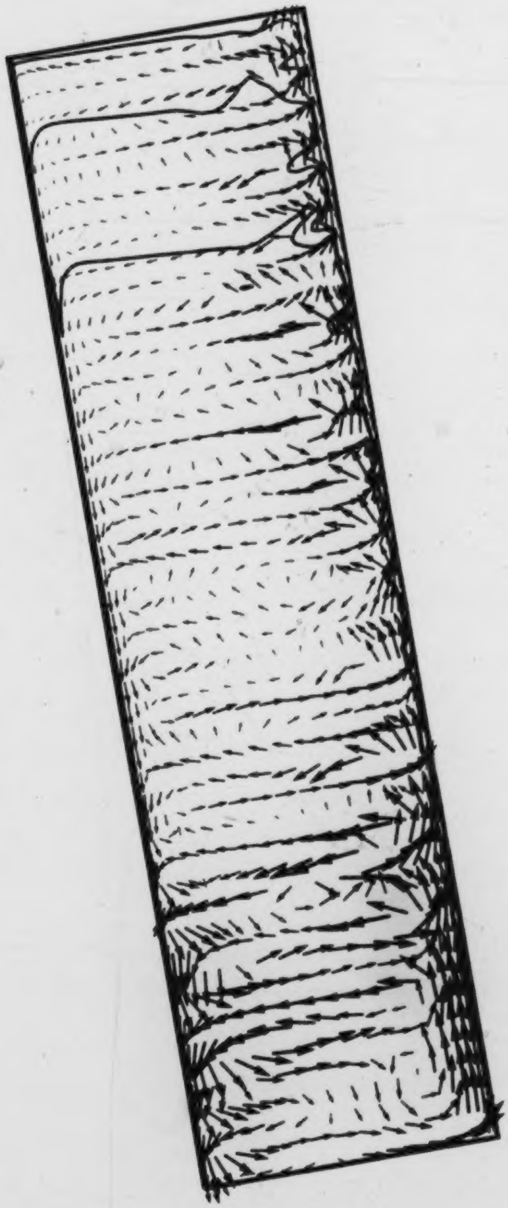

Figure 7.24: Flow pattern for $\hat{\phi} = 0.10$, $\bar{\mu}_f = 18.8\,\mathrm{mPa\,s}$, $\theta = 20°$.

7.4 Comparison of the wave amplitude growth rates

Herbolzheimer [18] suggests the wave inception point is related to the amplitude growth rate α by

$$\frac{1}{y_i - y_c} = -\frac{1}{\ln W}\left(\frac{\phi_0}{h(\phi_0)\tan\theta}\right)^{1/3}\left(\frac{\alpha}{\delta}\right)_{Ave} \tag{7.2}$$

W is the factor by which a disturbance must grow to become visible. y_c is the point at which the wave becomes visible and is negligible compared to the inception distance y_i. Equation 7.2 suggests

$$y_i\alpha = \text{constant} \tag{7.3}$$

The wave inception distances obtained from the experimental data and the numerical simulations are then related by

$$(y_i)_E(\alpha)_E = (y_i)_N(\alpha)_N \tag{7.4}$$

where the subscripts E and N denote the values from the experimental data and the numerical simulations. The fractional deviation of the growth rate determined from the numerical simulation and the experimental data is defined to be ϵ where $(\alpha)_N = \alpha_E(1+\epsilon)$. This fractional deviation is obtained from Equation 7.4

$$\epsilon = \frac{(y_i)_E}{(y_i)_N} - 1 \tag{7.5}$$

Figure 7.25 shows the numerical simulation under-predicted most of the wave growth rates by 10 - 40 % for suspensions with $\hat{\phi} = 0.05$ and various angles. The closest matches were for the most viscous suspension.

Larger deviations between the numerical results and the experimental data are apparent in Figure 7.26 for suspensions at 20° inclination and various concentrations. The agreement between the simulation results and experimental data improved with increasing viscosity for $\hat{\phi} \leq 0.05$. At larger concentrations the simulation over-predicts the growth rate by 50 - 100 %. This corresponds to the transition from the uniform to the well mixed flow patterns in the sedimentation vessel.

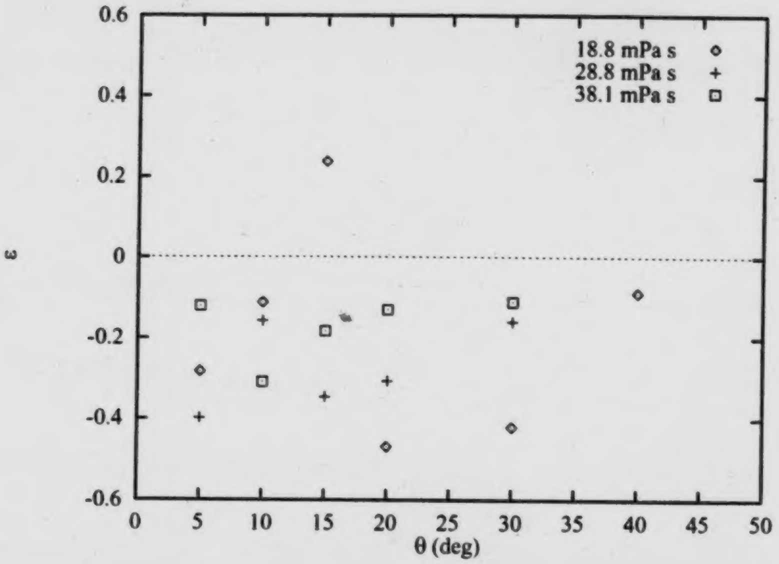

Figure 7.25: Fractional deviation of the wave growth rate between the numerical simulation and the experimental data for $\hat{\phi} = 0.05$: ◇ is 18.8 mPa s; + is 28.8 mPa s; □ is 38.1 mPa s.

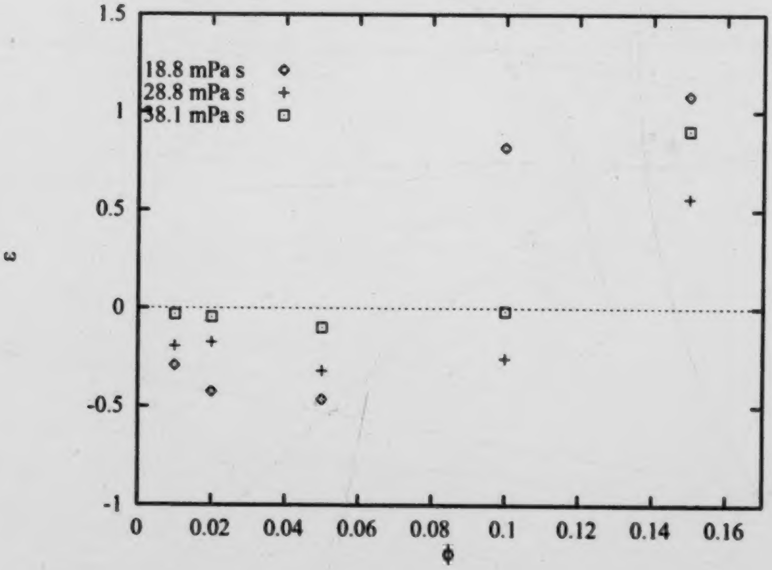

Figure 7.26: Fractional deviation of the wave growth rate between the numerical simulation and the experimental data for $\theta = 20°$: ◇ is 18.8 mPa s; + is 28.8 mPa s; □ is 38.1 mPa s.

7.5 Summary

Quantitative comparisons were made between the numerical results and detailed experimental data for the inception point of unstable waves. Good agreement with the inverse inception distances measured by Herbolzheimer [18] for $\hat{\phi} = 0.05$ confirms the numerical simulation captures the proper growth rate of the wavy interface. The wave growth rates obtained by the numerical simulation were estimated to be within 50 % of the experimental values. Poorer agreement in the wave inception point at higher concentrations may be attributed to the accuracy of the physical model (constant viscosity and Boussinesq approximations) or differences in the geometry used in the numerical simulations and the experimental apparatus.

Experimental data are required to confirm the transition from the uniform to well-mixed flow patterns as predicted by the numerical simulation for inclined plate sedimentation in the bottom feed mode.

Chapter 8

Sedimentation with a uniform internal resistance to motion

A parameter study of inclined plate sedimentation was performed where the motion is retarded by a uniform resistance proportional to the mixture velocity. Numerical results for the wave inception point were compared with the results with no resistance obtained in the previous chapters.

8.1 Uniform resistance term

The Darcy-Brinkman equation was used to model a uniform internal resistance that is proportional to velocity:

$$\rho\left(\frac{\partial \boldsymbol{u}}{\partial t} + \boldsymbol{u}\cdot\nabla\boldsymbol{u}\right) = -\nabla p + \mu\nabla^2\boldsymbol{u} - \rho\boldsymbol{g} - \frac{\mu}{k}\boldsymbol{u} \tag{8.1}$$

The permeability k is constant. The convection terms have been retained in Equation 8.1.

The permeability k is expressed in terms of an equivalent wall separation s: this analogy is that used to relate flow through porous media to flow in a Hele-Shaw cell of thickness s.

$$k = \frac{s^2}{12} \tag{8.2}$$

The uniform resistance term is incorporated in the dimensionless vorticity transport equation:

$$\hat{\rho}\left(\frac{\partial\hat{\omega}}{\partial\hat{t}} + \frac{\partial(\hat{u}\hat{\omega})}{\partial\hat{x}} + \frac{\partial(\hat{v}\hat{\omega})}{\partial\hat{y}}\right) = -\frac{\Gamma}{\mathrm{Fr}}\left(\frac{\partial\hat{\phi}}{\partial\hat{x}}\theta_y - \frac{\partial\hat{\phi}}{\partial\hat{y}}\theta_x\right) + \frac{1}{\mathrm{Re}}\left(\frac{\partial^2\hat{\omega}}{\partial\hat{x}^2} + \frac{\partial^2\hat{\omega}}{\partial\hat{y}^2}\right) - \frac{12}{\mathrm{Re}}\left(\frac{L}{s}\right)^2\hat{\omega} \tag{8.3}$$

It is clear from Equation 8.3 that uniform internal resistance acts as a sink of vorticity: this will tend to straighten the flow. It is hypothesized that internal resistance will suppress the formation of wavy structures at the suspension/clear fluid interface. This should increase the efficiency and throughput of an inclined plate sedimentation device.

The internal resistance term makes the discretized vorticity transport equation 8.3 stiff. A Crank-Nicolson discretization of the resistance term was used to discretized this term.

A parameter study was carried out to compare the flow profiles and wave inception points for equivalent wall separations of 50, 20, 15, 10, 7 and 5 mm to the numerical results obtained earlier for infinite equivalent wall separation. Results were also obtained for a 10.0 mPa s suspension to extend the parameter study to suspensions with more unstable waves.

8.2 Dependance of batch sedimentation rate on equivalent wall separation

The batch settling curves in Figures 8.1 and 8.2 for no internal resistance show a slow initial falling rate followed by a higher rate. This trend was observed in the experimental data of Oliver & Jenson [34]. The addition of internal resistance to motion increases the sedimentation rate up to $\hat{t} = 0.25$ for 10° inclination. Internal resistance has little influence on the sedimentation rate for $\hat{t} > 0.25$. A similar trend is observed in Figure 8.2 for 30° inclination: the initial sedimentation rate ($\hat{t} < 0.1$) was increased by internal resistance to motion.

The flow pattern for batch sedimentation at 10° inclination and infinite equivalent wall separation shown in Figure 8.3 is well mixed in the entire vessel. The addition of internal resistance to flow with 20 mm equivalent wall separation made the flow pattern uniform in the lower part of the suspension seen in Figure 8.4. There is less mixing in the upper portion of the suspension compared to the flow pattern with infinite equivalent wall separation. This trend is repeated with batch sedimentation at 30° inclination shown in Figures 8.5 and 8.6. At this inclination the addition of internal resistance to flow moved the wave inception point from roughly one third of the vessel length to half of the vessel length.

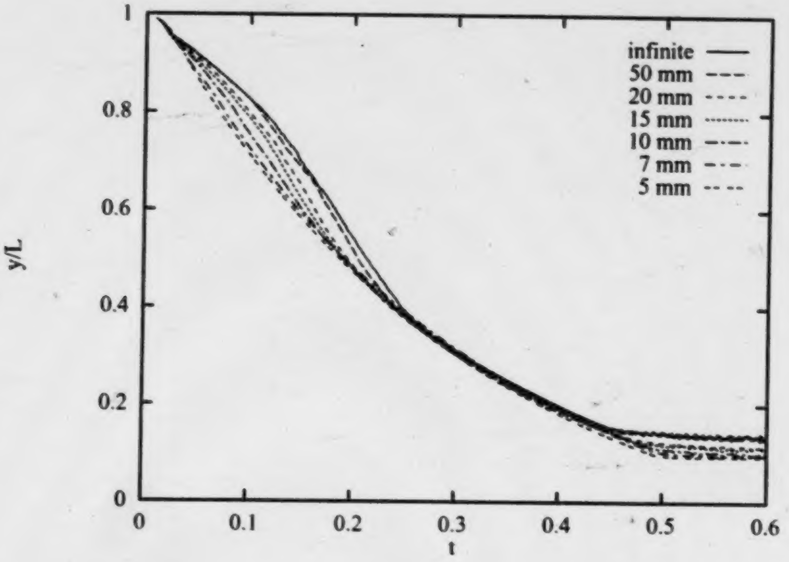

Figure 8.1: Horizontal interface height for batch sedimentation with $\bar{\mu}_f$ = 18.8 mPa s, $\phi = 0.05$, $\theta = 10°$

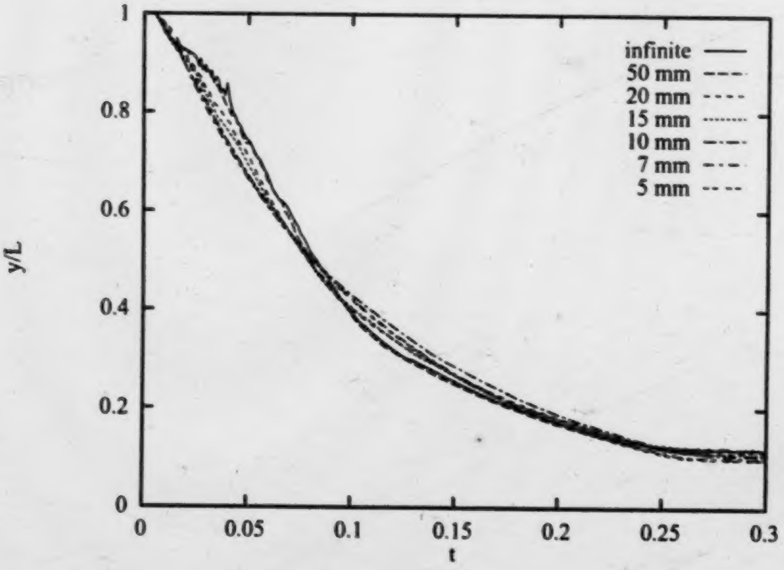

Figure 8.2: Horizontal interface height for batch sedimentation with $\bar{\mu}_f$ = 18.8 mPa s, $\phi = 0.05$, $\theta = 30°$

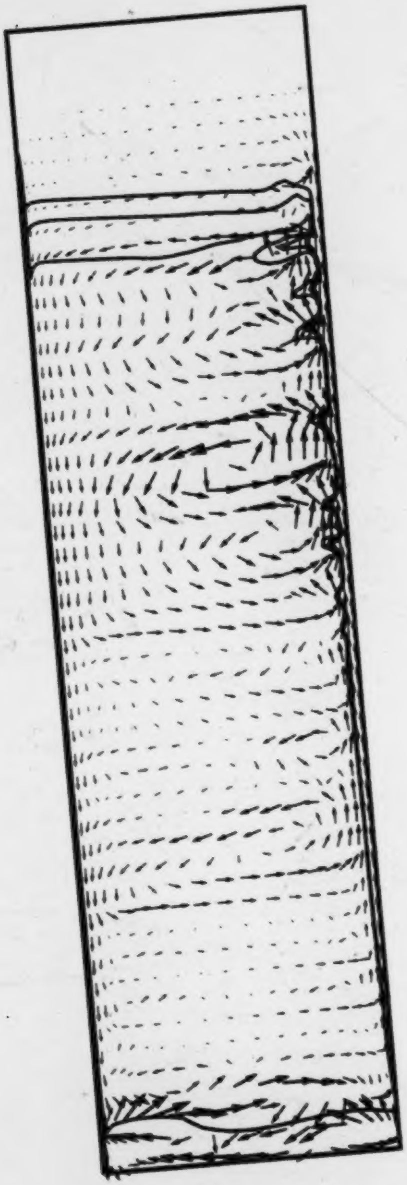

Figure 8.3: Flow pattern for batch sedimentation at $t = 0.1$ with $\phi = 0.05$, $\bar{\mu}_f = 18.8\,\mathrm{mPa\,s}$, $\theta = 10°$ and no internal resistance to motion.

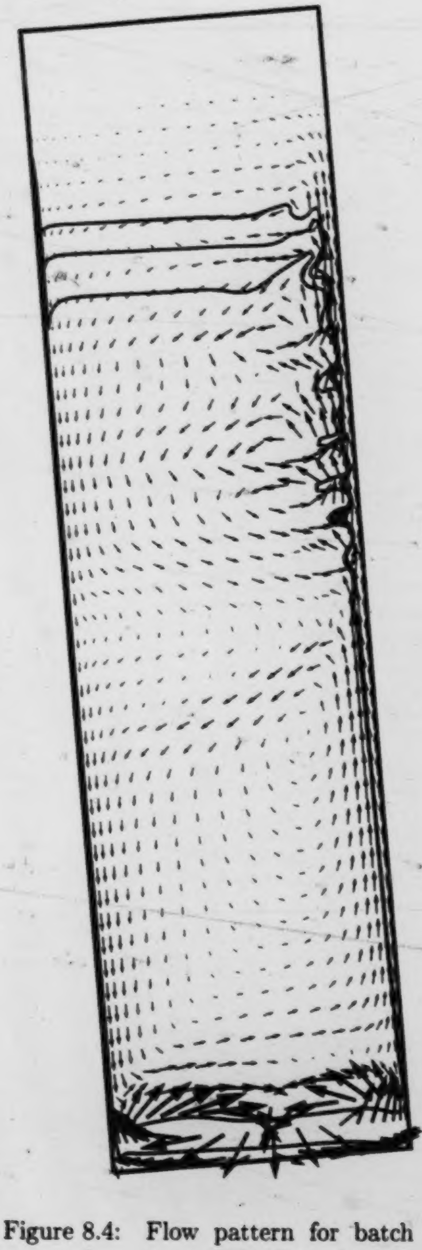

Figure 8.4: Flow pattern for batch sedimentation at $t = 0.1$ with $\phi = 0.05$, $\bar{\mu}_f = 18.8\,\mathrm{mPa\,s}$, $\theta = 10°$ and 20 mm equivalent wall separation.

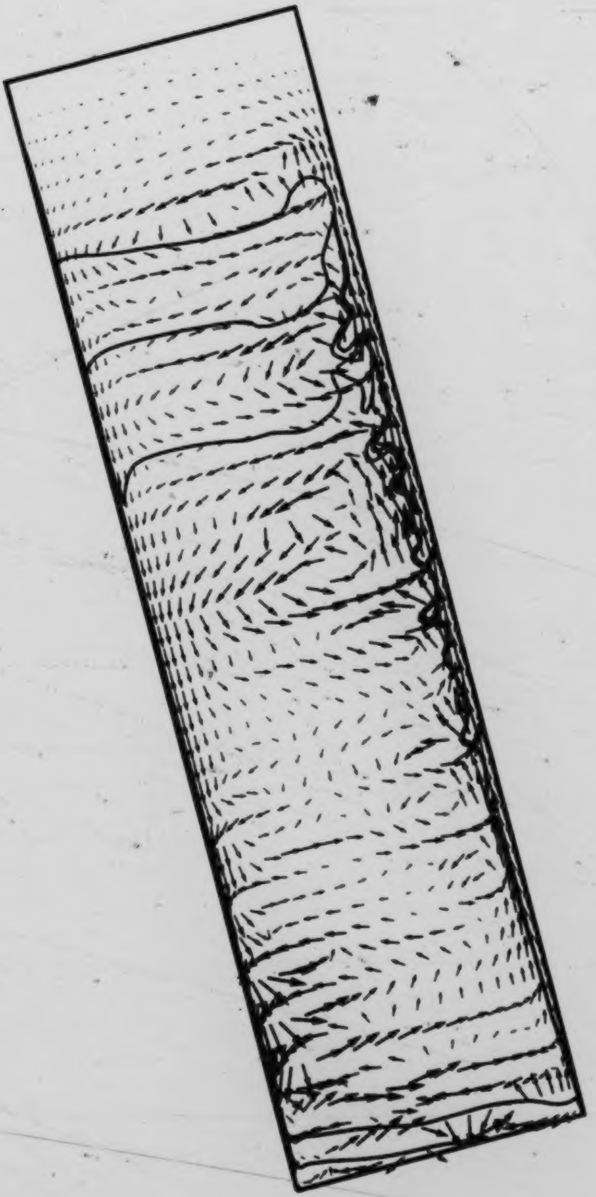

Figure 8.5: Flow pattern for batch sedimentation at $t = 0.05$ with $\phi = 0.05$, $\bar{\mu}_f = 18.8\,\mathrm{mPa\,s}$, $\theta = 30°$ and no internal resistance to motion.

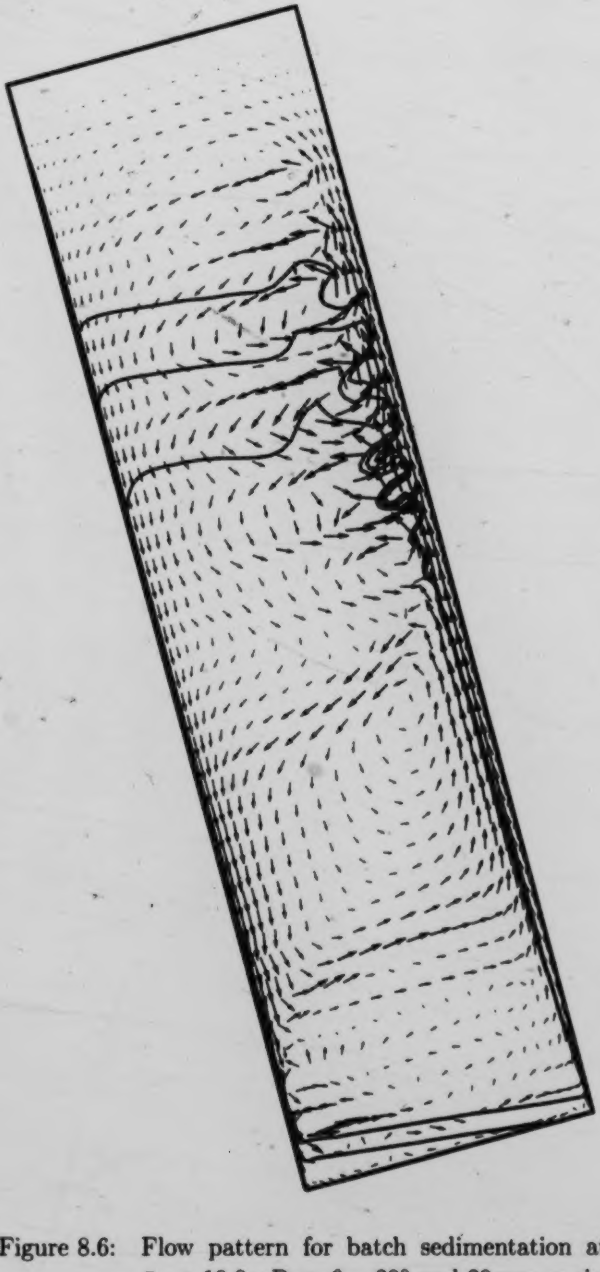

Figure 8.6: Flow pattern for batch sedimentation at $t = 0.05$ with $\phi = 0.05$, $\bar{\mu}_f = 18.8\,\mathrm{mPa\,s}$, $\theta = 30°$ and 20 mm equivalent wall separation.

8.3 Dependance of inverse inception distance on internal resistance and fluid viscosity

Figure 8.7 shows a large decrease in the inverse inception distance (or wave growth rate) for the 18.8 mPa s suspension with 50 mm equivalent wall separation ($L/s = 20$). Equation 7.5 for the wave growth rate suggests the wave growth rate for the 50 mm equivalent wall separation is 53 % of that for no internal resistance. The inverse inception distance continues to decrease with decreasing equivalent wall separation (increasing internal resistance) until waves are not detected along the length of the vessel ($L/s = 200, L/y_i = 1$).

There was little change in the inception point for the 28.8 mPa s suspension where the equivalent wall spacing was changed from infinite to 50 mm and a noticeable change where the equivalent wall separation was further reduced to 20 mm: the growth rate at this plate separation was 69 % of that for no internal resistance to motion. The suspension interface was stabilized completely with 7 mm equivalent wall separation ($L/s = 143$).

Figure 8.7 suggests that 50 mm equivalent wall separation increased the wave growth rate and destabilized the flow for the 38.1 mPa s suspension. However there is some scatter in the numerical results for the inverse inception distance: it is believed the inverse inception distance for the case with no internal resistance should be similar to that with 50 mm equivalent wall spacing. The inverse inception distances with $L/s > 20$ for the 38.1 mPa s suspension followed the same trend as the data for the 28.8 and 18.8 mPa s suspensions.

Figures 8.8 – 8.13 show the effect of decreased equivalent wall separation (increased internal resistance) on the velocity field in the sedimentation vessel. The well mixed pattern seen with no internal resistance is replaced by a more uniform pattern of large weak vortices in the bulk of the suspension for 20 mm equivalent wall separation. The strength of the vortices is lower for $s = 15$ mm. At 10 mm equivalent wall spacing the vortices in the bulk of the suspension have almost disappeared and are replaced by a uniform velocity profile similar to that in porous media. A portion of the feed short-circuits to the bottom outlet. Small vortices are visible near the top of the clear fluid slit for 7 mm equivalent wall separation. No waves are present where the equivalent wall separation is reduced to 5 mm.

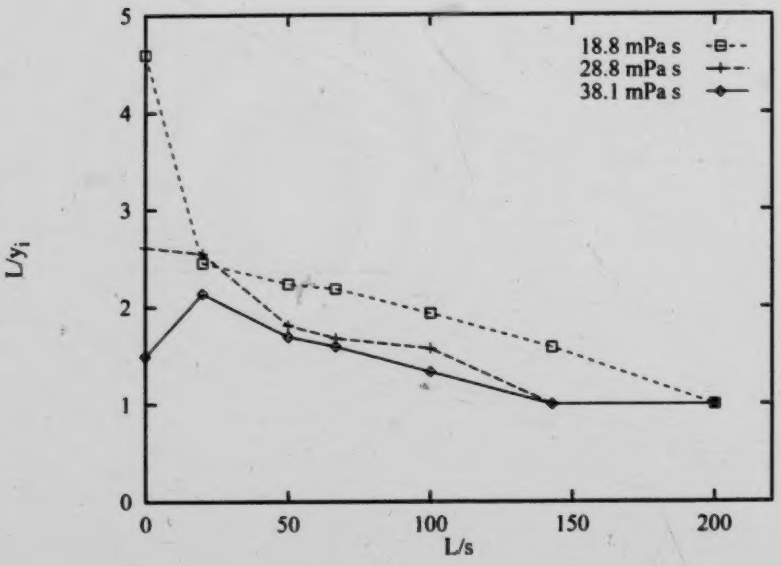

Figure 8.7: Dependance of the inverse of the inception distance on equivalent wall separation for $\phi = 0.05$, $\theta = 10°$: ◇ is 18.8 mPa s; + is 28.8 mPa s; □ is 38.1 mPa s.

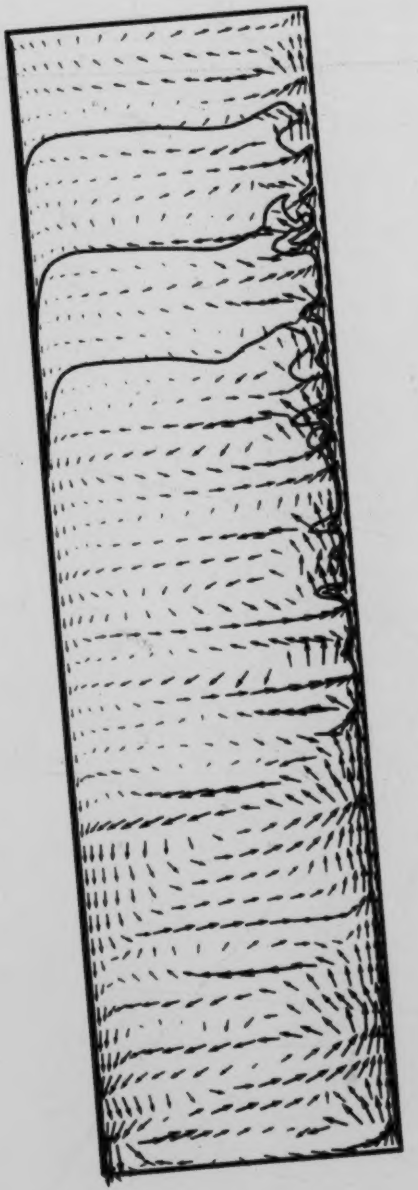

Figure 8.8: Flow pattern for $\phi = 0.05$, $\bar{\mu}_f = 18.8\,\mathrm{mPa\,s}$, $\theta = 10°$ and infinite equivalent wall separation.

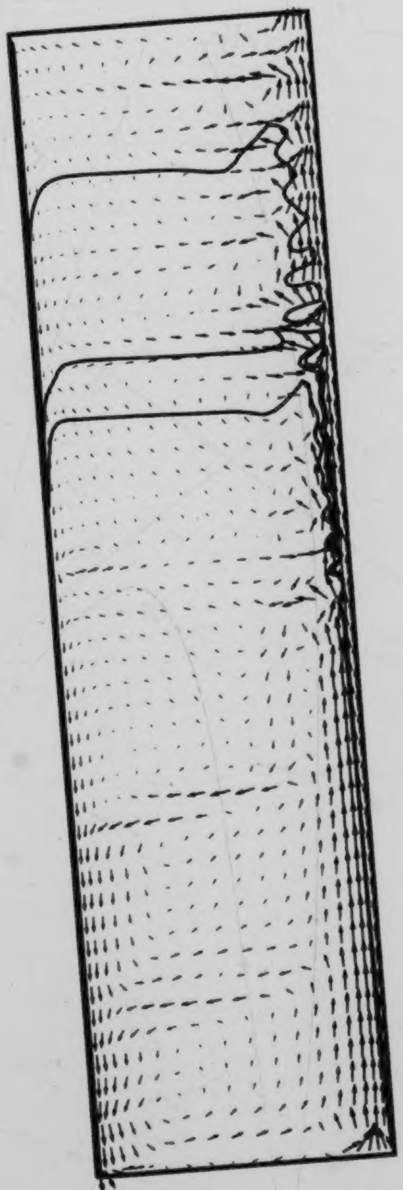

Figure 8.9: Flow pattern for $\phi = 0.05$, $\bar{\mu}_f = 18.8\,\mathrm{mPa\,s}$, $\theta = 10°$ and 20 mm equivalent wall separation.

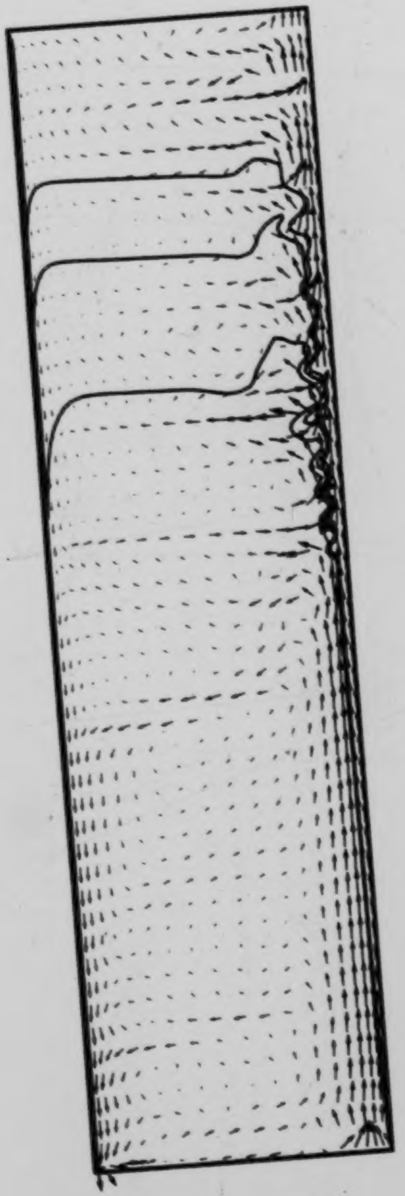

Figure 8.10: Flow pattern for $\phi = 0.05$, $\bar{\mu}_f = 18.8\,\mathrm{mPa\,s}$, $\theta = 10°$ and 15 mm equivalent wall separation.

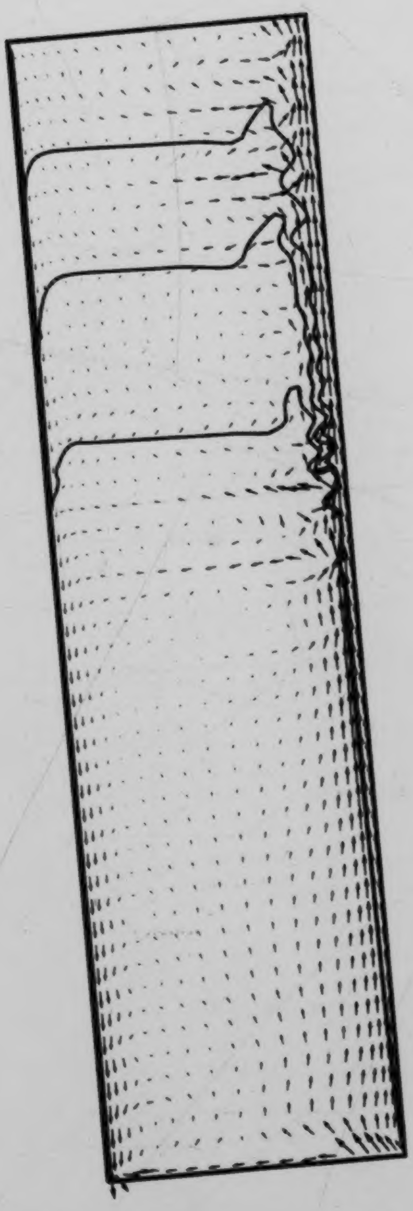

Figure 8.11: Flow pattern for $\phi = 0.05$, $\bar{\mu}_f = 18.8\,\mathrm{mPa\,s}$, $\theta = 10°$ and 10 mm equivalent wall separation.

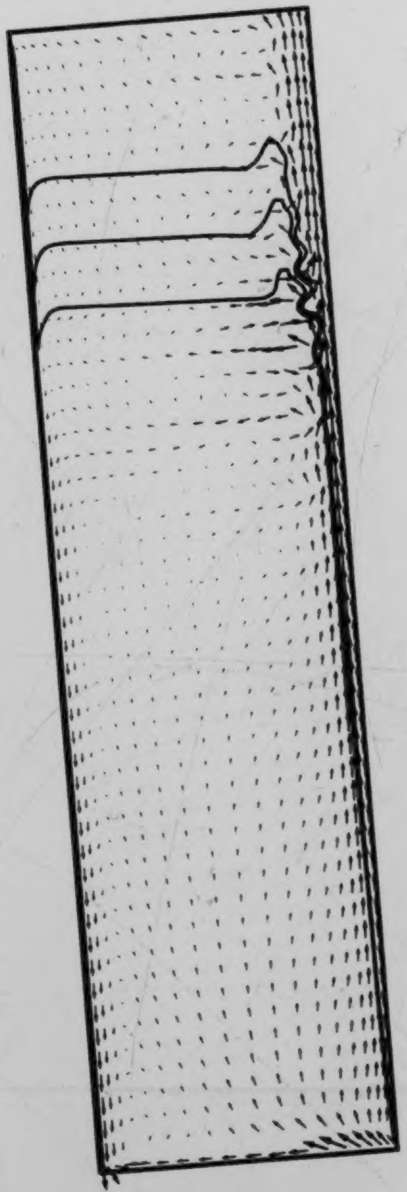

Figure 8.12: Flow pattern for $\phi = 0.05$, $\bar{\mu}_f = 18.8\,\mathrm{mPa\,s}$, $\theta = 10°$ and 7 mm equivalent wall separation.

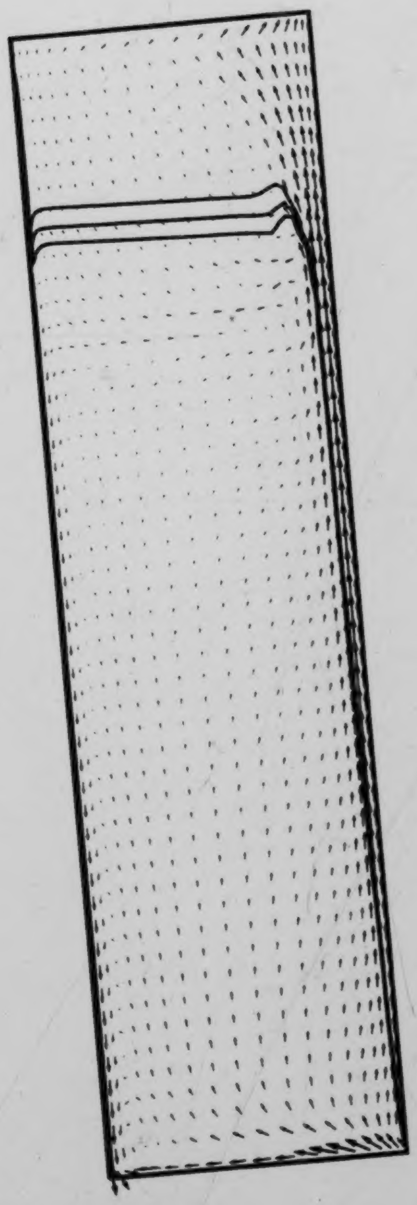

Figure 8.13: Flow pattern for $\phi = 0.05$, $\bar{\mu}_f = 18.8\,\text{mPa s}$, $\theta = 10°$ and 5 mm equivalent wall separation.

Figure 8.14 shows the 10 mPa s suspension filled most of the vessel with zero internal resistance to motion while the more viscous suspensions filled 70 – 80 % of the vessel. Decreased equivalent wall separation caused the position of the horizontal suspension interface to match more closely that given by PNK theory ($y/H = 0.80$ in these cases). Acrivos & Herbolzheimer note that large deviations from PNK theory are due to the formation of waves between the suspension and clear fluid zone and the subsequent entrainment of particles in the clear fluid zone. Increased internal resistance to motion suppresses the formation of waves and, hence, yields horizontal interfaces that match closely with PNK theory.

The reduced entrainment associated with increased internal resistance to motion is most apparent in Figure 8.15: the particle concentration in the top outlet was reduced at least one order of magnitude where the equivalent wall separation was reduced from infinite to 5 mm. The most significant reduction in the outlet concentration was for the 38.1 mPa s suspension.

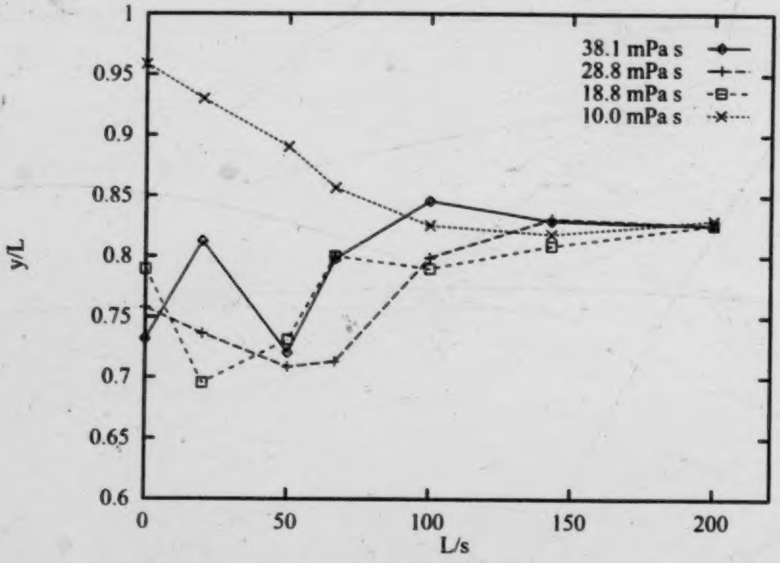

Figure 8.14: Dependance of the horizontal interface height on equivalent wall separation for $\phi = 0.05$, $\theta = 10°$: ◇ is 38.1 mPa s; + is 28.8 mPa s; □ is 18.8 mPa s; × is 10.0 mPa s.

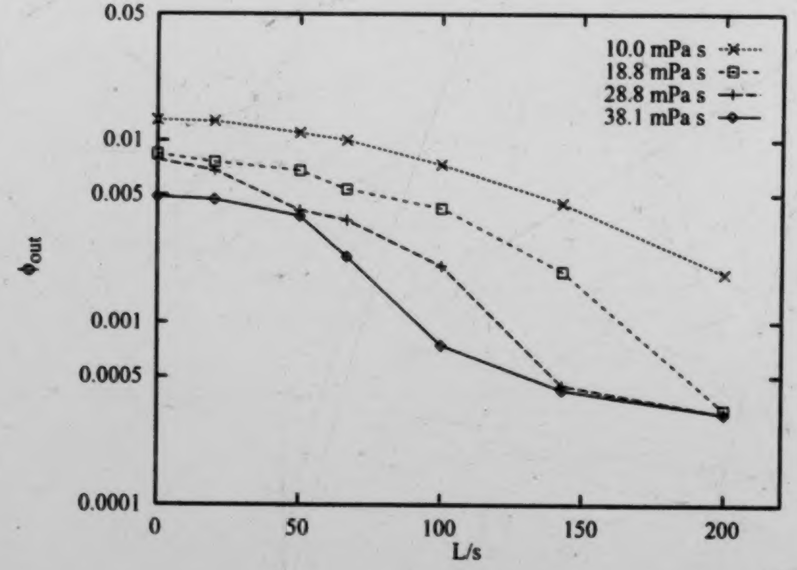

Figure 8.15: Dependance of the top outlet concentration on equivalent wall separation for $\phi = 0.05$, $\theta = 10°$: ◇ is 38.1 mPa s; + is 28.8 mPa s; □ is 18.8 mPa s; × is 10.0 mPa s.

8.4 Dependance of inverse inception distance on internal resistance and inclination angle

Figure 8.16 shows the stabilizing effect of increased internal resistance is largest at low inclinations: the flow pattern is well mixed at low angles. The stabilizing influence of internal resistance to motion with 10, 20 and 30° inclinations is better depicted in Figure 8.17. The suspension interface is very unstable at 10° inclination with zero internal resistance and is much more stable with 50 mm equivalent wall separation ($L/s = 20$). The interfaces at 20° and 30° inclinations are already quite stable without internal resistance to motion and increased resistance does little to improve the stability.

Figures 8.18 – 8.23 show the effect of increased internal resistance to motion on the uniform velocity field in the sedimentation vessel at 20° inclination. The large smooth vortex in the bulk of the suspension is replaced by a series of smaller vortices with weaker circulation where the equivalent wall separation is reduced from infinite to 20 mm. There is little effect on the wave inception point. The circulation rate of the small vortices in the bulk of the suspension and the amount of mixing in the upper portion of the vessel are reduced where the equivalent wall separation is decreased to 15 mm. The vortices in the bulk of the suspension have almost disappeared with 10 mm equivalent spacing. The wavy interface is eliminated with an equivalent wall separation of 7 mm.

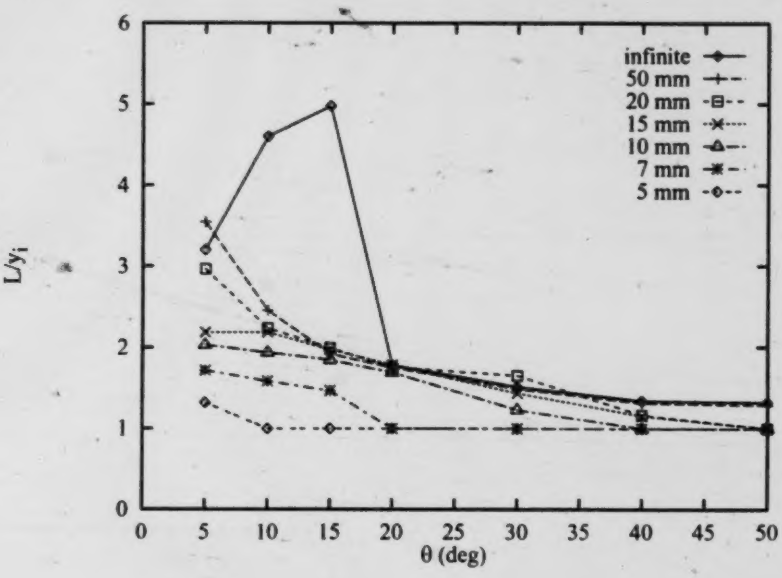

Figure 8.16: Dependance of the inverse of the inception distance on equivalent wall separation for various angles and $\bar{\mu}_f = 18.8, \text{mPa s}$, $\phi = 0.05$.

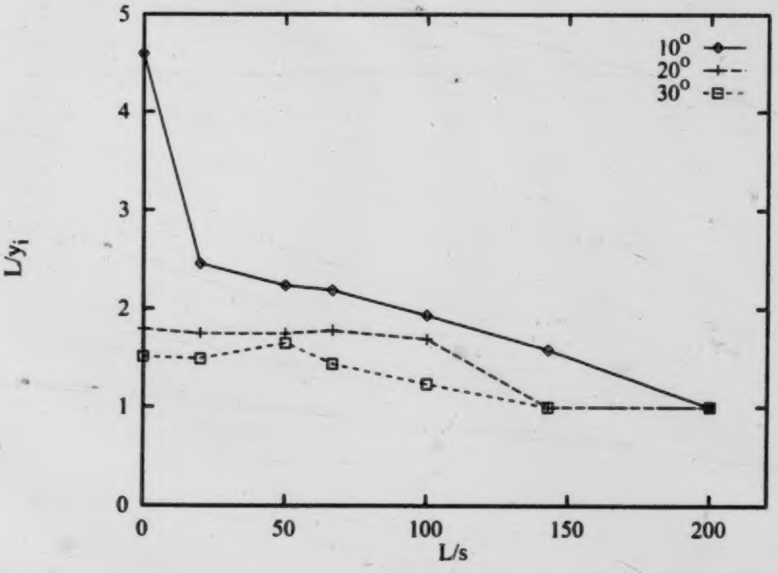

Figure 8.17: Dependance of the inverse of the inception distance on equivalent wall separation for $\phi = 0.05$, $\bar{\mu}_f = 18.8\,\text{mPa s}$: ◇ is 10°; + is 20°; □ is 30°.

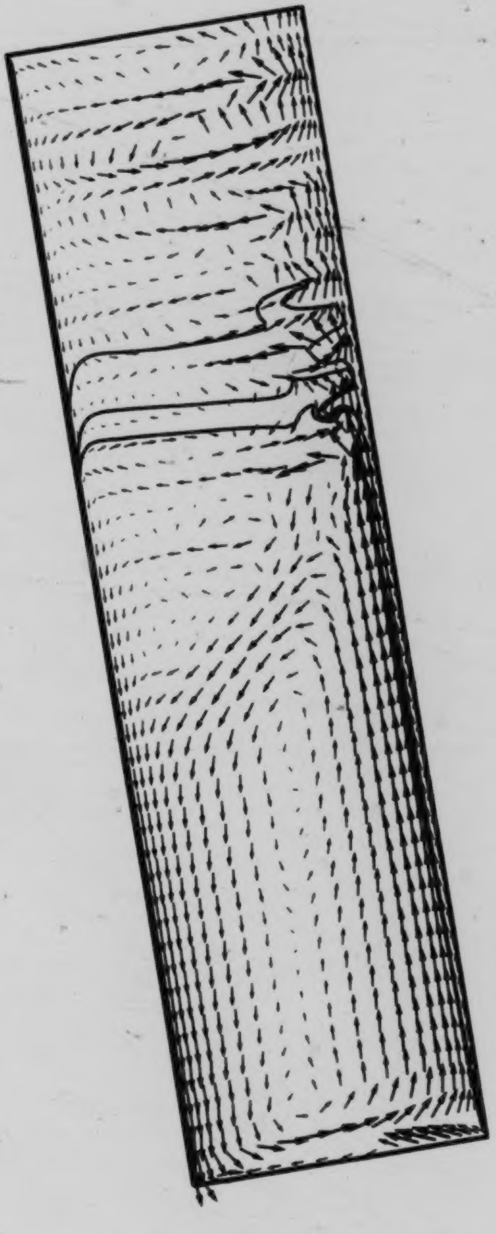

Figure 8.18: Flow pattern for $\phi = 0.05$, $\bar{\mu}_f = 18.8\,\mathrm{mPa\,s}$, $\theta = 20°$ and no internal resistance to motion.

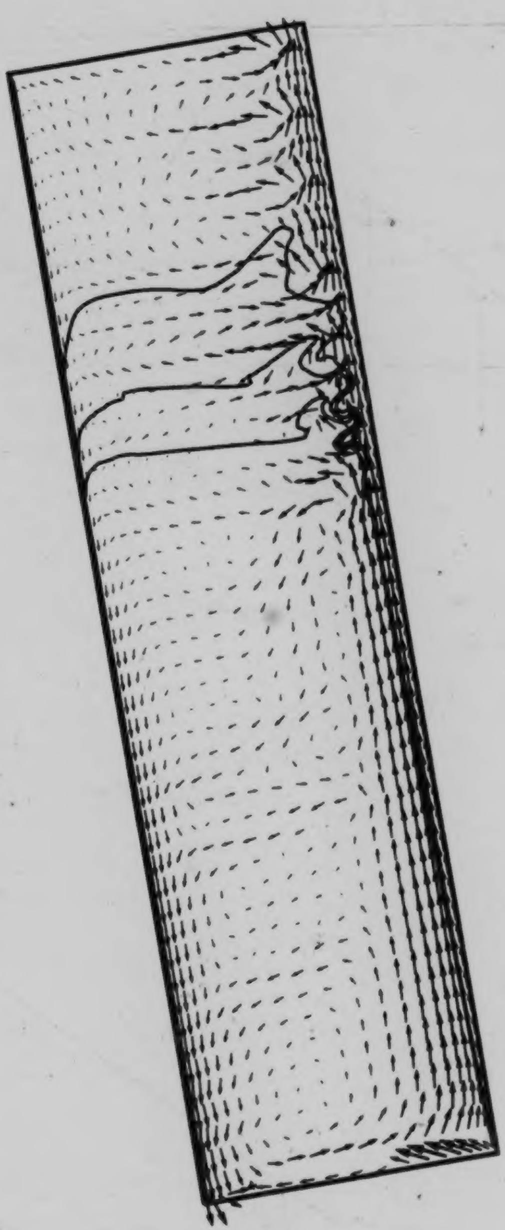

Figure 8.19: Flow pattern for $\phi = 0.05$, $\bar{\mu}_f = 18.8\,\mathrm{mPa\,s}$, $\theta = 20°$ and 20 mm equivalent wall separation.

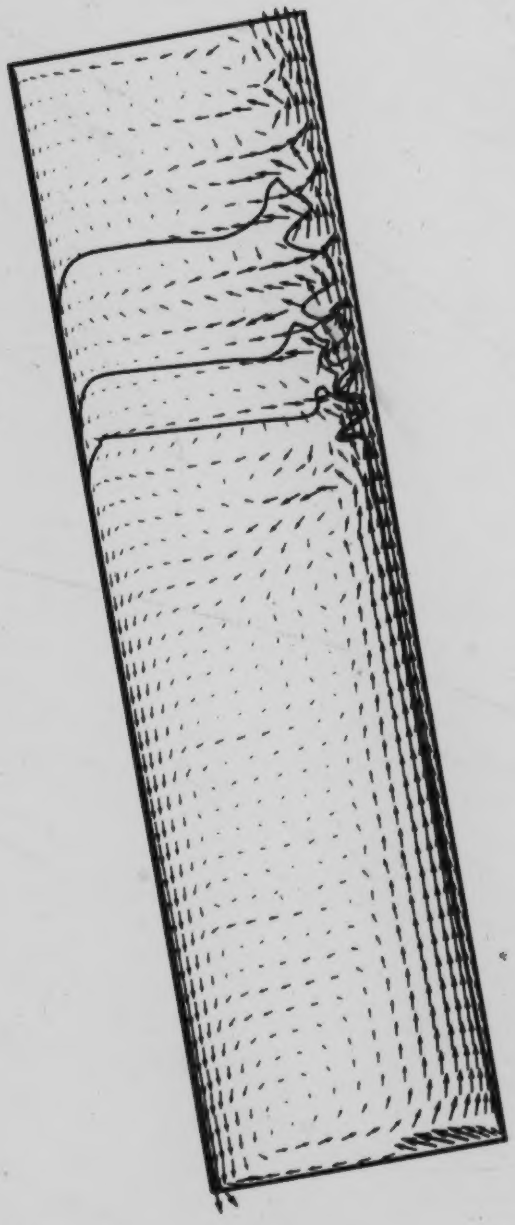

Figure 8.20: Flow pattern for $\phi = 0.05$, $\bar{\mu}_f = 18.8\,\mathrm{mPa\,s}$, $\theta = 20°$ and 15 mm equivalent wall separation.

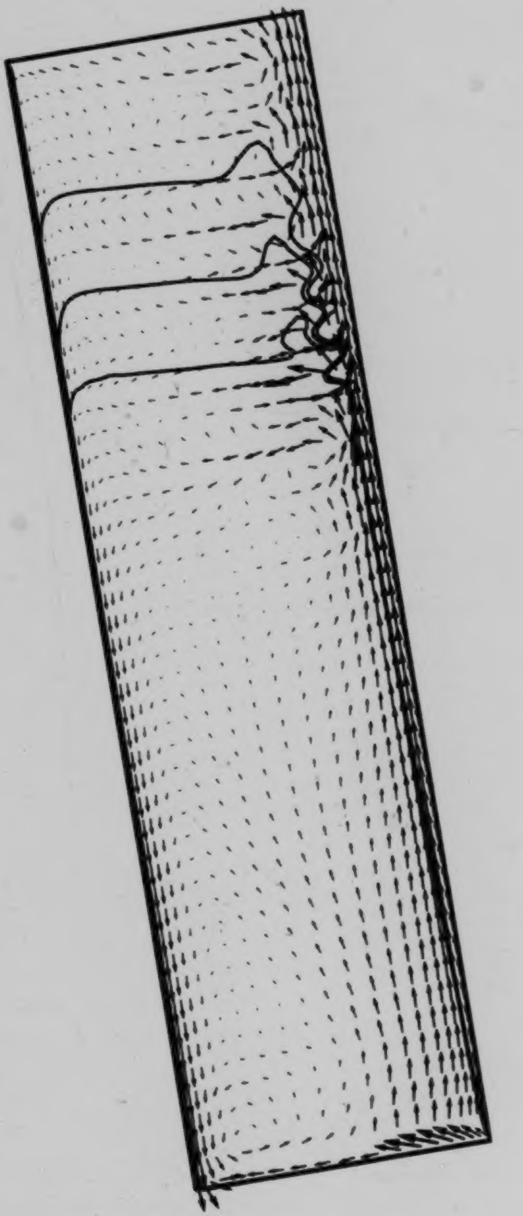

Figure 8.21: Flow pattern for $\phi = 0.05$, $\bar{\mu}_f = 18.8\,\mathrm{mPa\,s}$, $\theta = 20°$ and 10 mm equivalent wall separation.

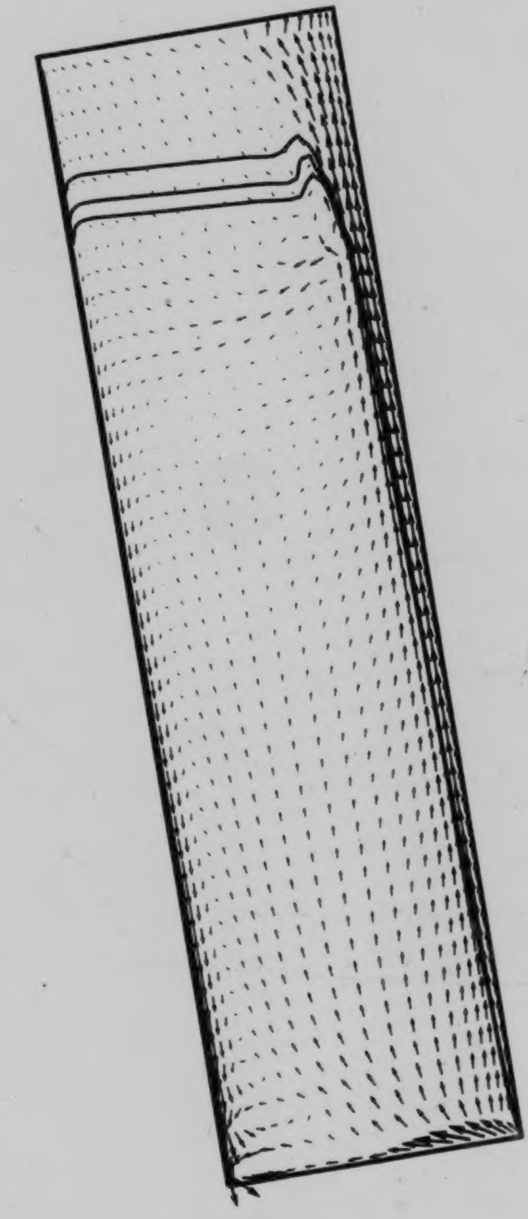

Figure 8.22: Flow pattern for $\phi = 0.05$, $\bar{\mu}_f = 18.8\,\mathrm{mPa\,s}$, $\theta = 20°$ and 7 mm equivalent wall separation.

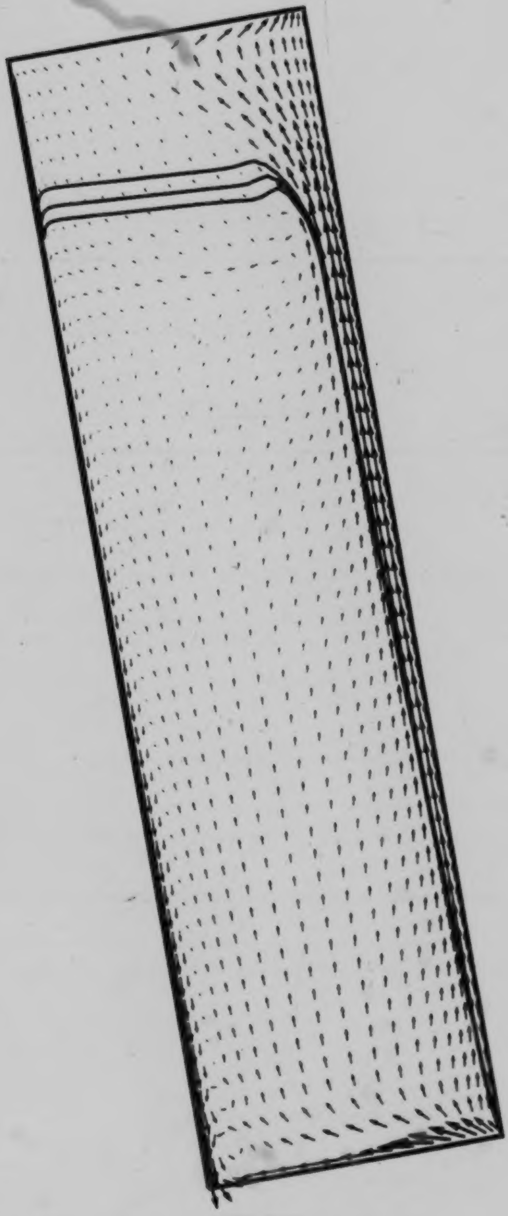

Figure 8.23: Flow pattern for $\phi = 0.05$, $\bar{\mu}_f = 18.8\,\mathrm{mPa\,s}$, $\theta = 20°$ and 5 mm equivalent wall separation.

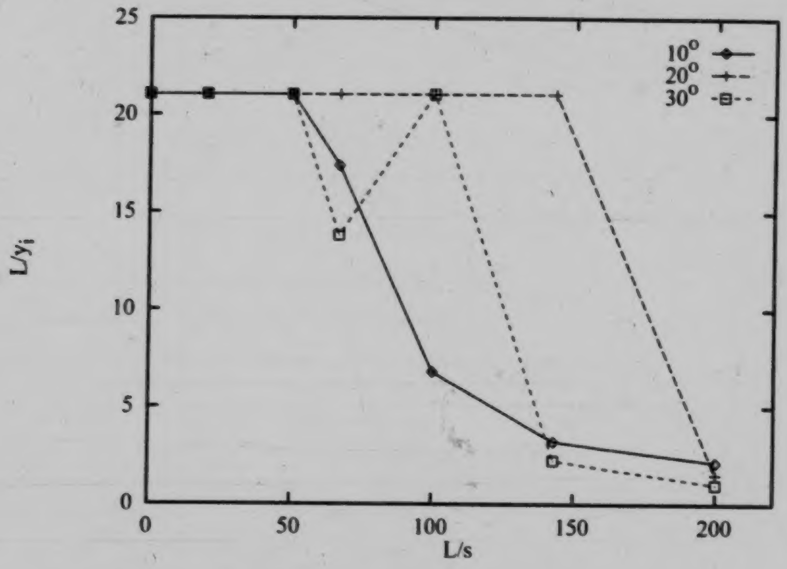

Figure 8.24: Dependance of the inverse of the inception distance on equivalent wall separation for $\phi = 0.05$, $\bar{\mu}_f = 10.0\,\mathrm{mPa\,s}$: ◇ is 10°; + is 20°; □ is 30°.

Waves formed near the bottom of the sedimentation vessel for the 10.0 mPa s suspension at 10, 20 and 30° inclinations and no internal resistance to motion. The inverse inception distance $L/y_i = 21$ seen in Figure 8.25 corresponds to the starting position of the search for waves.

Increased internal resistance had the strongest stabilizing effect at 10° inclination: this was observed with the 18.8 mPa s suspension. Very small equivalent wall separations (5 and 7 mm) were required to stabilize the wavy interface for 20 and 30° inclinations.

Figure 8.25 shows the vessel is nearly filled with the 10.0 mPa s suspension at 10, 20 and 30° inclinations and no internal resistance to motion. Increased internal resistance lowers the position of the horizontal suspension interface. The outlet concentration is reduced by more than an order of magnitude at 20 and 30° inclinations seen in Figure 8.26. This is important because the simulations with larger angles also have higher inlet flow rates and increased internal resistance to motion decreases substantially the contamination level of the clear product.

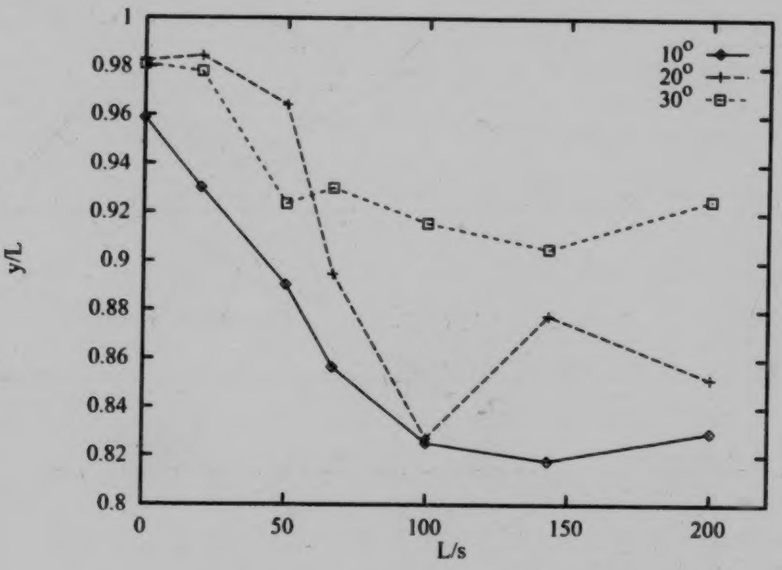

Figure 8.25: Dependance of the horizontal interface height on equivalent wall separation for $\phi = 0.05$, $\bar{\mu}_f = 10.0\,\mathrm{mPa\,s}$: ◇ is 10°; + is 20°; □ is 30°.

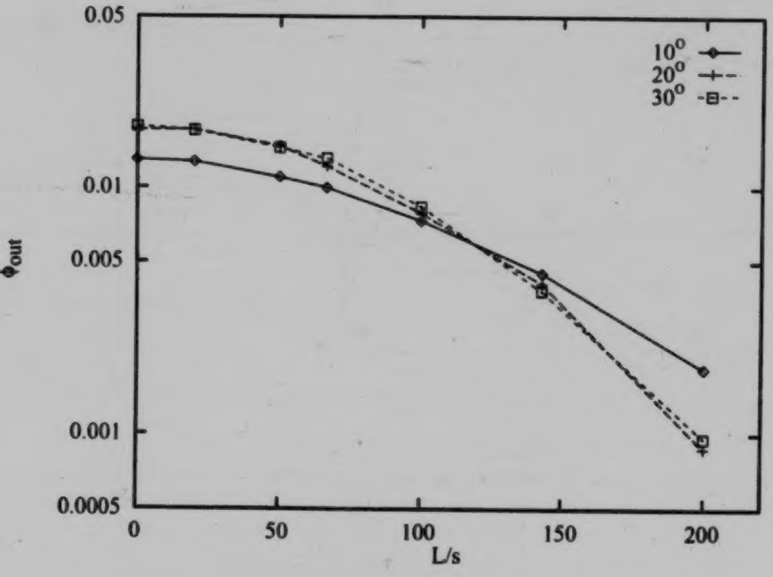

Figure 8.26: Dependance of the top outlet concentration on equivalent wall separation for $\phi = 0.05$, $\bar{\mu}_f = 10.0\,\mathrm{mPa\,s}$: ◇ is 10°; + is 20°; □ is 30°.

8.5 Dependance of inverse inception distance on internal resistance and feed concentration

Uniform internal resistance to flow suppresses the formation of unstable waves better for more concentrated suspensions seen in Figure 8.27. The flow patterns for the suspensions with $\phi = 0.10$ and 0.15 and zero internal resistance are well mixed and are sensitive to the amount of internal resistance.

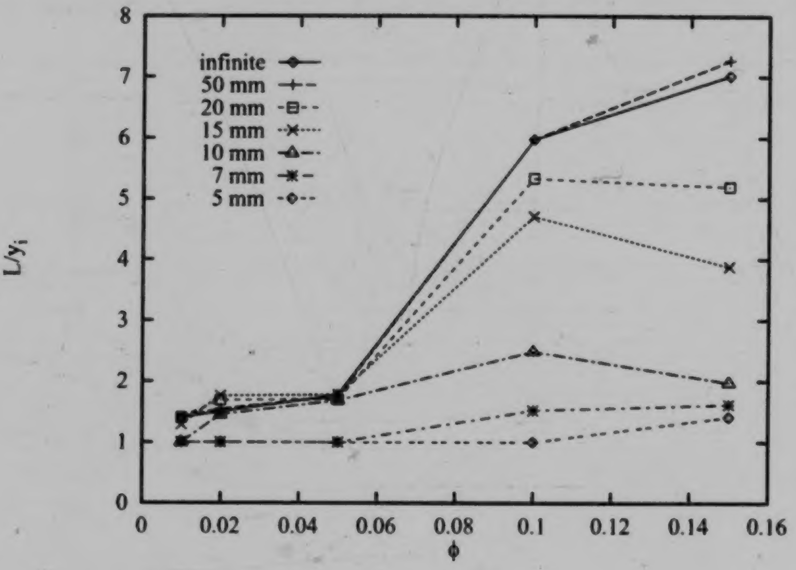

Figure 8.27: Dependance of the inverse of the inception distance on plate separation for various feed concentrations and $\bar{\mu}_f = 18.8$, mPa s, $\theta = 20°$.

8.6 Summary

Uniform internal resistance to flow suppresses the formation of waves at the suspension/clear fluid interface. The stabilizing effect is most effective where the bulk of the suspension is well mixed for the case with no internal resistance. The particle concentration of the top product was reduced with increased internal resistance.

Experimental sedimentation apparatus often have wall separations of 5 - 10 mm in the depth dimension while commercial vessels are much deeper with wall separations greater than 100 mm. The simulation results suggest that wall friction caused by 5 - 10 mm wall separations will stabilize the wavy suspension interface and suppress mixing. In this case the sedimentation behaviour in the experimental apparatus may not represent the behaviour in deeper larger vessel.

The addition of internal resistance to an industrial inclined plate sedimentation vessel should reduce the amount of entrainment of the suspension in the clear fluid. This will allow higher throughputs of feed without contaminating the clear product.

Experimental results for the batch settling rate, the wave inception point and the velocity field are needed to verify the predictions made by the numerical simulation. In particular the formation of large weak vortices where the equivalent wall separation is decreased from infinite to 10 mm may serve as a definitive test of the numerical model.

Chapter 9

Comparison of results with different buoyancy discretizations

The truncation error analysis in Chapter 4 showed the buoyancy driving force term could be discretized in a second order accurate manner with the implicitness factor $\beta_{\hat{\phi}} = 1$. It was argued that second order accuracy was obtained at the expense of a large oscillatory truncation error in the buoyancy source term. This would lead to an oscillatory vorticity field at the next time step.

Comparisons were made between the non-diffusive simulations with first order accurate and second order accurate discretizations of the buoyancy driving force: $\beta_{\hat{\phi}} = 0$ and $\beta_{\hat{\phi}} = 1$. Results were obtained with maximum Courant numbers of $N_C \simeq 0.08$, 0.35 and 0.8 for both the first and second order accurate discretizations. The transient simulations were carried to a dimensionless time of $\hat{t} = 4$ instead of $\hat{t} = 2$ used for the results presented earlier. Simulations were performed for the 18.8 mPa s suspensions with $\hat{\phi} = 0.05$. These suspensions were the most prone to wave formation in the experimental study of Herbolzheimer [18].

9.1 Horizontal interface position

The time series plot (Figure 9.1) of the horizontal suspension interface for the unstable 10° inclination shows very strong dynamics in the simulations with $\beta_{\hat{\phi}} = 0$ for $N_C \simeq 0.08$ and 0.35. Although the initial flow development has completed by $\hat{t} = 1$ the results show a strong time periodic nature up to $\hat{t} = 4$. The interface position for $N_C \simeq 0.08$ displays a periodic 15 cm variation over a period of $\Delta\hat{t} \simeq 0.4$. Oscillations of a similar magnitude are evident with the $N_C \simeq 0.35$ simulation with a period of $0.2 < \Delta\hat{t}1$. This period is similar to that with the smaller time steps. The simulation with the largest time steps ($N_C \simeq 0.8$) predicted the vessel would fill with suspension.

The simulations with second order accurate discretization of the buoyancy driving force show much less oscillation in the position of the horizontal suspension interface in Figure 9.2. The run with $N_C \simeq 0.08$ did not show any oscillations in the interface position until $\hat{t} > 3$. The results after this time suggest the variation in the interface position was around 10 – 20 cm with a period of $0.2 < \Delta\hat{t} < 1$. The less accurate simulation with $N_C \simeq 0.35$ showed 10 cm oscillations in the interface position with a period of $\Delta\hat{t} \simeq 0.2$. The simulation with $N_C \simeq 0.8$ showed very little variation in the position of the horizontal suspension interface.

Herbolzheimer [18] does not report the magnitude of the oscillations in the position of the horizontal suspension interface. This type of observation would be a useful validation of the numerical results.

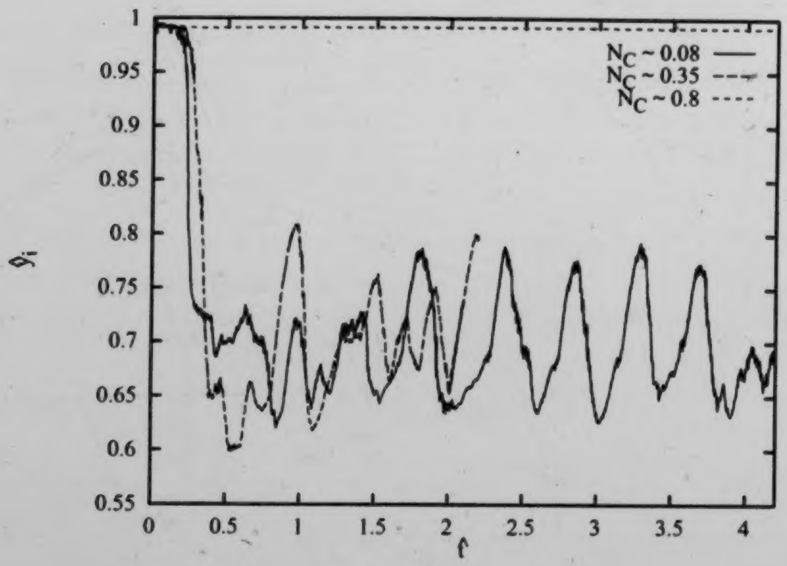

Figure 9.1: Horizontal interface position for $\beta_{\hat{\phi}} = 0$, $\hat{\phi} = 0.05$, $\bar{\mu}_f = 18.8\,\mathrm{mPa\,s}$, $\theta = 10°$.

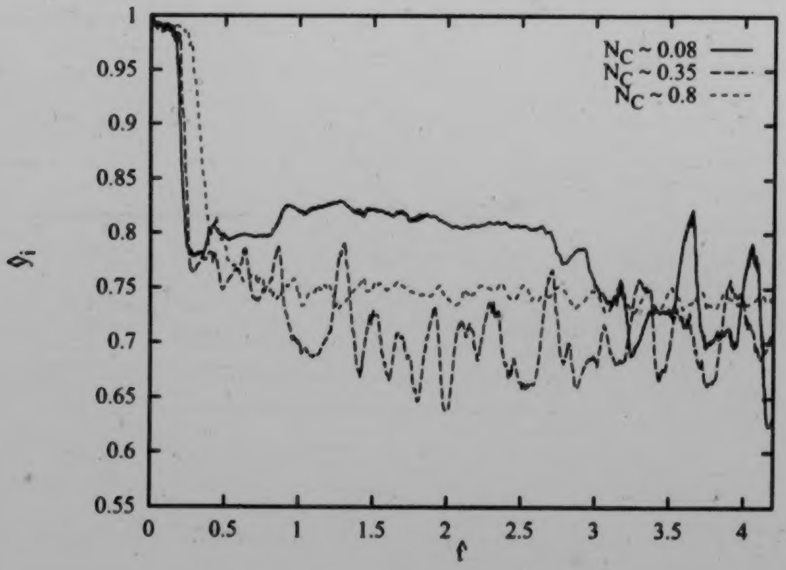

Figure 9.2: Horizontal interface position for $\beta_{\hat{\phi}} = 1$, $\hat{\phi} = 0.05$, $\bar{\mu}_f = 18.8\,\mathrm{mPa\,s}$, $\theta = 10°$.

9.2 Velocity profiles

Two large vortices are present in the velocity profile for $\beta_{\dot{\phi}} = 0$ and $N_C \simeq 0.08$ show in Figure 9.3. In contrast Figure 9.4 shows many smaller vortices and the bulk of the suspension is well mixed where the Courant number is $N_C \simeq 0.35$. The difference in the interface heights between these two simulations will influence the number of vortices present in the bulk of the suspension. This result has been demonstrated in thermally driven natural convection in rectangular vessels [6, 27]. As well the results are periodic: it was demonstrated in Chapter 7 that the flow changes from a uniform to a well-mixed pattern. Herbolzheimer does not report the flow patterns inside the vessel. The flow pattern in Figure 9.5 shows large changes in the velocity where the Courant number is $N_C \simeq 0.8$: this result is probably inaccurate.

The flow profiles in Figures 9.6 and 9.7 obtained with $N_C \simeq 0.08$ and $N_C \simeq 0.35$ are virtually identical for the second order accurate discretization of the buoyancy term. These results are also virtually identical to the profile for $\beta_{\dot{\phi}} = 0$ and $N_C \simeq 0.08$ shown in Figure 9.3. This suggests the results with $N_C \simeq 0.35$ from the second order accurate discretization of the buoyancy term are just as accurate as those with the first order accurate discretization and $N_C \simeq 0.08$. The flow profile with $N_C \simeq 0.8$ in Figure 9.8 is different from the previous results obtained with $\beta_{\dot{\phi}} = 1$. One cannot determine if this result is invalid.

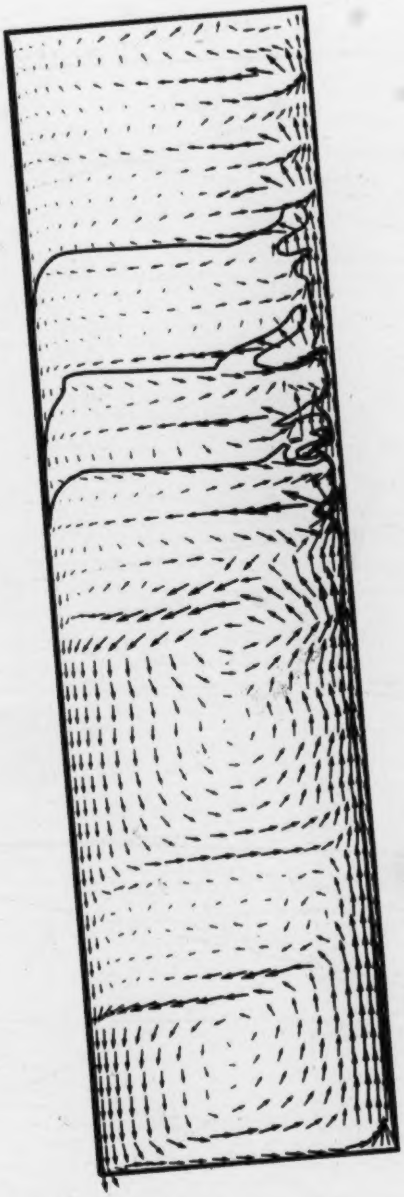

Figure 9.3: $\beta_{\hat{\phi}} = 0$, $N_C \simeq 0.08$: flow pattern for $\hat{\phi} = 0.05$, $\bar{\mu}_f = 18.8\,\mathrm{mPa\,s}$, $\theta = 10°$.

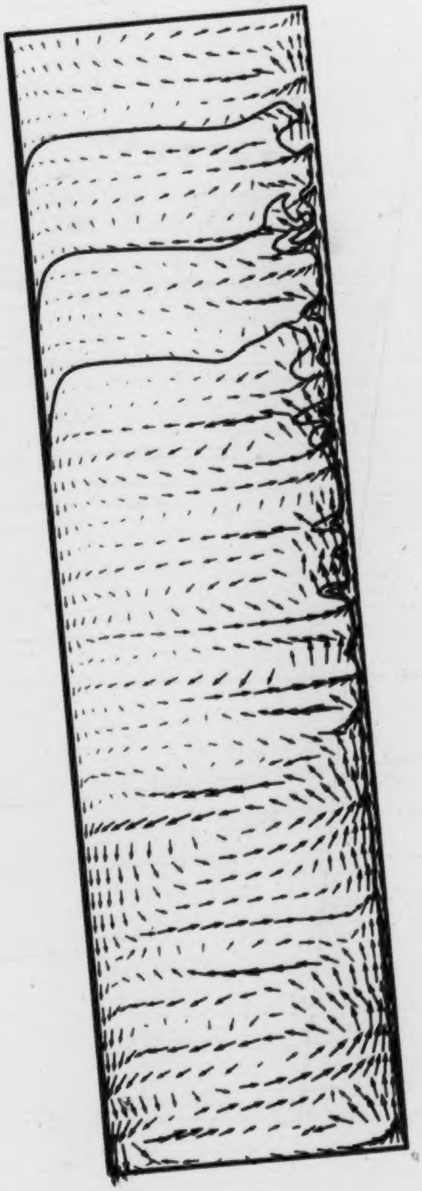

Figure 9.4: $\beta_{\hat{\phi}} = 0$, $N_C \simeq 0.35$: flow pattern for $\hat{\phi} = 0.05$, $\bar{\mu}_f = 18.8\,\mathrm{mPa\,s}$, $\theta = 10°$.

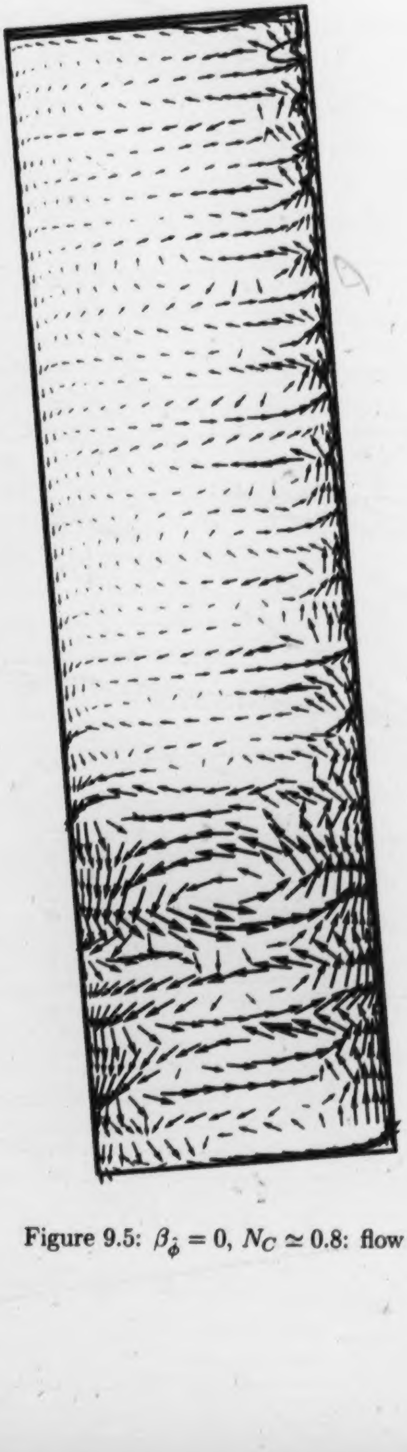

Figure 9.5: $\beta_{\hat{\phi}} = 0$, $N_C \simeq 0.8$: flow pattern for $\hat{\phi} = 0.05$, $\bar{\mu}_f = 18.8\,\mathrm{mPa\,s}$, $\theta = 10°$.

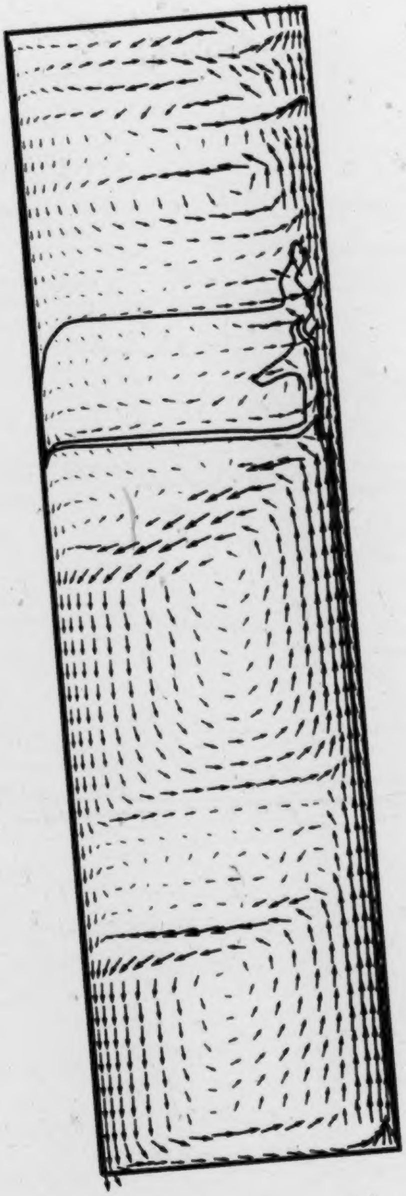

Figure 9.6: $\beta_{\hat{\phi}} = 1$, $N_C \simeq 0.08$: flow pattern for $\hat{\phi} = 0.05$, $\bar{\mu}_f = 18.8\,\mathrm{mPa\,s}$, $\theta = 10°$.

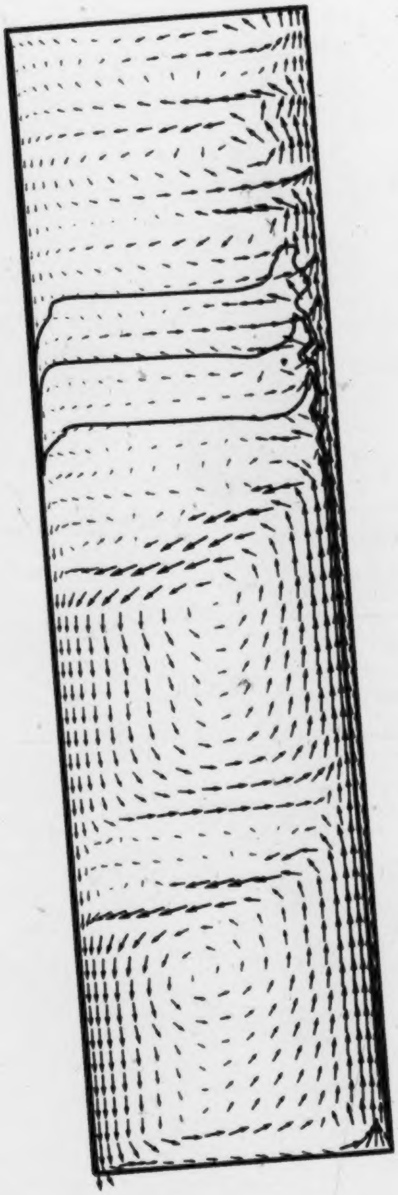

Figure 9.7: $\beta_{\hat{\phi}} = 1$, $N_C \simeq 0.35$: flow pattern for $\hat{\phi} = 0.05$, $\bar{\mu}_f = 18.8\,\mathrm{mPa\,s}$, $\theta = 10°$.

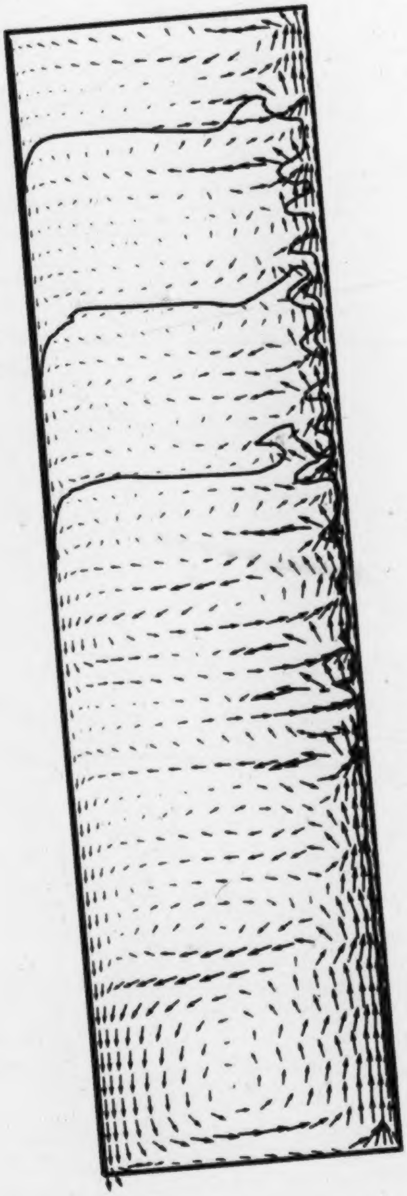

Figure 9.8: $\beta_{\hat{\phi}} = 1$, $N_C \simeq 0.8$: flow pattern for $\hat{\phi} = 0.05$, $\bar{\mu}_f = 18.8\,\mathrm{mPa\,s}$, $\theta = 10°$.

9.3 Inverse of the wave inception distance

Figure 9.9 shows the simulations with $\beta_{\hat{\phi}} = 0$ and $N_C \simeq 0.08$ predict inverse wave inception distances to be lower than the experimental values but follow the same trend. Compared to the simulations with $N_C \simeq 0.08$ the runs with $N_C \simeq 0.35$ over-predict the inverse wave inception distance for the most unstable inclinations of 5°, 10° and 15°. The simulation with $N_C \simeq 0.8$ predicts that waves occur very near the bottom of the vessel: this is numerical result is probably inaccurate.

The inverse inception distances in Figure 9.10 obtained with the second order accurate discretization of buoyancy term show the same trend as the experimental data for $N_C \simeq 0.08$, 0.35 and 0.8. The close agreement between the simulations with $N_C \simeq 0.08$ and 0.35 suggest the second order accurate simulations with $N_C \simeq 0.35$ are just as accurate as the simulations with much smaller Courant numbers.

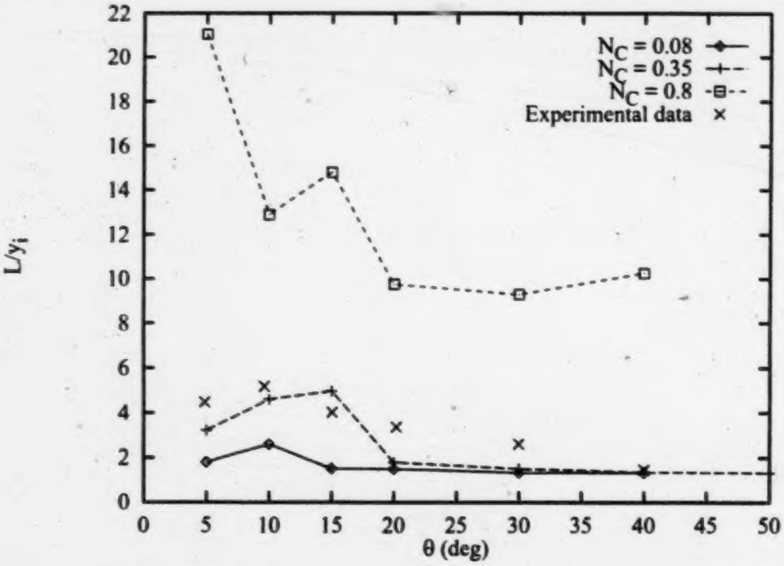

Figure 9.9: Inverse of inception distance for $\beta_{\hat{\phi}} = 0$, $\hat{\phi} = 0.05$, $\bar{\mu}_f = 18.8\,\mathrm{mPa\,s}$, $\theta = 10°$.

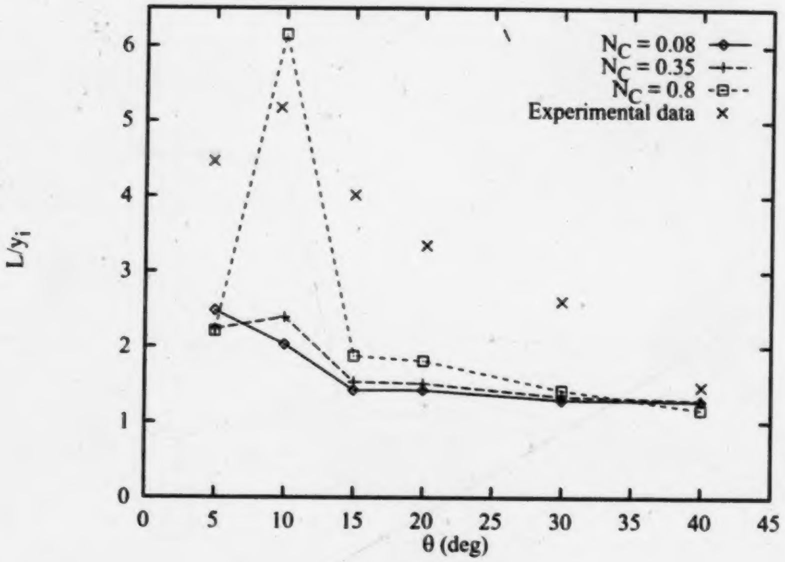

Figure 9.10: Inverse of inception distance for $\beta_{\hat{\phi}} = 1$, $\hat{\phi} = 0.05$, $\bar{\mu}_f = 18.8\,\mathrm{mPa\,s}$, $\theta = 10°$.

9.4 Summary

The numerical results obtained with the second order accurate discretization of the buoyancy term are more accurate than those obtained with the first order accurate discretization for moderate Courant numbers for suspensions with very unstable interfaces. Both the first order accurate and second order accurate discretizations of the buoyancy term predict the same behaviour for small Courant numbers, $N_C \simeq 0.08$. The numerical results presented in the previous chapters with the first order buoyancy discretization may exhibit a more unstable suspension interface than the results obtained with the second order accurate buoyancy discretization. This chapter has shown the results obtained with first order accurate discretization of the buoyancy term follow the same trends as the results obtained with the more accurate discretization.

It is not known how the results obtained with the first and second order accurate discretization of the buoyancy term will be affected by increased spatial resolution.

Chapter 10

Summary

Non-diffusive shock capturing techniques provide accurate simulations of inclined plate sedimentation. The results capture well the important features of the flow inside the vessel. These features include the formation of the wavy suspension interface and the subsequent mixing that leads to the poor performance of a sedimentation vessel.

10.1 Conclusions

The application of accurate shock capturing techniques from computational aerodynamics to inclined plate sedimentation is new. The use of non-diffusive TVD based methods (such as UNO2) is necessary to obtain an accurate representation of the dispersed phase volume fraction profile in two-phase flow. First order accurate upwinding is too diffusive in both the vorticity transport and material transport equations to provide a valid numerical model of sedimentation.

The non-diffusive numerical model captures the wavy suspension interface and the mixing in the bulk of the suspension. Numerical results of this sort have not been published. Agreement with the wave inception distance demonstrates the accuracy of the numerical simulation: these experimental results of Herbolzheimer [18] are the most delicate measurements available.

The effect of internal resistance on the flow stability in sedimentation vessels has not been addressed in the literature. Numerical simulations showed internal resistance to motion reduced the growth rate of unstable waves between the suspension and clear fluid. This has two implications. One is in the design of laboratory scale settling devices: experimental results with laboratory scale apparatus may be stabilized by wall friction while the flow is very unstable in the industrial scale apparatus. The other implication is in the design of enhanced sedimentation vessels. The reduction of unstable waves results in less mixing of the suspension with clear fluid and allows higher feed throughput. The use of internal resistance to stabilize the flow is a new design for enhanced inclined plate sedimentation vessels.

A small change in the discretization of the buoyancy term led to an approximation with second order accurate truncation errors. Solutions obtained with this method were more accurate than the solutions obtained with the first order method with moderate Courant numbers. The first order accurate discretization was associated with more unstable behaviour at the suspension interface. This does not invalidate the previous results: the first order accurate results follow the same trend as the more accurate second order results. This result demonstrates that accurate discretization methods must be used to approximate the buoyancy term for the modelling of sedimentation. Accurate numerical techniques must be developed before one examines more complicated physical models (such as turbulence models).

10.2 Recommendations for future work

The most immediate extension of this work is to determine if the second order discretization of the buoyancy term remains accurate for finer meshes and different suspension concentrations. The oscillatory high order derivative in the leading truncation error may cause numerical problems on finer meshes. A dilute suspension produces an interface that is smeared over several grid points while the interface is much sharper for a concentrated suspension. It is not known if the oscillatory truncation error will be acceptable with moderate Courant numbers in these cases.

The Boussinesq approximation and constant viscosity assumption should be relaxed in future modelling work. This will extend the applicable range of the numerical model to higher dispersed phase concentrations. Different numerical techniques are required for rapid solution of the coupled vorticity transport/stream function equations because the matrix coefficients will change with time. An iterative technique (such as ADI) with multigrid acceleration may be a feasible solution method.

An implicit TVD method may be devised for the material transport and vorticity transport equations. There are two advantages to an implicit shock capturing method over the explicit treatment used for the convection terms used in this work. First the stability limit imposed by the Courant number is eliminated and allows for larger time steps and faster simulations. Second the implicit scheme can be formulated with a second order accurate truncation error. The coupling between the material transport and stream function equation suggests the vorticity transport, stream function and material transport equations can be solved simultaneously.

A primitive variable (velocity/pressure) formulation of the homogeneous model is more general than the vorticity/stream function formulation used in this research. This will allow the modelling of sedimentation in more complicated geometries than those possible with the vorticity/stream function approach. Continuous sedimentation could be modelled with a point source feed in the middle of the vessel or with baffles between the feed and sludge withdrawal points. A primitive variable formulation can be extended to three dimensional problems easier than the vorticity/stream function approach.

Accurate numerical solutions of the general two-fluid model equations (where there is a velocity for each phase) will be difficult to obtain. The velocity fields for each phase are discontinuous and the flow is much more viscous than the flows studied in computational aerodynamics. This approach may tax the current state-of-the-art in shock capturing techniques for the Navier-Stokes equations.

More detailed experimental results are required to validate the predictions made by the numerical model. Quantitative measurements of the flow pattern in the vessel and the shape of the wavy suspension interface are required. Optical techniques may not work for measuring the suspension velocity and concentration due to the opaqueness of the suspension. Nuclear magnetic resonance imaging has been used in sedimentation experiments [26] but is expensive.

Experimental results are required for inclined plate sedimentation where there is a porous media type of resistance: this work is needed to validate the predictions made with the numerical simulation. The resistance to flow may be caused by a loose porous media such as a wire mesh or by close spaced walls in the manner of a Hele-Shaw cell.

Bibliography

[1] A. Acrivos and E. Herbolzheimer. Enhanced sedimentation in settling tanks with inclined walls. *J. Fluid Mech.*, 92:435–457, 1979.

[2] G. Amberg and A. A. Dahlkild. Sediment transport during unsteady settling in an inclined channel. *J. Fluid Mech.*, 185:415–436, 1987.

[3] E. Barnea and J. Mizrahi. A generalized approach to the fluid dynamics of particulate systems part 1. general correlation for fluidization and sedimentation in solid multiparticle systems. *Chem. Engng. J.*, 5:171–189, 1973.

[4] G. K. Batchelor and J. T. Green. The determination of the bulk stress in a suspension of spherical particles to order c^2. *J. Fluid Mech.*, 56:401–427, 1972.

[5] A. E. Boycott. Sedimentation of blood corpuscles. *Nature*, 104:532, 1920.

[6] A. Chikhaoui, J. F. Marcillat, and R. L. Sani. Successive transitions in thermal convection within a vertical enclosure. Natural convection in enclosures - 1988, Chicago, 1988.

[7] P. Colella and P. R. Woodward. The piecewise parabolic method (PPM) for gas-dynamical simulations. *J. Comp. Phys.*, pages 174–201, 1984.

[8] R. H. Davis, E. Herbolzheimer, and A. Acrivos. Wave formation and growth during sedimentation in narrow tilted channels. *Phys. Fluids*, 26:2055–2064, 1983.

[9] D. A. Drew. Two-phase flows: Constitutive equations for lift and brownian motion and some basic flows. *Archive for Rational Mechanics and Analysis*, 62:149–163, 1976.

[10] H. Faxén. *Arkive för Matemakik, Astronomi och Fysik*, 17:1, 1922.

[11] R. Font. Analysis of the batch sedimentation test. *Chem. Eng. Sci*, 46:2473–2482, 1991.

[12] J. Garside and M. R. Al-Dibouni. Velocity-voidage relationship for fluidization and sedimentation in solid-liquid systems. *Ind. Engng Chem. Proc. Des. Rev.*, 16:206–214, 1977.

[13] A. George, J Liu, and E. Ng. User guide for sparspak: Waterloo sparse linear equation package. Technical report, University of Waterloo, 1980.

[14] F. H. Harlow and J. E. Welch. Numerical calculation of time-dependent viscous incompressible flow of fluid with free surface. *Phys. Fluids*, 8(12):2182–2189, 1965.

[15] A. Harten. High resolution schemes for hyperbolic conservation laws. *J. Comp. Phys.*, 49:357–393, 1983.

[16] A. Harten. On a class of high resolution total-variation-stable finite-difference schemes. *SIAM J. Numer. Anal.*, 21:1–23, 1984.

[17] A. Harten and S. Osher. Uniformly high-order accurate nonoscillatory schemes. I. *SIAM J. Numer. Anal.*, 24:279–309, 1987.

[18] E. Herbolzheimer. Stability of the flow during sedimentation in inclined channels. *Phys. Fluids*, 26:2043–2054, 1983.

[19] W. D. Hill, R. R. Rothfus, and Kun Li. Boundary-enhanced sedimentation due to settling convection. *Int. J. Multiphase Flow*, 3:561–583, 1977.

[20] B. P. Ho and L. G. Leal. Inertial migration of rigid spheres in two dimensional unidirectional flow. *J. Fluid Mech.*, 65:365–400, 1974.

[21] K. A. Hoffmann. *Computational Fluid Dynamics*. Engineering Education System, Texas, 1985.

[22] M. Ishii and G. Kocamustafaogullari. Two-phase flow models and their limitations. In S. Kakaç and M. Ishii, editors, *Advances in Two-Phase Flow and Heat Transfer*, volume 1 of *NATO advanced science institutes series*, pages 1–14. Martinus Nijhoff Publishers, The Hague, 1982.

[23] K. Kinosita. Sedimentation in tilted vessels. *J. Colloid Interface Sci.*, 4:525–536, 1949.

[24] G. J. Kynch. A theory of sedimentation. *Trans. Faraday Soc.*, 48:166–176, 1952.

[25] D. H-S. Law, R. S. MacTaggart, K. Nandakumar, and J. H. Masliyah. Settling behaviour of heavy and buoyant particles from a suspension in an inclined channel. *J. Fluid Mech.*, 187:301–318, 1988.

[26] S. Lee, Y. Jang, C. Choi, and T. Lee. Combined effect of sedimentation velocity fluctuation and self-sharpening on interface broadening. *Phys. Fluids A*, 4(12):2601–2606, 1992.

[27] Y. Lee and S. A. Korpela. Multicellular natural convection in a vertical slot. *J. Fluid Mech.*, 126:91–121, 1983.

[28] W-F. Leung. Lamella and tube settlers. 2. flow stability. *Ind. Eng. Chem. Process Des. Dev.*, 22:68–73, 1983.

[29] W-F. Leung and R. F. Probstein. Lamella and tube settlers. 1. model and operation. *Ind. Eng. Chem. Process Des. Dev.*, 22:58–67, 1983.

[30] J. H. Masliyah. Hindered settling in a multi-species particle system. *Chem. Eng. Sci.*, 34:1166–1168, 1979.

[31] D. F. McTigue, R. C. Givler, and J. W. Nunziato. Rheological effects of nonuniform particle distributions in dilute suspensions. *J. Rheol.*, 30(5):1053–1076, 1986.

[32] H. Nakamura and K. Kuroda. La cause de l'accélération de la vitesse de sédimentation des suspensions dans les récipients inclinés. *Keijo J. Med.*, 8:256–296, 1937.

[33] J. W. Nunziato. A multiphase mixture theory for fluid-particle flows. In R. E. Meyer, editor, *Theory of dispersed multiphase flow: Proceedings of an advanced seminar*, pages 191–226. Academic Press, New York, 1983.

[34] D. R. Oliver and V. G. Jenson. The inclined settling of dispersed suspensions of spherical particles in square-section tubes. *Can. J. Chem. Eng.*, pages 191–195, 1964.

[35] S. V. Patankar and D. B. Spalding. A calculation procedure for heat, mass and momentum transfer in three dimensional parabolic flows. *Int. J. Heat Mass Transfer*, 15:1787–1806, 1972.

[36] Robert H. Perry and Don W. Green, editors. *Perry's Chemical Engineers' Handbook.* McGraw-Hill Book Company, New York, sixth edition, 1984.

[37] E. Ponder. On sedimentation and rouleaux formation. *Quart. J. Expt. Physiol.*, 15:235–252, 1925.

[38] J. F. Richardson and W. N. Zaki. Sedimentation and fluidization: Part I. *Trans. Instn. Chem. Engrs.*, 32:35–53, 1954.

[39] A. Rizzi and B. Engquist. Selected topics in the theory and practice of computational fluid dynamics. *J. Comp. Phys.*, 72:1–69, 1987.

[40] P. G. Saffman. The lift on a small sphere in slow shear flow. *J. Fluid Mech.*, 22:385–400, 1965.

[41] R. Schreiber and H. B. Keller. Driven cavity flows by efficient numerical techniques. *J. Comp. Phys.*, 49:310–333, 1983.

[42] R. Schreiber and H. B. Keller. Spurious solutions in driven cavity calculations. *J. Comp. Phys.*, 49:165–172, 1983.

[43] E. S. G. Shaqfeh and A. Acrivos. The effects of inertia on the buoyancy-driven convection flow in settling vessels having inclined walls. *Phys. Fluids*, 29(12):3935–3948, 1986.

[44] E. S. G. Shaqfeh and A. Acrivos. The effects of inertia on the stability of the convective flow in inclined particle settlers. *Phys. Fluids*, 30(4):960–973, 1987.

[45] E. S. G. Shaqfeh and A. Acrivos. Enhanced sedimentation in vessels with inclined walls: Experimental observations. *Phys. Fluids*, 30(7):1905–1914, 1987.

[46] J. W. Slooff and W. Schmidt. Computational aerodynamics based on the Euler equations. Technical report, AGARD, 1994.

[47] S. L. Soo. *Fluid Dynamics of Multiphase Systems.* Blaisdell Publishing Co., Waltham, Mass., 1967.

[48] G. C. Stokes. *Trans. Cambridge Phil. Soc.*, 9:8, 1851.

[49] J. F. Thompson. Numerical solution of flow problems using body-fitted coordinate systems. In Wolfgang Kollmann, editor, *Computational Fluid Dynamics.* McGraw-Hill, New York, 1980.

[50] A. Tripathi and A. Acrivos. A new criterion for the continuous opertation of supersettlers in the bottom feeding mode. *Int. J. Multiphase Flow*, 22:353–361, 1996.

[51] G. B. Wallis. *One dimensional two-phase flow.* McGraw-Hill, New York, 1963.

[52] S. Wolfram. *Mathematica: A system for doing mathematics by computer.* Addison-Wesley Publishing Company, Ltd., Redwood City, California, 1991.

[53] P. Woodward and P. Colella. The numerical simulation of two-dimensional fluid flow with strong shocks. *J. Comp. Phys.*, 54:115–173, 1984.

[54] C. S. Yih. *Phys. Fluids*, 6:321, 1963.

[55] J. W. Yokota. Vorticity dynamics of inviscid shear layers. *AIAA J.*, 31:1430–1439, 1993.

[56] J. W. Yokota and H. T. Huynh. A nonoscillatory, characteristically convected, finite volume scheme for multidimensional convection problems. Technical report, NASA, 1990.

Appendix A

Order of magnitude analysis of the two fluid momentum equations

An order of magnitude analysis is performed on the momentum equations for the two fluid model. The results of this analysis justify the simplifications made with the homogeneous model: the slip velocity of the dispersed phase is independent of the fluid velocity.

A.1 Momentum interactions

The general momentum interaction between the continuous and a dilute dispersed phase is given by McTigue et al. [31]:

$$\begin{aligned}
\boldsymbol{m}_{si} = {} & \phi_s \frac{18\bar{\mu}_f}{d_s^2}(\boldsymbol{u}_f - \boldsymbol{u}_s) && \text{Stokes drag} \\
& +\phi_s \frac{3(6.46)}{2\pi d_s} \left(\frac{\bar{\rho}_f^2 \bar{\mu}_f^2}{2 \operatorname{tr} \mathbf{D}_f^2} \right)^{1/4} \boldsymbol{D}_f(\boldsymbol{u}_f - \boldsymbol{u}_s) && \text{Saffman lift} \\
& +2\phi_s \frac{7\bar{\mu}_f}{4} \nabla \cdot \boldsymbol{D}_f && \text{Faxén force} \\
& +2\phi_s \left[\frac{(\operatorname{tr} \mathbf{D}_f^2)^{1/2}}{| \nabla \cdot \mathbf{D}_f |} g_1(y) - g_2(y) \right] \boldsymbol{D}_f \cdot \nabla \cdot \boldsymbol{D}_f && \text{Ho \& Leal lift}
\end{aligned} \tag{A.1}$$

where $\boldsymbol{D} = 0.5(\nabla \boldsymbol{u} + (\nabla \boldsymbol{u})^T)$ is the symmetric rate of deformation tensor, d_s is the particle diameter and $\bar{\mu}_f$ is the viscosity of the continuous phase material. Ho & Leal tabulate g_1 and g_2 for simple shear flow and Poiseuille flow.

Stokes drag [48] is the most familiar interaction between dispersed and continuous phases. Faxén force [10] accounts for residual viscous effects exerted by a deforming fluid on particles. Saffman lift [40] is caused by the interaction of slip velocity with the mean shearing of the continuous phase and is responsible for the Segrè Silberberg effect. Ho & Leal lift [20] accounts for wall effects causing lift.

Ho & Leal lift is ignored because the fluid velocity field is not simple shear flow or Poiseuille flow.

Particle diameter d_s, continuous phase density $\bar{\rho}_f$ and the settling velocity at infinite dilution $V_{s,\infty}$ are used to nondimensionalize Equation A.1:

$$\begin{aligned} \hat{\boldsymbol{m}}_{si} = {} & \hat{\phi}_s \frac{18}{\mathrm{Re}_{s,\infty}} (\hat{\boldsymbol{u}}_f - \hat{\boldsymbol{u}}_s) && \text{Stokes drag} \\ & + \hat{\phi}_s \frac{3(6.46)}{2\pi} \sqrt{\frac{1}{\mathrm{Re}_{s,\infty}}} \hat{\boldsymbol{D}}_f \left(\frac{1}{2 \operatorname{tr} \hat{\boldsymbol{D}}_f^2} \right)^{1/4} (\hat{\boldsymbol{u}}_f - \hat{\boldsymbol{u}}_s) && \text{Saffman lift} \\ & + \hat{\phi}_s 2 \, \frac{7}{4} \frac{1}{\mathrm{Re}_{s,\infty}} \hat{\nabla} \cdot \hat{\boldsymbol{D}}_f && \text{Faxèn force} \end{aligned} \tag{A.2}$$

$\mathrm{Re}_{s,\infty}$ is the particle Reynolds number at infinite dilution.

The slip velocity $(\hat{\boldsymbol{u}}_f - \hat{\boldsymbol{u}}_s)$ is $O(1)$. The largest velocity gradient associated with inclined plate sedimentation occurs near the top of the clear fluid slit. For the suspensions used in the experimental work of Shaqfeh & Acrivos the maximum velocity was $O(100\, V_{s,\infty})$ and the distance was $O(5\,\mathrm{mm})$ or $O(40\, d_s)$. The dimensionless velocity gradients are $O(\hat{\boldsymbol{D}}) = 100/40$ and $O(\nabla \cdot \hat{\boldsymbol{D}}) = 100/40^2$. The contributions to the momentum interaction has the following orders of magnitude:

$$\begin{aligned} O(\boldsymbol{m}_{si}) = {} & \hat{\phi}_s \frac{18}{\mathrm{Re}_{s,\infty}} && \text{Stokes drag} \\ & + \hat{\phi}_s \, 4.1 \sqrt{\frac{1}{\mathrm{Re}_{s,\infty}}} && \text{Saffman lift} \\ & + \hat{\phi}_s \frac{0.22}{\mathrm{Re}_{s,\infty}} && \text{Faxèn force} \end{aligned} \tag{A.3}$$

Faxén force is ignored because it is two orders of magnitude smaller than Stokes drag force. The suspensions of interest have $\mathrm{Re}_{s,\infty} < O(0.1)$. Stokes drag force is of order $O(180\, \phi_s)$ in the vertical direction and Saffman lift is of order $O(13\, \phi_s)$ normal to the inclined surface. Saffman lift is negligible for $\mathrm{Re}_{s,\infty} < 0.1$ and for inclined vessels.

A.2 Slip velocity

An order of magnitude analysis is performed on the simplified two fluid momentum equations 2.4 to demonstrate the dispersed phase slip velocity $(\boldsymbol{u}_s - \boldsymbol{u}_f)$ is independent of the fluid motion. The momentum equations 2.4 for the continuous and dispersed phases are written in nonconservative form and divided by volume fraction:

$$\begin{aligned}\bar{\rho}_f\left(\frac{\partial \boldsymbol{u}_f}{\partial t}+\boldsymbol{u}_f\cdot\nabla\boldsymbol{u}_f\right) &= -\nabla p+\frac{\nabla\cdot\phi_f\boldsymbol{\tau}_f}{\phi_f}+\bar{\rho}_f\boldsymbol{g} \\ &\quad -\frac{\phi_s}{\phi_f}\frac{18\bar{\mu}_f}{d_s^2}\frac{f(\phi_f)}{\phi_f}(\boldsymbol{u}_f-\boldsymbol{u}_s)\end{aligned} \tag{A.4}$$

$$\bar{\rho}_s\left(\frac{\partial \boldsymbol{u}_s}{\partial t}+\boldsymbol{u}_s\cdot\nabla\boldsymbol{u}_s\right) = -\nabla p+\bar{\rho}_s\boldsymbol{g}+\frac{18\bar{\mu}_f}{d_s^2}\frac{f(\phi_f)}{\phi_f}(\boldsymbol{u}_f-\boldsymbol{u}_s) \tag{A.5}$$

Shear stress was neglected from the dispersed phase momentum equation A.5. Equation A.5 is subtracted from Equation A.4 to eliminate the pressure gradient:

$$\begin{aligned}&\bar{\rho}_f\left(\frac{\partial \boldsymbol{u}_f}{\partial t}+\boldsymbol{u}_f\cdot\nabla\boldsymbol{u}_f\right)-\bar{\rho}_s\left(\frac{\partial \boldsymbol{u}_s}{\partial t}+\boldsymbol{u}_s\cdot\nabla\boldsymbol{u}_s\right) \\ &= \frac{\nabla\cdot\phi_f\boldsymbol{\tau}_f}{\phi_f}+(\bar{\rho}_f-\bar{\rho}_s)\boldsymbol{g}-\frac{18\bar{\mu}_f}{d_s^2}\frac{f(\phi_f)}{\phi_f^2}(\boldsymbol{u}_f-\boldsymbol{u}_s)\end{aligned} \tag{A.6}$$

Equation A.6 is the force balance that governs the slip velocity of the dispersed phase. The slip velocity $(\boldsymbol{u}_f-\boldsymbol{u}_s)$ is independent of the fluid motion if the gravitational force $(\bar{\rho}_f-\bar{\rho}_s)\boldsymbol{g}$ is much greater than the shear stress contribution $(\nabla\cdot\phi_f\boldsymbol{\tau}_f)/\phi_f$ and the convection terms $\bar{\rho}_f\boldsymbol{u}_f\cdot\nabla\boldsymbol{u}_f$ and $\bar{\rho}_s\boldsymbol{u}_s\cdot\nabla\boldsymbol{u}_s$. The shear stress contribution is assumed to be

$$\frac{\nabla\cdot\phi_f\boldsymbol{\tau}_f}{\phi_f}\simeq\bar{\mu}_f\nabla^2\boldsymbol{u}_f \tag{A.7}$$

Equation A.6 is nondimensionalized with the particle diameter d_s, continuous phase density $\bar{\rho}_f$ and the settling velocity at infinite dilution $V_{s,\infty}$:

$$\begin{aligned}&\left(\frac{\partial \hat{\boldsymbol{u}}_f}{\partial \hat{t}}+\hat{\boldsymbol{u}}_f\cdot\hat{\nabla}\hat{\boldsymbol{u}}_f\right)-\frac{\bar{\rho}_s}{\bar{\rho}_s}\left(\frac{\partial \hat{\boldsymbol{u}}_s}{\partial \hat{t}}+\hat{\boldsymbol{u}}_s\cdot\hat{\nabla}\hat{\boldsymbol{u}}_s\right) \\ &= \frac{1}{\mathrm{Re}_{s,\infty}}\hat{\nabla}^2\hat{\boldsymbol{u}}_f+\frac{18}{\mathrm{Re}_{s,\infty}}-\frac{18}{\mathrm{Re}_{s,\infty}}\frac{f(\phi_f)}{\phi_f^2}(\hat{\boldsymbol{u}}_f-\hat{\boldsymbol{u}}_s)\end{aligned} \tag{A.8}$$

The nondimensional gravitational force is $18/\mathrm{Re}_{s,\infty}$.

The previous order of magnitude analysis shows the shear stress contribution is $O((100/40^2)/\mathrm{Re}_{s,\infty})$ and is much smaller than the gravitational term $18/\mathrm{Re}_{s,\infty}$.

The ratio $\bar{\rho}_s/\bar{\rho}_f$ is $O(1)$. Both of the convection terms $\hat{\boldsymbol{u}}_f\cdot\hat{\nabla}\hat{\boldsymbol{u}}_f$ and $\hat{\boldsymbol{u}}_s\cdot\hat{\nabla}\hat{\boldsymbol{u}}_s$ have the same order of magnitude: the largest value is $\hat{v}_f\partial\hat{v}_f/\partial\hat{y}$ in the y momentum equation. The vertical velocity varies from zero to $O(100\,V_{s,\infty})$ over the length of the vessel ($O(0.8\,\mathrm{m})$ or $O(5700\,d_s)$). This convection term is $O(100\,100/5700)=O(1.8)$. The suspensions have $\mathrm{Re}_{s,\infty}<O(0.1)$: the gravitational term is $O(18/\mathrm{Re})>O(180)$. The convection terms are negligible compared to the gravitational term.

The slip velocity of the dispersed phase is independent of the fluid motion for the suspensions considered in this work.

Appendix B

Derivation of the momentum equations for the homogeneous model

The momentum equation is derived for the homogeneous mixture model from the two-fluid momentum equations

$$\begin{aligned} \bar{\rho}_f \left[\frac{\partial \phi_f \boldsymbol{u}_f}{\partial t} + \nabla \cdot (\phi_f \boldsymbol{u}_f \boldsymbol{u}_f) \right] &= -\phi_f \nabla p + \nabla \cdot \boldsymbol{\tau}_f - \phi_f \bar{\rho}_f \boldsymbol{g} + \boldsymbol{m}_s^f & \text{(B.1)} \\ \bar{\rho}_s \left[\frac{\partial \phi_s \boldsymbol{u}_s}{\partial t} + \nabla \cdot (\phi_s \boldsymbol{u}_s \boldsymbol{u}_s) \right] &= -\phi_s \nabla p + \nabla \cdot \boldsymbol{\tau}_s - \phi_s \bar{\rho}_s \boldsymbol{g} - \boldsymbol{m}_s^f & \text{(B.2)} \end{aligned}$$

The momentum equation for the mixture is the sum of equations B.1 and B.2:

$$\bar{\rho}_f \left[\frac{\partial \phi_f \boldsymbol{u}_f}{\partial t} + \nabla \cdot (\phi_f \boldsymbol{u}_f \boldsymbol{u}_f) \right] + \bar{\rho}_s \left[\frac{\partial \phi_s \boldsymbol{u}_s}{\partial t} + \nabla \cdot (\phi_s \boldsymbol{u}_s \boldsymbol{u}_s) \right] = -\nabla p + \nabla \cdot \boldsymbol{\tau}_m - \rho_m \boldsymbol{g} \quad \text{(B.3)}$$

The mixture density is $\rho_m = \phi_f \bar{\rho}_f + \phi_s \bar{\rho}_s$ and the shear stress on the mixture is $\boldsymbol{\tau}_m$ The objective is to write Equation B.3 in terms of the volume average mixture velocity $\boldsymbol{u}_m = \phi_f \boldsymbol{u}_f + \phi_s \boldsymbol{u}_s$ and the velocity of the dispersed phase relative to the mixture $\boldsymbol{u}_s^s = \boldsymbol{u}_s - \boldsymbol{u}_m$. The velocity of the continuous phase relative to the mixture is $\boldsymbol{u}_f^s = \boldsymbol{u}_f - \boldsymbol{u}_m$.

Equation B.3 is rearranged to

$$\begin{aligned} \bar{\rho}_f \left[\frac{\partial \boldsymbol{u}_m}{\partial t} + \nabla \cdot (\boldsymbol{u}_m \boldsymbol{u}_m) \right] &+ \bar{\rho}_f \left[\nabla \cdot (\phi_f \boldsymbol{u}_f \boldsymbol{u}_f^s) + \nabla \cdot (\phi_s \boldsymbol{u}_s \boldsymbol{u}_s^s) \right] & \text{(B.4)} \\ &+ (\bar{\rho}_s - \bar{\rho}_f) \left[\frac{\partial \phi_s \boldsymbol{u}_s}{\partial t} + \nabla \cdot (\phi_s \boldsymbol{u}_s \boldsymbol{u}_s) \right] = -\nabla p + \nabla \cdot \boldsymbol{\tau}_m - \rho_m \boldsymbol{g} \end{aligned}$$

The first term in Equation B.4 is

$$\bar{\rho}_f \left[\frac{\partial \boldsymbol{u}_m}{\partial t} + \nabla \cdot (\boldsymbol{u}_m \boldsymbol{u}_m) \right]$$

The continuity equation $\nabla \cdot \boldsymbol{u}_m = 0$ is imposed on this expression: the first term in Equation B.4 becomes

$$\bar{\rho}_f \left[\frac{\partial \boldsymbol{u}}{\partial t} + \boldsymbol{u} \cdot \nabla \boldsymbol{u} \right] \tag{B.5}$$

The second term of equation B.4 is

$$\bar{\rho}_f \nabla \cdot \left[\phi_f \boldsymbol{u}_f \boldsymbol{u}'_f + \phi_s \boldsymbol{u}_s \boldsymbol{u}'_s \right]$$

Since $\boldsymbol{u}_f = \boldsymbol{u}_m + \boldsymbol{u}'_f$ and $\boldsymbol{u}_s = \boldsymbol{u}_m + \boldsymbol{u}'_s$ the above equation becomes

$$\bar{\rho}_f \nabla \cdot \left[\phi_f (\boldsymbol{u}_m + \boldsymbol{u}'_f) \boldsymbol{u}'_f + \phi_s (\boldsymbol{u}_m + \boldsymbol{u}'_s) \boldsymbol{u}'_s \right]$$

The above equation is expanded and terms with $\boldsymbol{u}_m$ are collected

$$\bar{\rho}_f \nabla \cdot \left[\boldsymbol{u}_m (\phi_f \boldsymbol{u}'_f + \phi_s \boldsymbol{u}'_s) + \phi_f \boldsymbol{u}'_f \boldsymbol{u}'_f + \phi_s \boldsymbol{u}'_s \boldsymbol{u}'_s \right]$$

The definitions of the $\boldsymbol{u}'_f$ and $\boldsymbol{u}'_s$ are substituted in the $\boldsymbol{u}_m(\phi_f \boldsymbol{u}'_f + \phi_s \boldsymbol{u}'_s)$ term:

$$\bar{\rho}_f \nabla \cdot \left[\boldsymbol{u}_m (\phi_f \boldsymbol{u}_f - \phi_f \boldsymbol{u}_m + \phi_s \boldsymbol{u}_m - \phi_s \boldsymbol{u}_s) + \phi_f \boldsymbol{u}'_f \boldsymbol{u}'_f + \phi_s \boldsymbol{u}'_s \boldsymbol{u}'_s \right]$$

Terms with $\boldsymbol{u}_m$ are collected

$$\bar{\rho}_f \nabla \cdot \left[\boldsymbol{u}_m ((\phi_f \boldsymbol{u}_f + \phi_s \boldsymbol{u}_s) - \boldsymbol{u}_m (\phi_f + \phi_s)) + \phi_f \boldsymbol{u}'_f \boldsymbol{u}'_f + \phi_s \boldsymbol{u}'_s \boldsymbol{u}'_s \right]$$

Since $\phi_f + \phi_s = 1$ and $\boldsymbol{u}_m = \phi_f \boldsymbol{u}_f + \phi_s \boldsymbol{u}_s$ the above equation is

$$\bar{\rho}_f \nabla \cdot \left[\phi_f \boldsymbol{u}'_f \boldsymbol{u}'_f + \phi_s \boldsymbol{u}'_s \boldsymbol{u}'_s \right] \tag{B.6}$$

The continuous phase slip velocity $\boldsymbol{u}'_f$ is related to $\boldsymbol{u}'_s$ through the definitions of the slip velocities:

$$\begin{aligned} \boldsymbol{u}'_f &= \boldsymbol{u}_f - \boldsymbol{u}_m \\ &= \boldsymbol{u}_f - (\boldsymbol{u}_s - \boldsymbol{u}'_s) \\ &= \boldsymbol{u}_f - \boldsymbol{u}_s + \boldsymbol{u}'_s \end{aligned}$$

But $\boldsymbol{u}_f - \boldsymbol{u}_s = -\boldsymbol{u}'_s/(1-\phi_s)$ so

$$\boldsymbol{u}'_f = \frac{-\phi_s \boldsymbol{u}'_s}{1-\phi_s}$$

This expression is substituted into Equation B.6:

$$\bar{\rho}_f \nabla \cdot \left[\phi_f \frac{\phi_s \boldsymbol{u}'_s}{1-\phi_s} \frac{\phi_s \boldsymbol{u}'_s}{1-\phi_s} + \phi_s \boldsymbol{u}'_s \boldsymbol{u}'_s \right]$$

The second term of Equation B.4 is

$$\bar{\rho}_f \nabla \cdot \left[\frac{\phi_s}{1-\phi_s}\boldsymbol{u}'_s\boldsymbol{u}'_s\right] \tag{B.7}$$

The third term of Equation B.4 is

$$(\bar{\rho}_s - \bar{\rho}_f)\left[\frac{\partial \phi_s \boldsymbol{u}_s}{\partial t} + \nabla \cdot (\phi_s \boldsymbol{u}_s \boldsymbol{u}_s)\right]$$

The dispersed phase continuity equation $\frac{\partial \phi_s}{\partial t} + \nabla \cdot (\phi_s \boldsymbol{u}_s) = 0$ is imposed on the above expression to produce

$$\phi_s(\bar{\rho}_s - \bar{\rho}_f)\left[\frac{\partial \boldsymbol{u}_s}{\partial t} + \boldsymbol{u}_s \cdot \nabla \boldsymbol{u}_s\right] \tag{B.8}$$

The definition of the dispersed phase slip velocity $\boldsymbol{u}_s = \boldsymbol{u}_m + \boldsymbol{u}'_s$ is substituted for $\boldsymbol{u}_s$ in B.8:

$$\phi_s(\bar{\rho}_s - \bar{\rho}_f)\left[\frac{\partial \boldsymbol{u}_m}{\partial t} + \boldsymbol{u}_m \cdot \nabla \boldsymbol{u}_m + \frac{\partial \boldsymbol{u}'_s}{\partial t} + \boldsymbol{u}_m \cdot \nabla \boldsymbol{u}'_s + \boldsymbol{u}'_s \cdot \nabla \boldsymbol{u}_m + \boldsymbol{u}'_s \cdot \nabla \boldsymbol{u}'_s\right] \tag{B.9}$$

Equations B.5, B.7 and B.9 are substituted for the first, second and third terms in equation B.4. The definition of the mixture density $\rho_m = \bar{\rho}_f + \phi_s(\bar{\rho}_s - \bar{\rho}_f)$ is used to combine expressions in Equations B.5 and B.9

$$\begin{aligned} \rho_m\left[\frac{\partial \boldsymbol{u}}{\partial t} + \boldsymbol{u}_m \cdot \nabla \boldsymbol{u}_m\right] &+ \bar{\rho}_f \nabla \cdot \left[\frac{\phi_s}{1-\phi_s}\boldsymbol{u}'_s\boldsymbol{u}'_s\right] \\ + \quad & \phi_s(\bar{\rho}_s - \bar{\rho}_f)\left[\frac{\partial \boldsymbol{u}'_s}{\partial t} + \boldsymbol{u}_m \cdot \nabla \boldsymbol{u}'_s + \boldsymbol{u}'_s \cdot \nabla \boldsymbol{u}_m + \boldsymbol{u}'_s \cdot \nabla \boldsymbol{u}'_s\right] \\ & = -\nabla p + \nabla \cdot \boldsymbol{\tau}_m - \rho_m \boldsymbol{g} \end{aligned} \tag{B.10}$$

The second and third terms on the left hand side of Equation B.10 contain gradients of the dispersed phase slip velocity. The slip velocity is a discontinuous function across the suspension interface and results in these gradient terms being undefined. The expression $\phi_s(\bar{\rho}_s - \bar{\rho}_f)\boldsymbol{u}'_s \cdot \nabla \boldsymbol{u}$ in the third term is much smaller than the expression $\rho_m \boldsymbol{u} \cdot \nabla \boldsymbol{u}$ in the first term of Equation B.10 because $\phi_s(\bar{\rho}_s - \bar{\rho}_f) \ll \rho_m$ and $\boldsymbol{u}'_s \ll \boldsymbol{u}_m$. The second and third terms of Equation B.10 are negligible.

The momentum equation for the homogeneous mixture is

$$\rho_m\left[\frac{\partial \boldsymbol{u}_m}{\partial t} + \boldsymbol{u}_m \cdot \nabla \boldsymbol{u}_m\right] = -\nabla p + \nabla \cdot \boldsymbol{\tau}_m - \rho_m \boldsymbol{g} \tag{B.11}$$

Appendix C

Flow of a stratified fluid between inclined parallel plates

Analytic solutions for two density stratified flows between inclined parallel plates are presented. These examples are limiting cases where the suspension/clear fluid interface is represented as a discontinuity and the interface is smeared over a large distance.

In the first case two fluids of density $\rho-\delta\rho/2$ and $\rho+\delta\rho/2$ occupy equal portions of the inclined vessel shown in Figure C.1 For fully developed flow the y-direction momentum equations for the two fluids are

$$0 = -\frac{\partial p}{\partial y} + \mu\frac{\partial^2 v_l}{\partial x^{2^2}} - (\rho - \delta\rho/2)g_y \tag{C.1}$$

$$0 = -\frac{\partial p}{\partial y} + \mu\frac{\partial^2 v_h}{\partial x^{2^2}} - (\rho + \delta\rho/2)g_y \tag{C.2}$$

The boundary conditions are no slip at the walls,

$$v_h(-l/2) = 0, \qquad v_l(l/2) = 0$$

the velocity field is continuous at the interface $x = 0$,

$$v_h(0) = v_l(0)$$

and the shear stress is continuous at the interface $x = 0$,

$$\frac{\partial v_h(0)}{\partial x} = \frac{\partial v_l(0)}{\partial x}$$

The global material balance requires the net flow across the channel to be zero

$$0 = \int_{-l/2}^{0} v_h\,dx + \int_{0}^{l/2} v_l\,dx$$

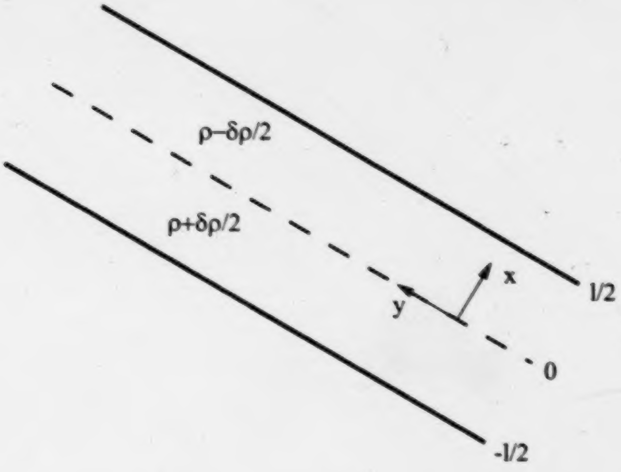

Figure C.1: Gravity driven flow of a density stratified fluid between inclined parallel plates.

The second case is for a fluid where the density varies linearly across the vessel. The y-direction momentum equation is

$$0 = -\frac{\partial p}{\partial y} + \mu \frac{\partial^2 v}{\partial x^{22}} - \left(\rho + \frac{x\,\delta\rho}{l}\right) g_y \tag{C.3}$$

The boundary conditions are no slip at the walls,

$$v(-l/2) = 0, \qquad v(l/2) = 0$$

The net flow across the channel is zero

$$0 = \int_{-l/2}^{l/2} v\,dx$$

The Mathematica script for solving these two problems follows.

In[1]:=

```
/*
Solution for fully developed gravity driven flow of two
superposed fluids between inclined parallel plates.

Fluid on the left is 'g', that on the right is 'a'.
Density difference is 'dr' and the interface is at x=0.

Boundary conditions:
    no slip at the walls (x = +- 1/2)
    continuous velocity and first derivative at x = 0
    total volumetric flow is zero.
*/

Syntax::sntxb: Expression cannot begin with "/*".

vgrule = DSolve[{vg''[x]==(dp - (rho+dr/2)*gy)/mu,
        vg[-1/2] == 0,
        vg[0] == vint},
        vg, x]
```

Out[1]=

```
{{vg -> (((1 + 2 #1) (8 mu vint + 2 dp 1 #1 -
            dr gy 1 #1 - 2 gy 1 rho #1)) / (8 1 mu) & )}}
```

In[2]:=

```
varule = DSolve[{va''[x]==(dp - (rho-dr/2)*gy)/mu,
        va[0] == vint,
        va[1/2] == 0},
        va, x]

General::spell1:
   Possible spelling error: new symbol name "varule"
     is similar to existing symbol "vgrule".
```

Out[2]=

```
{{va -> (((1 - 2 #1) (8 mu vint - 2 dp 1 #1 -
            dr gy 1 #1 + 2 gy 1 rho #1)) / (8 1 mu) & )}}
```

In[3]:=

```
vintrule = Solve[(vg'[0] /. vgrule) == (va'[0] /.varule),
           vint]
```

Out[3]=

```
                     2        2
             -(dp 1  - gy 1  rho)
{{vint -> ---------------------}}
                   8 mu
```

In[4]:=

```
totalflow = Simplify[Integrate[(vg[x] /. vgrule),
        {x, -1/2, 0}] +
Integrate[(va[x] /. varule), {x, 0, 1/2}] /. vintrule]
```

Out[4]=

```
    3
  l   (-dp + gy rho)
{{-------------------}}
        12 mu
```

In[5]:=

```
dprule = Solve[totalflow == 0, dp]
```

Out[5]=

```
{{dp -> gy rho}}
```

In[6]:=

```
vgeqn = Simplify[{{vg[x] /. vgrule} /. vintrule}/.dprule
```

Out[6]=

```
{{{{{-(dr gy x (1 + 2 x))}}}}}
     ---------------------
             8 mu
```

In[7]:=

```
vaeqn = Simplify[{{va[x] /. varule} /. vintrule}/.dprule
```

```
General::spell1:
   Possible spelling error: new symbol name "vaeqn"
     is similar to existing symbol "vgeqn".
```

Out[7]=

```
{{{{{-(dr gy (1 - 2 x) x)}}}}}
     ---------------------
             8 mu
```

In[8]:=

```
Plot[{mu=0.001;
    rho=1000;dr=10;
    l=0.1;del=0.05;
    gy=-0.5*9.81;vgeqn,vaeqn}, {x, -0.05, 0.05},
    AxesLabel -> {x, v}]
```

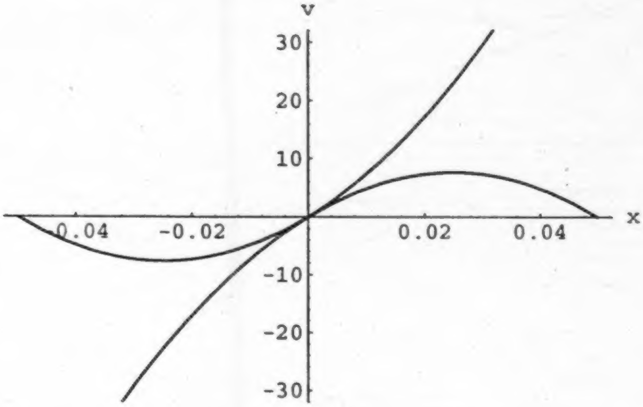

Out[8]=

```
-Graphics-
```

In[9]:=

```
Plot[{mu=0.001;
    rho=1000;dr=10;
    l=0.1;del=0.05;
    gy=-0.5*9.81;vaeqn}, {x, 0, 0.05},
    AxesLabel -> {x, v}]
```

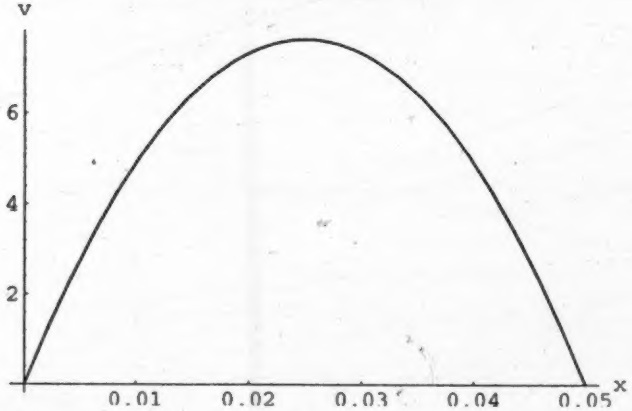

Out[9]=

```
-Graphics-
```

In[10]:=

```
/*
Solution for fully developed gravity driven flow of a
fluid with a uniform density gradient between inclined
parallel plates.

Density gradient is 'drf/lf'.

Boundary conditions:
    no slip at the walls (x = +- 1/2)
    total volumetric flow is zero.
*/

Syntax::sntxb: Expression cannot begin with "/*".

vrule = DSolve[{v''[x]==(dpf-(rhof-(drf/lf)*x)*gfy)/muf,
        v[-lf/2] == 0,
        v[lf/2] == 0},
        v, x]

General::spell:
   Possible spelling error: new symbol name "vrule"
     is similar to existing symbols {varule, vgrule}.

General::spell1:
   Possible spelling error: new symbol name "rhof"
     is similar to existing symbol "rho".
```

Out[10]=

```
{{v -> (((3 dpf lf - 3 gfy lf rhof + drf gfy #1)
                2          2
           (-lf  + 4 #1 )) / (24 lf muf) & )}}
```

In[11]:=

```
totalflow2 = Simplify[Integrate[(v[x] /. vrule),
        {x, -lf/2, lf/2}] ]
```

Out[11]=

```
   3
 lf  (-dpf + gfy rhof)
{---------------------}
       12 muf
```

In[12]:=

```
dprule2 = Solve[totalflow2 == 0, dpf]
```

Out[12]=

```
{{dpf -> gfy rhof}}
```

In[13]:=

```
veqn = Simplify[{v[x] /. vrule} /. dprule2]
```

```
General::spell:
   Possible spelling error: new symbol name "veqn"
     is similar to existing symbols {vaeqn, vgeqn}.
```

Out[13]=

```
                        2      2
    {{{drf gfy x (-lf  + 4 x )}}}
        -----------------------
              24 lf muf
```

In[14]:=

```
Plot[{muf=0.001;
    rhof=1000;drf=10;
    lf=0.1;
    gfy=-0.5*9.81;veqn}, {x, -0.05, 0.05},
    AxesLabel -> {x, v}]
```

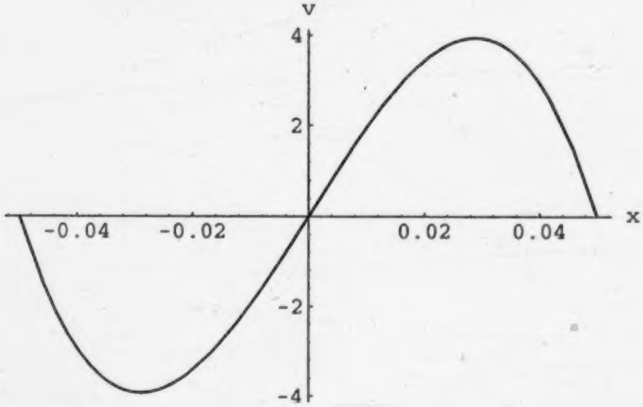

Out[14]=

```
-Graphics-
```

In[15]:=

```
Plot[{muf=0.001;
    rhof=1000;drf=10;
    lf=0.1;
    gfy=-0.5*9.81;veqn}, {x, 0, 0.05},
    AxesLabel -> {x, v}]
```

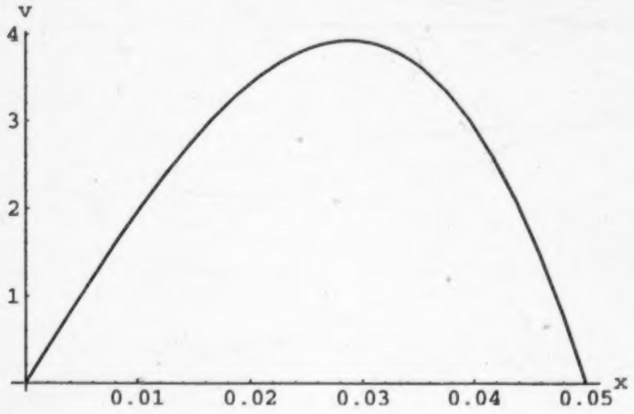

```
Out[15]=
   -Graphics-
```